Detection and characterisation of stellar companions to transiting extrasolar planets through high resolution imaging

Daniel Fred Evans

Doctor of Philosophy

Department of Physics, Keele University

June 2019

Abstract

Since the discovery over two decades ago of the first 'hot Jupiter', there has been persistent debate regarding the formation and origins of this class of planets. Some of the many 'migration' theories for hot Jupiters suggest that these planets form in binary star systems, being driven inwards towards their host star by dynamical interactions. If this is the case, many hot Jupiters should be found in multiple stellar systems, which might only be resolved with dedicated high resolution imaging. An additional use for high resolution imaging is the detection of previously unresolved sources of contaminating light, which can significantly bias the properties derived for planets.

Observations were carried out of 156 transiting exoplanet systems with lucky imaging, and of 46 systems with near-infrared adaptive options, in order to detect stars at small angular separation, and to identify binary companions. The lucky imaging survey identified 39 plausible multiple systems, and historical measurements allowed binary orbits to be determined for WASP-77 and WASP-85. The AO survey identified companion stars to 26 of its 46 targets, although further work is needed to confirm the nature of several of these companions.

A surprising trend among the confirmed binary companions, both in this work and others, is that they are generally much less massive than the planet host stars. This contrasts with studies of solar type stars have shown that binaries most often consist of components with similar masses, and further investigation is needed to explain the trend among exoplanet host stars.

The Gaia survey has proved a useful source of additional astrometric data in this work, and is already competitive with lucky imaging for detection of companions. Future Gaia data releases will further improve this further, and detailed searches for binary companions present in the Gaia data are strongly encouraged.

Acknowledgements

I thank my supervisor, John Taylor (Southworth), for his continual encouragement and guidance in all aspects of the project, whilst also permitting me a relatively free hand to pursue my own independent ideas and projects, and for ensuring the entire Ph.D. was a relatively light-hearted experience. The work was a learning experience for both of us, and we both now realise how tortuous high resolution imaging can be. His knowledge of the field of transiting exoplanets, in addition to his experience analysis of exoplanet light curves and radial velocity measurements, helped to place much of my work in context, in addition to providing useful input to the re-analysis of the WASP-20AB system. I also appreciate the large number of observing trips that John was able to organise (and secure funding for) during the course of my Ph.D., giving valuable hands-on experience in addition to a good excuse to see distant parts of the world.

Barry Smalley, my second supervisor, also provided a helpful source of knowledge, in particular through his great expertise on spectroscopic analysis, in addition to the utterly terrible quips and jokes he can (and does) produce at a moment's notice. Pierre Maxted and Rob Jeffries, also of the Keele Astrophysics group, also provided useful scientific advice.

I must most certainly acknowledge one fellow Ph.D. student in particular, Jessica, who I met and subsequently married during the course of our Ph.D. studies, which expresses my appreciation for her far more succinctly than I could do in writing. We have spent far too many of our free hours discussing binary stars, whether they be my wide binaries of questionable veracity, or her very precisely characterised eclipsing binaries that never seem to contain only two stars.

I appreciate the support and friendship of the numerous Ph.D. students who I have met and worked with during my time at Keele, even if none of us could ever agree on the setting for the air conditioning in the office. I'm glad that many of us found one another's research useful during our time at Keele.

The MiNDSTEp consortium has been integral in ensuring the success of this work, having graciously provided the telescope, instrument, and observing time needed for the TCI lucky imaging campaign. The creation of the TCI instrument and its associated reduction pipeline are much appreciated. Through my collaboration with the group and observing runs on their behalf, I have made a great many friends, and have received much help and encouragement in my scientific endeavours.

For their assistance in the proposal, planning, and interpretation of the SPHERE observations, thanks go to Julien Girard and Sasha Hinkley. I thank the SPHERE Data Center team, in particular Philippe Delorme, for their patience and fast responses to my many questions and bug reports. Similarly, the User Support Department and Instrument Scientists at ESO have provided assistance, related to both the SPHERE observations and to other issues. Thanks also go to Brian Mason of the US Naval Observatory, for his prompt and helpful responses to requests for data from the Washington Double Star catalogue.

Work contributed by others

The lucky imaging observations taken during 2014 predate the start of this Ph.D. thesis. Planning and organisation was carried out by Dr. John Taylor, with observations performed by numerous members of the MiNDSTEp consortium. For both of the two six-month lucky imaging observing campaigns in 2015 and 2016, the author performed on-site observations for two weeks, with the assistance of a remote observer for the second half of the night. The remaining observations were carried out by the MiNDSTEp consortium. The basic reduction of the lucky imaging data (bias and flat field corrections, and selection of high quality images) was performed by an automatic pipeline developed and maintained by the MiNDSTEp consortium.

The SPHERE observations were carried out by ESO staff astronomers from observing blocks prepared by the author. The reduction of the data was carried out using

both the official ESO reduction pipeline and the VLTPF pipeline.[1]

[1]Developed by A. Vigan, `https://github.com/avigan/VLTPF`

Contents

List of Figures

List of Tables

1 Introduction

The field of observational exoplanetary science was kickstarted in the mid-1990s, following first the initial discovery of 'pulsar planets', exoplanets orbiting the compact remnant of a star (Wolszczan & Frail 1992), and then the subsequent discovery of a planet orbiting a star like our own Sun (Mayor & Queloz 1995). Initially, many planets were detected through their radial velocity signal, but transit detection has since become dominant, following the first measurement of an exoplanet transiting the face of its host star (Henry et al. 2000, Charbonneau et al. 2000), and the subsequent initial discovery of a planet through its transit signal (Konacki et al. 2003). Currently, transiting planets are by far the most favourable for detailed characterisation, as they allow the mass, radius, and atmospheric properties of the planet to be measured with relative ease. Furthermore, it is possible to survey hundreds of thousands of stars simultaneously for transits with modest observing facilities, as compared to more targeted survey techniques, such as radial velocity and direct imaging searches, which require a large amount of observing time for each target using large telescopes. As a result, there are a wide variety of transiting planet surveys, both those on the ground, such as WASP (Pollacco et al. 2006), HAT/HATSouth (Bakos et al. 2002, Bakos et al. 2013), KELT (Pepper et al. 2007), and NGTS (Wheatley et al. 2018), and those in space, including CoRoT (Auvergne et al. 2009), *Kepler*/K2 (Borucki et al. 2010, Howell et al. 2014), and the upcoming TESS (Ricker et al. 2014) and PLATO (Rauer et al. 2014) missions.

With current technology, it is not possible to separately resolve any known transiting planets from their host stars with high resolution imaging – the stars are too distant, the planets are too close to their host stars, and the planets are much too faint. However, high resolution imaging of transiting exoplanet systems is still of interest for the purposes of resolving additional stars, either those forming a wide binary with the planet host star, or instead physically unassociated stars along the line of sight. For stars physically associated with the system, it is of interest to determine the properties of planet-hosting binaries – approximately half of all stellar systems contain

multiple stars, some of which will have significant dynamical interactions with planets or protoplanetary disks, affecting the formation and evolution of planetary systems. Resolving stars at small angular separations also has the pragmatic benefit of allowing the parameters of the planet to be correctly determined, as the light from additional stars will alter both the photometric and spectroscopic signals caused by the planet. In some cases, high resolution imaging can identify cases where the observed signal is not caused by a planet, but instead another form of astrophysical variability.

1.1 Planet formation in the solar system

Our knowledge of the eight planets orbiting our own Sun long guided the efforts to understand the process of planetary formation. It was noted at an early stage that the solar system is much better aligned than expected by chance (e.g. Laplace 1796). The orbital planes of the planets are aligned to within a couple of degrees of one another, and the major moons of the solar system share this alignment. This alignment is also seen in the rotation of the Sun and most of the planets, which rotate in the same direction as the orbits.[1] Furthermore, the planets have nearly circular orbits, with Mercury having the highest eccentricity of $e = 0.2$.

Such a high degree of alignment is extremely unlikely to have happened by chance, indicating some common origin of the angular momentum within the solar system. The 'nebular hypothesis' was initially suggested in the 18th century, with Laplace (1796) providing one of the more detailed considerations of the idea. The hypothesis assumes that at an earlier stage in the life of the solar system, a vast, rotating cloud extended far enough out from the Sun to include the orbits of all the planets. Laplace envisioned the cloud being the hot, extended atmosphere of the Sun, which began cooling and condensing from its outermost edge. The condensed material then accreted to form the

[1]Venus rotates retrograde, whilst Uranus is tilted by 98° from its orbital axis. Hypotheses to explain the latter include a collision with another body (Safronov 1966) or secular interactions with other planets (Boué & Laskar 2010).

planets that we see today, with a similar process occurring around the planets invoked to explain the existence of the moons and the rings of Saturn. Laplace noted two outstanding issues with the hypothesis: firstly, the highly inclined and eccentric orbits of the comets suggested a different, unexplained origin; and secondly, that gravitational and viscous attraction between the cloud and planet within it should have caused the planets to lose orbital energy and eventually become engulfed by the Sun.

1.1.1 Creating rocky bodies

Following early work on the nebular hypothesis, many alternative theories for the formation of the planets were put forward during the early 20th century (see Woolfson 1993 for an overview of the early history of formation theories), but the nebular hypothesis has now reached widespread acceptance, following in particular the detailed investigation of Safronov (1972). The initial rotating cloud of material remains a key part of the hypothesis, but it is not thought to be the initial material from which the Sun was born, providing the link between the Sun's rotation and that of the planets and their orbits. The cloud collapses under its own self gravity, with conservation of angular momentum resulting in this collapse occurring perpendicular to the axis of rotation, forming a dense disk of material orbiting around the young Sun.

The contents of such clouds and disks are typically divided into two components: gas, consisting of hydrogen and helium; and dust, which includes heavier elements in the form of silicates, hydrocarbons, or condensed 'ices' – molecules with low melting points, such as H_2O, CO_2, and CH_4. In the disk, dust particles begin to collide and stick together to form small grains of a few micrometres in size. This process of collisional growth continues in a hierarchical fashion – grains are grouped together into dusty aggregates, which form into small pebbles, and eventually these collect together to form planetesimals, which are of the order of a few kilometres in size (Montmerle et al. 2006).

At the stage of planetesimals, the gravitational attraction between the orbiting bodies becomes non-negligible, and they must no longer wait for slow growth by

random collisions. As the planetesimals gain more mass, their rate of growth only increases, leading to a phase of 'runaway growth'. Eventually, a few of the largest bodies become dominant within the disk, being responsible for the majority of the accretion whilst inhibiting the growth of smaller bodies, this stage being referred to as 'oligarchic growth'. In the inner solar system, the eventual collision and merger of these planetary 'embryos' is the final stage of planet formation, resulting in the creation of the four terrestrial planets (Montmerle et al. 2006).

1.1.2 Giant planet formation

Observational evidence puts limits on the timescales for the formation of ice giants[2] and gas giants.[3] Whilst terrestrial planets can be formed from continued collisions between planetary embryos after the protoplanetary disk dissipates, giant planets must accrete their gas from the disk. Observations of young stars have shown that disks last only a few million years, with very few reaching an age of 10 Myr (Haisch, Lada & Lada 2001).

The core accretion model of Pollack et al. (1996) suggests that the initial growth of the giant planets is similar to the terrestrial planets. At the large orbital separations of these objects, the disk is cool enough for ices to condense, increasing the reservoir of material from which planetary embryos are able to accrete, and hence accretion occurs more quickly. Upon reaching ten Earth masses or so, the embryo is sufficiently massive to begin accreting a small amount of gas. Bodies that reach twenty or thirty times the mass of the Earth before the disk dissipates are able to reach a second stage of runaway growth, accreting a massive gaseous envelope in a very short time, perhaps only a few tens of thousands of years (Montmerle et al. 2006).

Computational models of core accretion have historically encountered a series of

[2]Planets such as Uranus or Neptune, with masses several tens times that of Earth. These planets mainly consist of rock and 'ices', with a small H/He atmosphere

[3]Planets such as Jupiter or Saturn, containing up to hundreds of times the mass of the Earth, mainly comprised of Hydrogen and Helium

difficult problems (Montmerle et al. 2006). Despite the additional material available in the form of condensed ices, difficulty has still been found in forming the planetary embryo and accreting the gaseous envelope in the short time available, especially for the more distant ice giants. However, more recent modelling efforts have proved successful in providing Jupiter analogues (e.g. Lissauer et al. 2009, D'Angelo et al. 2014), whilst the 'Nice model' suggests that the ice giants were initially located much closer to the Sun (Tsiganis et al. 2005). Another issue relates to interactions with the disk, both during the formation of the massive embryo and after accreting a significant amount of gas from the disk, which often result in models predicting planets will migrate inwards towards the star (Baruteau et al. 2014).

An alternative model for giant planet formation is that of gravitational instability (Boss 1997). This model suggests that the formation of the giant planets was unlike the mechanism that created the terrestrial planets, but instead closer to that of stars. It is assumed that the proto-planetary disk was sufficiently massive for regions to collapse under self-gravity, forming the giant planets. Gravitational instability is particularly attractive as it avoids the difficulties in creating a large enough planetary embryo during the limited disk lifetime, and the problems with fast migration of planetary embryos.

However, gravitational instability has historically had difficulty in explaining the large amounts of heavy elements present in the giant planets, and whilst recent efforts suggest a wide range of compositions are possible (e.g. Boley, Helled & Payne 2011), the production of the ice giants – which are dominated by heavy elements – remains difficult to explain (Helled et al. 2014). It has also proved difficult to prevent the protoplanets from dissipating when placed closer than a few tens of au from the star (Vazan & Helled 2012), much more distant than the current positions of Jupiter and Saturn, although a possible solution is fast inwards migration of these collapsing fragments (e.g. Nayakshin 2010).

1.2 The hot Jupiter formation problem

By the early 1990s, it was generally considered that our understanding of planet formation was relatively complete, except for a few minor details. The subsequent discoveries from exoplanet science have since revealed a vast array of unexpected planetary system architectures. Approximately 1% of Sun-like stars host a gas giant planet with an orbital period below 10 days (Gould et al. 2006, Wright et al. 2012, Howard et al. 2012, Petigura et al. 2017), a situation completely unexpected from standard planet formation theory. A vast number of tightly-packed systems of terrestrial planets have been discovered around both sun-like stars (e.g. Lissauer et al. 2011, Lissauer et al. 2014) and smaller cool dwarfs (e.g. Dressing & Charbonneau 2013, Gillon et al. 2017), unlike the widely spaced planets in our own solar system. There are also many open questions about planets intermediate in size between Earth and Neptune, which are absent in the solar system, but are now thought to be incredibly common elsewhere (Howard et al. 2010).

This thesis is concerned with those planets known as 'hot Jupiters', roughly defined as those planets more massive than $0.3\mathrm{M_{Jup}}$ with periods less than 10 days. The short orbital periods of these planets have made them especially favourable for detection, being the first planets detected around main sequence stars by both the radial velocity method (Mayor & Queloz 1995) and the transit method (Charbonneau et al. 2000), and they remain the most common class of planet detected by ground-based transit surveys such as WASP (Pollacco et al. 2006) and HAT/HATSouth (Bakos et al. 2004, Bakos et al. 2013).

The existence of hot Jupiters poses a clear challenge to planet formation theory. In core accretion, a gas giant is expected to form far from the host star, where volatile molecules can condense into ices, assisting the creation of massive protoplanetary cores (Pollack et al. 1996). For gravitational instability, the gas must be both cold and dense (Toomre 1964), and it is not thought these conditions can be met close to the star (Dawson & Johnson 2018); furthermore, close-in orbits have a velocity gradient that is much too high to allow fragments to coalesce (Rafikov 2005). Given that neither

theory suggests that such planets should be formed close to stars with any regularity – if they can be formed there at all – how can we explain their existence?

The following sections review the competing theories for hot Jupiter formation, and the observational evidence available. Further detail can be found in the recent review by Dawson & Johnson (2018).

1.2.1 Proposed formation pathways

A vast body of theoretical work surrounds the hot Jupiter formation problem, considering many different physical mechanisms to produce these planets. The theories put forward can generally be grouped into three broad categories:

1. **In-situ formation:** planet formation mechanisms produce hot Jupiters in their current orbits.
2. **Disk migration:** an initially 'cold' Jupiter, formed far from the star, shrinks its orbit through interactions with the protoplanetary disk.
3. **High eccentricity migration:** a 'cold' Jupiter is forced onto a highly eccentric orbit, and then loses energy through tidal interactions, shrinking the orbit.

Each of these theories is now considered in turn.

1.2.1.1 In-situ formation

Rather than invoking some process to bring a giant planet from an initial orbit of several au to the present day orbits of hot Jupiters, in-situ formation theories present a seemingly simple answer: hot Jupiters were formed on the short period orbits we observe today. However, reconciling this hypothesis with either gravitational instability or core accretion is difficult. Rafikov (2005) argued that gravitational instability is completely infeasible at 1 au, let alone closer to a star, and hence argues that this

formation theory cannot be used to explain hot Jupiters. The disk is initially supported by high temperatures due to irradiation, and by the fast orbits close to the star, requiring a very massive disk in order to allow fragmentation to occur. For these fragments to then collapse before differential rotation breaks them apart, they must lose a large fraction of their thermal energy in a short time. Rafikov (2005) finds that the high initial temperature needed for such a fast loss of thermal energy is entirely implausible, with the thermal velocity of the gas at such temperatures exceeding the escape velocity of the disk.

For core accretion, the growth of the protoplanet is limited by the size of the 'feeding zone', the region of the protoplanetary disk from which material can be accreted. Far from the star, the rate of change in orbital velocity with separation is small, and hence material from a wide range of orbital separations can be attracted towards and accreted by the planetary embryo. However, close to the star, only a small change in separation results in a significant velocity difference, and only a small pool of material is available for accretion. Adopting typical disk properties, Dawson & Johnson (2018) show that an embryo would struggle to reach the mass of the Moon, never mind the $10\,M_\oplus$ needed to begin gas accretion (e.g. Rafikov 2006).

In-situ formation has recently been revived following to observations of a large population of 'super-Earths' at short orbital periods. Roughly defined as planets with radii in the range 1–1.6 $R_\oplus$, super-Earths are almost entirely composed by rock with only a small gaseous envelope (e.g. Weiss & Marcy 2014), closely matching the expectations for the cores of gas giants. In addition, they are much more common than hot Jupiters themselves (e.g. Howard et al. 2010, Howard et al. 2012), suggestive of a large population of 'failed' hot Jupiters that did not manage to accrete a large fraction of gas (e.g. Lee, Chiang & Ormel 2014, Boley, Granados Contreras & Gladman 2016, Batygin, Bodenheimer & Laughlin 2016). However, it has proven difficult to reconcile the orbital distribution of super-Earths with hot Jupiters: whilst the latter typically have orbital periods below 10 days, the super-Earths are rarely found in such short period orbits (e.g. Youdin 2011, Mulders, Pascucci & Apai 2015, Lee & Chiang 2017).

1.2.1.2 Disk migration

Gravitational interactions between a planet and the protoplanetary disk allow the exchange of angular momentum and energy, modifying the orbit of the planet. If such a mechanism is capable of moving a planet that initially formed at several au into an orbit of only a few days, the initial formation of the planet can occur under 'normal' conditions, whether that be core accretion or gravitational instability. However, the actual effect of planet-disk interactions is highly variable depending on the assumed properties of the disk, the planet, and any other planets that may be in the system; a comprehensive review of the various possible processes and outcomes can be found in Baruteau et al. (2014). The most commonly considered route is the so-called 'type II migration', in which the planet opens a gap in the disk. The planet is pushed towards the centre of the gap by the gas both inside and outside its orbit, and as the disk is accreted onto the star, the planet is dragged inwards with it, eventually being left on the orbit that we observe it on today.

A major issue that commonly appears in models of disk migration is that once the right conditions can be found for migration to start, it is subsequently difficult to stop the migration process before the host star tidally disrupts or engulfs the planet. Suggested methods for preventing such situations include interactions between the star and planet (e.g. Lin, Bodenheimer & Richardson 1996, Trilling et al. 1998), or instead the truncation of the disk close to the star (e.g. Lin, Bodenheimer & Richardson 1996, Kuchner & Lecar 2002, Rice, Armitage & Hogg 2008).

1.2.1.3 High eccentricity migration

This group of theories covers a wide range of interaction mechanisms which excite a distant giant planet onto a highly eccentric orbit. If sufficient eccentricity is reached, the planet loses a significant amount of orbital energy due to tidal deformation by its host star at periastron, eventually resulting in a tight, circular orbit. Eccentricity excitation is usually attributed to interactions with other massive bodies in the systems,

either planets or wide binary stars.

Planet-planet scattering invokes a series of close encounters between multiple planets in the system, eventually resulting on one of the planets becoming highly eccentric, and often the ejection of the other bodies in the system (e.g. Rasio & Ford 1996, Weidenschilling & Marzari 1996, Chatterjee et al. 2008). Alternatively, many theories consider secular interactions, occurring over many orbits and taking thousands or millions of years to complete. These interactions may be between groups of co-planar planets (e.g. Wu & Lithwick 2011, Petrovich 2015b, Hamers et al. 2017), or instead between a planet and a highly inclined companion through the Lidov-Kozai (LK) mechanism, in which the planet is forced alternately to high inclination and high eccentricity. Theories invoking the LK mechanism often consider a binary stellar companion as the perturber (e.g. Wu & Murray 2003, Fabrycky & Tremaine 2007), although pairs of planets may also undergo a similar process (Naoz, Farr & Rasio 2012); see Naoz (2016) for a broad review of the LK mechanism.

1.2.2 Observational evidence

Each of the hot Jupiter formation theories provides numerous predictions of the observable properties of hot Jupiters, but each still has significant discrepancies with the observational data. In the following sections, some of the more prominent pieces of observational evidence are presented. For further information, the recent review by Dawson & Johnson (2018) covers a vast array of observational evidence, including the potential links between hot Jupiters and other classes of planets.

1.2.2.1 Orbital alignments

The rotational axis of the host star and the orbital axis of a protoplanetary disk – and hence any planets forming from it – are expected to be aligned, as both originate from the same rotating cloud of material. In-situ formation and disk migration are therefore expected to produce well-aligned planets. On the other hand, high eccen-

tricity migration mechanisms can relatively easily alter the inclination of a planet as well as its eccentricity, and inclination changes are an integral part of theories invoking the LK mechanism. It was therefore expected that evidence of high obliquity (the angle between the rotational and orbital axes), also referred to as 'spin-orbit misalignment', among the hot Jupiters population would be a key piece of evidence supporting high-eccentricity migration.

The majority of measurements of obliquity have been obtained through observations of the Rossiter-McLaughlin effect. Due to the rotational motion of the host star, one hemisphere will appear blueshifted whilst the other appears redshifted. As a planet (or other occulting body) transits the face of the star, the occultation of different regions of the stellar photosphere will result in an apparent net redshift or blueshift of the star. If the rotational and orbital axes are aligned, the blueshifted half of the star will be transited first; if the axes are misaligned, the effect may be weakened, constrained to only one hemisphere, or reversed. The effect is most commonly analysed as an anomalous change in radial velocity (e.g. Queloz et al. 2000, Winn et al. 2010, Albrecht et al. 2012), although analysis methods such as Doppler tomography (Collier Cameron et al. 2010) and the 'reloaded' RM effect (Cegla et al. 2016) have recently seen increasing use.

Several other techniques can also be used to determine or constrain the spin-orbit misalignment angle from photometric data. Occultations of starspots on the face of the star can be used, with repeated occultations of the same spot being expected if the orbit is aligned (e.g. Sanchis-Ojeda & Winn 2011, Désert et al. 2011). Alternatively, the projected angle of the star's rotation axis can be inferred using a variety of methods, using methods such as asteroseismology (e.g Huber et al. 2013) or by comparing rotation periods with the observed rotational broadening (e.g. Winn et al. 2017). A review of the RM effect and the various other techniques used can be found in Triaud (2017).

Whilst these various methods have provided a wealth of data on spin-orbit alignment, the interpretation of the results has proved much more difficult than expected. It became apparent at an early stage that misalignment angle appears to be strongly

correlated with stellar temperature, with only stars hotter than approximately 6250K showing high obliquities (Winn et al. 2010, Albrecht et al. 2012). This has been interpreted as evidence that hot Jupiters around cool stars are somehow able to realign the rotation of their host stars, masking the initial obliquity distribution. However, explaining such a phenomenon with our understanding of tidal interactions has proved challenging, due to the long timescales expected for such realignment to occur, and the large amount of angular momentum transfer required to realign a star. The latter is somewhat alleviated by the proposal that only the outer envelope of the star needs to be realigned, with the lack of misalignment in hot stars being due to the strong coupling between exterior and interior in these stars (Winn et al. 2010).

A further complication is that it may be possible to generate high obliquities without high eccentricity migration. If the protoplanetary disk becomes tilted due to the influence of external bodies (e.g. Batygin 2012, Xiang-Gruess 2016), then disk migration and in-situ formation would also be able to produce misaligned hot Jupiters. However, recent measurements of the obliquities of other types of planetary systems find that high obliquities are very rare if a hot Jupiter is not involved, suggesting that the majority of protoplanetary disks and planets retain their initial alignments (e.g. Winn et al. 2017 and references therein), and hence that the high obliquities of hot Jupiters are indeed related to their formation.

1.2.2.2 Orbital eccentricity

In high eccentricity migration theories, the circularisation timescale of an eccentric planet is strongly dependent on the planet's periastron distance, and hence its final orbital separation. It is therefore expected that hot Jupiters below a certain orbital period would have circularised very quickly, whilst those at larger orbital separation will retain much of their initial eccentricity.

A distinct cutoff is indeed seen at an orbital period of approximately 3 days, below which almost all hot Jupiters are found to be circular. At longer orbital periods the situation is less clear, with a mixture of both circularised and eccentric hot Jupiters

being observed, suggesting that additional factors are involved. It may be that the circularised planets were placed on highly eccentric orbits at an earlier stage in the system's lifetime, or alternatively that the circularisation timescale is not only dependent on the orbit, but also the properties of the planet (e.g. Pont et al. 2011). The mix of circular and eccentric hot Jupiters has also been interpreted as evidence of multiple formation processes occurring, producing an observed population that consists of both a 'high eccentricity' and a 'low eccentricity' sample (e.g. Shabram et al. 2016, Nelson, Ford & Rasio 2017).

It is also possible to excite the eccentricity through interactions with other nearby planets, allowing planets formed in situ or via disk migration to obtain moderate eccentricities. However, attempts to detect companions to hot Jupiters through additional transits (Huang, Wu & Triaud 2016), transit timing variations (Steffen et al. 2012), or radial velocity trends (Knutson et al. 2014) have all found that hot Jupiters are highly unlikely to have companions sufficiently close for eccentricity excitation. It is therefore difficult to explain the existence of eccentric hot Jupiters without high eccentricity migration.

1.2.2.3 Hot Jupiter occurrence rates

Planet formation theories can provide predictions for the fraction of stars that host hot Jupiters, or alternatively the fraction of cold Jupiters that migrate inwards to form hot Jupiters. Approximately 1% of stars with spectral types F, G, and K host hot Jupiters (e.g. Howard et al. 2010, Wright et al. 2012, Fressin et al. 2013, Santerne et al. 2016), although transit surveys systematically determine a lower rate (approximately 0.5%) than radial velocity surveys (often in excess of 1%), for reasons that are as yet unexplained (e.g. Guo et al. 2017). The overall occurrence rate of giant planets around FGK stars is on the order of 10–20% (Cumming et al. 2008, Johnson et al. 2010, Cassan et al. 2012), though it should be noted that the rate is correlated with both stellar mass and metallicity (Johnson et al. 2010). From these results, it can be concluded that hot Jupiters account for approximately 5–10% of all giant planets.

Models of high eccentricity migration generally predict hot Jupiter fractions that are at the lower end of the observed fraction. Depending on the exact migration mechanism and initial conditions, models of planet–planet interactions produce hot Jupiter fractions around 3–7% (e.g. Petrovich 2015b, Petrovich & Tremaine 2016). Models invoking stellar binaries and the LK mechanism struggle to produce enough hot Jupiters, with the predicted fractions being around 2% (e.g. Anderson, Storch & Lai 2016, Muñoz, Lai & Liu 2016) and hence somewhat difficult to match with the observed data.

Recent results from disk migration models have shown good agreement with the observed hot Jupiter population. Coleman & Nelson (2016) presented results that not only reproduced the fraction of giant planets below a certain orbital period, but also showed remarkable agreement with the overall period distribution of giant planets derived from the *Kepler* mission. In situ formation theories have yet to provide detailed predictions for the hot Jupiter fraction (Dawson & Johnson 2018); much of the work in the literature focuses on the accretion of the gaseous envelope after a protoplanetary core has formed, but does not consider the formation of those cores in detail (e.g. Lee & Chiang 2016, Batygin, Bodenheimer & Laughlin 2016).

1.2.2.4 The ages of hot Jupiters

In situ formation and disk migration clearly require that a hot Jupiter has formed and migrated by the time that the protoplanetary disk dissipates, and hence the distribution of hot Jupiters should be relatively unchanged after the disk is removed at an age of 10 million years or less. In contrast, high eccentricity migration allows hot Jupiters to arrive much later, and hence it would be expected that the fraction of hot Jupiters would increase with age, although most hot Jupiters will still arrive earlier rather than later (Dawson & Johnson 2018).

Such a trend has generally proved difficult to identify, given the large uncertainties (both statistical and systematic) that are typical when measuring the ages of main sequence stars. Young open clusters – and hence the stars they contain – tend to

have much more accurately determined ages, and hence there is interest in finding hot Jupiters in these environments. A handful of examples are now known in clusters such as Praesepe (Quinn et al. 2012) and the Hyades (Quinn et al. 2014), although conclusive answers are difficult to identify from this relatively small sample. Furthermore, the short circularisation timescales of two out of the three planets known in young clusters are, in fact, consistent with high eccentricity migration and circularisation having already occurred within the current age of the system (Quinn et al. 2014).

A recent result that has strongly challenged the predictions of high eccentricity migration is the discovery of hot Jupiters orbiting T Tauri stars, very young objects with ages of only a few million years. Despite the difficulties in filtering out the activity signal for such systems, secure detections of hot Jupiters have been announced for the 2 Myr old V830 Tau (Donati et al. 2016) and the 17 Myr old TAP 26 (Yu et al. 2017), which are both plausible candidates for either in-situ formation or disk migration, but incredibly difficult to explain via high eccentricity pathways.

1.2.3 Migration via the Lidov-Kozai mechanism in stellar binaries

The Lidov-Kozai effect occurs in certain arrangements of the three-body problem. The system is arranged in a hierarchical manner, with one pair of bodies orbiting each other closely, and a third body orbiting more distantly. In Lidov (1962), Kozai (1962), and many subsequent studies, one of the inner bodies is modelled as a massless test particle, and the outer orbit is assumed to be circular. The inner and outer systems are sufficiently well separated that they are stable on orbital timescales, but if the inner and outer orbits are inclined to one another by a critical angle (40–140°), the test particle undergoes large excursions in eccentricity and inclination. Further theoretical work has since considered cases such as of the outer body being the test particle, non-zero eccentricity in the outer orbit, and non-zero masses for all three bodies. The theory has been applied to a variety of situations in the solar system, as well as explaining astrophysical phenomena such as close binary stars, binary black holes, and the creation

of hot Jupiters. A recent review on the LK mechanism and its various applications can be found in Naoz (2016).

For planet formation, the Lidov-Kozai mechanism falls under the broad family of high eccentricity migration theories. In addition to the proto-hot-Jupiter and its host star, an additional, more distant body is introduced to the system, often in the form of a wide binary stellar companion (Wu & Murray 2003, Wu, Murray & Ramsahai 2007, Fabrycky & Tremaine 2007, Naoz, Farr & Rasio 2012, Storch, Anderson & Lai 2014, Storch & Lai 2015, Petrovich 2015a, Anderson, Storch & Lai 2016) but occasionally as an outer planet (e.g. Naoz et al. 2011). The orbit of the perturbing outer body is usually highly inclined to the inner orbit. Through secular interactions, the inner planet is forced onto a highly eccentric orbit, on which it begins to lose orbital energy from tidal friction. The planet is not always fully circularised on its first excursion to high eccentricity, but may instead go through multiple cycles before tidal forces become strong enough to significantly modify the orbit. The inclination changes produced by the Lidov-Kozai effect allow the creation of misaligned or retrograde planets..

There are several testable predictions of the Lidov-Kozai hot Jupiter formation hypothesis. Firstly, if hot Jupiters require an external stellar companion to start their migration, then hot Jupiters should be found solely in wide binary systems, with the possible exception of some small fraction of systems where the binary was later disrupted by stellar encounters. The binary companion should be inclined to the orbit of the planet, as the Lidov-Kozai effect becomes stronger as the misalignment between the inner and outer orbits increases. Furthermore, the stellar companion must also be both sufficiently massive and close enough to the planet in order to overcome the effects of general relativistic precession in the planet's orbit – despite relativistic effects being incredibly weak for planets orbiting several au from their host star, they can still be sufficient to inhibit the very weak gravitational forces involved in Lidov-Kozai mechanism.

In addition, the properties of hot Jupiters are also predicted by theoretical work. The fraction of stars that host hot Jupiters is often predicted, based on an assumed initial population of binaries and distant giant planets. Many sets of initial conditions

will not result in significant migration occurring, whilst a fraction of those planets that do migrate will be engulfed by their host star. Estimates for the orbital properties of hot Jupiters are also produced, in particular the distributions of obliquity, eccentricity, and semi-major axis. A small fraction of planets may be observed before tidal circularisation has been completed, and the discovery of highly eccentric planets in wide binaries such as 16 Cyg Bb (Holman, Touma & Tremaine 1997) and HD 80606b (Naef et al. 2001) spurred early interest in the Lidov-Kozai mechanism.

1.3 Contaminating light in exoplanet observations

The term 'contaminating light' is used to refer to light received from nuisance sources other than the planet host star and planet itself (although in many cases, the light from the planet is negligible). Such light may originate from non-stellar sources as the instrument or telescope (e.g. reflections) or from sky illumination (e.g. artificial sources or lunar illumination), which vary between different telescopes, instruments, and observations. However, the work in this thesis considers light from stellar sources, located at small angular separation from the planetary system of interest, in which the light from the planetary system and contaminating star are 'blended' together when observed. These stars may be physically associated with the observed exoplanet system, forming a wide binary or multiple stellar system, or may be an entirely unrelated star that is by chance aligned with the system of interest, as seen from Earth.

Both photometric measurements, such as time-series observations of a planetary transit, and spectroscopy, such as radial velocity measurements, are affected by contaminating light. In general, contaminating light biases the planetary properties derived from observations towards a smaller, less massive planets. For radius measurements, a detailed investigation is presented in Ciardi et al. (2015). Following the outline of that work, the fractional change between the out-of-transit observation flux level $F_{\rm out}$ and the mid-transit flux $F_{\rm tr}$ can be described as

$$\delta = \frac{F_{\rm out} - F_{\rm tr}}{F_{\rm out}}. \tag{1.1}$$

If the transit is non-grazing, and the visible surface of the star is assumed to be uniformly bright (i.e. ignoring limb darkening), the fraction of flux blocked at mid-transit is given by the ratio of the visible areas of the planet and star. If the bodies are spherical, this is the square of the ratio of their radii $k = \frac{R_p}{R_s}$, where R_p is the radius of the planet and R_s that of the star. Allowing for the general case where n stars may be contributing light, $F_{\rm out}$ and $F_{\rm tr}$ are given by

$$F_{\rm out} = \sum_{1}^{n} F_n, \tag{1.2}$$

$$F_{\rm tr} = F_{\rm out} - F_1\, k^2, \tag{1.3}$$

where F_1 is the flux contributed by the planet host star. Substituting the expression for $F_{\rm tr}$ into Equation 1.1 gives

$$\delta = \frac{F_{\rm out} - (F_{\rm out} - F_1\, k^2)}{F_{\rm out}} = \frac{F_1}{F_{\rm out}}\, k^2. \tag{1.4}$$

In the limiting case where $n = 1$ and hence only the planet host star is present, the expression simplifies to $\delta = k^2$ as expected. However, if this is incorrectly assumed when multiple stars are contributing flux, the radius of the planet will be underestimated. The ratio of the measured radius to the true radius is given by

$$\frac{R_{p,\rm obs}}{R_{p,\rm true}} = \frac{k_{\rm obs}}{k_{\rm true}} = \sqrt{\frac{F_1}{F_{\rm out}}}. \tag{1.5}$$

Figure 1.1 illustrates the reduction in determined planet radius as a result of contaminating light. The analysis above ignores any bias in the derived stellar parameters, and hence it is assumed that R_s is correctly determined. For cases where the planet host star still dominates the flux contribution, or alternatively where the contaminating star is very similar to the host star, this is likely to be true. However, if it is the contaminating star that dominates the flux contribution, the derived stellar properties may be significantly biased, further altering the measured properties of the planet.

The effect of contamination on radial velocity is more complex to characterise. The effect on the measured planetary radial velocity signal depends on both the flux contributed by the contaminating star, the spectral lines present in the contaminating

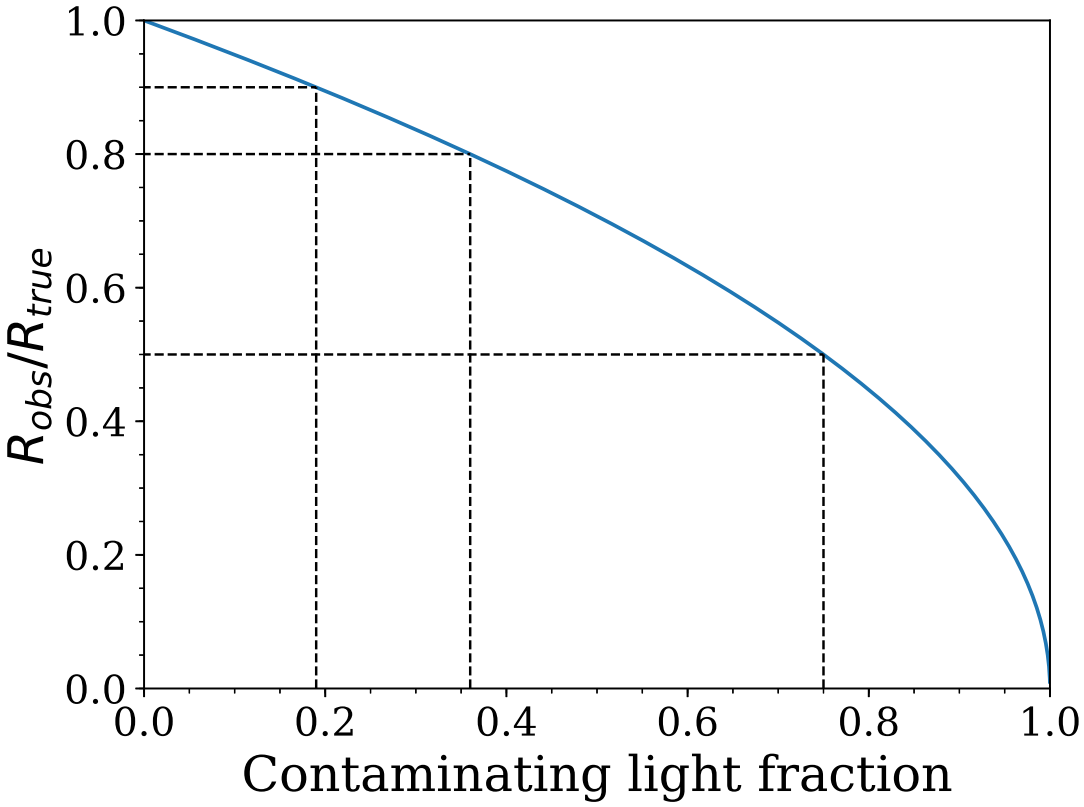

Figure 1.1: The change in apparent planet radius due to contaminating light. The ratio of the observed to the true planet radius is plotted against the fraction of light contributed by contaminating stars, i.e. $\frac{F_{\rm out}-F_{\rm l}}{F_{\rm out}}$. As expected, the true planet radius is retrieved when no contaminating light exists. Also indicated are the points at which the planet radius is underestimated by 10%, 20%, and 50%, corresponding to contaminating light fractions of 19%, 36%, and 75% respectively.

star's spectrum, and its radial velocity offset relative to the planet host. If the two stars are well separated in radial velocity space, then the two stars will be resolved spectroscopically, and the radial velocity signal will not be significantly affected. Santerne et al. (2015) presented a detailed investigation of various radial velocity contamination scenarios, finding that the effects of contamination are not restricted to diluting the measured radial velocity amplitude, being able to anomalously enhance the observed radial velocity amplitude in certain situations.

Contamination can clearly alter the derived properties of a specific planetary system, perhaps causing a given planet to appear much more unusual than it actually is, resulting in scientific resources being allocated to studying objects that would not otherwise be considered worthwhile. Another effect of contamination is to alter our understanding of populations of planets, causing planets to systematically appear smaller and less dense than they actually are. This problem was considered in detail by Ciardi et al. (2015) for large surveys such as *Kepler* and TESS. This work pointed out that even if corrections are made for all detectable contaminating stars, there will still be a significant effect from unknown cases of contamination, causing the radii of planets found by *Kepler* to be systematically underestimated by up to 20%. As a result, a naive analysis would find smaller, rocky planets to be more abundant than they truly are.

1.3.1 Astrophysical false positives

In addition to altering the measured radius and mass of planets, contamination can also alter the apparent properties of other astrophysical phenomena, making them appear more planet-like in origin. A large proportion of the follow-up work in planet surveys is dedicated to distinguishing between true planetary systems from a variety of similar-looking phenomena. The majority of false positive detections are eclipsing binary stars (EBs), in which periodic dips in brightness occur as one of the stellar components eclipses the other. For systems where the two binary components are relatively similar and the eclipses are non-grazing, eclipsing binaries can be easily distinguished by the

much greater depth of their eclipses compared to planetary transits (approximately 1% for a Jupiter-sized planet transiting a Sun-like star). However, there are a number of troublesome configurations which are difficult to distinguish from photometry alone, with the most common cases being:

1. **Grazing eclipsing binaries** – EBs in which the orbit is inclined such that only a small part of each star is seen to be eclipsed by the other, resulting in eclipse depths similar to planetary transits.

2. **Extreme flux ratios** – Systems where one component contributes much more flux, such as an evolved giant star orbited by a main sequence star, or a low mass (sub-)stellar object orbiting a Sun-like star.

3. **Blended eclipsing binaries** – Cases where another star dilutes the EB, causing intrinsically deep eclipses to resemble much shallower planetary transits.

A comparison between the light curves of true exoplanet transits and common astrophysical mimics can be found in Figure 1.2

Photometric and spectroscopic measurements can discern between these false positives and true planets, but the ease of doing so varies widely, depending on the arrangement of the stars involved. If both primary and secondary eclipses are seen, this is usually good evidence of an eclipsing binary. Common techniques to find secondary eclipses include the modelling 'odd' and 'even' transits separately (e.g. Batalha et al. 2010), covering systems where the two eclipses are similar but not identical, and searching for faint secondary eclipses at a phase of 0.5, although it is worth noting that secondary eclipses are detectable for some hot Jupiters (e.g. Borucki et al. 2009), and that eclipses may be offset in phase if the orbit is eccentric (e.g. Shporer et al. 2017). If the binary components have different temperatures the eclipse depths may vary strongly as a function of wavelength, and close eclipsing binaries can exhibit photometric variability linked to tidal effects between the two stars, such as ellipsoidal variation or starspot modulation. EBs also often produce inconsistent results when

treated as a single star, with the stellar properties determined independently via optical photometry, near infrared photometry, and light curve fitting being inconsistent with one another (Cameron 2016). If an EB is not distinguished from the lightcurve alone, radial velocity measurements will often reveal that the mass of the orbiting body is inconsistent with a planet.

Blended systems make up a significant fraction of the most convincing planet mimics (e.g. Almenara et al. 2009, Bayliss et al. 2009). Several blended EBs have been sufficiently difficult to detect that they were announced or published as bona fide transiting planets before the true nature of the system was determined (e.g. the unpublished WASP-9b). The indicators listed above for other EB systems are also applicable to blended EBs, but like the eclipses themselves, these indicators are reduced in amplitude due to the effects of contaminating light.

An additional detection method available for blends is high resolution imaging, which aims to spatially resolve the individual blended components. Whilst the identification of multiple stellar sources does not in itself prove whether the variability is caused by a blended EB or a true planet, it does highlight the possibility of a false positive, encouraging further investigation of a possible blend. The detection of a potential blend (or lack thereof) can also be used to place statistical limits on the false positive probability when combined with assumptions about the distribution of stars in the sky, the population of eclipsing binaries, and so forth. This technique is used in tools such as Blender (Torres et al. 2011) and PASTIS (Díaz et al. 2014, Santerne et al. 2015), which consider high resolution imaging in conjunction with a variety of other false positive indicators.

1.4 High resolution imaging studies of exoplanet host stars

Previous to and in parallel with the work in this thesis, high resolution images have been taken of (suspected) exoplanet host stars, with the subsequent analysis covering

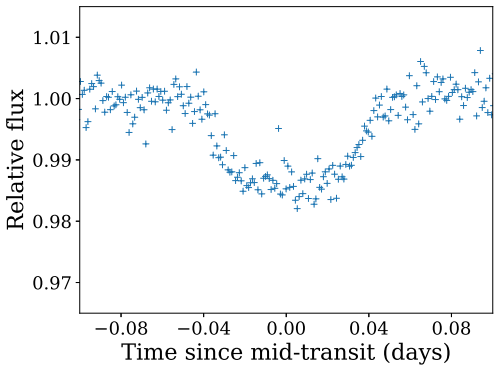

(a) Transiting exoplanet (WASP-49)

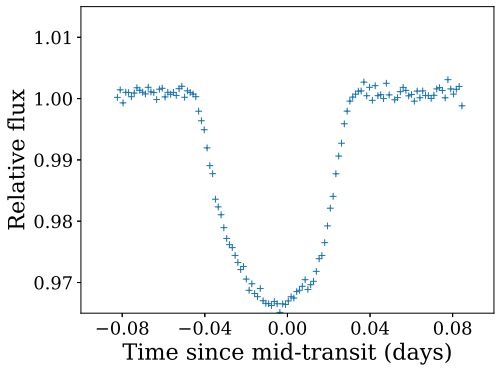

(b) Transiting exoplanet (WASP-52)

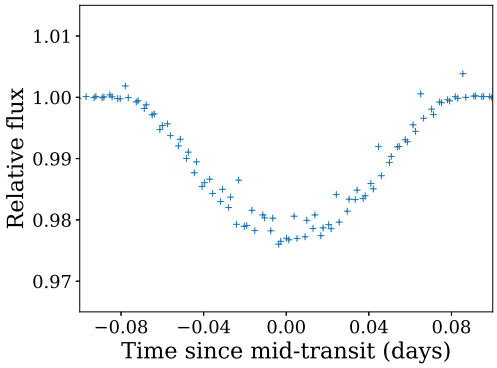

(c) Blended eclipsing binary

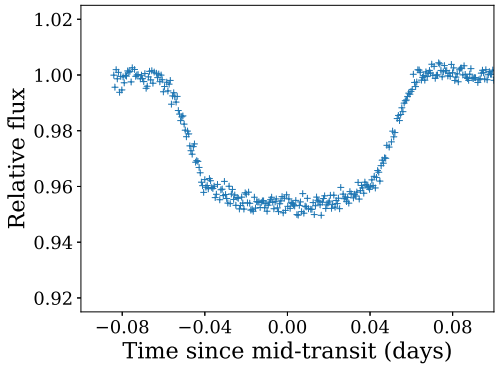

(d) Eclipsing binary with low mass secondary

Figure 1.2: Examples of the light curves of two confirmed transiting exoplanets (a and b), a blended eclipsing binary (c), and an eclipsing binary with a low mass stellar secondary (d). Note that the range in the x-axis (time) is identical for all four plots, and the y-axis (flux) is identical for plots a, b, and c. The overall profiles, depths, and timescales of all three events are similar, and there is a large diversity among exoplanet transit light curves alone. All four objects were initially identified as candidate transiting exoplanets by photometric surveys.

Sources: (a) SAAO 1m I-band lightcurve of WASP-49b. (b) Danish 1.54m R-band light curve of WASP-52b (Mancini et al. 2017). (c) Phase-folded K2/EVEREST (Luger et al. 2016) lightcurve of 'verified' planet candidate EPIC 210483889, later determined to be a false positive (see Cabrera et al. 2017 for details). (d) SAAO 1m R-band lightcurve of EBLM J2308-46 (Gill et al., in prep.), initially identified as a planet candidate by the WASP survey.

both of the science cases outlined above. The motivation and results of these efforts are summarised in the following sections. It is worth nothing that companion stars may also be discovered via means other than high resolution imaging, and beyond separations of a couple of arcseconds, archival images or follow-up transit photometry have resulted in the detection of many wider companions. There have also been several cases where the presence of a companion has been inferred from an elongated point spread function, evidence of multiple stars contributing to the observed spectrum, or long-term radial velocity trends/drifts (although the latter are often due to outer planets or brown dwarfs).

1.4.1 Efforts by transit surveys

Some of the many teams searching for transiting exoplanets have utilised high resolution imaging to assist in confirming the true nature of suspected planetary systems. The motivation and results of these efforts are considered in turn for surveys where such data have been obtained.

1.4.1.1 The Lupus and SuperLupus surveys

The Lupus survey (Bayliss et al. 2009) was a relatively early and short-duration transit survey, obtaining 54 nights of photometry of a relatively crowded field (galactic coordinates $l = 331°$, $b = 11°$) with a 1m telescope. Further observations of the same field were obtained in the subsequent year, with the extended dataset referred to as the SuperLupus survey (Bayliss & Sackett 2011). The original part of the survey identified four candidate planetary systems (Bayliss et al. 2009), of which two were determined to be blended EBs from the light curve photometry alone (secondary eclipses observed for Lupus-TR-2, and the blended system was separately resolved for Lupus-TR-4). Lupus-TR-1 was rejected after 'good-seeing' images were obtained, revealing a nearby companion.

The most plausible of the Lupus' surveys candidates was Lupus-TR-3. Despite

the identification of multiple stars within the photometric aperture, the system was deemed sufficiently planet-like in nature to be published as a tentative planet detection (Weldrake et al. 2008). Later follow-up observations included two additional imaging sequences in good seeing. These data were intended for performing 'on-off' photometry, in which short imaging sequences or single images are obtained separately in-transit and out-of-transit, in order to identify which star is variable (see e.g. Sect. 3.3 of Deeg et al. 2009). However, in addition to this purpose, data were processed using a frame selection algorithm to select the best quality data (akin to the lucky imaging technique, which is described in Chapter 2), resulting in the discovery of at least six stars within the photometric aperture, with the suspected planet host star itself being resolved into two components with 0.25″ separation (Sackett et al. 2009). To date, no analysis has been published determining the true nature of the system, but the Lupus survey consortium considered the system to be a cautionary tale of the issues with stellar contamination, especially in crowded fields.

1.4.1.2 CoRoT

The CoRoT spacecraft was launched with the dual purpose of detecting transiting planets and performing asteroseismic observations of stars (Fridlund et al. 2006, Auvergne et al. 2009). To date, 31 transiting exoplanet or brown dwarf systems have been announced, of which two contain multiple planets (Queloz et al. 2009, Alonso et al. 2014).[4] The mission targeted relatively crowded fields at the intersection of the galactic plane with the ecliptic, and hence quantifying contamination and excluding blends were an important part of the work. For the majority of targets, contamination estimates were derived from seeing-limited imaging of the target field, along with on-off photometry to confirm the source and amplitude of the detected transit signal. The smallest planets detected by the mission – CoRoT-7b (Léger et al. 2009), CoRoT-22b

[4]There has been some debate over the existence of the non-transiting planet CoRoT-7c, announced in Queloz et al. (2009) – see e.g. Pont, Aigrain & Zucker (2011), Haywood et al. (2014), and Faria et al. (2016).

(Moutou et al. 2014), and CoRoT-24bc (Alonso et al. 2014) – additionally received dedicated adaptive optics imaging to confirm their planetary nature, due to the small transit signals observed and hence the potential faintness of any blended EB systems.

1.4.1.3 HATNet and HATSouth

The Hungarian Automated Telescope Network (HATNet, Bakos et al. 2002, Bakos et al. 2004, Bakos 2018) and its Southern hemisphere extension HATSouth (Bakos et al. 2013) is one of the leading ground-based transit surveys in terms of confirmed planets. The original HATNet telescopes have a modest plate scale – 14″/px originally, 9″/px following a CCD upgrade in 2009 (Bakos 2018) – and hence the transit search photometry suffers from a large amount of blending and contamination; the HATSouth telescopes have a finer scale of 3.7″/px.

Unlike early exoplanet surveys such as Lupus and the OGLE transit survey, or space-based missions such as CoRoT or *Kepler*, the HAT projects have focused on observing bright stars in uncrowded areas of the sky away from the galactic plane. As a result, the fraction of systems that are blended is much lower, and follow-up observations are simplified, in particular radial velocity observations, which are technically challenging for faint stars. As a result, the vast majority of HATNet and HATSouth planets have been confirmed through follow-up photometry with sufficient quality and spatial resolution to confirm the source and nature of the transit signal, in conjunction with radial velocity observations to confirm the mass of the transiting body. There has therefore not been a dedicated effort to obtain high resolution images routinely for candidates.

There have been a handful of high resolution images taken of HATNet candidates in the near-infrared as part of the follow-up procedure. A companion was found near HAT-P-41 (Hartman et al. 2012), ~ 3 mag. fainter; HAT-P-57 was found to be a likely hierarchical triple system, with the planet host orbited by an M-dwarf binary (Hartman et al. 2015); and adaptive optics and speckle imaging were obtained for HAT-P-65, -66, and -67 (Hartman et al. 2016, Zhou et al. 2017).

For HATSouth, lucky imaging observations were presented for several of the survey's more recently announced systems. These include HATS-19 and -20 (Bhatti et al. 2016); HATS-22 (Bento et al. 2017); HATS-26, -27, and -30 (Espinoza et al. 2016); HATS-31 and -34 (de Val-Borro et al. 2016); HATS-45 (Brahm et al. 2018); and HATS-51 and -52 (Henning et al. 2018). Of these, only HATS-52 was found to have a nearby companion star.

1.4.1.4 WASP

The Wide Angle Search for Planets (WASP, Pollacco et al. 2006) has discovered the most transiting planets of any ground-based transit survey. The survey works similarly to the HATNet survey discussed above, performing a wide field transit search with a coarse pixel scale of 14″/px. Planets are typically confirmed through follow-up photometry and radial velocity observations, and hence high resolution images are not obtained in the majority of cases.

Adaptive optics imaging was obtained for the first three planets, WASP-1, -2 and -3. No stars were detected near to WASP-3 (Pollacco et al. 2008). A companion was found 4.7″ from WASP-1, but this was located well outside the spectroscopic fibre aperture used for radial velocity measurements, and hence the target star was confirmed as the source of the detected signal (Collier Cameron et al. 2007). A companion star was detected only 0.7″ from WASP-2, and was sufficiently bright to form a potential blended EB in combination with WASP-2A. A further 20 minute AO imaging sequence was obtained during transit, but no evidence was found of the estimated 1.5 mag. deep eclipse required to produce the observed planetary signal (Collier Cameron et al. 2007).

Lucky imaging observations were obtained of WASP-77AB, a known visual binary with a separation of 3.3″. As the two stellar components were difficult to fully resolve in follow-up photometry, multicolour high resolution imaging was used to measure the fraction contaminating light from the secondary component, allowing correction of the photometric data (Maxted et al. 2013).

Other uses of high resolution imaging are rare and sporadic. Such data were

obtained for WASP-21, for which no companion was found (Bouchy et al. 2010). For WASP-93, a companion was detected at 0.7″, but was too faint in the optical to be responsible the detected transit signal (Hay et al. 2016).

1.4.1.5 KELT

The Kilodegree Extremely Little Telescope (KELT, Pepper et al. 2007) is another of the large ground-based transit surveys. Compared to WASP and HAT, the KELT survey targets somewhat brighter stars, and has a coarser pixel scale of 23″/px. An important way in which KELT stands out from other ground-based transit surveys is the follow-up of planet candidates orbiting hotter stars of spectral type A and F, which have traditionally been avoided by other surveys due to the difficulty of obtaining precise radial velocity measurements from these rapidly-rotating stars.

Given the sometimes poor or nonexistent detections of planetary radial velocity signal around these hot host stars, the KELT follow-up process regularly involves obtaining adaptive optics imaging of the planet host star. The KELT planets are often found to be in potential wide binary systems, with 11 out of the 20 published KELT systems[5] being in confirmed or suspected wide binaries. This is much higher than the fraction of planets from WASP or HAT that are initially identified as binaries, likely due to the consistent use of high resolution imaging, in addition to the higher multiplicity rate of hotter A and early F type stars (Raghavan et al. 2010).

1.4.1.6 Kepler/K2

The *Kepler* mission (Borucki et al. 2010) was a space-based transit survey, combining very high photometric accuracy, a relatively large 0.95m mirror, and a nearly continuous 4-year 'stare' at a single region of sky to detect the largest number of transiting planets of any mission, the vast majority being smaller and in longer period orbits than

[5]This number includes KELT-14, an independent re-discovery of WASP-122, and the jointly published WASP-167/KELT-13.

those found by ground-based surveys. Following the failure of components crucial for maintaining the accurate pointing of spacecraft, it was subsequently repurposed into the K2 mission, performing shorter photometric campaigns of approximately 80 days in duration, covering fields along the ecliptic plane (Howell et al. 2014).

Due to the high photometric sensitivity of *Kepler*, many of the planet host stars are too faint for precise radial velocity measurements to be performed. Furthermore, as many of the planets are significantly smaller (hence less massive) and on longer period orbits than the hot Jupiters that ground-based surveys find, the intrinsic radial velocity signal is also much smaller. For those planets where radial velocity follow-up is feasible, a very large amount of observing time would be required to follow-up the thousands of *Kepler* candidates. As a result, the *Kepler* team has relied heavily on high resolution imaging to statistically 'validate' or 'confirm' planet candidates, along with other diagnostics, such as the presence of multiple transiting components (Lissauer et al. 2012, Lissauer et al. 2014, Rowe et al. 2014).

For some of the best studied *Kepler* planets, high resolution imaging results have been presented alongside a detailed characterisation of the planet. For example, Kepler-14Ab was presented as a detailed case study of the effects of contaminating light (Buchhave et al. 2011). However, most candidates have yet to be (and likely will not be) the focus of a detailed follow-up paper, and instead high resolution images are typically presented en-masse for large numbers of planetary candidates. The majority of these observations have been performed by the Kepler Follow-up Program using adaptive optics or speckle imaging techniques, but there have also been many independent contributions, extending the list of techniques to include lucky imaging and interferometric methods. A comprehensive catalogue of the results of these surveys can be found in Furlan et al. (2017), who note that companion stars have been detected within $4''$ of 30% of *Kepler* candidates. One of the more novel projects is the use of the Robo-AO instrument, a robotic adaptive optics system, with the highly efficient observations of this robotic system allowing relatively quick coverage of almost all *Kepler* candidates using only a single telescope (Law et al. 2014, Baranec et al. 2016, Ziegler et al. 2017).

The K2 mission suffers from reduced photometric accuracy and shorter campaign length compared to the original *Kepler* mission, and hence the planetary candidates found from K2 data are typically brighter and more accessible for radial velocity measurements. Another major difference between the original *Kepler* mission and K2 is how the planet search and follow-up process is organised: whilst a dedicated follow-up team worked on the original *Kepler* data, in K2 planet detection and follow-up is performed by the wider community without any official oversight, although collaboration is encouraged through use of the ExoFOP website.[6] High resolution imaging has been performed for many candidates by a variety of independent teams, although the structure of these observations mimics those for the *Kepler* mission, relying on adaptive optics or speckle imaging. The results of these imaging studies have been presented in a variety of ways: in conjunction with candidate lists from planet hunting teams (e.g. Crossfield et al. 2016, Mayo et al. 2018); obtained as part of the detailed characterisation of individual systems (e.g. Vanderburg et al. 2015); or made available to the community on ExoFOP and later combined with other data (e.g. Dressing et al. 2017).

1.4.1.7 Other ground-based surveys

A number of further transit surveys have produced a handful of exoplanets each, summarised below.

The Transatlantic Exoplanet Survey (TrES, Alonso et al. 2004, Alonso et al. 2007) published five planet discoveries. For the first planet announced, TrES-1b, high resolution imaging was obtained (Alonso et al. 2004); such observations were not repeated for the remaining planets.

The Qatar Exoplanet Survey (QES, Alsubai et al. 2013) has published six planets to date. Lucky imaging was obtained for Qatar-2 (Bryan et al. 2012), and adaptive optics imaging was obtained of Qatar-6 after the detection of a faint companion in

[6] `https://exofop.ipac.caltech.edu/`

images taken for follow-up photometry (Alsubai et al. 2018).

The Pre-OmegaTranS project (POTS, Koppenhoefer et al. 2013) presented a single confirmed planet and another candidate planetary system, with adaptive optics imaging presented for the POTS-1 system. A fainter star was found at a separation of 1.3″ from the planet host star, but this was too faint to explain the relatively deep 3% transit signal. Furthermore, no change in transit depth was found in multicolour photometry, despite evidence that the companion was significantly redder, and hence the transit depths would display a strong correlation with wavelength if originating from this star.

The WFCAM Transit Survey (WTS, Birkby et al. 2011) published two planets, with lucky imaging being obtained of WTS-2 (Birkby et al. 2014). Similarly to the case of POTS-1, a companion star was found only 0.56″ from the target star, but multiband photometry again ruled out this fainter star being the source of the transit signal, which should have varied by a factor of two in depth across the wavelength range covered.

1.4.2 Independent imaging surveys

Interest in obtaining high resolution images of publicly announced transiting planets has mainly been motivated by continued interest in the formation of hot Jupiters, and concerns about the lack of any quantification of contaminating light for the majority of published papers. Studies of the binarity of transiting exoplanet host stars were preceded by several initial studies covering planets discovered through radial velocity measurements (e.g. Mugrauer & Neuhäuser 2005, Chauvin et al. 2006, Eggenberger et al. 2007).

Note that results obtained by independent teams for the *Kepler* and K2 missions are covered in Section 1.4.1, as these were mainly obtained in order to assist the initial planet characterisation process.

1.4.2.1 Lucky imaging with AstraLux Norte and AstraLux Sur

Daemgen et al. (2009) presented the first dedicated high resolution imaging survey of transiting exoplanet systems utilising the AstraLux Norte lucky imager. Further observations from the same instrument, and also from its southern twin AstraLux Sur, were presented by the same team in Bergfors et al. (2013), Wöllert et al. (2015), Wöllert & Brandner (2015). Separately, a survey covering mainly radial velocity exoplanet systems has been performed with both of the AstraLux instruments, with a small number of transiting exoplanet systems being included in Ginski et al. (2016).

Fourteen systems were considered in Daemgen et al. (2009), with companions being discovered near TrES-2 and TrES-4, in addition to second epoch observations of the known companion to WASP-2. As is standard for AstraLux data, images were obtained in both the i' and z' filters, with the colours of the companions used to estimate their properties. Updated parameters were provided for each of the three systems with a companion, with the changes being relatively minor, due to the faintness of the companions. No definite conclusions were reached as to whether any of the companions were gravitationally bound to the planet host stars.

Bergfors et al. (2013) analysed 21 systems, including the three with detected companions from Daemgen et al. (2009), using the same observation and data reduction techniques. The companions to TrES-4 and WASP-2 were found to exhibit common proper motion at a high level of significance, and additional companions were found to HAT-P-7, HAT-P-8, WASP-12 and XO-3. As with the previous study, the four newly discovered companions were all significantly fainter than the planet host stars. An analysis of the multiplicity rate of exoplanet host stars was performed, based on the number of detections, with the conclusion that exoplanet host stars have a similar multiplicity fraction to that found among field stars. HAT-P-7 was considered in greater detail in Narita et al. (2010), where the AstraLux results were combined with adaptive optics imaging from Subaru/HiCIAO, which considered the implications for Lidov-Kozai migration in the context of the stellar companion, the recently measured orbital misalignment of HAT-P-7b and suspected existence of an additional non-transiting

planet, dubbed HAT-P-7c.

Larger samples were presented in Wöllert et al. (2015), covering 49 systems, and Wöllert & Brandner (2015), covering 74. The observing and analysis techniques again remained unchanged, and between the two papers, 13 new companion stars were detected. Photometric and astrometric measurements were presented, but no further analysis was performed. Echoing the results of previous work, all newly discovered companion stars were much fainter.

Ginski et al. (2016) presented observations of a mix of transiting and non-transiting exoplanet systems, continuing earlier work that considered transiting exoplanets only (Ginski et al. 2012). Imaging was obtained in only the i' filter, preventing colour-based analysis of the companion from the new observations alone. However, for several of the companions, previous observations were available in the literature, allowing investigation of the proper motions of the companions. Eight of the companions analysed were found to show common proper motion, whilst two were found to be be physically unassociated.

1.4.2.2 Lucky imaging with LuckyCam

Faedi et al. (2013) presented lucky imaging observations from LuckyCam, a lucky imager mounted on the Nordic Optical Telescope at the time of observations. Data were taken in the i' filter only, covering 16 transiting planet host stars. Known companions to five targets were re-detected, and additionally two companions to TrES-1 were discovered. Further to these, possible detections of companions to HD 209458, HAT-P-5, and HAT-P-6 were discussed in an appendix, but in all cases the significance of the detection was below the formal detection limit chosen by the authors. In the case of the potential companion HD 209458, it was noted that no such companion had been identified by several other surveys, nor was it found in archival adaptive optics imaging of the system, and hence the detection was very likely to be spurious.

1.4.2.3 Adaptive optics with MMT/ARIES

Adams et al. (2013) was nominally part of a survey of candidate planets identified by the *Kepler* mission, but included near infrared observations of 15 previously published transiting exoplanetary systems. Observations in the Ks filter were presented, with three new companions detected, in addition to repeat observations of the companions to WASP-2 and WASP-33.

1.4.2.4 Adaptive optics with Keck/NIRC2

The 'Friends of Hot Jupiters' survey was a comprehensive effort to identify companions to transiting hot Jupiters through a number of different techniques, which included a search for long-term radial velocity trends (Knutson et al. 2014), multi-epoch and multi-colour adaptive optics imaging (Ngo et al. 2015, Ngo et al. 2016), and detailed analysis of spectra to identify blended companion stars (Piskorz et al. 2015).

Ngo et al. (2015) reported near infrared AO observations of 50 transiting hot Jupiter host stars, with the sample being extended to 32 additional targets in Ngo et al. (2016). The data revealed that the previously reported companions to HAT-P-8 and WASP-12 were themselves made up of two stars, and the discovery of these hierarchical triples was announced separately in Bechter et al. (2014). Each system was initially observed in the K filter, and the data were inspected for evidence of companions. If these were identified, additional data were obtained in further bands (either J, H, or both) to better characterise the companion, and the target was reobserved in subsequent years to determine if the companion showed common proper motion.

In Ngo et al. (2015), two of the observed companions were determined to be background objects, with the remaining companions being physically associated. The similar analysis in Ngo et al. (2016) did not give such conclusive results for all companion stars, mainly due to insufficient time coverage in the AO data and larger uncertainties in independent published measurements.

In addition to astrometry and photometry, the properties of the potentially bound

companions were determined based on differential photometry, the known properties of the planet host star, and the assumption of physical association (i.e. same distance). A statistical analysis was then performed to determine the multiplicity fraction of the overall sample, and also of two subsamples, consisting of those systems where the planetary orbit is aligned with the stellar rotation (low obliquity), and those with misaligned orbits (high obliquity). The key result of the analysis was the finding that the two samples were not significantly different – the existence of a misaligned planetary system did not correlate with the presence of a binary companion. However, this result may not be too surprising in light of work suggesting that the observed spin-orbit misalignment distribution is not primordial, as discussed in Section 1.2.2.1. Another finding of the survey was that the fraction of systems for which a companion beyond 50au was detected was significantly higher than expected of a sample of field stars, whilst the fraction with companions below this (projected) separation was significantly lower. This was considered to be tentative evidence of a possible link between very wide binaries and hot Jupiters, although many of the detected stars were determined to be too distant for Lidov-Kozai oscillations to occur, and so the actual mechanism responsible for such a correlation remains unclear (Ngo et al. 2016).

The same instrument was also used by a separate team to discover the companion to WASP-33 (Moya et al. 2011), and it is worth noting that many of the high resolution imaging studies performed in connection with the *Kepler* mission have also used Keck/NIRC2.

2 High resolution imaging

> " *...the star is then seen (in favourable circumstances of tranquil atmosphere, uniform temperature, &c.) as a perfectly round, well-defined planetary disc, surrounded by two, three, or more alternately dark and bright rings...*"
>
> – Herschel, J.F.W., '*Treatises on Physical Astronomy, Light and Sound contributed to the Encyclopaedia Metropolitana*', 1828.

The angular resolution of a telescope or other imaging device describes its ability to resolve two objects into separate images. As a consequence of the wave-like nature of light, even a perfect optical system is not able to focus light from a point source to an infinitesimally small point on an image. Instead, light is diffracted by the entrance aperture of the imaging system, and for a circular aperture this results in the 'Airy pattern', consisting of bright central peak and a series of concentric rings of decreasing brightness (Airy 1834). The size of the Airy pattern, and hence the angular resolution of the instrument, depends on the ratio of the wavelength of light λ to the size of the telescope aperture D. The most commonly used definition of angular resolution, the Rayleigh criterion, states that two objects would be just resolvable when their angular separation, θ, corresponds to,

$$\sin\theta = 1.22\frac{\lambda}{D} \tag{2.1}$$

which occurs when the first minimum of one Airy pattern coinciding with the peak of the second Airy pattern. However, objects at smaller angular separations can still be resolved with suitable image analysis techniques, and Lord Rayleigh noted in his definition that a bright source could potentially obscure a nearby faint source at wider separations than his stated criterion (Rayleigh 1879).

It is clear from the Rayleigh criterion that there are two changes that can increase the angular resolution of a telescope. Moving towards shorter wavelengths of light improves resolution, but strong atmospheric absorption makes ground-based observations beyond the blue optical infeasible. Alternatively, larger telescope apertures give improved angular resolution, with a 10cm aperture resulting in a theoretical limit of $1.4''$, compared to modern 10m-class telescopes having diffraction limits of only

tens of milliarcseconds. However, the effective angular resolution of large telescopes is significantly limited by seeing, an effect caused by atmospheric turbulence above the telescope, which degrades images to an effective angular resolution of approximately 1 arcsecond at favourable observing sites when the atmosphere is calm, and several times worse in many other locations.

2.1 The effects of atmospheric turbulence

The refractive index of air changes slightly with temperature (and, to a lesser extent, pressure). The Earth's atmosphere has a complex vertical temperature profile, and turbulence results in the stochastic mixing of patches of air with differing temperatures. Incoming light from astronomical sources therefore passes through many regions of air with slightly different refractive indices, distorting the incoming light from the star. The quality of the resulting image formed by a telescope or the human eye is degraded, significantly so for large telescopes. The actual image of the star resulting from seeing varies on very short timescales, with a characteristic timescale of 10 milliseconds or so.

For any telescope with an aperture greater than $\sim$ 10cm, the image of a star is blurred to an angular resolution well below the diffraction limit of the telescope. Instead, the profile of an imaged star is approximately 1 arcsecond in size, sometimes referred to as the 'seeing disc'. The size of the seeing disc is set by the Fried parameter, r_0, which describes the size of the turbulent eddies that most affect the incoming light (Fried 1966). The resolution resulting from seeing-limited images is equivalent to that of telescope with diameter r_0, and at good observing sites r_0 is typically 10cm for optical light, corresponding to the observed angular resolution of approximately an arcsecond. At longer wavelengths r_0 is increased, increasing with $\lambda^{6/5}$, and as such the effects of seeing are reduced for near- and mid-infrared observations – although the gain is counteracted by the decrease in theoretical angular resolution with wavelength (see Equation 2.1).

For a large telescope with $D > r_0$, each individual turbulent patch of diameter

r_0 acts to create its own diffraction-limited image, resulting in multiple images of a star being created. Each of these images or 'speckles' will be seen to vary in brightness and position with the changing turbulence. For long exposures, the motion of these speckles causes the blurring of the stellar profile, although sufficiently short exposures ($t_{\mathrm{exp}} \ll 1$s) are able to 'freeze' these changes.

The optical aberrations caused by seeing are typically divided into 'low order' and 'high order' effects, referring to the relevant Zernike polynomials (Zernike 1934) used to describe these aberrations. The lowest order effects, tip and tilt, result in a star appearing to wander across the image as wavefronts enter the telescope at an angle. This effect is more pronounced for small telescopes, as the chance of a net wavefront 'tilt' is reduced for larger apertures. Compensating for tip-tilt error requires correction of the apparent position of the star, whether through real-time correction via actively controlled optical components, or post-processing of short-exposure images which 'freeze' these motions. Higher order effects give rise to the speckled nature of the image, and require more complex correction, mitigation, or analysis techniques. A series of short exposures illustrating both tip-tilt error and the more complex speckles are shown in Figure 2.1.

Whilst turbulence, and hence seeing, are inherently random processes, the effects of seeing on stars near to one another are correlated. The light from a pair of stars at small separation will follow very nearly identical paths through the atmosphere, and hence the wavefront errors induced by turbulence will be common to both. The angle within which the wavefront errors for two stars remain correlated is referred to as the isoplanatic angle, which defines a region around any given star in which other stars will show similar image aberrations, the isoplanatic patch. The correlation length of wavefront errors, and hence the isoplanatic angle, varies with wavelength, with larger isoplanatic angles towards longer wavelengths. As a result, many instruments that correct for atmospheric turbulence operate in the near infrared, as a larger area of the sky can be corrected and hence imaged at high resolution simultaneously, increasing the efficiency of the instrument.

In addition to limiting angular resolution, atmospheric turbulence also limits

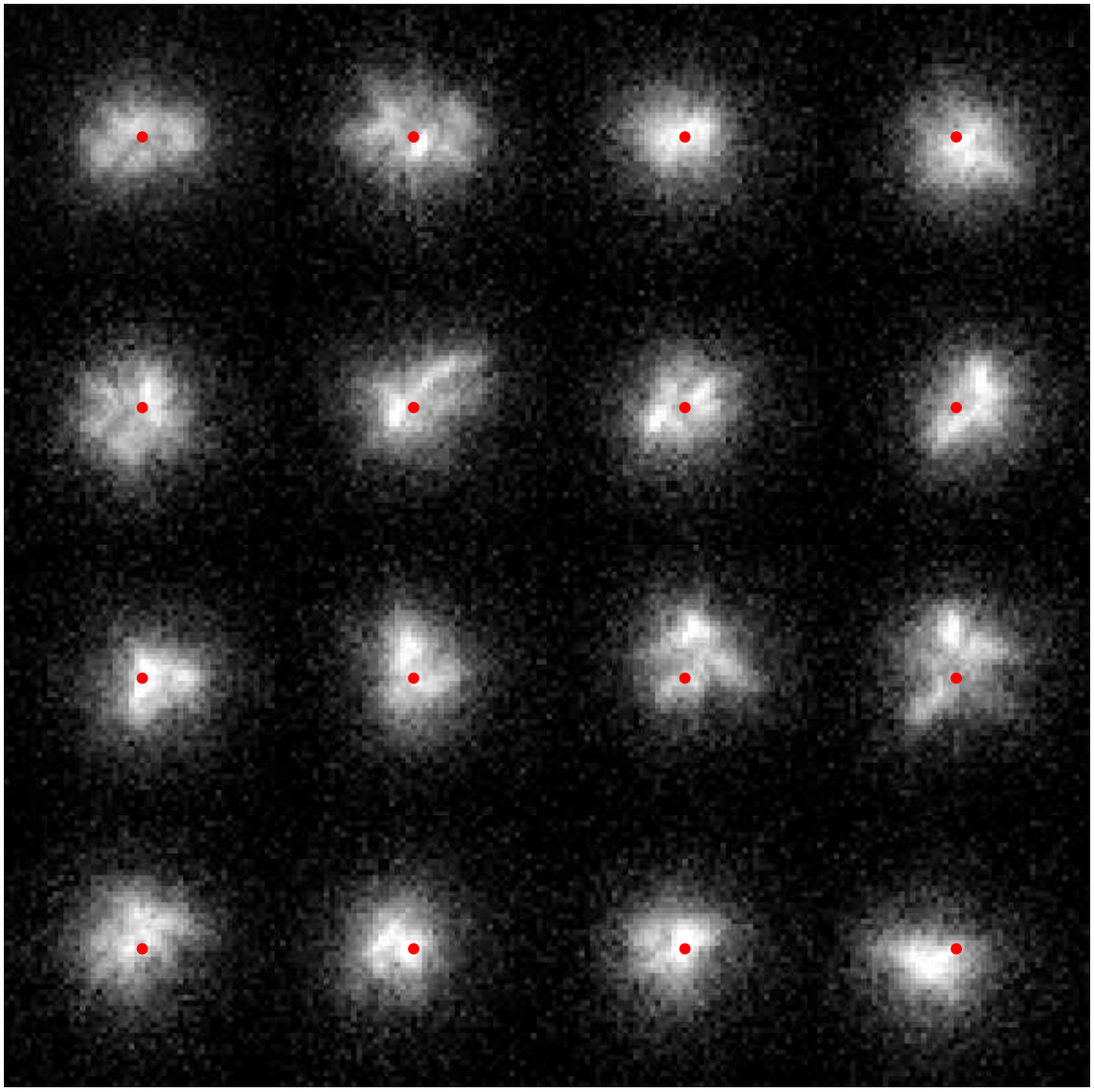

Figure 2.1: Individual 100ms exposures of a star from the Two Colour Instrument on the Danish 1.54m telescope, using a logarithmic colour scale. Every fifth exposure in a sequence is shown, running left-to-right and top-to-bottom. For each exposure, a red dot indicates the observed location of the star in the first exposure. The star is seen to wander around the original position due to tip-tilt error, and also exhibits a complex and highly variable speckle pattern.

photometric accuracy. Scintillation is commonly observed as the twinkling of stars to the naked eye, with turbulence causing variable focusing and defocusing of the incoming starlight, resulting in intensity fluctuations on the image formed by the telescope (Young 1967, Osborn et al. 2015). The effect is reduced for larger telescopes, which include many turbulent patches of diameter r_0 included within their aperture, averaging out the scintillation from each individual patch. When aiming for high photometric accuracy, long exposure times ($t_{\rm exp} \gg 1$s) can be used to reduce the time varying noise induced by scintillation (e.g. Southworth et al. 2009). Unlike seeing, scintillation is dominated by high altitude turbulent motions, and the amplitudes of the two effects are not necessarily closely correlated (Dravins et al. 1998, Osborn et al. 2015).

2.2 High resolution imaging techniques

For many areas of astrophysical research, high resolution images are of vital importance. Examples include the study of the environment at the galactic centre (Clénet et al. 2004, Ghez et al. 2008, Gillessen et al. 2009); the direct detection and analysis of protoplanetary discs (Apai et al. 2004), brown dwarfs (Chauvin et al. 2004), and young planets (Marois et al. 2008, Kraus & Ireland 2012); the detection and study of multiple stars (Close et al. 2003, Tokovinin et al. 2015); the measurement of the angular sizes of stars (Kervella et al. 2004, Monnier et al. 2007) and the direct detection of features on the surfaces of stars (Roettenbacher et al. 2016); the kinematics of galaxies (Davies et al. 2006) and their formation in high redshift universe (Stark et al. 2008); and observations of solar system objects including the Sun (Scharmer et al. 2003, Denker et al. 2007), the planets and their moons (de Pater et al. 2010, Gendron et al. 2004), and asteroids (Descamps et al. 2011).

As a result, many techniques have been developed for correcting optical aberrations, improving image quality, or for teasing out high resolution information from the affected data. Several of the methods outlined below are not mutually exclusive – for example, large telescopes routinely operate with both active and adaptive optics

systems.

2.2.1 Active optics

Unlike most image correction methods, active optics systems are not used to correct for the rapidly changing wavefront aberrations induced by high altitude atmospheric turbulence. Instead, they correct for slower changes (or constant errors) in image quality caused by the telescope itself and its surrounding environment. The structure and optical elements in large telescopes will expand and distort with variations in temperature and telescope pointing, and it is infeasible to build 10m-class mirrors with negligible thermal expansion and sufficiently high stiffness to combat such effects. The use of segmented mirrors can reduce the problems caused by thermal expansion and flexing, but it is then vital to ensure that adjacent mirror segments are correctly aligned with one another. Wind can also reduce telescope image quality, buffeting large primary mirrors and exciting vibrations in the telescope structure.

Active optics systems involve a series of active optical element to correct such sources of optical errors. This is typically done by deforming the primary or secondary mirrors of a telescope through a series of sensitive actuators, in addition to controlling the separation and optical alignment of those mirrors. Such systems are ubiquitous for 10m-class telescopes, and are also present on numerous 4m-class telescopes. Active optics systems can operate in an open-loop configuration, in which the system provides pre-determined corrections based on variables such as zenith angle and temperature, or in a closed-loop configuration, in which optical aberrations are measured and corrected in real time; many systems combine elements of both. To further reduce optical errors caused by the telescope itself, features such as climatic control of telescope enclosures and temperature control of large mirrors are commonly used to limit day-night temperature shifts, and hence the associated changes in optical configuration. Noethe (2002) provides a comprehensive review of active optics systems.

2.2.2 Adaptive optics

Adaptive optics (AO) systems measure and correct wavefront aberrations in real time. AO systems usually perform corrections using a small deformable mirror (DM) equipped with tens to hundreds of small actuators, applying corrections at a rate of $10 - 1000$ Hz. This differs from active optics systems, as it is not generally feasible to modify the shape of large primary mirrors with sufficient accuracy and speed to correct atmospheric wavefront distortions, although some systems have used adaptive secondary mirrors (e.g. Lloyd-Hart et al. 2003, Guerra et al. 2013).

Wavefront aberrations are measured through the observation of a reference source of light, which may be a star (a natural guide star, NGS), or instead artificially generated point of light (a laser guide star, LGS). Measurements are most often performed using a Shack-Hartmann wavefront sensor which consists of an array of small apertures or lenses, each of which produces an image of the guide star onto a detector. Due to their small size, the apertures only receive a small portion of the incoming wavefront each; as a result, tip-tilt aberration is dominant, and the image created by each aperture will move on the detector. By measuring the motion of the image from each aperture, the local wavefront tilt can be determined, and the combination of all image shifts allows the 2D profile of the incoming wavefront to be reconstructed. The deformable mirror is then modified to cancel out the measured wavefront aberration, providing a seeing-corrected image to the attached instrument or detector.

Better correction can provided by 1) increasing number of apertures in the Shack-Hartmann array to provide better sampling of the wavefront; 2) adding more actuators in the deformable mirror to provide a more accurate correction of the wavefront; and 3) through higher rates of operation to reduce the residual wavefront errors caused by time delays between sensing and correction. However, each of these changes also comes with drawbacks. Adding additional apertures and actuators increases the required computational difficulty of modelling the wavefront and determining the necessary corrections, noting that only a small fraction of a second is available for each iteration of the algorithm. Higher rates of operation also cause such issues by reducing the time available

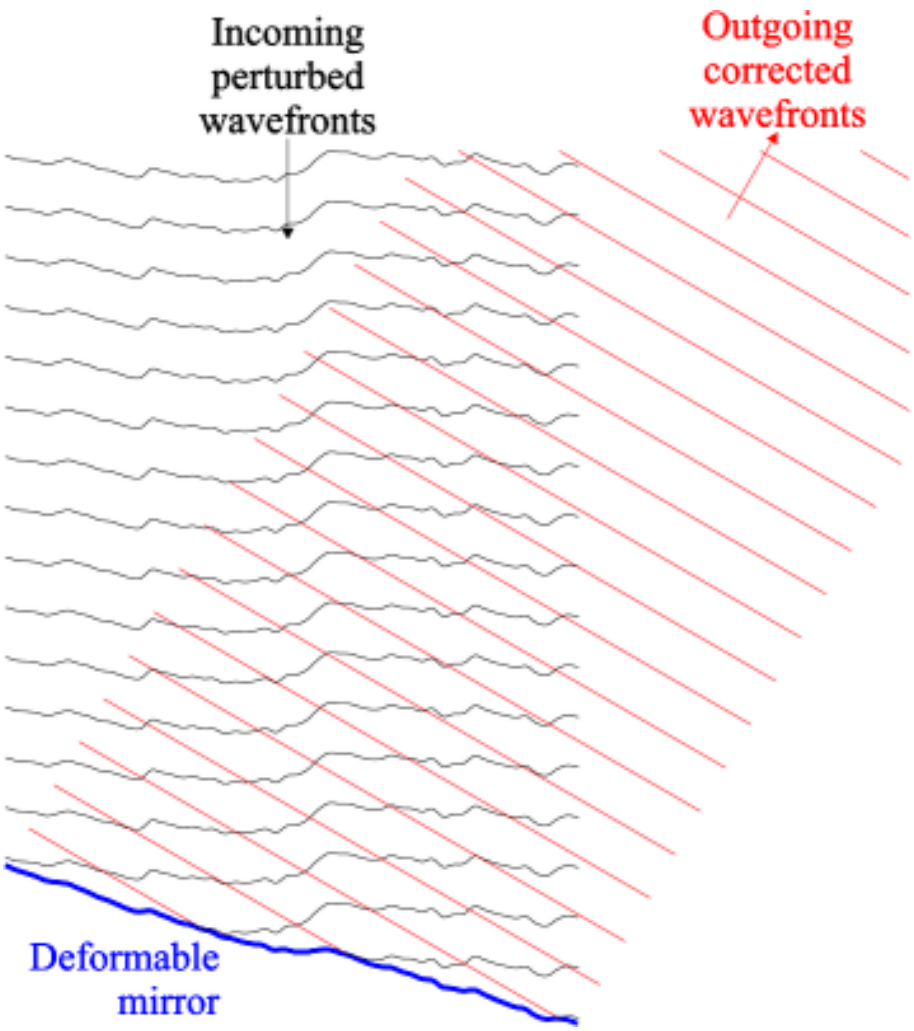

Figure 2.2: A cartoon illustrating wavefront correction using a deformable mirror. The incoming wavefronts (black) have been perturbed by atmospheric turbulence. Based on information collected by a wavefront sensor (not shown), the deformable mirror (blue) is shaped so as to cancel out the wavefront errors introduced by the atmosphere. The reflected light (red) consists of corrected, plane-parallel wavefronts, which are passed on to another instrument, such as a photometer or a spectrograph.
Image created by Bob Tubbs, released into the public domain via Wikimedia Commons:
`https://commons.wikimedia.org/wiki/File:Adaptive_optics_correct.png`

for each iteration, and also reduce the number of photons collected by the Shack-Hartmann sensor during each exposure. Similarly, providing more apertures divides the same number of incoming photons across a larger number of images, reducing the signal-to-noise (SNR) of the wavefront tilt measurement from each individual aperture.

Due to the requirements for sufficient SNR in the wavefront measurements, AO systems are limited to using bright stars for guiding. Whilst the guide star does not need to be the target star, correction becomes increasingly poor outside the isoplanatic angle. In the visible, this limitation results in as little as 0.001% of the sky being available to NGS AO systems due to the sparsity of bright guide stars, depending on the limiting magnitude of the system. This issue is somewhat alleviated by designing an AO system operating in the infrared, where the isoplanatic angle is larger, but even in the best case, only a few percent of the sky remains observable (Rigaut 2015).

2.2.2.1 Laser guide stars

To combat the limited sky available to NGS systems, an artificial guide star can be created using a ground-based laser positioned near the telescope. The concept relies on the laser light being scattered back towards the telescope by atmospheric particles, passing through same turbulent atmosphere as the starlight, allowing wavefront errors to be measured and corrected for (Foy & Labeyrie 1985). In order to achieve a sufficient amount of returned light from high altitude, the wavelength of the laser is carefully chosen to match specific re-emission or scattering mechanisms. The most common choices of mechanism are the sodium resonance, which involves stimulated emission by atmospheric sodium at an altitude of approximately 90km, and Rayleigh scattering, which uses blue or ultraviolet light that is backscattered by the atmosphere at altitudes of 10–30km. Whilst sodium lasers are preferable for seeing correction due to their ability to probe a larger fraction of the atmosphere, the strict wavelength tuning required to exactly match the sodium resonance makes such lasers much more complex – and hence expensive – than Rayleigh scattering lasers.

However, the use of laser guide stars introduce two new optical problems. Unlike

the column of air that is probed by starlight, the laser is off-axis and cannot be treated as a source at infinity, and hence the laser probes a cone of air that may contain significantly different turbulence; this is known as the cone effect (Foy & Labeyrie 1985). Secondly, the light is not only affected by atmospheric turbulence when passing downwards through the atmosphere, but is also affected when passing upwards before scattering; as a result, an unknown amount of tilt error is introduced to the laser wavefront that is not present in the stellar wavefronts, making it difficult or impossible to correct stellar tip-tilt motion with the LGS alone (Rigaut & Gendron 1992). Other issues present in LGSAO facilities are increased cost and complexity compared to NGS systems, aircraft and satellite avoidance, and the light pollution created by the lasers (adjacent observing facilities can be badly affected by bright laser beams passing through their field of view, as discovered by the NGTS survey, Wheatley et al. 2018).

2.2.2.2 Advances in adaptive optics

In addition to the simple NGS and LGS AO systems discussed above, many variants of the AO concept exist. Rigaut (2015) provides an overview of these advances, with a brief summary being given below:

- Extreme AO (ExAO) focuses on very high quality correction for high contrast imaging close to targets, at the expense of being unable to use a laser guide star due to the cone effect. Several instruments such as SPHERE (Beuzit et al. 2008), GPI (Macintosh et al. 2014), and SCExAO (Martinache & Guyon 2009) utilise this concept, with the main aim being the direct detection of hot, young exoplanets in wide orbits around nearby stars.

- Ground Layer AO (GLAO) corrects only for the atmosphere closest to the telescope (the 'ground layer'), and is able to correct much wider fields of view due to the larger angular extent of turbulence features near the ground, as seen by the telescope. The ground layer contributes a large fraction of the wavefront error, allowing a significant improvement over seeing-limited observations

(Tokovinin 2004).

- Multiple Object AO (MOAO) uses multiple guide stars spread over several arcminutes of sky. Rather than correcting for atmospheric turbulence across the entire field, multiple deformable mirrors are used to correct the light from individual targets. Instruments such as CANARY (Gendron et al. 2011) and RAVEN (Andersen et al. 2012) utilise this concept.

- Multi-Conjugate AO (MCAO) also invokes multiple guide stars and deformable mirrors, aiming to correct the entirety of a wider field of view ($\simeq$2 arcmin.). The multiple guide stars are used to reconstruct a 3D turbulence profile, with multiple deformable mirrors being used to correct for individual layers of atmospheric turbulence (Beckers 1988). The concept has been utilised by instruments such as MAD, which used three natural guide stars (Marchetti et al. 2007), and the GeMS system, with a constellation of LGSs (Neichel et al. 2014).

These improvements on 'classical' AO concepts are being actively pursued, with some systems already active on 10m class telescopes, and others in development for both 10m class (e.g. ESO's Adaptive Optics Facility) and 30m class telescopes, with AO capabilities being considered a fundamental component of the latter.

2.2.3 Interferometry

Following Equation 2.1, the angular resolution of a telescope can be improved by increasing its diameter. However, the telescope aperture does not need to be filled by a single mirror or lens; light from two or more sub-apertures with a separation d can be combined to give the same effective resolution as a single aperture with diameter d. Using interferometry, it is possible to combine light from multiple separate telescopes at separations much greater than the maximum feasible mirror diameter, achieving very high angular resolution.

Michelson (1890) considered the observation of a single source through two slits or circular apertures, a variation on Young's double slit experiment. An interference pattern is created when a light source of small angular diameter α passes through two slits with separation D. However, if the source has a critical angular size α_0, the fringes are no longer observed; this angular size corresponds to

$$\alpha_0 = 1.22 \frac{\lambda}{D}, \tag{2.2}$$

which corresponds to the angular resolution given by Equation 2.1 in the case of small angles (i.e. $\sin\theta \approx \theta$). If D is further increased beyond this limit, the fringes are observed to regularly appear and disappear, modulated by the Airy pattern.

By modifying the separation between the two slits or apertures and observing the modulation of the interference pattern, it is possible to accurately determine the size of an observed object, even when seeing would prevent the source being resolved in an image. The technique was demonstrated on both solar system objects (Michelson 1891) and on large, nearby stars (Michelson & Pease 1921).

Michelson (1890) also noted that light from two closely separated point sources would produce a distinct interference pattern, with fringes that vary in spacing inversely with the separation of the two sources, and the pattern's direction corresponding to the angle between orientation of the two sources. This was first applied to the orbit of the Capella binary system (Anderson 1920), where the two components have an angular separation of only $0.05''$.

The examples given so far only consider the intensity or visibility of the interference pattern; however, its phase also contains valuable information. For distant objects such as stars, the Van Cittert-Zernike theorem states that the phase and visibility of the interference pattern are related to the Fourier transform of the brightness distribution of the source – that is, the Fourier transform of an image of the object (van Cittert 1934, Zernike 1938). Therefore, an image of the object can be re-constructed from interferometric observations if the phase of incoming light can be preserved, a technique known as aperture synthesis.

However, preventing the introduction of phase errors is difficult for optical or

near infrared astronomy. As an object moves through the sky, the distance or *path length* from the source to each aperture or telescope varies independently, and must be compensated for. To ensure that light reaches the interferometer in phase, the pathlengths from each telescope must be controlled to less than the wavelength of the incoming light, requiring sub-micron accuracy in the manufacture and positioning optical components. Even if such accurate control can be achieved, atmospheric turbulence imparts random phase variations, although this can be overcome by using more than two apertures in conjunction with certain assumptions about a source (Shao & Colavita 1992, Quirrenbach 2009).

Despite these challenges, interferometric instruments such as CHARA (ten Brummelaar et al. 2005) and GRAVITY (Eisenhauer et al. 2011) have successfully produced scientific data. Such systems often operate in the near infrared, where path length control requirements are somewhat less stringent than in the optical, due to the increased wavelength. Due to the high SNR required to correctly track and correct for path length errors, combined with significant losses due to the high number of optical components, these interferometers are typically limited to targets brighter than 10th magnitude in H or K.

Outside of optical and NIR astronomy, interferometry has seen widespread adoption in the radio and, more recently, the sub-millimetre regime. Longer wavelengths of light reduce the precision needed to build an interferometer, and correspond to frequencies that are low enough for the detected wavefront to be digitised and recorded at the telescope. As a result, interferometry can be performed electronically or digitally using the recorded data, allowing data collected and stored at widely spaced telescopes to be combined after observations have been completed. Baselines of hundreds or thousand kilometres are routinely achieved with such techniques, and radio interferometers can achieve angular resolutions that exceed those of the best NIR interferometers.

2.2.4 Speckle interferometry

Interferometric techniques can also be applied to short optical or NIR exposures obtained with a single, large aperture. Whilst a long exposure of a star will show a large, blurred PSF due to the effects of seeing, short exposures show a distinct speckle pattern, as shown in Figure 2.1. The speckles are themselves individual images of the source, and can be as small as the diffraction limit of the telescope. Similar speckle patterns will be observed for two sources that are within the isoplanatic angle, and hence a short exposure image will consist of two superimposed speckle patterns, one for each star. This allows the two sources to be distinguished from one another, even if they are well below the seeing limit encountered in long exposure images. Similarly, if the observed object is not a point source, the speckles will be constructed from resolved images of the source.

The analysis of raw speckle images is difficult due to the complex and varying nature of the speckle patterns, especially for larger telescopes; instead, Labeyrie (1970) illustrated that the Fourier analysis of speckle images allows high resolution information to be retrieved relatively easily. If multiple sources were present, the superimposed copies of the speckle pattern result in interference fringes when the image is Fourier transformed. Similarly, the Fourier transforms of resolved and unresolved sources are distinct, with unresolved sources having more power at high spatial frequencies in order to create a sharp PSF.

The basic concepts of speckle interferometry are illustrated in Figure 2.3. Panel (a) shows a single, short (100ms) exposure of a double star, with the two PSFs having similar speckle patterns. Panel (b) shows the squared modulus of the Fourier transform of panel (a), with the interference pattern resulting from the double star being obvious. The pattern has the same orientation as the binary, and the fringe spacing is inversely proportional to the binary star separation. Panel (c) shows the combined interference pattern from 1,200 exposures of the target, with the squared moduli of their Fourier transforms having been summed to increase the signal-to-noise of the interference fringes, and to average out features related to the individual speckle patterns.

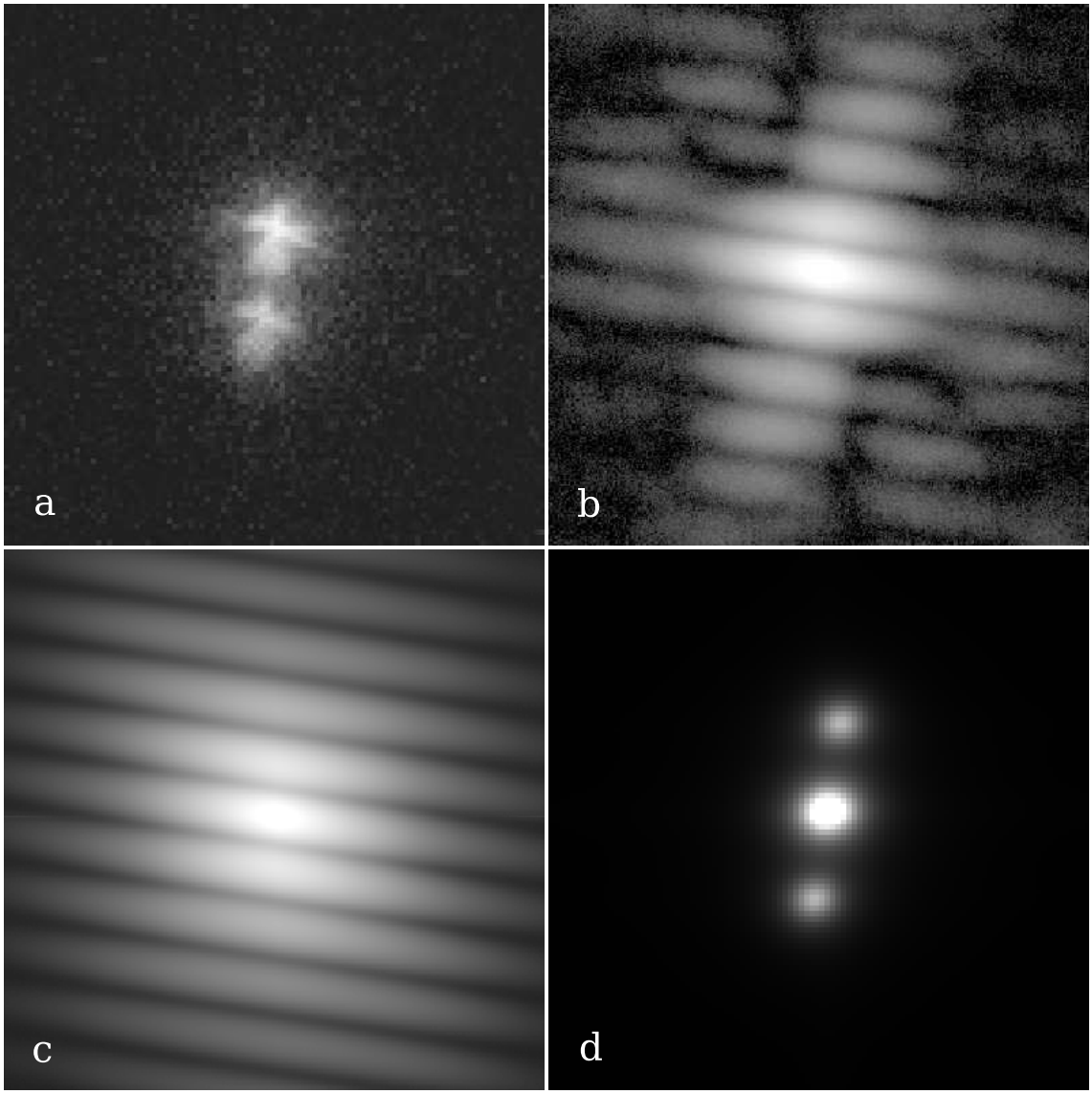

Figure 2.3: An illustration of the speckle imaging technique. (a) A 100ms exposure of a double star, showing speckle noise which is correlated between the two stars. (b) The modulus of the Fourier transform of the single exposure shown in (a), exhibiting a series of fringes with the same orientation as the binary. (c) Composite of the Fourier transform moduli of 1,200 exposures, with the fringe pattern having a much higher SNR. (d) A reconstructed image generated from (c), showing the 180° degeneracy in the position of the companion that is characteristic of speckle interferometry.

Panel (d) is a reconstructed image of the binary, generated using the summed Fourier transforms in (c). As the moduli of the Fourier transforms were used, phase information was lost, resulting in a 180° ambiguity as to the true orientation of the binary. Further analysis can be performed to enhance and model the interference fringes, such as the reduction process outlined in Tokovinin, Mason & Hartkopf (2010).

Initial applications of the technique reproduced many earlier interferometric results (Gezari, Labeyrie & Stachnik 1972), and it was quickly taken up for the detection and monitoring of binary stars (e.g. McAlister 1977, Tokovinin 1982). Compared to the large, dedicated instruments required for adaptive optics or multi-telescope interferometry, speckle interferometry is relatively simple to implement, and can be achieved with any detector that is able to take sufficiently short exposures. Speckle interferometry features strongly in population studies of multiple stars (e.g. Fischer & Marcy 1992, Tokovinin et al. 2006, Raghavan et al. 2010), as it is feasible to obtain observations of large samples of targets in a reasonable amount of observing time.

2.2.5 Lucky imaging

As the turbulence above a telescope varies, there is a chance that a certain column of atmosphere will induce minimal wavefront errors on incoming starlight for a short period of time. If an imager operating at a sufficiently high frame rate is attached to a telescope, the wavefront errors present in each exposure will vary, and on occasion the observer will be 'lucky' and obtain an exposure with minimal wavefront distortion. By determining the image quality of each exposure through some metric, it is possible to pick out only the 'lucky' exposures, which are combined to give an image with a significantly higher resolution than an equivalent long exposure. This technique is known as Lucky Imaging.

The chance of a minimal wavefront error being produced by a column of air, and hence the chance of obtaining a lucky exposure, depends on the diameter of that column of air, which is itself set by the telescope aperture. The Fried parameter, r_0, describes the distance over which turbulence remains correlated; this parameter

is typically of the order of 10-40cm in the optical (e.g. Nieto, Llebaria & di Serego Alighieri 1987), with good astronomical observing sites being at the upper end of this range. For small telescopes with $D \lesssim r_0$, it is relatively likely that the correlated turbulence will result in minimal distortion across the aperture; however, for telescopes with diameters $D \gg r_0$, it is very unlikely that the many effectively independent turbulent regions above the telescope will spontaneously result in minimal wavefront distortion. Fried (1978) performed a theoretical analysis of the concept, also coining the 'lucky' terminology, predicting that approximately 10% of short exposures would be 'good' for $D = 5r_0$. However, the predicted probability dropped off sharply with increasing D, with a telescope of diameter $10r_0$ only being able to obtain one 'good' exposure per 10^{15} exposures.

Hecquet & Coupinot (1985) provided a further analysis of the technique, considering the gain in angular resolution as a function of the fraction of frames rejected and the telescope diameter relative to the Fried parameter, D/r_0. The work highlighted the fact that resolution can be significantly improved by rejecting only the worst few percent of exposures: when rejecting the worst 24% of frames, the angular resolution of a telescope with diameter $3\,D/r_0$ (approximately 1.2m at a good observing site) would be improved by a factor of two. Achieving further improvement becomes increasingly difficult, with the rejection of the worst 99% of exposures from the same telescope only improving resolution by a factor of 2.9. For a given exposure rejection rate, the improvement in image resolution was found to peak at a certain telescope size. For smaller telescopes, the improvement is limited simply due to reaching diffraction limit of the telescope; for larger telescopes, the chance of observing a lucky exposure falls. For large telescopes, very stringent frame selection criteria are needed to achieve a good improvement in angular resolution, making the technique infeasible on such telescopes due to the large amount of observing time needed, and the fraction of data that is rejected.

Despite this theoretical basis and the encouraging predictions for 1–2m class telescopes, the adoption and development of lucky imaging instruments was relatively slow until the turn of the 21st century. Much of the difficulty occurred in obtaining

a sufficiently high SNR: with standard CCDs, the readout noise can overwhelm the relatively small counts per pixel obtained in short exposures of all but the brightest stars. Furthermore, standard CCDs have readout times that are typically on the order of several seconds, resulting in a highly inefficient use of observing time; increasing the readout rate can reduce this overhead, but results in further increased readout noise. In addition to the issues with observing, there was also difficulty in obtaining the computational power needed to process long sequences of images, and only in the 21st century has it become feasible to perform data reduction and analysis for large datasets consisting of thousands of exposures, each containing data from several hundreds of thousands of pixels.

Early work in the field focused on the method of 'image stabilization', in which tip-tilt errors are corrected in real time before reaching the detector. This technique is somewhat comparable to the concept of autoguiding, commonly used to combat image drift due to telescope tracking errors when obtaining long exposures, but occurs on a much shorter timescale. Utilising a bright guide star and a dedicated sensor to measure image motion in real time, an actuated mirror is moved to counteract the apparent motion of the star due to seeing, resulting in a stabilised image being received by the detector. The fact that the image is corrected in real time allows the science detector to take long exposures, avoiding issues with high readout noise and low readout speeds on CCDs. Instruments that used this technique include ISIS (Thompson & Ryerson 1984), DISCO (Maaswinkel et al. 1987), HRCam (Racine & McClure 1989, McClure et al. 1989), and MARTINI (Doel et al. 1990). HRCam was also capable of performing real-time rejection of starlight when seeing was particularly bad, mimicking the modern process of frame selection. Measurements of peak PSF brightness were performed in real time by the tip-tilt sensor, and a shutter was closed whenever the image sharpness fell below a threshold. Image stabilisation work also fed into the development of adaptive optics, with some systems using a separate tip-tilt correction mirror before further correction with a high-order deformable mirror.

Despite the limitations of computational facilities, correction of tip-tilt errors with post processing techniques was also investigated during the same period, with

this computational method known as 'shift-and-add'. As the name suggests, each individual exposure shifted in order to centre the brightest pixel to correct for tip-tilt error, and the sequence of realigned images then summed to produce the final image. The concept was initially outlined in Bates & Cady (1980), who noted two issues with the resulting data, dubbed 'ghosts' and 'fog'. Ghosts are a phenomenon caused by incorrect shifting of images when two or more sources of light are present; whilst the brightest pixel will usually correspond to the brightest source, interference effects or unlucky combinations of speckle patterns occasionally cause another source to appear brighter. This results in a small number of frames being shifted incorrectly, resulting in the appearance of additional faint sources on the resulting image. Fog refers to the reduced contrast of the shift-and-added image compared to the ideal image taken without the effects of seeing, related to the varying instantaneous image quality across the individual exposures. The combination of both good and poor exposures will result in a stellar profile that is much less sharp (and hence has less contrast) than the profile observed in the best exposures alone.

Observations in which both image recentring and frame selection were performed computationally were first presented by Nieto, Llebaria & di Serego Alighieri (1987). The data consisted of a series of 30ms exposures, but the signal in the individual exposures was found to be too low for correction, with the target being so faint that less than one photon was detected per second. The exposures were combined to create effective exposures of several seconds, and these images were cross-correlated with the combination of all exposures. The offset in cross correlation peak corresponded to the tip-tilt correction, and the sharpness of the cross-correlation peak provided a measure of image quality. Recentring of exposures, followed by selection of the best 11% of frames, resulted in an improvement of approximately 15% in image FWHM. Consideration of various problems and design choices for such systems was presented in Nieto & Thouvenot (1991) following further experience with the technique. Particular attention was given to the signal to noise (or number of photon events) needed for accurate recentring, and also to issues with imperfect recentring and quality measurements, especially when the reference object was not a well-resolved point source, as

was discovered during observations of double stars (Lelievre et al. 1988).

Around the turn of the 21st century, advances in both computational power and detector technology began to make frame selection and hence full lucky imaging feasible with relatively modest technology. Dantowitz, Teare & Kozubal (2000) presented high resolution imaging of Mercury, using images obtained with an off-the-shelf video camera and a frame selection algorithm running on a standard desktop computer, following on from encouraging observations of artificial satellites and other bright solar system objects (Dantowitz 1998). This work soon caught the attention of both the professional and amateur astronomy communities.[1] Scientific research in the area was strongly assisted by the development of electron multiplying CCD (EMCCD) technology,[2] which overcome the limitations of readout noise by amplifying the stellar signal by a factor of several hundred before the readout stage (Mackay et al. 2001). The low readout noise allows the very high readout rates and short exposure times needed for lucky imaging, and permits observations of objects much fainter than the solar system bodies commonly observed by amateur astronomers.

The first EMCCD lucky imaging results were presented in Tubbs et al. (2002). The system was found to be capable of operating reliably with reference stars as faint as $I = 15.9$ on the 2.5m Nordic Optical Telescope, and the FWHM of the isoplanatic patch when observing with the instrument was found to be as high as $50''$, much larger than the region of correction provided by adaptive optics systems. Combining these two factors, it was predicted that 20% of the sky would be within range of a suitable reference star, far greater than the few percent available to NGSAO systems (Rigaut 2015). This instrument was further developed and eventually dubbed LuckyCam, with the findings and results of this development summarised in Law, Mackay & Baldwin (2006) and Law (2006).

The success of the instrument, combined with the increasing availability and cost

[1]Following the work of Dantowitz, the application of lucky imaging techniques has become very common in amateur astronomy, supported by dedicated software packages, such as Registax `https://www.astronomie.be/registax/`

[2]EMCCDs are also referred to as as Low Light Level CCDs, LLLCCDs, or L3CCDs.

effectiveness of EMCCD technology compared to AO systems, has led to increased adoption of lucky imaging during the past decade. The two AstraLux lucky imagers, consisting of AstraLux Norte (Hormuth et al. 2008) and its southern hemisphere twin Astralux Sur (Hippler et al. 2009), have been in routine operation for a decade. These have contributed to many studies of stellar multiplicity in a variety of contexts (e.g. Daemgen et al. 2009, Maíz Apellániz 2010, Janson et al. 2012). Other such instruments include FastCam (Oscoz et al. 2008) and the Two Colour Instrument (Skottfelt et al. 2015b), with the latter being equipped to perform lucky imaging in two photometric bands simultaneously.

There is currently ongoing research into combining the techniques of lucky imaging and adaptive optics, a concept known as AO+LI or AOLI. The correction provided by AO systems is not perfect, and so some gain can still be had by applying frame selection algorithms to short exposures. Alternatively, to achieve the same resolution gain as a system relying on AO correction only, a combined AO+LI system would require a less accurate (and hence less expensive) AO subsystem. Furthermore, whilst lucky imaging alone is not usually considered feasible for large telescopes due to the very low chance of actually obtaining a 'lucky' exposure, the addition of an AO system increases the overall quality of the resulting exposures. Early proof-of-concept was carried out with the LAMP instrument, combining this lucky imager with the Palomar AO system (Law et al. 2009), with a further test performed by combining FastCam and the NAOMI adaptive optics system on the 4.2m William Herschel Telescope (Femenía et al. 2011). A dedicated instrument, the Adaptive Optics Lucky Imager (AOLI), is under active development to further explore this principle (Mackay et al. 2012, Crass et al. 2012), integrating the AO system directly into the instrument.

2.2.6 Space telescopes

One seemingly simple solution to the problem of atmospheric turbulence is to place the telescope outside of the Earth's atmosphere. Space telescopes are able to achieve diffraction limited observations with ease, and the relatively humble 2.4m mirror on the

Hubble Space Telescope (HST) achieves a better angular resolution than any ground-based telescope that is not equipped with an image correction system. A space telescope is not limited to a relatively small corrected field of view that is typical of AO systems or other high resolution imaging techniques, and furthermore, observations can also be performed at shorter wavelengths than ground-based telescopes due to the lack of atmospheric absorption. Following Equation 2.1, the move to shorter wavelengths further improves the angular resolution. There are also several other potential advantages that are not related to angular resolution, such as the possibility of avoiding day-night cycles, depending on the telescope's orbit.

Despite these advantages, space telescopes remain relatively rare, mainly due to the incredible costs associated with such missions. The Hubble Space Telescope project, involving a single 2.4m telescope, had a cost of $4,700m at time of launch in 1990; an extra $1,100m was spent by 1993 due to costly in-orbit modifications of the malformed primary mirror (Ballhaus et al. 2010). In comparison, the VLT project – consisting of four 8m telescopes with several auxiliary telescopes, interferometric abilities, and a wide variety of instrumentation – had a projected total cost of approximately DM990m (approx. $500m) as of 1998 (Giacconi 1998). Space missions are also risky, and reliable operation in space is difficult to achieve. It is generally infeasible to repair or upgrade space telescopes after launch, and highly costly to perform if it is possible. Recent examples include the ASTRO-E and Hitomi missions, lost due to malfunctions, and the *Suzaku* and *Kepler* spacecraft, which suffered equipment failures restricting their functionality.

At the time of writing, HST is the only available space telescope that can perform high angular resolutions in the optical and UV. HST remains competitive with large, ground-based adaptive optics systems, with scientific results including measurements of stellar kinematics in globular clusters (Sarajedini et al. 2007, Bellini et al. 2014), observations of gravitational lensing by objects ranging from white dwarfs (Sahu et al. 2017) to large galaxy clusters (Postman et al. 2012), and measurements of the orbits of moons (Buie, Tholen & Grundy 2012), brown dwarf binaries (Bedin et al. 2017), and satellite galaxies (Kallivayalil et al. 2006). Furthermore, many non-astrometric

results rely on HST's ability to detect and resolve faint objects, such as the detection of distant supernovae (Riess et al. 1998, Perlmutter et al. 1999), measurements of Cepheid variables outside the galaxy (Freedman et al. 1994), and the study of the high redshift universe (Madau et al. 1996, Koekemoer et al. 2011).

2.2.7 Coronography

The techniques discussed previously permit the resolution of objects at small angular separation by improving the angular resolution of the system. However, the contrast of the two objects is also an important consideration - it is more difficult to reliably detect and characterise a faint object adjacent to a bright one than a pair of objects of similar brightness. While PSF modelling and subtraction techniques would ideally allow for the full removal of light from one star, leaving fainter objects easily detectable, uncertainties in the modelling and noise in the recorded image can leave residuals that mask or can be confused with the fainter objects of interest. Furthermore, scattered starlight caused by imperfections in the optical system can add a significant amount of background noise. Finally, a practical consideration is that the presence of a bright star within the field of view limits the maximum possible exposure time that can be achieved before causing effects such as detector saturation and persistence; these short exposure times can significantly compromise the chances of detecting a faint companion at all.

A coronograph is a device designed to block a significant amount of light from a source at the centre of the image before it reaches the detector, while light from other objects in the field of view passes through with minimal attenuation and aberration. The technique was first applied successfully by Lyot (1939), after whom the classical Lyot coronograph is named. Two important concepts that are common to all coronographic techniques are the pupil plane, in which the incoming rays of light are parallel and the telescope pupil is imaged, and the image or focal plane, in which the rays of light are focus and the astronomical objects are imaged. A lens allows light to be transformed from one plane to the other, and the intensity of light in one plane is the

Fourier transform of the intensity in the other.

In general, the incoming light is transformed from the pupil plane to the image plane, in which a focal plane mask is placed. The remaining light is then transformed back to the pupil plane, in which a Lyot stop is placed, which rejects additional unwanted light that remains after the focal plane mask. Finally, the light is once again transformed back to the image plane on the detector. In a classical Lyot coronograph, the focal plane mask takes the form of a small occulting spot, which for solar observations blocks the disc of the Sun, and for observations of more distant (unresolved) sources, blocks the core of the star's diffraction pattern. The Lyot stop in such a system is a baffle that removes light at the edges of the image plane, this light having leaked past and been diffracted by the occulting spot.

A large number of alternative coronograph designs exist, each attempting to optimise one or more of the characteristics of the device. Guyon et al. (2006) provides a review of the numerous competing designs that were being considered for the current generation of exoplanet direct imaging instruments such as SPHERE (Beuzit et al. 2008), GPI (Macintosh et al. 2008), and SCExAO (Jovanovic et al. 2015), all of which include coronographs as a fundamental component. Kasdin et al. (2003) details four parameters that influence the design of coronographs:

- The contrast of the object of interest relative to the diffuse background in the image,

- The transmission of the system for light from object of interest (and hence the required exposure time),

- The inner working angle (IWA) or inner working distance (IWD), the angular separation below an object of interest becomes strongly affected by the coronograph,

- The discovery space, the fraction of the field of view in which an object of interest can be found.

For a classical Lyot coronograph, the contrast, transmission, and IWA are closely linked. A larger baffle forming the Lyot stop improves contrast by reducing scattered starlight, but reduces transmission by blocking some light from the object of interest too. A larger occulting spot will block a larger fraction of the star's PSF, but as the spot grows larger, objects of interest at larger angular separation are also blocked, increasing the IWA. The discovery space of the classical Lyot coronograph is one of its advantages, as the full field of view is available – a notable example of a design in which there is a strong angular dependence is the Four-Quadrant Phase-Mask, which significantly attenuates companions that fall near the boundaries between the mask's four quadrants (Rouan et al. 2000). Fig. 1 of Guyon et al. (2006) provides a detailed visual comparison of the behaviour of various coronograph designs in relation to the four parameters listed above.

3 Lucky imaging of transiting exoplanet host stars

The main work covered in this thesis is a multi-year campaign to obtain lucky imaging observations of transiting exoplanet systems. The main objective of this work has been to constrain the existence of contaminating stars at small angular separation from these systems, and to analyse and catalogue any detected 'companion' stars. For each of these, relative photometry was obtained in at least one photometric band, with simultaneous observations in two bands becoming routine from September 2014 onwards. In addition, astrometric measurements (i.e. separation and position angle) relative to the planet host star were derived for each companion star.

Where photometry was obtained in both bands, the temperature of each detected companion star was determined, which was further used to determine if the companion star's photometric distance was consistent with the distance of the planet host star, and hence that the two stars potentially form a bound binary system. For systems identified as potential binaries, a literature search was performed for additional photometric, astrometric, or spectroscopic data which supported (or rejected) the binary star hypothesis. Various features of the population of confirmed or plausible planet-hosting binaries derived from both this work and others were studied, such as the proportion of hot Jupiters in stellar binaries, and the distribution of companion star masses.

The work in this chapter has been published in two separate refereed papers, with Evans et al. (2016) covering the analysis of observations during 2014, and Evans et al. (2018) covering those results from 2015 and 2016.

3.1 The Two Colour Instrument

All lucky imaging observations were obtained using the Two Colour Instrument (TCI), a lucky imaging instrument mounted on the Danish 1.54m Telescope, La Silla Obser-

vatory, Chile. As is standard for modern lucky imaging instruments, it is equipped with Electron Multiplying CCD (EMCCD) detectors, which are capable of providing the high framerate and signal-to-noise ratio (SNR) required for lucky imaging. The TCI is equipped with two identical cameras, which image the same field of view simultaneously in two passbands. The instrument therefore generates two sets of lucky imaging exposures, which are processed independently. The cameras, and the datasets originating from them, are dubbed 'Red' and 'Visual' (Vis), based on the wavelength of light received by each camera.

The instrument is primarily used for photometric follow-up of planetary microlensing events in the galactic bulge (e.g. Calchi Novati et al. 2015, Street et al. 2016, Henderson et al. 2016), which involves measuring the light curves of relatively faint stars (typical V magnitudes of 16–18) in highly crowded fields, with higher image resolution providing better detection efficiency and data quality for the 'anomalies' created by planets during microlensing events (Sajadian et al. 2016). Obtaining photometry in two bands assists the characterisation of microlensing events, and is also a useful check for astrophysical false positives, with true microlensing events being identifiable due to being one of relatively few astrophysical phenomena that are wavelength-independent. In addition to microlensing observations and the high resolution imaging survey described here, the instrument has been successfully used for projects, such as the monitoring of stellar variability in crowded globular clusters (Skottfelt et al. 2013, Kains et al. 2013, Skottfelt et al. 2015a, Figuera Jaimes et al. 2016a, Figuera Jaimes et al. 2016b), and high-cadence observations of stellar occultations by solar system bodies, resulting in measurements of the atmosphere of Pluto (Dias-Oliveira et al. 2015) and the discovery of rings around the asteroid 10199 Chariklo (Braga-Ribas et al. 2014).

3.1.1 Instrument description

Skottfelt et al. (2015b) describes in detail the design and operation of the instrument, with a brief summary presented here. Two dichroics are used in the instrument to split incoming light from the telescope. The first dichroic transmits light at wave-

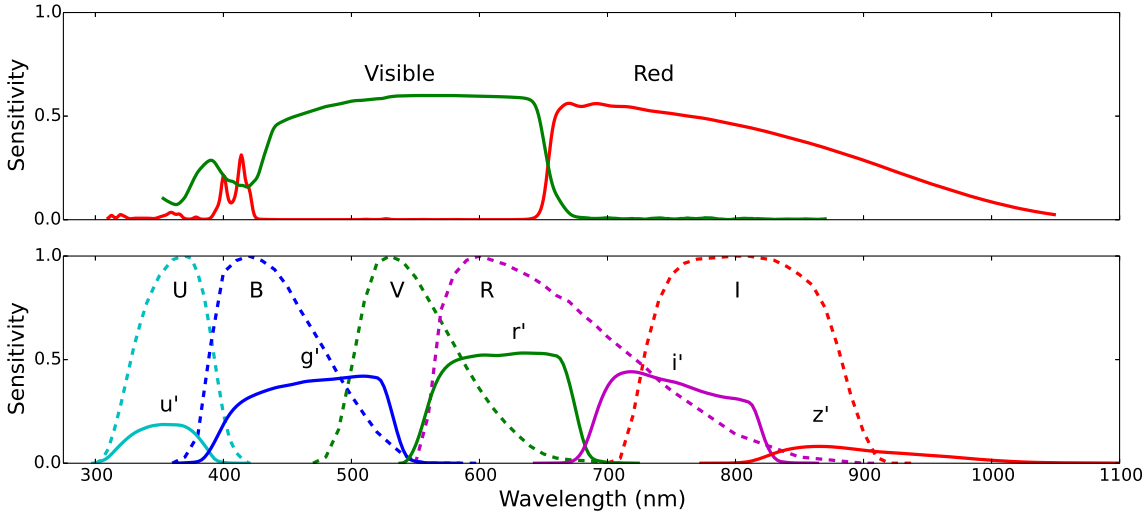

Figure 3.1: Passbands of the TCI instrument (top) compared to the Johnson-Cousins and SDSS photometric systems (bottom). This figure is based on Figure 4 of Skottfelt et al. (2015b), including the effects of the dichroics and detector response curves.

lengths longer than 655 nm to the 'Red' camera. A second dichroic transmits light at wavelengths longer than 466 nm to the 'Visual' (Vis) camera, resulting in this camera receiving light between 466 nm and 655 nm. Light with wavelengths below 466 nm is sent towards a third camera intended for real-time focusing monitoring, but this system was never commissioned due to technical issues. The Red camera's passband is similar to the Cousins I band, or the combination of the SDSS i and z bands, whilst the Vis camera is most similar to the Johnson V band. The theoretical passbands and sensitivity of the two cameras are shown in Figure 3.1, along with the passbands of the Johnson-Cousins and SDSS photometric systems.

An automated routine is used to determine the best focus through observations of a bright star with the Red and Vis cameras. The telescope control system provides automatic corrections for focus variations with temperature, and the focus has empirically been found to be stable for approximately 2 hours, after which another

focus routine is performed. The instrument is not currently equipped with any filters (although consideration is being given to fitting a long-pass filter to the red camera) and does not have an atmospheric dispersion corrector.

The Danish 1.54m Telescope has an equatorial mount, and both EMCCD cameras have their $+x$ axis aligned to within a few degrees of true north. Both cameras have 512×512 pixel arrays with a plate scale of 88.9mas/px, corresponding to a field of view of approximately $45'' \times 45''$. The cameras are normally operated in unison with a frame rate of 10 Hz and an EM Gain setting of $\gamma = 300$ e^-/photon. These settings are designed to ensure a sufficient SNR for the post-processing of the raw lucky imaging frames in the microlensing campaign Skottfelt et al. (2015b). Shorter exposure times could be advantageous for improved seeing correction, with the 100ms exposure time being at the upper end of the range of atmospheric coherence times, but such a change would also reduce the SNR on each exposure, potentially impacting the quality of the LI correction.

During 2014, only the Red camera was available for much of the observing season, with the Vis camera being successfully commissioned in September 2014. Since then, both cameras have been routinely used for all observations.

3.1.2 TCI reduction pipeline

All observations performed with the TCI are automatically reduced by a dedicated reduction pipeline, outlined in Harpsøe et al. (2012) and Skottfelt et al. (2015b). The reduction of imaging data from EMCCDs is similar to that for conventional CCDs. Bias frames are obtained on a nightly basis, and twilight flat fields are obtained once every few days. These data are automatically processed to create a master bias frame and master flat frame, with the reduction pipeline using the most recent good calibrations when reducing new data.

Lucky imaging observations are received as two separate 'spools' of raw 0.1 s exposures, one from each camera. For each frame, the master bias frame is subtracted, and an additional correction is made based on a measurement of the bias level in

the overscan region of the raw frame. This latter step is required due to the non-negligible heating of the detector and readout electronics caused by the high framerate and readout speed, which results in a variable bias level (Harpsøe et al. 2012). Flat field correction is applied by dividing each frame by the corresponding (Red or Vis) master flat field.

For each spool, a reference image is created from the average of all exposures, providing the mean position of the stars in the field during the observing sequence. The 2D cross-correlation of each exposure with the reference image is computed, and the offset in the cross-correlation peak is used to determine the x, y shift needed to correct the tip-tilt error present in that exposure. Some corrections are made during the processing to avoid 'edge effects', caused by sky positions near the edge of the frame moving in and out of the field of view due to tip-tilt, and the expectation that the isoplanatic patch is slightly smaller than the full field of view (Skottfelt et al. 2015b). For each pixel, the average photon flux is calculated, and the probability of the pixel having the recorded value is calculated for each exposure. If the counts in a pixel are abnormally high in a given exposure, it is concluded that a cosmic ray event occurred, and the pixel's value is replaced by a random sample from an Erlang PDF representing the count distribution in that pixel (Skottfelt et al. 2015b). Finally, the value of the cross-correlation peak is measured and divided by the sum of pixel values within some radius of the peak. This provides a measurement of the sharpness of the peak, and hence of the instantaneous image quality of each exposure, which is used to rank the frames for the lucky imaging frame selection.

Many implementations of lucky imaging retain only the best few percent of frames in order to obtain the highest possible angular resolution, but this comes at the cost of rejecting most of the received photons. Alternatively, shift-and-add techniques employ only tip-tilt correction with no frame rejection, utilising all of the detected photons at the expense of image resolution. Depending on the science goal, the required acceptance fraction can vary widely between these two extremes. One potential solution is to return the individually processed exposures, allowing different selection criteria to be selected during data analysis. However, the amount of data generated by the TCI in

a typical night prohibits routine transfer of all raw frames via the internet.[1] Instead, the TCI pipeline provides a compromise between frame selection and photon efficiency, grouping the raw exposures by image quality into one of ten 'cuts', and then summing the exposures within each cut.

The resulting 10-layer FITS cube allows the user to change the frame selection cutoff by selecting only the first n layers. Noting also that the main use cases are likely to be either 1) the selection of only the best few exposures, or 2) the rejection of the worst few exposures, the cuts between each set are spaced non-linearly. In percentage terms, the cuts are positioned at (1, 2, 5, 10, 20, 50, 90, 98, 99, 100), and hence the cuts contain (1, 1, 3, 5, 10, 30, 40, 8, 1, 1) percent of the raw frames respectively. The final data product is a fully reduced 10-layer FITS cube for each camera. The number of exposures making up each cut is recorded, in addition to an estimation of the stellar point spread function (PSF) full width at half maximum (FWHM) within each cut.

3.2 Observations

Observations were carried out during April-September each year from 2014-2016 corresponding to the period when the MiNDSTEp consortium – through which these observations were arranged – has access to the telescope. Target lists were derived from the TEPCat catalogue[2] of well-studied transiting exoplanet systems (Southworth 2011), selecting targets that were visible from La Silla observatory during each observing period, and with V magnitudes between 9 and 14. The faint cutoff was chosen based on the point at which lucky imaging correction became unreliable. Whilst fainter targets are routinely observed successfully with the same instrument for microlensing observations, these target crowded stellar fields with many stars contributing to the total signal available for data reduction; the TEP host stars studied in this work are often

[1] Raw data are sent back for selected projects such as time-series observations of asteroid occultations.

[2] `www.astro.keele.ac.uk/jkt/tepcat/`

the only bright source within the instrument's field of view, and poor results have been encountered for stars fainter than 14th magnitude, or brighter stars observed through thin cloud.

For each target, the total exposure was set to achieve an SNR of 5 for a well resolved companion 10 magnitudes fainter than the target in the Red data, allowing physically associated companion stars of almost any mass (and hence brightness) to be detected. This requirement corresponded to exposure times between 60s and 900s (600-9000 individual exposures), with identical exposure times and settings for both cameras. The Danish 1.54m telescope is operated in service mode, with observers from the MiNDSTEp consortium performing observations on behalf of all projects, allowing observations to be flexibly scheduled throughout the season. This flexibility allowed the restriction of lucky imaging observations to periods of good seeing, in which the best results are achieved by lucky imaging. 'Good' seeing was loosely defined as 0.6-0.7″ or better, noting that the seeing reported by different instruments and monitoring systems varies.[3] All photometry of the detection companion stars was measured relative to the brightness of the target star, and hence observations were permitted to be performed through light cloud, which can significantly complicate absolute photometry but has a lesser effect on relative measurements.

Targets were typically observed once per season, although repeat observations were requested when data quality was poor (usually due to seeing worse than the requested limit), or when unusual features were noted in the data (see Section 3.6.3). In 2015, many of the targets observed in 2014 were reobserved, both so that measurements could be obtained with the now-commissioned Vis camera, and also to search for potential evidence of common proper motion for previously detected companions. The multiband photometry obtained in 2015 allowed much more efficient rejection of candidate binary companions that had distances inconsistent with the exoplanet host star, and hence from 2016 onwards repeat measurements were only made for a small

[3]The author has experienced cases where excellent lucky imaging conditions corresponded to very poor seeing for more conventional instruments at La Silla. It has been hypothesised that this is related to the atmospheric coherence time and the exposure times used.

number of potential (or confirmed) bound companions, to obtain further proper motion data. In addition to these repeat observations, new targets were continually added to the target list as they were publicly announced and entered into TEPCat.

In addition to observations of exoplanets, similar data were obtained for a number of eclipsing binaries. As with the observations of exoplanet host stars, the objective was to place quantitative limits on the contamination present in the photometry and spectroscopy of these systems, for which highly precise stellar parameters are being derived, allowing for the testing and calibration of stellar models. The results of this work will be published in papers by Gill et al. (submitted) and Kirkby-Kent et al. (in prep.), and are not further discussed in this thesis.

3.2.1 Target lists and properties

Lists of targets observed, in addition to details such as date of observation, exposure time, and magnitude limits, are located in Appendix A.

As noted in the previous section, targets were selected from the TEPCat catalogue, using observability and magnitude cutoffs. No other selection criteria were applied; instead, the survey was intended to provide validation for as large a sample of planets as possible. However, given the timing and observing location, this restricted the survey almost entirely to hot Jupiters without any further selection – Kepler targets from the Northern hemisphere were not visible, with the target list dominated by the CoRoT, HAT, and WASP surveys, all of which mainly detect hot Jupiters. Similarly, this restricted the sample to mainly Sun-like stars, due to the small number of transiting planets detected around significantly hotter or cooler types of stars at the time of the survey.

Figs. 3.2 and 3.3 show respectively the distribution of host star masses and effective temperatures for the targets observed. Excluding the M-dwarf GJ 1214, visible at the low end of each plot, the remaining stars fall into the category of FGK stars, which are the most commonly studied in transiting planet searches. 95% of stars have masses in the range 0.68-1.53$M_{\odot}$, and have effective temperatures between 4330K and

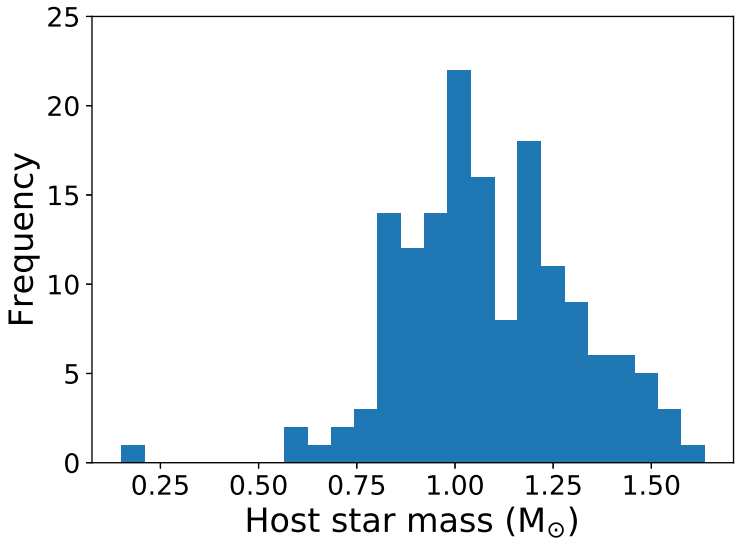

Figure 3.2: Distribution of host star masses for the sample of observed systems.

6560K.

The distributions of orbital period, orbital separation, mass, and radius for the planets themselves are shown in Fig. 3.4.[4] The two most massive transiting objects, CoRoT-3b (Deleuil et al. 2008) and WASP-30b (Anderson et al. 2011), are considered by their discoverers to be brown dwarfs due to their high masses. At the opposite end of the mass spectrum, five planetary systems are considered to contain 'super-Earths' due to the low mass/radius and high density of the planetary companions: CoRoT-7 (Charbonneau et al. 2009), GJ 1214 (Léger et al. 2009), K2-2 (Vanderburg et al. 2015), K2-3 (Crossfield et al. 2015), and K2-38 (Sinukoff et al. 2016). Additionally, the mass of CoRoT-22b is poorly constrained, and it is consistent with both rocky and gaseous compositions (Moutou et al. 2014).

96% of the targets have orbital periods below 10 days, and only the planets of the

[4]For CoRoT-24, planet 'c' is shown. For all other multi-planet systems, the 'b' component is shown.

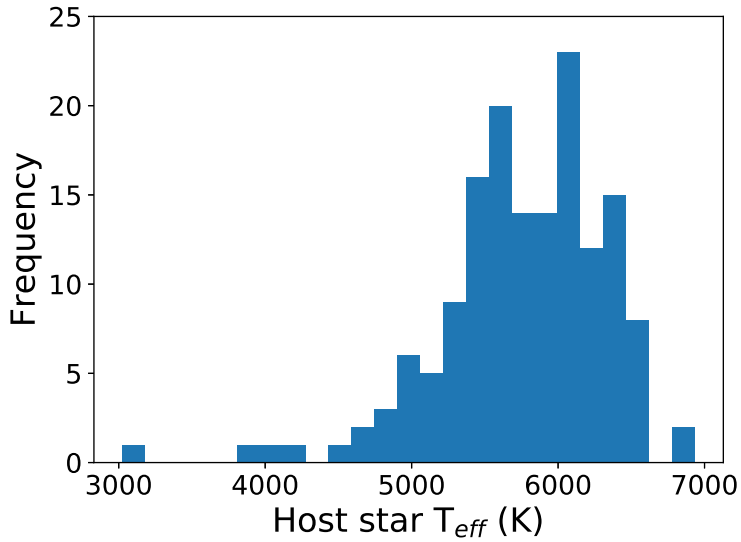

Figure 3.3: Distribution of host star effective temperatures for the sample of observed systems.

K2-24 (Petigura et al. 2016) and CoRoT-9 (Deeg et al. 2010) systems exceed orbital periods of 20 days. Therefore, the vast majority of the systems observed are in the regime where planetary migration is argued to be necessary for formation.

3.3 Photometric calibration

In order to determine the properties of stars (such as temperature) from observed stellar fluxes and colours, the photometric response of the imaging system must be calibrated. In September 2014, observations were obtained of several stars included in the ESO Optical and UV Spectrophotometric Standard Stars catalogue.[5] The stars covered a wide range in colour, with spectral types from B to G, and were observed at

[5] http://www.eso.org/sci/observing/tools/standards.html

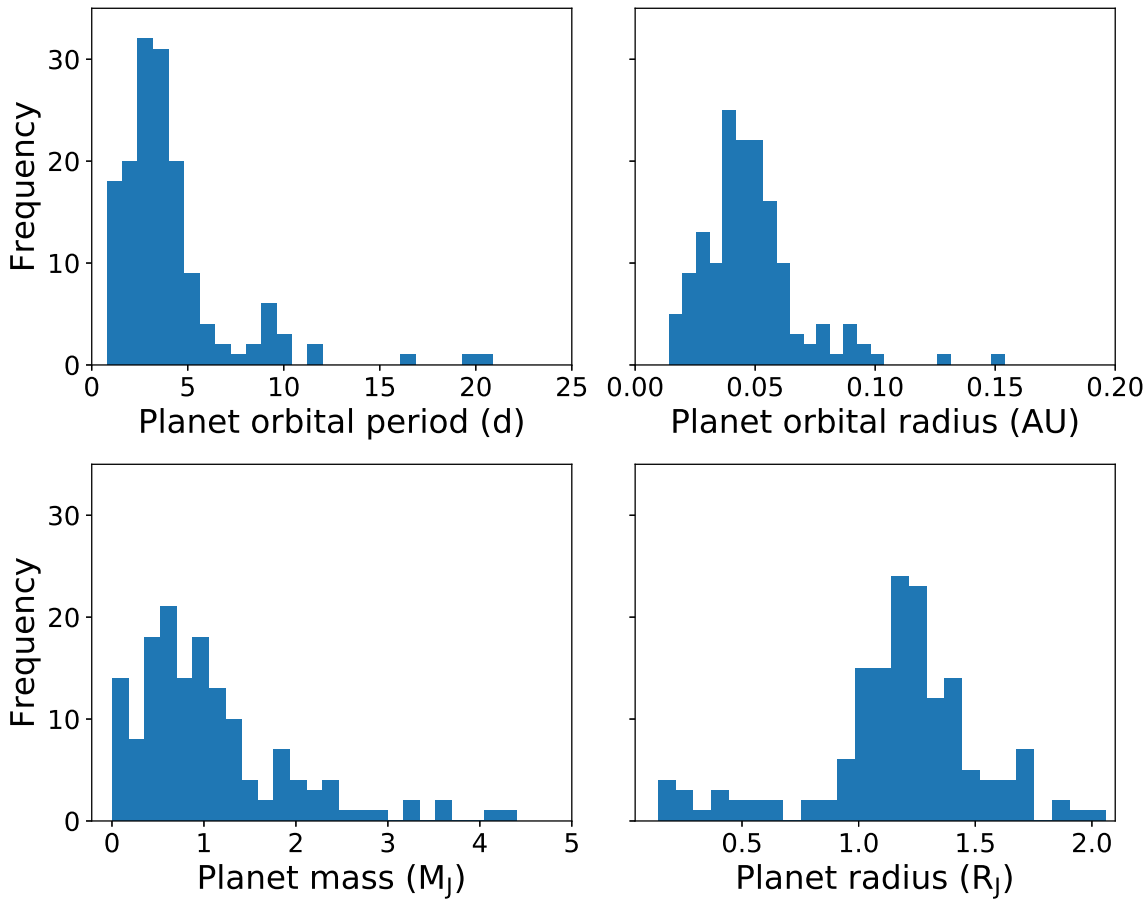

Figure 3.4: Distributions of planet properties for the sample of observed systems. CoRoT-09b, with an orbital period of 95 days and separation of 0.4 au, is not shown in the top two plots. In the mass plot, WASP-18b ($10.5 M_{Jup}$), CoRoT-03b ($22.0 M_{Jup}$), and WASP-30b ($62.5 M_{Jup}$) are not shown.

different altitudes, allowing both colour-dependent and airmass-dependent variations in the observed fluxes to be determined. These stars were used to obtain a photometric calibration for the 2014 dataset; for the 2015 and 2016 datasets, the photometric calibration was further refined using the dual band photometry obtained of exoplanet host stars.

3.3.1 Standard star photometry - 2014

Seven standard stars were observed, and for all seven stars spectrophotometric measurements were available in the ESO Optical and UV Spectrophotometric Standard Stars catalogue. The spectrophotometry was convolved with the TCI Red and Vis camera response curves shown in Figure 3.1 to determine the expected colour of each star. The difference between observed and predicted colour was then modelled as

$$(\mathrm{v\,_{TCI}} - \mathrm{r\,_{TCI}}) = (\mathrm{v\,_{TCI}} - \mathrm{r\,_{TCI}})_{\mathrm{Obs}} - kZ - z, \tag{3.1}$$

where $(\mathrm{v\,_{TCI}} - \mathrm{r\,_{TCI}})$ is the predicted colour, $(\mathrm{v\,_{TCI}} - \mathrm{r\,_{TCI}})_{\mathrm{Obs}}$ the observed colour, and Z the airmass; k is a coefficient describing the change in observed as a function of airmass, caused by absorption and scattering by the atmosphere, and z is a zero-point offset, accounting for any constant difference between predicted and observed colour. Stellar fluxes were obtained through aperture photometry, and airmass values were adopted from the FITS file headers. Using these inputs in conjunction with the predicted colours, the values of k and z were fitted simultaneously using a least squares minimisation routine.

For three of the standard stars, the spectrophotometric measurements do not cover the full range of the TCI Red camera's sensitivity. G158-100 and NGC 7293 lack data beyond 900nm, while LTT 9491 lacks data beyond 970nm. As can be seen in Figure 3.1, the TCI Red camera's sensitivity remains high at 900nm, and these three stars showed large differences between observed and predicted colours when using the incomplete data. For G158-100, the missing part of the spectrum was replaced with a `PHOENIX` model atmosphere (Husser et al. 2013). The properties of the model atmo-

sphere were set to $T_{eff} = 5300$K, $\log g = 4.00$, and [Fe/H] $= -3.0$, the latter two values being being the closest model grid steps to the observed stellar properties ($\log g = 4.16$, and [Fe/H] $= -2.52$, Boesgaard, Stephens & Deliyannis 2005), and the temperature having been varied to give the best match to the observed part of the spectrum (the literature value being 4981K, Boesgaard, Stephens & Deliyannis 2005). NGC 7293 and LTT 9491 are both hot white dwarfs with relatively featureless spectra, and hence black body flux distributions were assumed. The temperatures of these black bodies were again chosen to best match the available data, with 110,000K adopted for NGC 7293 and 12,500K for LTT 9491. The observed, model, and combined spectrophotometric data for G158-100 are compared in Figure 3.5.

The fitting process determined a value of $+0.08 \pm 0.03$ mag./airmass for k and of $+0.46$ mag. for z, which was used to process the 2014 data. At that time, two issues were noted. Firstly, that the standard stars showed relatively high scatter between the predicted and observed colours even after correction, with potential evidence of a trend with intrinsic stellar colour. However, the number of standard stars was too low to fully characterise these effects. Secondly, in the observations of exoplanet host stars, some confirmed binary companions appeared much redder than expected from the literature temperatures. This was later determined to be the effect of interstellar reddening, which was neglected in the 2014 analysis.

3.3.2 Target star photometry - 2015/2016

For the 2015 and 2016 datasets, the photometric calibration was further refined, based on the large number of colour measurements obtained of exoplanet host stars targeted by the survey. These provided a much larger dataset than the standard star observations, with exoplanet host stars generally having well-determined spectroscopic parameters (T_{eff}, $\log g$, and [Fe/H]), from which stellar colours can be estimated. A further advantage is that the target stars cover a range of sky positions and stellar distances, allowing for the effect of interstellar reddening on the TCI colours to be measured, provided that an estimate of $E(B-V)$ could be determined.

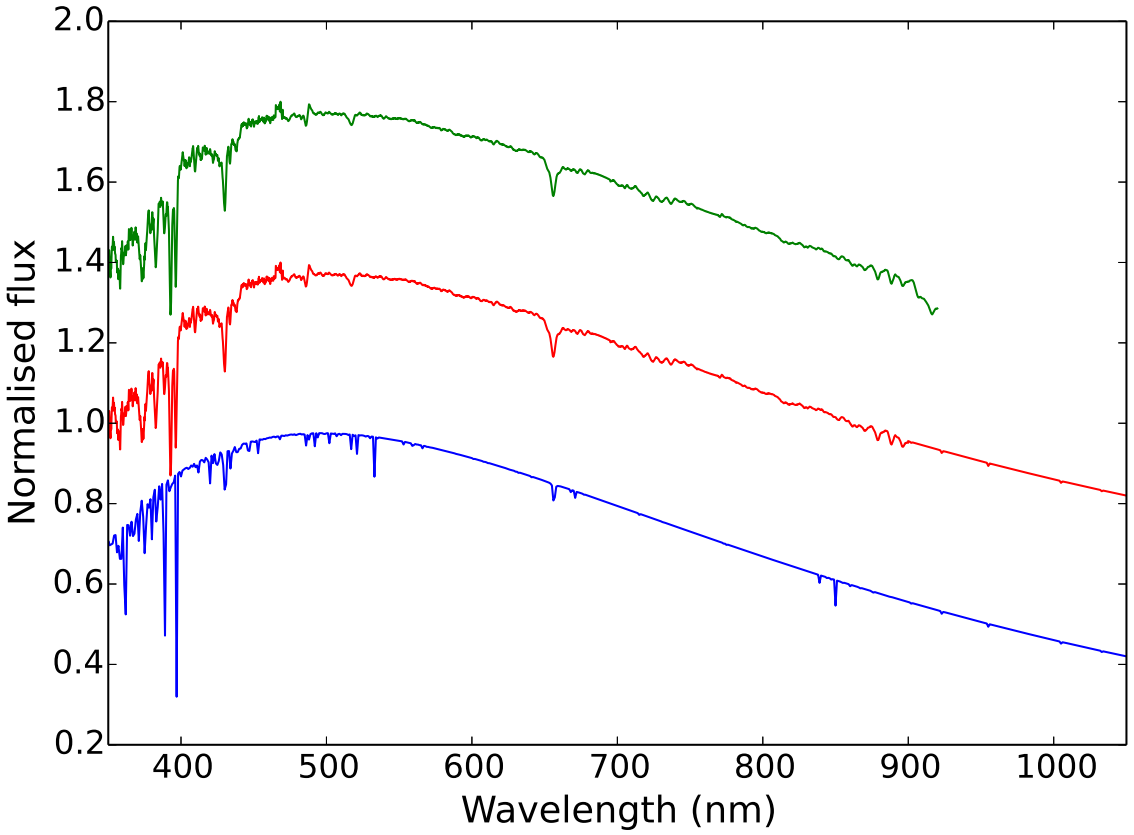

Figure 3.5: Replacement of missing spectrophotometric data of G158-100. The top green line represents the available measured spectrum (Oke 1990), which cuts off at 900nm. The bottom blue line shows the best matching `PHOENIX` spectrum, with the model temperature having been varied to provide the best match to the observed data. The combined dataset is shown in the intermediate red line. The curves are offset vertically for clarity, with each having a peak flux of 1.0. Evans et al., A&A, 589, A58, 2016, reproduced with permission © ESO

3.3.2.1 Determining interstellar reddening

Absorption of light by the interstellar medium causes a star to appear both fainter and redder, with these two effects being known as extinction and reddening respectively. Reddening is caused by the fact that the interstellar medium is more highly absorbing at short wavelengths. Extinction is commonly quantified through the A(V) parameter, giving the flux change (measured in magnitudes) in the V band. Reddening is typically presented as $\mathrm{E\,(B-V)}$, the difference between the observed and intrinsic $B-V$ colour. The properties of interstellar dust are relatively consistent across all lines of sight through galaxy (though see e.g. Mathis & Cardelli 1992), and hence it is possible to relate extinction and reddening through the R(V) parameter,

$$\mathrm{R(V)} = \frac{\mathrm{A(V)}}{\mathrm{E\,(B-V)}} = \frac{\mathrm{A(V)}}{\mathrm{A(B)-A(V)}}, \tag{3.2}$$

with R(V) commonly assumed to have a value of 3.1 (Cardelli, Clayton & Mathis 1989, Valencic, Clayton & Gordon 2004). For passbands other than B and V, the effects of extinction and reddening are related to the values of A(V) or $\mathrm{E\,(B-V)}$. For commonly used filters and passbands, conversion factors have been determined and tabulated (e.g. Schlafly & Finkbeiner 2011); however, for the TCI passbands, no such values were available, and hence the conversion from $\mathrm{E\,(B-V)}$ to $\mathrm{E(v_{TCI}-r_{TCI})}$ had to be determined. It was assumed that the two were linked by a simple linear conversion,

$$\mathrm{E(v_{TCI}-r_{TCI})} = \mathrm{(v_{TCI}-r_{TCI})_{True}} - \mathrm{(v_{TCI}-r_{TCI})_{Obs}} = X \cdot \mathrm{E\,(B-V)} \tag{3.3}$$

where X is a numerical factor.

Determining the value of X, and hence the reddening correction for the TCI, requires knowledge of the $\mathrm{E\,(B-V)}$ values for each of the target stars used for calibration. Spectroscopic indicators can be used for the measurement of $\mathrm{E\,(B-V)}$ (e.g. Munari & Zwitter 1997), but such analysis has not been previously carried out for many of the target stars. Instead, $\mathrm{E\,(B-V)}$ values were taken from the 3D reddening map presented in Green et al. (2015), which provides reddening estimates as a function of distance over three quarters of the sky. Whilst it does not cover all targets in

this survey, it does cover those that are more distant and suffer from higher reddening (mainly consisting of CoRoT and some HAT targets). Stars outside the bounds of the map were not used in determining the reddening correction, and no correction was later applied to the data obtained for these targets.

In order to query the 3D reddening map, the distance to a target must be known in addition to its coordinates on the sky. For many exoplanet host stars, distances are determined during the initial characterisation of the system. However, a variety of different methods are used to derive the quoted distances, and hence there is the potential for significant systematic offsets between the distances derived by different exoplanet surveys. Furthermore, a small number of systems lack any distance determination at all. Distances were therefore determined based on the measured stellar effective temperature and literature stellar radius for each system, in conjunction with 2MASS Ks measurements (Skrutskie et al. 2006) and the surface brightness-temperature relations determined by Kervella et al. (2004) from interferometric observations. Effective temperatures and stellar radii were adopted from the May 2016 version of the `TEPCat` catalogue. To account for potential systematic errors in the stellar radii determined by different exoplanet surveys, an uncertainty of 10% was assumed for the radius of each star. The relations given in Kervella et al. (2004) are based on K band magnitudes, rather than Ks, and so the 2MASS values were converted to K band measurements using the transformation $\mathrm{K} = \mathrm{Ks} + 0.044$ (Carpenter 2001).

An initial distance estimate was then derived from these values, but for some of the more distant stars in the sample, the effect of interstellar extinction on the measured Ks magnitudes is not negligible. The initial distance estimate was therefore used to query the Green et al. (2015) reddening map, and the Ks value was corrected using $\mathrm{E}(\mathrm{B}-\mathrm{V})$ value, assuming the Ks extinction to be $\mathrm{A(Ks)} = 0.306 \cdot \mathrm{E}(\mathrm{B}-\mathrm{V})$ (Yuan, Liu & Xiang 2013). The process was then iterated using the exctinction-corrected Ks values, until the change in determined distance between subsequent iterations was below 1%. Where stars were located closer than the nearest distance with an estimated reddening in the Green et al. (2015) data, it was assumed that the extinction was evenly distributed along the line of sight, and that no extinction was present at zero distance.

The value of $\mathrm{E}(\mathrm{B}-\mathrm{V})$ was then linearly interpolated based on those assumptions and the closest reliable $\mathrm{E}(\mathrm{B}-\mathrm{V})$ measurement.

For the closer or brighter stars in the sample, parallax measurements were available from the Tycho-Gaia Astrometric Solution (TGAS), as part of Gaia Data Release 1 (Gaia Collaboration et al. 2016b, Gaia Collaboration et al. 2016a). These provide a useful check of the accuracy of both the literature distances, and those derived using the method outlines above. Deriving distances from parallaxes for a sample of stars is non-trivial, due to the bias caused by more stars being at large distances than small (Lutz & Kelker 1973); deriving distances therefore requires knowledge of the distribution of stars within the galaxy. In this work, the distances derived by Astraatmadja & Bailer-Jones (2016) using their 'Milky Way' prior were adopted.

Figure 3.6 compares the Gaia-TGAS distance estimates with those determined in the exoplanet literature, whilst Figure 3.7 compares the Gaia-TGAS results with those derived in this work from the K-band magnitudes. The literature distances are systematically underestimated by $4.4 \pm 1.5\%$ compared to the Gaia-TGAS data, whilst those from this work do not show any significant systematic difference ($0.3 \pm 1.7\%$). The literature distances are also more scattered relative to the Gaia-TGAS data, with an RMS difference of 14%, compared to 9% for this work.

3.3.2.2 Final results

Photometric measurements of each target exoplanet host star were obtained from two band photometry in 2015 and 2016. Expected stellar colours were determined using a similar method to the 2014 standard star calibration, convolving a series of `PHOENIX` model atmospheres (Husser et al. 2013) at different temperatures with the TCI passbands. The photometric model from Eqn. 3.1 was modified to include the correction for interstellar extinction,

$$(\mathrm{v}_{\mathrm{TCI}} - \mathrm{r}_{\mathrm{TCI}}) = (\mathrm{v}_{\mathrm{TCI}} - \mathrm{r}_{\mathrm{TCI}})_{\mathrm{Obs}} - kZ - z - X\mathrm{E}(\mathrm{B}-\mathrm{V}), \tag{3.4}$$

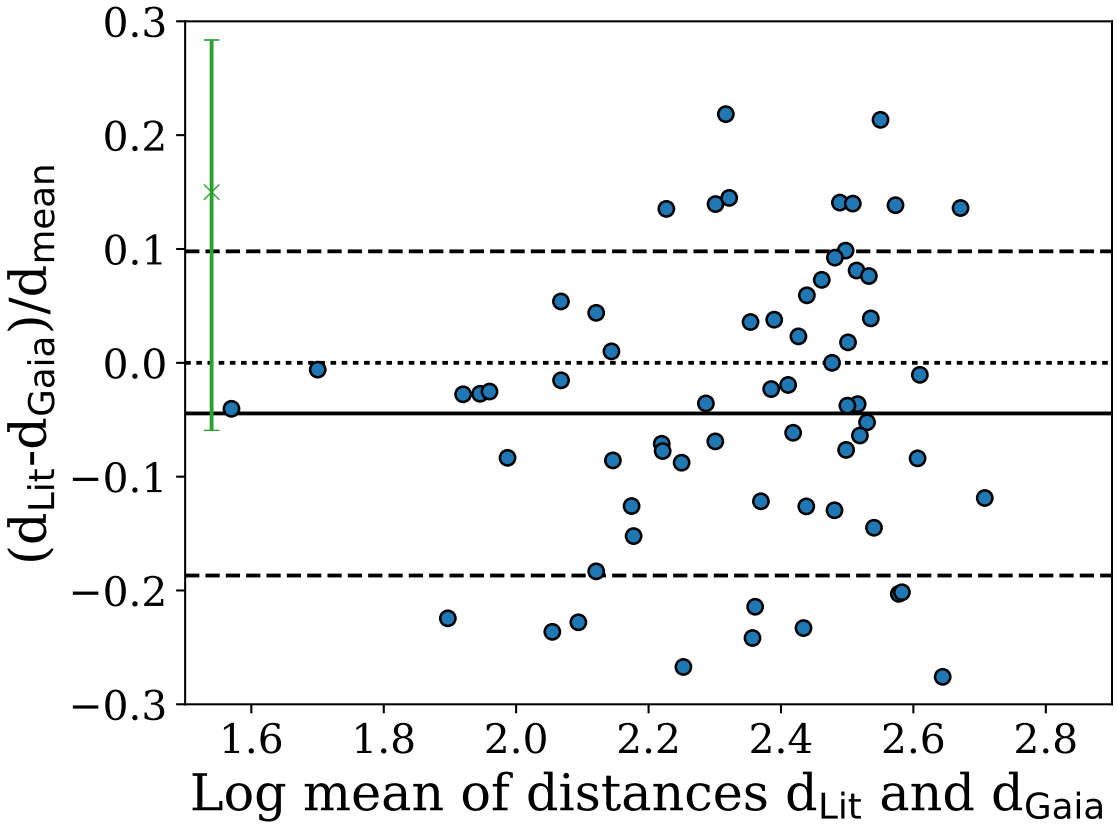

Figure 3.6: Comparison of literature exoplanet star distances to Gaia-TGAS results. Individual systems are plotted using the log of the mean of the distance (in pc) determined by Gaia-TGAS, d_{Gaia}, and those quoted in exoplanet discovery or planet papers, d_{Lit}, on the x-axis, and the fractional difference between the two values on the y-axis. The average uncertainty is shown in green at top left. The solid line indicates the average difference between the two datasets and the dashed lines above and below indicate the RMS scatter; the dotted line indicates where the values should cluster if there is no systematic difference between the two datasets. The literature distances are systematically $4.4 \pm 1.5\%$ lower than the Gaia-TGAS results, and there is an RMS scatter of 14% between the two datasets. Evans et al., A&A, 610, A20, 2018, reproduced with permission © ESO

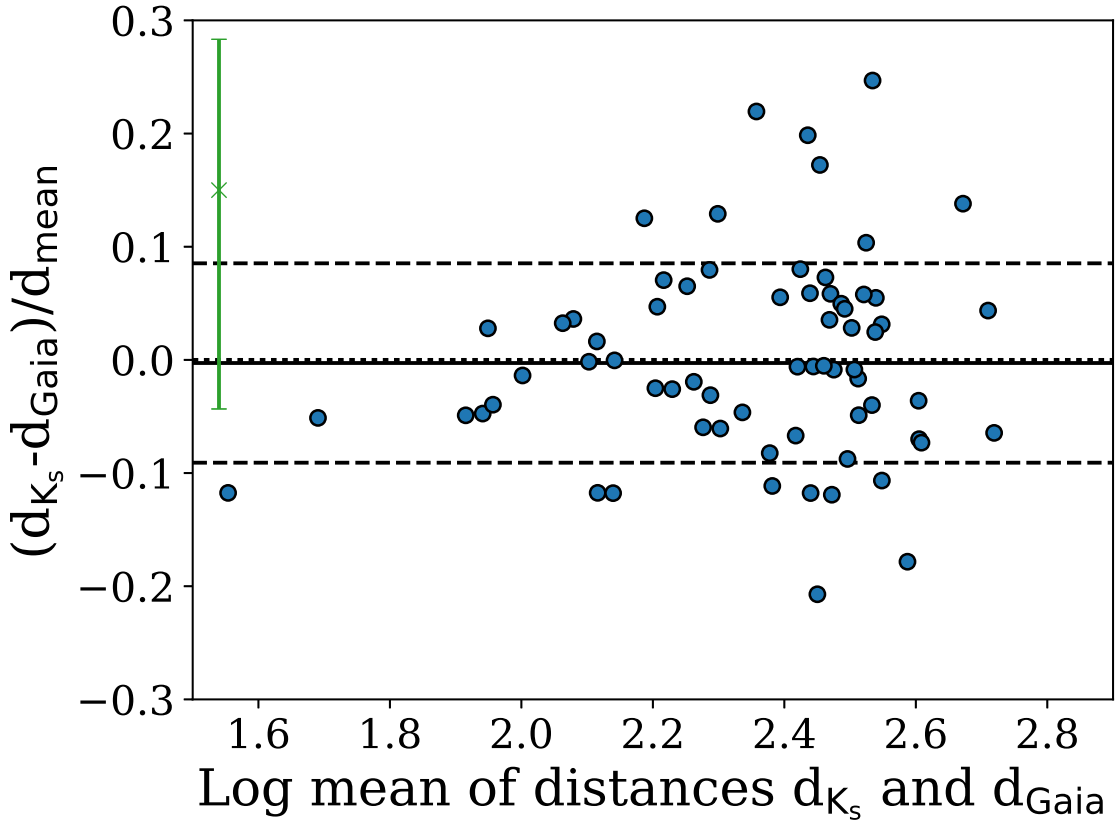

Figure 3.7: Comparison of distances derived in this work to Gaia-TGAS results. Explanation as for Figure 3.6, except comparing the Gaia-TGAS distances, d_{Gaia}, with those from the K-band surface brightness-temperature relation, d_{Ks}. The distances derived in this work using the K-band magnitudes show no systematic offset from the Gaia data ($0.3 \pm 1.7\%$ higher on average), with an RMS scatter of 9% between the results from the two methods. Evans et al., A&A, 610, A20, 2018, reproduced with permission © ESO

where X is a factor relating the $(B-V)$ reddening to that observed in the TCI colour bands. As before, the coefficients (k, z, and X) were fitted to the data using the least-squares method, minimizing the residuals between the corrected and expected colours.

The fitted value for k was identical to the 2014 calibration, at 0.08 ± 0.03 mag./airmass, whilst a somewhat lower zero-point offset of $z = +0.405 \pm 0.011$ mag. was found (+0.46 in the 2014 calibration). No evidence was found of the temperature-based offset in stellar colour hinted at by the 2014 calibration, with the magnitude of the apparent offset (0.06 mag.) being comparable to the residuals in the new photometric calibration (0.07 mag. RMS). The reddening coefficient X was fitted with a value of 0.53 ± 0.06. No systematic offset or trend as a function of $E(B-V)$ was seen, as shown in Figure 3.8. The corrected observed colours are all accurate to within 0.15 mag., corresponding to a photometric temperature determination that is accurate to better than 300K.

3.4 Flux-temperature relation

The photometric calibration in the previous section allows the temperatures of companion stars to be determined. Under the assumption that both the target stars and any binary companions have not evolved significantly off the main sequence,[6] the flux ratio of the two stars correlates with their respective temperatures, with cooler binary companions being fainter and vice versa. If the companion star appears significantly fainter or brighter than expected from the temperatures of the two stars, this is an indication that the companion is significantly more or less distant than the planet host star, and hence that the two stars do not form a physical binary system.

Stellar model atmospheres provide estimates for the flux per unit area on the

[6]There are a small number of companion stars which are not main sequence companions, e.g. the white dwarf companion to K2-02 (Vanderburg et al. 2015), which have been identified through common proper motion.

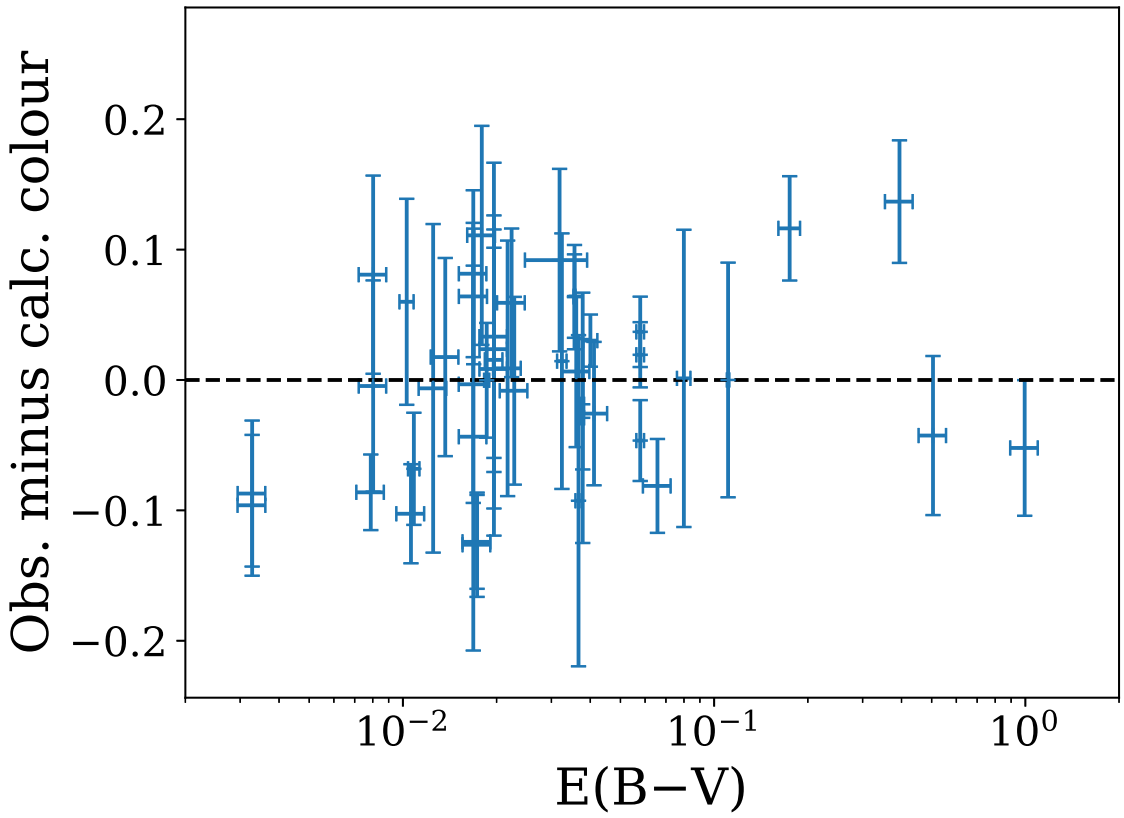

Figure 3.8: Offset between the observed and expected stellar colour as a function of $E(B-V)$. The difference between the corrected observed colour of each target star and the colour predicted from its effective temperature is plotted against $E(B-V)$. No systematic trend is present, and all stars are within 0.15 mag. of their expected colour, corresponding to a temperature measurement that is accurate to better than 300K. Evans et al., A&A, 610, A20, 2018, reproduced with permission © ESO

surface of stars, which must be multiplied by the visible surface area of a star in order to determine the observed flux. For the 2014 data, stellar radii (and hence surface areas) were calibrated based on empirical measurements of eclipsing binary (EB) systems. For the 2015 and 2016 analysis, it was determined that the EB calibration overpredicted the radii of cool stars (3500K and below), based on a number of known proper motion companions being fainter than expected from the 2014 calibration. As a result, the calibration was modified to be based on the results of stellar models below 4000K.

3.4.1 Eclipsing binary calibration

Eclipsing binary stars provide one of the few methods to determine the masses and radii of stars; most single stars have angular diameters that are too small to measure via interferometry, and stellar distance measurements are currently too uncertain to constrain the radii of stars. The `DEBCat`[7] catalogue (Southworth 2015) is a compilation of measurements of detached eclipsing binary systems (i.e. those were the stars are well separated and do not significantly affect one another's evolution), from which empirical relations between parameters such as mass, radius, and temperature can be derived. A temperature-radius relation was derived for the purposes of comparing observed flux ratios to those of equidistant binary components, and a further temperature-mass relation used to estimate the masses of bound companion stars.

The catalogue contains a number of systems where one or both stars have begun post-main-sequence evolution, with the increased luminosity and radii of these stars making them more likely to eclipse and easier to discover (Andersen 1991). Following Southworth (2009), several cuts were made in the dataset:

- Stars above $1.5M_{\odot}$ were rejected, given the relatively short main sequence lifetimes of more massive stars.
- For binaries where the more massive component is above $1M_{\odot}$, systems with a mass ratio above 0.9 were rejected, and only the secondary star used for the

[7] `http://www.astro.keele.ac.uk/jkt/debcat/`

remaining systems, as such stars are unlikely to be evolved even if the primary is.

- For binaries below $1M_{\odot}$, both components were included, due to the long main sequence lifetimes of these stars.

In addition, the V1174 Ori system was manually excluded, as this contains two pre-main-sequence stars which are significantly inflated relative to the main sequence (Stassun et al. 2004).

Whilst it is possible to fit polynomials directly to the variables of interest, i.e. $T_{\rm eff}$, the stellar radius R, and the stellar mass M, this can result in poor numerical behaviour due to the large range of values covered by each variable, and additionally the fact that valid values of $T_{\rm eff}$ are far from zero, with the resulting fits being highly sensitivity to small changes in the polynomial coefficients. The relations between the logarithms of these values are better behaved, and hence polynomials were fitted to $X = \log(T_{\rm eff}/K) - 3.6$, $\log(R/R_{\odot})$, and $\log(M/M_{\odot})$. The temperature–radius relation was fitted as a linear relationship, whilst the temperature–mass relation was fitted with a cubic polynomial. The measurement uncertainties for the binary component parameters are relatively insignificant compared to the intrinsic scatter in the data, caused by factors such as differences in age and metallicity. The RMS scatter around the best fit is therefore used as the uncertainty for both relations.

The linear temperature–radius relation is

$$\log(R/R_{\odot}) = 1.639 \cdot X - 0.240 \pm 0.070, \tag{3.5}$$

while the cubic temperature–mass relation is

$$\begin{aligned}\log(M/M_{\odot}) = 27.296 \cdot X^3 - 7.273 \cdot X^2 \\ +1.529 \cdot X - 0.198 \pm 0.080.\end{aligned} \tag{3.6}$$

The resulting fits are shown in Figs. 3.9 and 3.10.

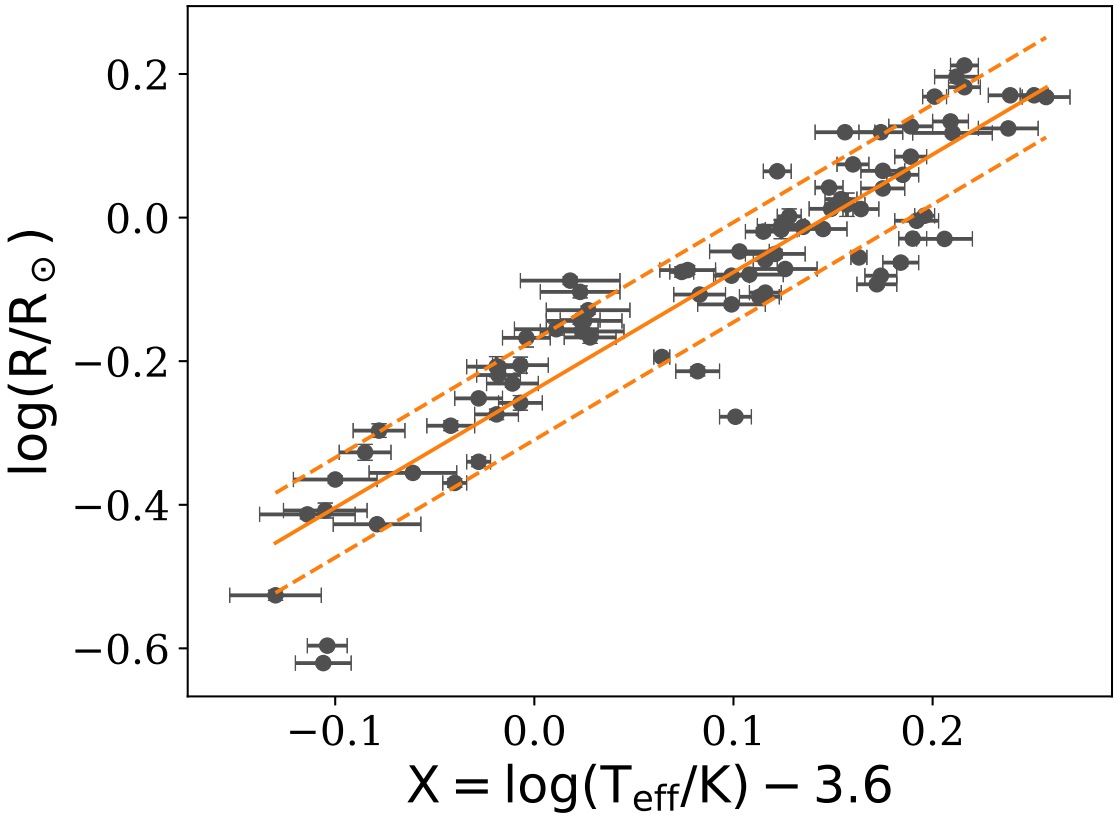

Figure 3.9: Empirical eclipsing binary temperature-radius fit. Black data points are stars taken from the `DEBCat` eclipsing binary catalogue, with the orange line indicating the best fit linear relationship. The dashed lines indicate the RMS scatter around the fit.

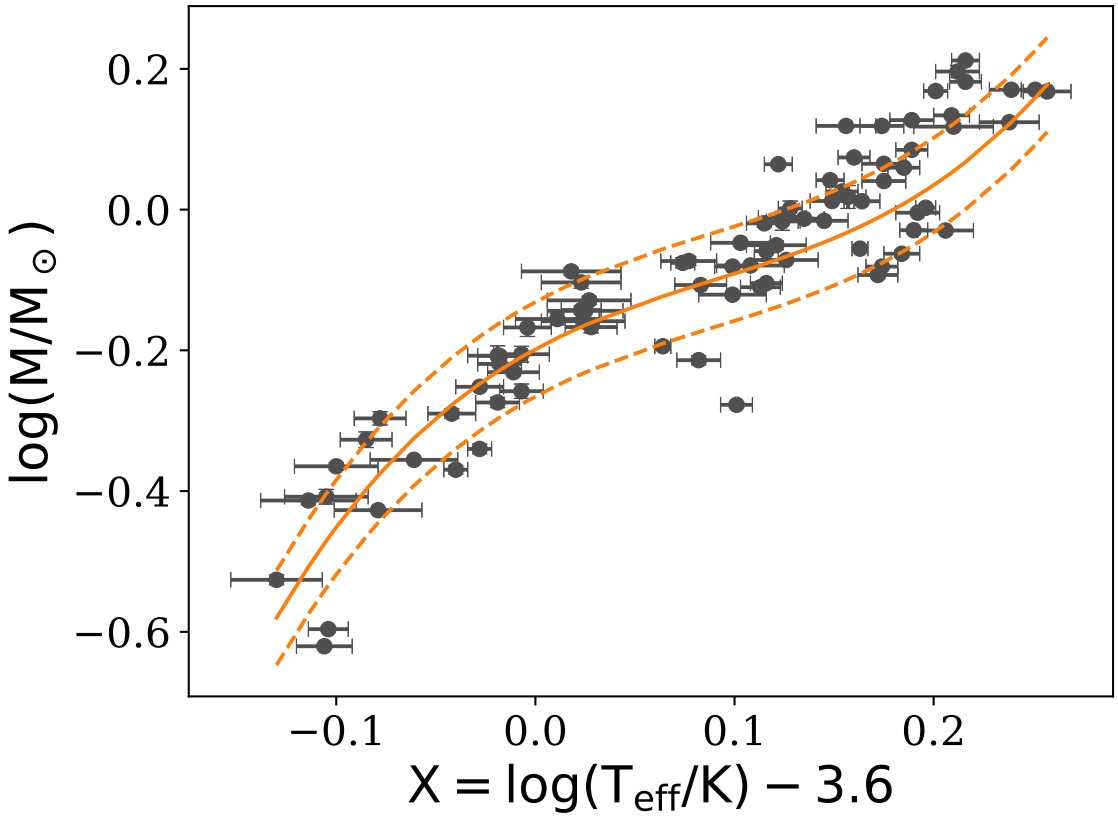

Figure 3.10: Empirical eclipsing binary temperature-mass fit. Black data points are stars taken from the `DEBCat` eclipsing binary catalogue, with the orange line indicating the best fit cubic relationship. The dashed lines indicate the RMS scatter around the fit.

3.4.2 Modification of temperature-radius relation

The temperature-radius relation given above was used to compare the observed flux of companion stars to that expected of a bound companion to the target star, based on the photometrically determined temperature of the companion, and the spectroscopically determined temperature of the target star. The majority of detected companions are much fainter than expected of a bound companion. This is not unexpected, as known transiting exoplanet host stars are generally bright and hence at relatively small distances, and hence most stars detected in the TCI data are more distant objects along the line of sight. However, when comparing the results of the 2015 and 2016 observations to similar analyses in the literature, it was noted that a number of previously confirmed binary companions were identified by the TCI analysis as distant background stars, in particular the fainter companions detected by Ngo et al. (2015), which were confirmed to exhibit common proper motion with the planet host star.

It was determined that this discrepancy was most pronounced for companion stars below 3500K, suggesting that the derived temperature-radius relation was incorrect for these cool stars. Comparison between was made with the temperature-radius relation predicted by the Baraffe et al. (2015) stellar models, which are specifically aimed at correctly modelling the properties of low mass stars. The stellar radii, and hence fluxes of bound companions, predicted by these models are in much better agreement with the observed fluxes of confirmed cool binary companions. Above 3500K, the Baraffe et al. (2015) models are in good agreement with the fitted relation. It was therefore decided to combine the two models, using the Baraffe et al. (2015) stellar radii below 4000K, and retaining the original empirical model above this temperature.

3.4.3 Predicted fluxes and colours

The `PHOENIX` model atmospheres were combined with the determined stellar radii and the TCI passbands to generate a series of expected fluxes and colours for main sequence stars. The model atmospheres covered the range from 2300K to 7000K in 100K steps,

and then in 200K steps up to 12000K; fluxes and colours were determined at these grid steps, with no interpolation performed. Stellar $\log g$ values were adopted from the tabulation for main sequence stars in Gray (1976), being in the range 4.0–5.0, and an [Fe/H] value of 0.00 was used throughout. Stellar colours were determined simply from the ratio of the fluxes in the two bands. Stellar fluxes were determined relative to a main sequence star with a temperature of 7000K, this being the upper limit of the range covered by the temperature–radius relation. After convolving the model atmospheres with the TCI passbands, these were then multiplied by the square of the predicted stellar radius, and divided by the flux determined for a 7000K star.

The predicted colours and magnitudes stars at 7000K and below are given in Table 3.1. The table includes the results of both the original 2014 and updated 2015/2016 radius calibrations; note that the two versions diverge rapidly in terms of predicted brightness below 3800K, with a difference of 1 magnitude already being present by 3400K.

3.5 Astrometric calibration

In order to express relative positions of two stars on the sky, it is necessary to convert the measured coordinates of the stars in detector (pixel) space to sky coordinates. Relative astrometry between two stars is usually expressed either as the difference in right ascension and declination, or instead as the angular separation of the two stars and the compass angle of one star relative to the other (typically the direction from brighter star to fainter). In both cases, it is necessary to know both the orientation of the detector – usually given as the angle between North and one of the detector axes – and the pixel scale of the detector. The conversion may also require additional corrections for effects such as pixel size variations, optical distortions present in the imaging system (generally more pronounced for wide field imaging), or flexure of the detector. The astrometric calibration may vary with time, and modifications to the instrument hardware often result in large changes to the astrometric solution.

Table 3.1: Predicted stellar fluxes and colours for the TCI for stars at 7000K and cooler, based on the PHOENIX model atmospheres and the temperature-radius relation. The '2014 Calib.' columns show the stellar fluxes using the empirical eclipsing binary radius calibration, which was found to overestimate the radii of faint companions. The '2015/6 Calib." uses the Baraffe et al. (2015) stellar model radii below 4000K. Not all model grid steps are shown.

				2014 Calib.		2015/16 Calib.	
$T_{\rm eff}$ (K)	M ($M_\odot$)	log g	$(v-r)_{\rm TCI}$	$\Delta r_{\rm TCI}$	$\Delta v_{\rm TCI}$	$\Delta r_{\rm TCI}$	$\Delta v_{\rm TCI}$
7000	1.38	4.5	−0.13	0.0	0.0	0.0	0.0
6800	1.28	4.5	−0.09	0.2	0.2	0.2	0.2
6600	1.19	4.5	−0.06	0.4	0.5	0.4	0.5
6400	1.11	4.5	−0.02	0.6	0.7	0.6	0.7
6200	1.05	4.5	0.02	0.9	1.0	0.9	1.0
6000	0.99	4.5	0.06	1.1	1.3	1.1	1.3
5800	0.95	4.5	0.10	1.3	1.6	1.3	1.6
5600	0.91	4.5	0.15	1.6	1.9	1.6	1.9
5400	0.87	4.5	0.20	1.9	2.2	1.9	2.2
5200	0.84	4.5	0.25	2.2	2.6	2.2	2.6
5000	0.81	4.5	0.32	2.5	2.9	2.5	2.9
4800	0.78	4.5	0.39	2.8	3.3	2.8	3.3
4600	0.75	4.5	0.48	3.2	3.8	3.2	3.8
4400	0.72	4.5	0.58	3.6	4.3	3.6	4.3
4200	0.68	4.5	0.71	4.0	4.8	4.0	4.8
4000	0.64	4.5	0.86	4.4	5.4	4.4	5.4
3800	0.59	5.0	1.03	4.8	6.0	4.9	6.1
3600	0.52	5.0	1.24	5.3	6.7	5.6	7.0
3400	0.45	5.0	1.49	5.9	7.5	6.8	8.5
3200	0.37	5.0	1.80	6.5	8.4	8.0	9.9
3000	0.28	5.0	2.21	7.1	9.5	9.1	11.4
2800	0.20	5.0	2.77	7.9	10.8	10.0	12.9
2600	0.12	5.0	3.39	8.8	12.3	10.8	14.3
2400	0.07	5.0	3.51	9.5	13.1	11.4	15.1

3.5.1 2014 astrometric calibration

For both the 2014 and 2015/2016 analyses, astrometric calibration was performed using TCI images of globular clusters, obtained for a separate variability monitoring campaign (Skottfelt et al. 2015a; Figuera Jaimes et al. 2016b). In 2014, eight images of globular clusters taken using the Red camera were used for astrometric calibration. The observations were spread across the entire observing season (April to September 2014), and additionally covered a variety of sky positions. Analysis was performed using tools in the Starlink software package (Currie et al. 2014), in particular the `AST` library of astrometric tools (Berry, Warren-Smith & Jenness 2016) via the `GAIA` image analysis tool. The sky positions of stars in the image were adopted from the NOMAD-1 catalogue (Zacharias et al. 2004), while the detector positions of stars were determined by the Starlink software. The detector orientation and pixel scales of the x and y axes were fitted using the `AST` library tools to reduce the offsets between observed and reference positions. The uncertainties in these fitted values were estimated from the RMS scatter of the eight separate fits.

The x-axis was determined to be rotated by $1.1 \pm 0.3^\circ$ from North with a scale of 88.9 ± 0.5 mas/px, and the y-axis was found to have similar values, being rotated by $1.1 \pm 0.2^\circ$ from North with a pixel scale of 88.7 ± 0.4 mas/px. Given the small difference in the orientations and pixel scales along each axis, it was assumed that any distortion between the axes was negligible, and hence that the detector had a global rotation of $1.1 \pm 0.2^\circ$ and a uniform scale of 88.8 ± 0.3 mas/pixel. At the time, no variation outside the precision of the astrometric calibration was found with either telescope pointing or observation date. No astrometric calibration was performed for the Vis data in 2014, which was only operational for a small fraction of nights, in addition to several changes to the instrument alignment as a result of commissioning work. However, it was noted that the pixel scale and alignment was similar, with the Vis camera being rotated by approximately 2° relative to the Red camera.

3.5.2 2015/2016 astrometric calibration – method

For the 2015/2016 data reduction, the calibration routine was improved, and also extended to cover the Vis camera. As before, images from the GC monitoring programme were used. The nature of this programme resulted in several dozen observations being taken per cluster, and hence a very large set of observations was available for calibration. It was infeasible to perform calibrations for all images using the process from 2014, which required manual input for each cluster, and instead an automated astrometric calibration routine was developed. Detector positions of the stars in each image were extracted automatically using the `DAOPHOT` package, utilising the best 1% of exposures only. This resulted in detection limits of the order V = 16–17, depending on the seeing conditions, the integrated exposure time, and also the crowding of the cluster (faint stars are more difficult to detect in crowded fields). The 'true' sky positions of stars were taken from a variety of dedicated surveys of GCs, listed in Table 3.2. These surveys focused heavily on accurate astrometry for the purpose of measuring the motions and distribution of stars in globular clusters, and many are based on data from one or several instruments on board the HST. No correction was made for the proper motions of stars in the GCs, as it was assumed the effect of such would be negligible; in addition, not all datasets included proper motion data. It was further assumed that no significant distortion was present in the TCI images, and hence the coordinate transformation was modelled simply as a scaling and rotation.

A least-squares algorithm was used to minimize the pairwise separation of the detected and reference stars. In each iteration of the algorithm, each detected star was matched with the nearest reference star. As the pairings were not fixed, even if stars were initially paired incorrectly, this would be resolved as the astrometric solution was improved by the fitting process. The process was repeated for each observation, in addition to being performed separately for the Red and Vis data. The fitting routine was found to work well when the starting parameters were set manually to give a good initial fit. However, many of the unsupervised fits were either unable to converge, or settled on astrometric solutions that were clearly incorrect when the observed and

Table 3.2: Sources of stellar positions for globular clusters. These datasets were matched to stars identified in TCI observations, and then used to calibrate the astrometric solution of both TCI cameras.The instrument which were the main source of astrometry for each cluster are listed for each survey, although several combined results from multiple instruments; see each reference for further details.

Cluster	Coordinates	Instrument	Reference
NGC 104	00 24 05 -72 04 53	HST/WFPC2	McLaughlin et al. (2006)
		HST/ACS	Anderson et al. (2008)
NGC 5139	13 26 47 -47 28 46	HST/ACS	Anderson et al. (2008)
		WFI@2.2m	Bellini et al. (2009)
		HST/WFC3	Bellini et al. (2010)
		HST/ACS	Anderson & van der Marel (2010)
NGC 5286	13 46 27 -51 22 27	HST/ACS	Anderson et al. (2008)
NGC 6093	16 17 02 -22 58 34	HST/ACS	Anderson et al. (2008)
NGC 6121	16 23 35 -26 31 33	HST/ACS	Anderson et al. (2008)
		VLT/HAWK-I	Libralato et al. (2014)
NGC 6388	17 36 17 -44 44 08	HST/ACS	Anderson et al. (2008)
NGC 6541	18 08 02 -43 42 54	HST/ACS	Anderson et al. (2008)
NGC 6652	18 35 46 -32 59 27	HST/ACS	Anderson et al. (2008)
NGC 6656	18 36 24 -23 54 17	HST/ACS	Anderson et al. (2008)

reference stellar positions were compared by eye. Several issues that contributed to these convergence problems were identified, which are discussed in turn below.

3.5.2.1 Sensitivity differences

The reference datasets were derived from observations which are much deeper than the TCI data, with the difference being up to 5 magnitudes. This resulted in a high fraction of spurious pairings between bright stars detected in the TCI data and much fainter objects identified in the reference data. To overcome this problem, a magnitude cutoff was used to reject reference stars that were too faint to be detected on the TCI images. This was done manually for each reference dataset and cluster, by inspecting the reference star positions overlaid on a high quality TCI image and modifying the magnitude cutoff to reduce the number of stars in one dataset but not the other. This

cutoff was set in either the V or I band, depending on whether or not I band magnitudes were available in the reference dataset.

3.5.2.2 Pointing offsets

The pointing model for the Danish 1.54m Telescope is only accurate to 10 arcseconds or so. As this is a significant fraction of the TCI field of view, the observing software automatically performs a pointing correction for previously observed targets to ensure the field of view is well aligned; for new targets, the user is requested to confirm the pointing. The automated correction typically reduces pointing offsets to the level of an arcsecond, but occasionally the automated process does not derive a good correction (usually due to poor SNR or a very large pointing offset). In addition, the reference pointing for some GCs was modified during the 2015 observing season, resulting in a systematic difference between previous and subsequent data. Due to the crowded nature of these fields, combined with the lack of prior knowledge as to which observed–reference pairings are correct, pointing offsets were found to be a major cause of astrometric fits that were either unable to converge on any single minimum, or instead produced solutions that were clearly incorrect upon visual inspection.

To combat this, an additional stage was introduced to the fitting process to determine the pointing offset of each image relative to a high quality reference image. The choice of reference image was based on both the image quality (dominated by seeing and image focus) and the pointing of the image – a high quality reference image with a large pointing offset relative to all other data would not be useful. For this image, the x and y pixel coordinates of the GC centre were manually determined, matching the observed and reference stars using the 2014 astrometric solution. A method similar to the `DONUTS` algorithm (McCormac et al. 2013) was then used to determine the pointing offset for each other image of the cluster. The observed and reference image were collapsed separately along both axes, giving the summed x and y profiles of each image. The x profiles of the observed and reference images were then cross-correlated with one another, and similarly for the y profiles, with the offset in the

x and y cross correlation peaks corresponding to the pointing offset. This information was used to improve the estimate of the sky position at the image centre, significantly improving the results of the fitting process.

For some low SNR observations, it was found necessary to downweight cross correlation peaks far from the centre of the image space, caused by the change alignments of different bright stars along the x or y axes. In addition, some images had pointing offsets similar in magnitude to, or larger than, the field of view, and hence even the cross-correlation technique was unable to correctly determine the offset. Such cases were identified by comparing the peak height of the x and y cross-correlations with the x and y autocorrelations of the reference image. If the cross-correlation peaks were significantly less than the autocorrelation, it was assumed the images were not of the same field of view, and hence the image was rejected from the fitting process. The minimum peak ratio threshold was set manually at 12.5%, following manual identification of images where the pointing offset was too large for correction.

3.5.2.3 Incorrect pairings

Each observed star was paired with the nearest reference star, under the assumption that these represented the same object, and hence it is assumed the positions of the two should be identical with the correct astrometric solution. However, as the initial (or subsequent) astrometric solution moves further from the correct solution, an increasing fraction of stars are paired incorrectly. It would then become very difficult for the minimisation routine to return towards the correct solution, instead reducing the separations of incorrect observed-reference star pairings. In addition, even when the majority of stars were correctly matched, a small fraction of observed stars were found not have a corresponding reference object, either due to spurious detections in the observed data, or instead due to stars not present in the reference data.

This issue was tackled by restricting pairings to stars offset by less than 2 arcseconds from one another, assuming that the initial pointing and astrometric solution would be accurate to at least this level. In future work, it may be advisable to more

smoothly downweight pairs of stars with unreasonably large position differences, rather than the step change induced by the current cutoff. Furthermore, a more 'intelligent' pairing routine would assist – the reference datasets contain flux measurements of all stars, often covering a variety of filters, which would be compared to flux measurements from the TCI data itself, rejecting matches between stars of very different brightness.

3.5.2.4 Atmospheric refraction

The apparent positions of stars are modified by refraction of starlight by the Earth's atmosphere, with the effect being zero at the zenith and most pronounced near the horizon. At an altitude of 45°, the position of an object is offset by approximately an arcminute, increasing to several degrees at the horizon. Telescope pointing models are able to account for the difference between true and apparent position of objects, and hence this is rarely an issue in observations. For astrometric calibration, it is instead the differential refraction due to changing zenith angle across the field of view that is important, which casues an apparent compression of the field of view along the zenith line (perpendicular to the horizon). Over the field of view of the TCI, the differential refraction at an altitude of 45° corresponds to approximately 0.2 pixels, and would cause a change in pixel scale of 0.04 mas/px along this direction, comparable to the precision of the final 2015 astrometric solution.

Correction for differential atmospheric refraction was performed following Gubler & Tytler (1998), in which the change in apparent separation of two stars along the zenith line, ΔR, is a function of the mean zenith angle of the two stars, z, and the true difference in separation along the zenith line, Δz. The derivation in Gubler & Tytler (1998) assumes that the separation of the stars is much less than the zenith angle, i.e. $\Delta z \ll z$, which is satisfied for separations of a few tens of arcseconds. Following Equation. 12 of that work, the relationship can be expressed as

$$\Delta R = C_1 \cdot \Delta z - C_2 \cdot \Delta z^2. \tag{3.7}$$

The variables C_1 and C_2 are defined as

$$C_1 = (1 - \tan^2(z)) \cdot (A + 3B\tan^2(z)), \tag{3.8}$$

$$C_2 = (1 - \tan^2(z)) \cdot (A\tan(z) + 3B(\tan(z) + 2\tan^3(z)), \tag{3.9}$$

in which the coefficients A and B vary with the properties of the atmosphere. The effect of differential refraction due to different stellar colours, covered in Equation 11 of Gubler & Tytler (1998), is ignored in this work. The colour-based effects are approximately an order of magnitude smaller than the separation effects for $\Delta z = 15''$, and correction requires prior knowledge of the spectral energy distribution of all stars in the field, which is not available for the majority of stars observed.

As in Gubler & Tytler (1998), the coefficients A and B were derived using the `refro` and `refco` routines in the `SLALIB` library (Wallace 1994). Following the atmospheric model of Sinclair (1982) and Hohenkerk & Sinclair (1985), the refractive index of air varies as a function the wavelength of light and atmospheric conditions (pressure, temperature, and humidity). The atmospheric properties vary significantly as a function of altitude, and so the refractive index of air at ground level is not representative of the integrated refraction experienced through the atmosphere. The `refro` routine performs an integration of the refractive index through the atmosphere from ground level to a cutoff at 80km (above which the atmosphere is assumed to have a negligible effect) for a specified zenith angle. The `refco` routine calls `refro` at several zenith angles, and uses the results to fit the cubic polynomial

$$R = A\tan(z) + B\tan^3(z), \tag{3.10}$$

in which R is the observed atmospheric refraction of a star, and the coefficients A and B are output for use in Equations 3.8 and 3.9.

Several parameters are required as inputs to the atmospheric model. The altitude of the observing site is used to define the lower limit of the atmosphere for the integration, and was taken as 2340m.[8] The temperature lapse rate defines the reduction in temperature with increasing altitude to the bottom of the tropopause (11km),

[8] `http://www.ls.eso.org/lasilla/Telescopes/2p2T/D1p5M/`

for which a value of 0.0065 K/m was adopted from Sinclair (1982) and Hohenkerk & Sinclair (1985). Gubler & Tytler (1998) note that the value of 0.0065 K/m is well supported by atmospheric studies, and also that the results of the algorithm change by less than 1 part in 10000 for any choice of value below 0.0085 K/m.

The temperature, pressure, and humidity at ground level are also required. These temperature and pressure in particular can have relatively large effects on the refraction, with the fractional change in either value corresponding to a similar fractional change in refraction (Gubler & Tytler 1998). It was initially intended to use the ESO La Silla meteorological conditions database[9] to lookup the measured values for all three parameters, but it was found that no data were available for the majority of the dates of observation.[10] Instead, typical night-time weather conditions for the site had to be adopted, which were taken to be 30% humidity, a temperature of 10 C (283 K), and a pressure of 770 mbar (this being noted as 'mean pressure' on several ESO La Silla weather monitors). The approximate range of normal temperatures covers a difference of approximately ±4% in absolute value (0 C to 20 C), whilst the range in pressure is approximately ±1.5% (760 mbar to 780 mbar), corresponding to an uncertainty in the correction of order 0.01 pixel at an altitude of 45°.

In addition to being applied to the astrometric calibration observations, a correction for differential atmospheric dispersion was also applied to all astrometry from the 2015 and 2016 observations of exoplanet host stars.

3.5.2.5 Field rotation

Field rotation is an effect which is usually considered in the context of alt-az telescopes, with stars being observed observed to rotate around the line of sight as the field is tracked across the sky due to the difference between the Earth's rotation axis and that of the telescope. Equatorially mounted telescopes such as the Danish 1.54m

[9] `http://archive.eso.org/wdb/wdb/asm/meteo_lasilla/form`

[10] ESO was made aware of this issue in July 2016, and was not able to provide a solution at the time. The data have since been located and entered into the database.

telescope are aligned with the Earth's rotation axis, and hence avoid the need for image derotation, either performed through a mechanical derotator or instead during the postprocessing of images.

It was therefore not expected that field rotation would be observed in the TCI data. However, on examination of the fit results for detector orientation for individual observations, a small trend in detector orientation angle as a function of hour angle was noted, occurring for all clusters. The amplitude of the effect varied by cluster, with NGC 104 showing the largest range of $\pm 0.05°$. If the polar axis of an equatorially mounted telescope is slightly misaligned with the celestial pole, a small amount of field rotation will be observed. This effect varies sinusoidally with hour angle and increases with the absolute value of declination, explaining why the effect is most noticeable for NGC 104, which is the most southerly of all the GCs observed.

The field rotation q observed by an alt-az telescope at a latitude ϕ is given by

$$\sin(q) = \frac{\sin(H)\cos(\phi)}{\cos(a)}, \tag{3.11}$$

where H and a are the hour angle and altitude at time of observation. For an equatorially mounted telescope which is misaligned by some angle θ, the field rotation observed is identical to that of an alt-az telescope at a latitude of $90° - \theta$.

The value of θ was fitted using a least-squares routine, assuming that the astrometric solutions should show no trend in detector orientation with hour angle, although each unique cluster was allowed to have a constant offset. The final value of θ was found to be $0.017 \pm 0.003°$. The variation in derived detector orientation for four clusters, in addition to the model fit, are shown in Figure 3.11

3.5.3 2015/2016 astrometric calibration – results

The astrometric fitting process was performed separately for each GC observation, and where multiple sets of reference data were available, separate solutions were derived for each dataset. The mean and standard deviation of the individual fit results were used to determine the final astrometric result and its uncertainty. The results are shown

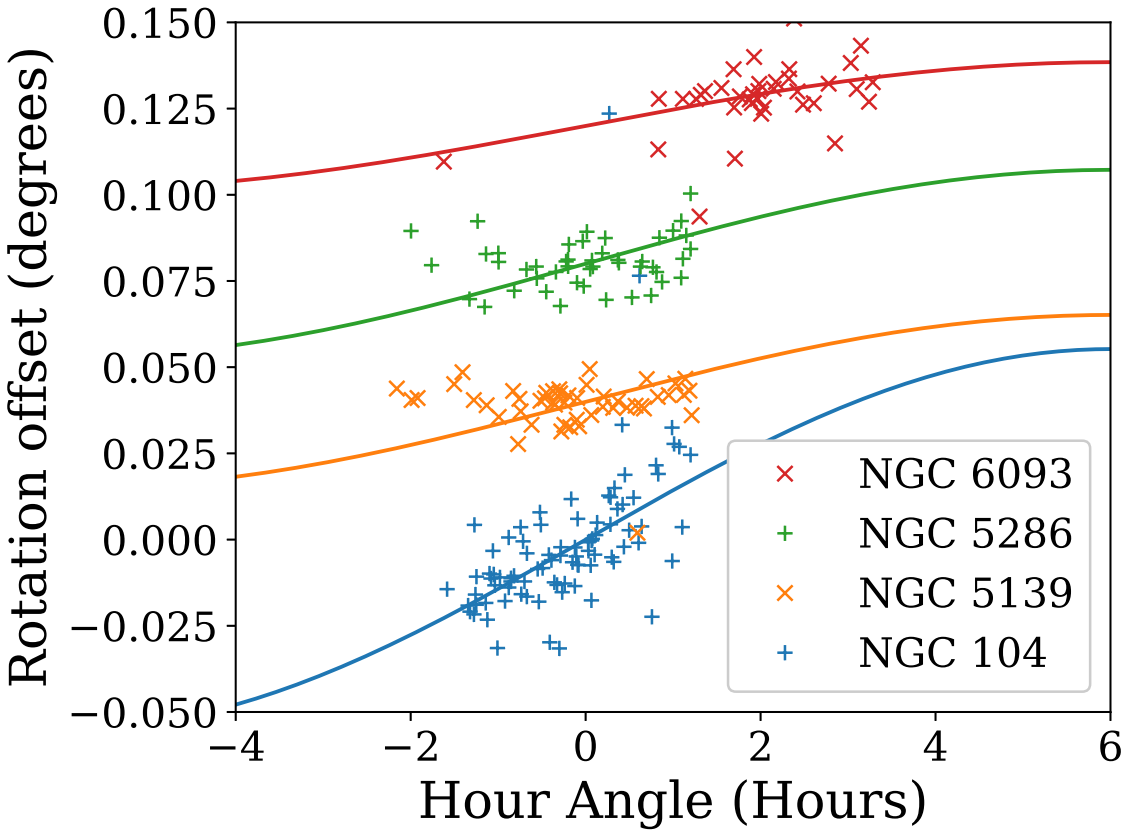

Figure 3.11: Detector orientation trends with hour angle. The offset in orientation for each individual observation of four globular clusters (NGCs 104, 5139, 5286, and 6093) are shown as a function of hour angle, in addition to the offset predicted by the telescope misalignment model. The data for each cluster are offset vertically in increments of 0.04°. The effect is most pronounced for NGC 104, which has the lowest declination of all four clusters. Evans et al., A&A, 610, A20, 2018, reproduced with permission © ESO

in Table 3.3, with the results for different clusters and different reference datasets presented separately.

The pixel scales derived for the Red and Vis cameras were consistent across all clusters and all reference datasets. The weighted mean plate scale for the Red camera is 88.91 ± 0.05 mas/px, consistent with the 2014 result, and the Vis camera was found to have a slightly coarser scale of 89.07 ± 0.05 mas/px.

The difference in detector orientation between the Red and Vis cameras has a weighted mean of $2.54 \pm 0.02°$, and shows no variation, implying that the two cameras are mounted securely. However, an unexpected result is that the derived detector orientation varies significantly between different datasets and clusters, covering a range of 0.17°, far in excess of the scatter in the individual fits for each cluster, which is below 0.03° in all cases. The constant offset angle between the two cameras indicates this effect is common to both for any given observation, and hence is not caused by errors in the fitting algorithm. Instead, it seems likely that the issue lies with the reference data used.

For NGC 5139, three of the four reference datasets produce consistent astrometric solutions. However, those three results are not truly independent: the astrometric results of Bellini et al. (2010) and Anderson & van der Marel (2010) are calibrated to match those of Anderson et al. (2008). For NGC 104, the two datasets do not share a common calibration, and whilst they show a large disagreement in terms of pixel scale, the derived detector orientation values are in good agreement. Similarly, the independent results for NGC 6121 show good agreement for all astrometric values, despite Anderson et al. (2008) utilising HST data and Libralato et al. (2014) using ground-based observations.

This is not the first identification of rotation offsets of this order of magnitude between datasets. Anderson & van der Marel (2010) noted a difference of 0.1° between their HST/ACS data and ground-based 2MASS observations, while van der Marel et al. (2007) found offsets of approximately 0.5° for M35 when comparing the UCAC2 catalogue, the McNamara & Sekiguchi (1986) catalogue, and the HST Fine Guidance Sensor calibration catalogue. These reports may indicate that the absolute orientation

of HST-derived data is uncertain at this level. For repeat observations of the same field, van der Marel et al. (2007) reported that the telescope roll angle is consistent at the level of 0.003°, perhaps explaining why minimal offsets are seen between the two NGC 104 datasets derived from separate HST observations.

A further possible source of errors is the actual determination of the telescope orientation provided by the HST reduction pipelines. Anderson et al. (2008) note briefly that the output of the ACS pipeline is 'tied to an absolute astrometric frame via the guide stars', referring to the stars observed by the telescope's Fine Guidance Sensors (FGS). The three FGS units are interferometers, capable of tracking small shifts in the positions of observed stars. During normal HST observations, two of the telescope's three FGS units are used to maintain pointing stability by tracking and correcting the apparent motion of selected guide stars. Guide stars for observations are chosen from the Guide Star Catalog (GSC), originally derived solely from photographic plates (Lasker et al. 1990), but since significantly updated with additional data to create the Guide Star Catalog II (Lasker et al. 2008). From the measurements of these guide stars and the coordinates contained within the GSC catalogues, the pointing of HST during observations can be determined. As noted in Koekemoer et al. (2006), this means that the astrometric accuracy of HST observations is limited by that of the GSC. Koekemoer et al. (2006) states that for the original GSC-I, the 'typical level of uncertainty' is quoted as 1.0″, whilst the GSC-II catalogue the RMS accuracy is at the level of 0.25″, although some objects show much larger offsets even after correction for proper motion.

The HST reference datasets were all derived from a large number of observations, covering a range of filters and telescope pointings/orientations. However, the astrometric calibration was typically derived from a single observation, with the stellar positions from all other observations matched to this single reference frame. It is possible that errors in the GSC or GSC-II catalogs could result in an error in the determined rotation angle for the reference frame, which would then carry through into the catalog. To test this possibility, a model of the HST FGS system was created, based on the instrument description in Nelan et al. (2016). Each of the three FGS units covers approximately

one quarter of the HST field of view, covering the range from 10 to 14 arcminutes radially from the HST optical axis, with rotation around an arc of 83.3° at the inner edge and 85° on the outer edge. The three fields of view are nominally offset by 90° relative to one another. The FGS model was capable of considering adjacent FGS units offset by 90° (the combination of either units 1 and 2, or units 2 and 3), or the wider combination of 180° (units 1 and 3). For each iteration of the model, one guide star was placed inside each FGS unit's field of view. The initial position of a generated star was taken as the 'catalogue' position, which then perturbed based typical uncertainty in the GSC (1.0″ or 0.25″, depending on the version) and the measurement uncertainty of the FGS units (0.015″) – assuming both are normally distributed – to give the 'measured' position. The position angle of the generated star relative to the optical axis of HST was calculated for both positions. The offset between catalogue and measured position angle was determined for both of the simulated guide stars and the average offset determined; this value was then taken as the error in the HST astrometric solution. A large number of iterations were performed to sample the distribution of position angle offsets.

The results of this model were published in Evans et al. (2018), based on the quoted position uncertainty for GSC-II. However, it has since been noted that the majority of reference datasets used were produced before the introduction of GSC-II, with the ACS Survey of Globular Clusters (Anderson et al. 2008) being performed during HST Cycle 14, the final cycle in which the original GSC-I catalogue was used. For the GSC-II uncertainties, 68% of the FGS simulations showed position angle offsets below 0.017°, and 95% below 0.046°, somewhat lower than the scatter observed in the TCI astrometric fitting. However, for the larger GSC-I uncertainties, the position angle offsets had a 68th percentile value of 0.058° and the 95th percentile value of 0.152°, in good agreement with the range of 0.17° seen across the nine different clusters.

If this model of the HST astrometric calibration uncertainties is correct, it is able to explain why the position angles found for separate clusters differ so significantly. However, it does not make it possible to determine or correct the error affecting each dataset, and hence the true astrometric solution for the TCI remains uncertain. The

final astrometric solution was derived from the weighted mean and standard deviation of the results for each independent dataset, with the detector orientation uncertainty being dominated by the scatter in the reference data. For the Red camera, a plate scale of 88.91 ± 0.05mas/px and orientation of $1.30 \pm 0.06°$ eastwards of North were found; for the Vis camera, the corresponding values are 89.07 ± 0.05mas/px and $-1.25 \pm 0.06°$.

It is interesting to note that whilst several other instruments have been astrometrically calibrated based on HST data, such discrepancies have not been widely identified. However, such calibrations often rely on a single source of reference astrometry – for example, the Service et al. (2016) Keck/NIRC2 astrometric solution is based on one HST/ACS dataset for M53, whilst the multiple VLT/SPHERE astrometric calibration fields have all been 're-calibrated' based on the data for 47 Tuc (Maire et al. 2016). These steps make any position angle discrepancy difficult to identify, except in the form of unexplained offsets in astrometry derived from separate telescopes and instruments.

3.6 Companion star identification

An automated detection algorithm was developed to identify companion stars in the TCI data. This was chosen over manual identification due to the large number of images involved, and additionally due to the difficulty in applying and quantifying consistent detection limits to a manual search. The automated search was run on all observations with the Red camera; Vis data were not used for object detection due to the degraded focus and lower SNR typically present, in addition to many of the faint companions of greatest interest being very red in colour. Some observations were rejected manually for reasons such as thick cloud, very poor seeing or poor focusing of the instrument, or an incorrect star being centred in the field of view. For each observation, the search was repeated for lucky imaging acceptance fractions from 1% to 90% based on the cuts provided in the reduced TCI data – i.e. the search was performed initially on only the first layer in the FITS cube, then on the sum of the first two layers, and so forth.

Table 3.3: Final astrometric solutions for each globular cluster dataset. The detector plate scale and orientation (measured eastwards of true north) is quoted for both cameras for each of the reference datasets used. The uncertainty quoted for each measurement is based on the standard deviation of the solutions derived for each individual observation. Note that large discrepancies exist between the derived detector orientations, which are discussed in the text.

	Red camera		Vis camera		
Cluster	Scale (mas/px)	Rotation (°)	Scale (mas/px)	Rotation (°)	Ref.
NGC 104	89.03 ± 0.07	$+1.222 \pm 0.012$	89.15 ± 0.07	-1.329 ± 0.013	McLaughlin et al. (2006)
	88.92 ± 0.07	$+1.215 \pm 0.010$	89.04 ± 0.07	-1.335 ± 0.013	Anderson et al. (2008)
NGC 5139	88.87 ± 0.05	$+1.206 \pm 0.004$	89.01 ± 0.05	-1.352 ± 0.005	Anderson et al. (2008)
	88.88 ± 0.05	$+1.296 \pm 0.006$	89.02 ± 0.05	-1.258 ± 0.007	Bellini et al. (2009)
	88.87 ± 0.05	$+1.200 \pm 0.005$	89.01 ± 0.05	-1.353 ± 0.008	Bellini et al. (2010)
	88.87 ± 0.05	$+1.205 \pm 0.004$	89.01 ± 0.05	-1.352 ± 0.006	Anderson & van der Marel (2010)
NGC 5286	88.91 ± 0.06	$+1.322 \pm 0.007$	89.06 ± 0.06	-1.236 ± 0.008	Anderson et al. (2008)
NGC 6093	88.90 ± 0.08	$+1.333 \pm 0.007$	89.03 ± 0.08	-1.222 ± 0.006	Anderson et al. (2008)
NGC 6121	88.86 ± 0.05	$+1.337 \pm 0.005$	89.01 ± 0.05	-1.216 ± 0.012	Anderson et al. (2008)
	88.85 ± 0.04	$+1.340 \pm 0.006$	89.00 ± 0.05	-1.213 ± 0.011	Libralato et al. (2014)
NGC 6388	88.91 ± 0.04	$+1.378 \pm 0.011$	89.13 ± 0.15	-1.177 ± 0.027	Anderson et al. (2008)
NGC 6541	88.92 ± 0.06	$+1.374 \pm 0.022$	89.10 ± 0.09	-1.182 ± 0.011	Anderson et al. (2008)
NGC 6652	88.98 ± 0.09	$+1.327 \pm 0.021$	89.15 ± 0.09	-1.213 ± 0.040	Anderson et al. (2008)
NGC 6656	88.94 ± 0.06	$+1.330 \pm 0.009$	89.10 ± 0.10	-1.232 ± 0.027	Anderson et al. (2008)

This technique allowed the TCI survey to reach much deeper sensitivity limits than are commonly achieved with lucky imaging.

3.6.1 Image preprocessing

Before analysis, the pipeline-reduced images were first processed to remove several prominent features that complicate automated detection. A trail or 'smear' of signal is observed on the North ($+x$) side of stars, corresponding to the readout direction of the detector. This was initially attributed to additional photons being received during the readout stage, due to the TCI having no shutter, but the effect may instead be caused by charge transfer inefficiency during the electron multiplication stage (e.g. Bush et al. 2014). The smearing effect is removed by removing a fraction of the cumulative signal in pixels at lower x coordinates in each row, the fraction being set at $k = 0.0000177$, which was determined by requiring the north-side diffraction spike (i.e. the side on which smearing occurs) of bright stars to match the amplitude of the south-side spike (unaffected by smearing).

The diffraction spikes themselves are sufficiently bright to hide faint companion stars, and hence require removal. Additionally, the background level in the data varies with the x position (and to a lesser extent, with y). These effects were removed on a row-by-row or column-by-column basis. For the correction of features varying with x coordinate, groups of three y columns were selected, and for each y coordinate, the median pixel value of the three columns was chosen. The list of median values was then iteratively sigma-clipped to remove exceptionally faint or bright pixel values, mainly those corresponding to stars, and hence providing a poor estimate of the background. Of the remaining pixel values, the median was again determined and adopted as the background level for the central y column of the initial three; the median was used over the mean to again avoid biases induced by bright stars. The process was repeated identically for each set of three adjacent x rows to remove features that vary with the y coordinate. The final result of the smear correction and linear background feature removal are shown in Figure 3.12.

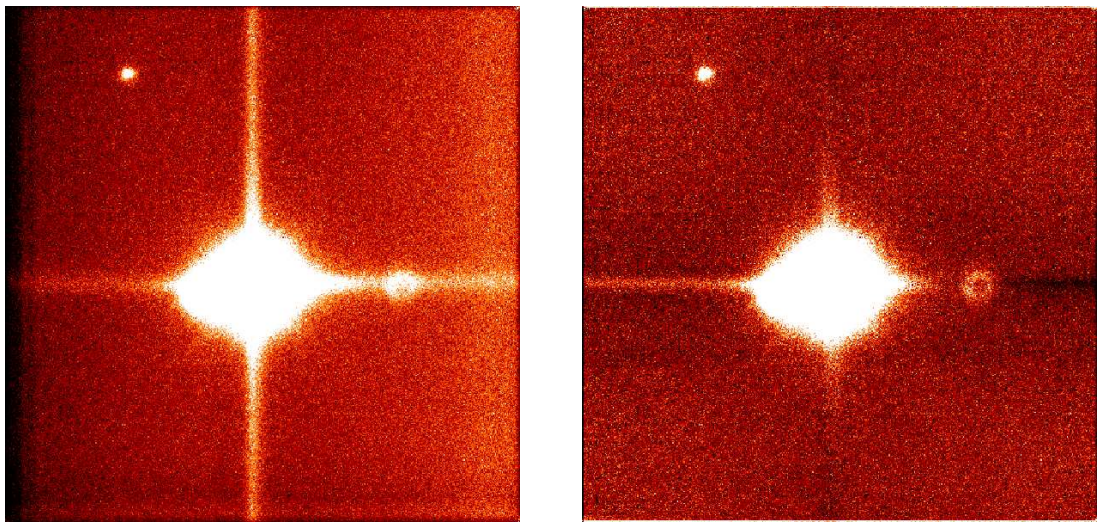

(a) Original frame (b) Background subtracted

Figure 3.12: TCI lucky imaging background subtraction. The left hand panel shows an uncorrected image, with the following features that are not desired: 1. variations in the background level along the x and y directions; 2. strong diffraction spikes from the target star; 3. an 'enhanced' diffraction spike to the right (North) due to the smearing effect. The right hand panel shows the resulting image after the treatment of these features. The ring-shaped feature to the right of the target star is an optical ghost of unknown origin, present in many TCI images.

3.6.2 Object detection

The technique used for object detection follows that outlined in Ginski et al. (2012), in which the image is convolved with a 2D Gaussian kernel and then subtracted from the original image. This method approximates the 'difference of Gaussians' technique used for feature enhancement and detection in computer vision (e.g. Gonzalez & Woods 2002), in which a source image is convolved with two Gaussian kernels of differing FWHM, and the results of one convolution subtracted from the other. For the case of astronomical images, the observed image corresponds to a series of unresolved, point source stars, which have been convolved with the (approximately Gaussian) PSF. The convolution of a Gaussian-convolved image with a second Gaussian kernel is equivalent to a single Gaussian convolution of the original point sources. The standard deviation of the convolving Gaussian was set at 4.0 pixels, corresponding to an FWHM of 11.7 pixels or an $1.04''$ on the sky, and hence approximately twice the FWHM of the observed images.

The difference of Gaussians image was then analysed to determine the averaged radial profile of the image around the target star. Under the assumption that the stellar PSF is circularly symmetric, any deviation from this symmetry would indicate the presence of a separate object. This has the inherent advantage of revealing stars that are not fully resolved, as compared to a simple peak-finding algorithm which would struggle to find close companions against the 'background' of the bright target star. The position of the target star was typically determined as the brightest pixel within the central 50×50 pixels of the image, although separate coordinates or window sizes were specified for cases where the target star was not the brightest object or significantly offset from the image centre. The radial profile was then determined in steps of 0.25 pixels, including the counts from all pixels with radii within 0.5px of the current step radius. The sub-pixel size for step radius was chosen to avoid artefacts near the target star caused by the background varying significantly across wider steps, whilst the inclusion of pixels more than a single 'step' away was motivated by the need to include a sufficiently large number of pixels, especially at small radii. A sigma

clipping routine was used to remove pixels with counts more than 3σ from the mean in each bin (typically those pixels representing stars), after which the mean and standard deviation of the remaining pixel counts were determined. Any pixel located within the 0.25px step (including those rejected by sigma clipping) with counts more than 1.7σ from the bin mean in each bin was then flagged as a 'detection'. The 1.7σ cutoff was found to provide the best compromise between false positive detections (typically due to PSF asymmetries) and the loss in completeness for faint objects.

The detection process was repeated for seven different lucky imaging selection criteria from 1% to 90%, as is possible with the reduced TCI data. A master detection list was created by counting the number of times a given pixel was flagged in these seven iterations and retaining only those pixels that were flagged two or more times. Adjacent pixels were grouped together into a single object detection, the location of which was set as the mean position of the grouped pixels. These detections were subsequently manually validated, which was found to be necessary in order to remove false positive detections, often caused by asymmetries in the target star PSF. This step additionally allowed the user to manually correct of close pairs of companion stars that were grouped into a single detection, as well as identification of other unusual companions or image features – for example, a number of companion stars were visually identified as galaxies or nebulae. To facilitate the manual inspection an interactive program was developed, displaying the detections on top the observed data. The user is able to view different images of the same target, including the simultaneously obtained Vis data where available, in addition to changing the lucky imaging selection fraction and the colour scale. It is possible for the user to inspect the difference of Gaussians image, or instead to see the number of separate detections registered for each pixel. The automated detections can be confirmed as is, or instead the user may specify new detections (e.g. splitting merged detections of two stars), with the possibility of adding notes to each detection.

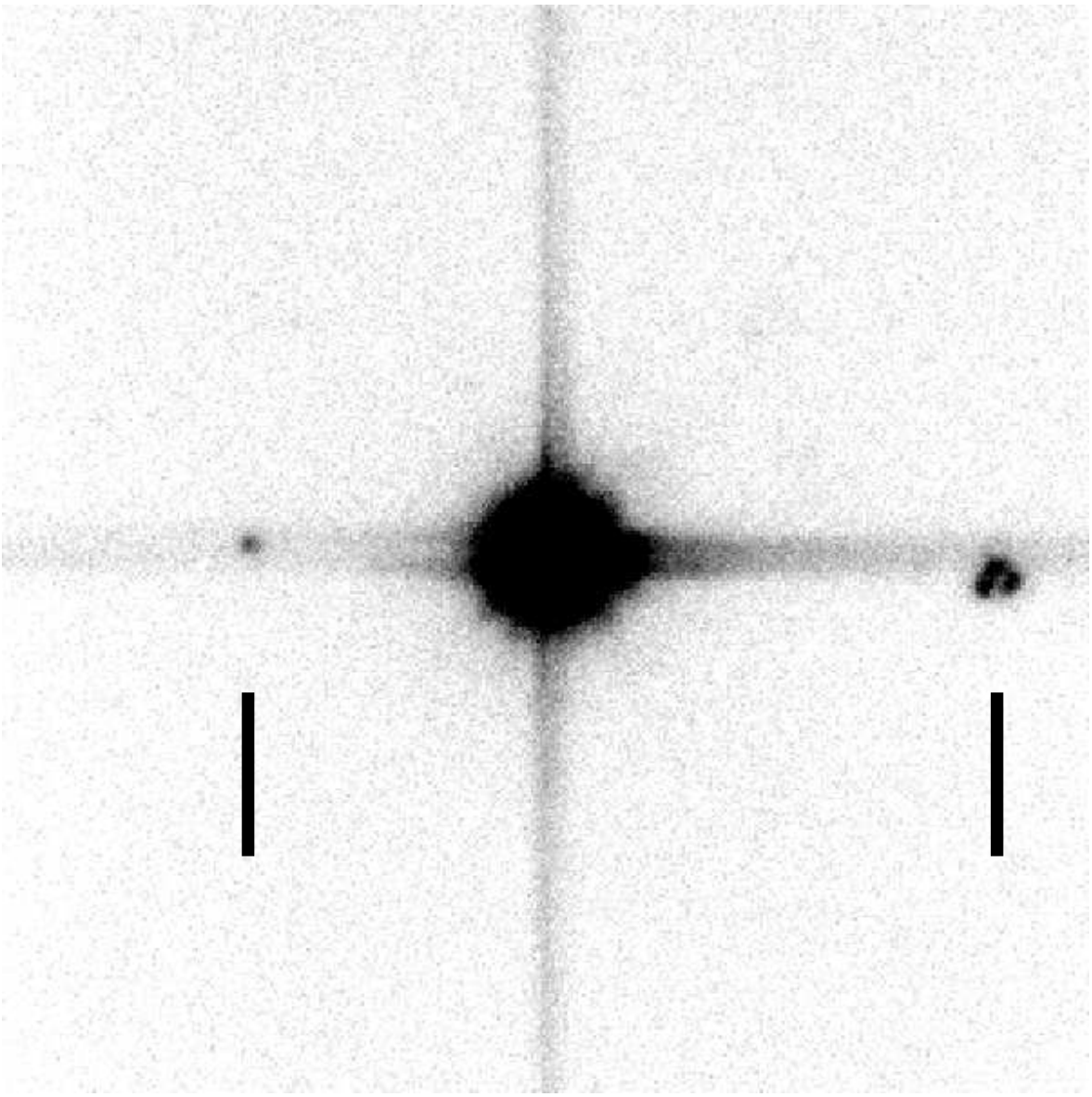

Figure 3.13: Optical ghosts in TCI images. This TCI Vis camera image of WASP-131 shows two clear features other than WASP-131, located to the left and right of the target, indicated with black lines. The ring-shaped source on the right is seen with both the Red camera and Vis camera, but is brighter relative to the target stars in Vis camera images. It resembles the defocused PSF of the TCI instrument, suggestive of it being caused by reflections within the optical system with a slightly different path length to the main starlight. The point-like source on the left is often bright in Vis camera data, but often undetectable in Red camera images.

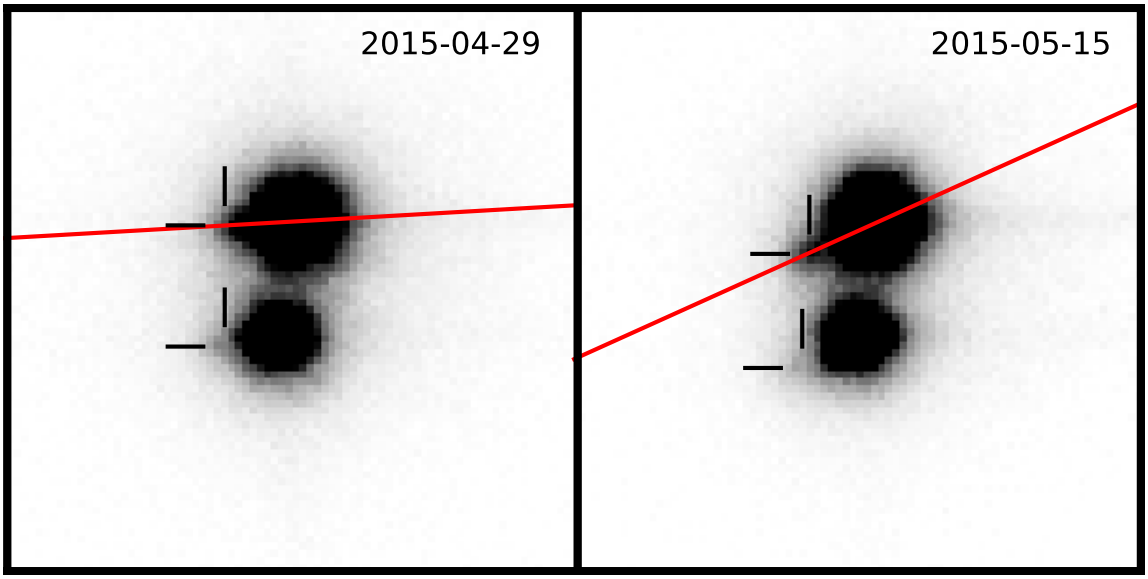

Figure 3.14: False companions caused by atmospheric dispersion. Both images show TCI Red camera observations the WASP-85AB system, a wide binary with the two components aligned nearly vertically on these images. Marked on each image are the false companions caused by the dichroic leak at 410nm and the effects of atmospheric dispersion, with both of the real stars having an associated 'companion'. The red line in each image indicates the direction of dispersion, which varies depending on telescope azimuth, with the lines drawn so as to pass through the centre of WASP-85A's PSF. Evans et al., A&A, 610, A20, 2018, reproduced with permission © ESO

3.6.3 Optical ghosts

Two types of optical ghosts have been noted in the TCI data. Firstly, a circular or ringed structure is occasionally observed in the Red camera data approximately 10 arcseconds north of the target star, with the exact position varying slightly, which is most apparent in very good seeing conditions. The shape of the ghost is similar to the defocused PSF of the TCI, and hence it is believed that internal reflections within the telescope or TCI optics result in a defocused image of the target field being superimposed on the main image. This ghost is occasionally accompanied by an in-focus image on the opposite (south) side of the target star, slightly closer in. Both ghosts are much more prominent in the Vis camera data, despite the lower signal typically received, presumably due to the transmission or reflection properties of the (unknown) optical components causing these ghost images. These ghosts are regularly detected as companion stars by the automated detection algorithm – occasionally with multiple detections for the ringed structure – and hence must be removed during the manual review process. Both of these features are illustrated in Figure 3.13.

The second, more troublesome type of optical ghost is an extension to, or in some cases a faint duplicate of, the PSF of all stars in the Red camera data. This is typically located to the southeast of the PSF, but the position, brightness, and separation of the duplicate vary, both from target to target and also in subsequent observations of the same target. In many cases the duplicate image is sufficiently close to be strongly blended with the target star, but it is occasionally well separated (sometimes exceeding an arcsecond) and can appear as a convincing companion star to both automated and manual detection methods. The nature of this ghost was not well understood at the time of publication for the 2014 data, and one such ghost was identified as a bona fide companion, located 1″ to the south of HAT-P-41. The understanding of this feature was improved by the detection of a pair of identical, well-separated ghosts during the observation of the WASP-85AB binary, which were seen to have moved in unison around the two stars in a subsequent re-observation a few nights later, indicating that such objects were clearly not of astrophysical origin. These observations of WASP-85

are shown in Figure 3.14, whilst the false positive companion to HAT-P-41 is shown in Figure 3.15

The cause of these companion-mimicking ghosts is a combination of differential atmospheric refraction and the transmission/reflectance properties of the dichroic used to split light between the Red and Vis cameras. As briefly mentioned in Section 3.5.2.4, the effect of atmospheric refraction varies slightly with wavelength, causing the apparent position of an object to vary with wavelength. Whilst many telescope instruments are fitted with atmospheric dispersion correctors (ADCs) to remove this effect, the TCI is not equipped with any corrective optics, and therefore stellar images in the TCI appear be slightly elongated perpendicular to the horizon, with the elongation varying as a function of atmospheric conditions and the altitude at time of observation. The existence of the well-separated optical ghost is caused by a leak in the dichroic at approximately 410nm, which transmits a small fraction of blue light towards the Red camera. Adopting the atmospheric conditions from Section 3.5.2.4 and an altitude of 50° (airmass 1.3), this blue light will appear offset by approximately an arcsecond from the redder light received by the red camera, matching the observed separation of the ghost at similar altitudes. The position of the ghost can be predicted from the telescope pointing at time of observation, and an additional option was added to the interactive analysis software to plot this during the manual confirmation stage, which proved very useful in distinguishing true companions from optical ghosts.

Consideration has been given to fitting a long-pass filter to the red camera to eliminate the effects of stray light through the dichroic. The TCI is itself a prototype instrument for a series of similar instruments on the SONG telescope network (Grundahl et al. 2007), with the full design including filer wheels and atmospheric dispersion correctors (Grundahl et al. 2009, Skottfelt et al. 2015b); however, these components were excluded from the installation on the Danish 1.54m telescope.

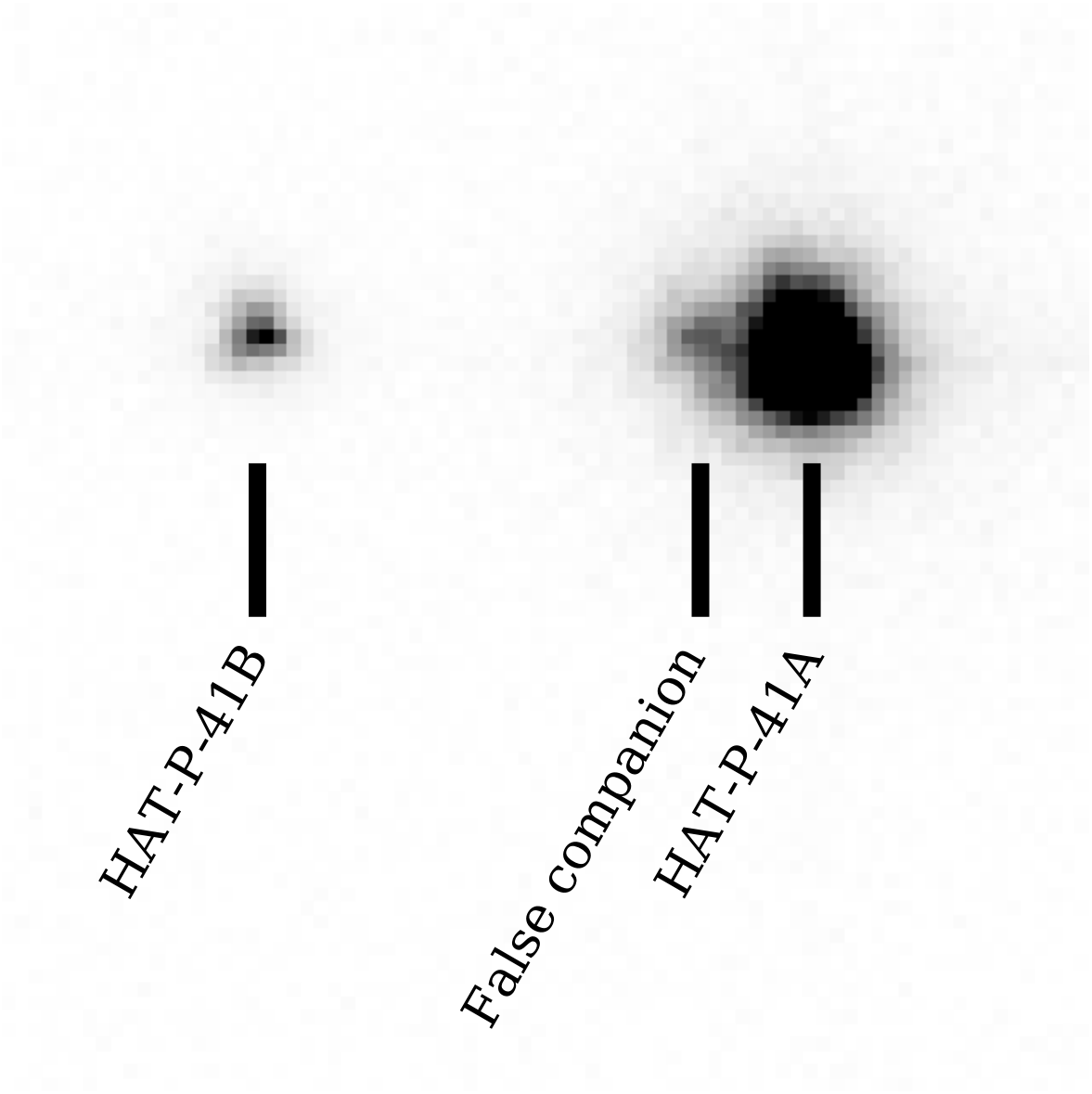

Figure 3.15: Falsely classified companion to HAT-P-41. This TCI Red camera image appears to show three stellar sources; however, star-like object marked 'false companion' is blue light from HAT-P-41A that passed through the dichroic leak at 410nm. The blue light image is offset by approximately 0.8″, far in excess of the image resolution, with the 1% image selection having a PSF FWHM of 0.35″.

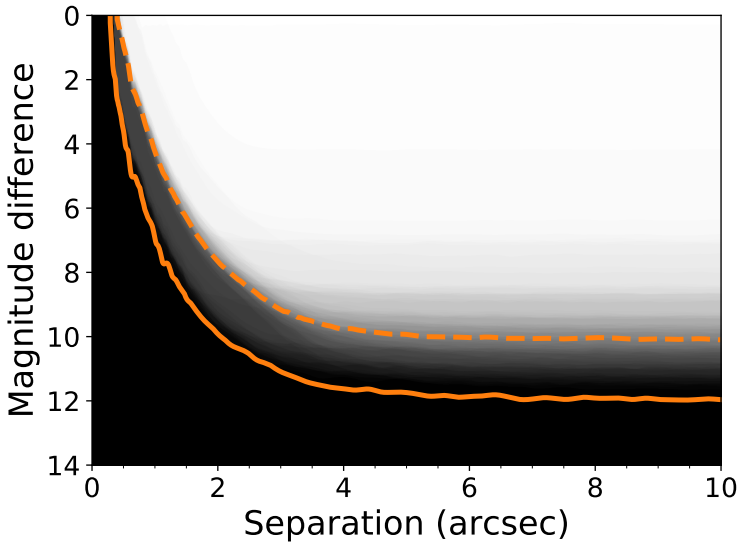

Figure 3.16: Detection limits for targets observed in 2014. Shading on the image indicates the fraction of observations for which a given contrast was achieved, with white indicating 100%, and black 0%. The dashed line indicates the median contrast across all targets. The solid line indicates the contrast of the best observation.

3.6.4 Detection limits

For each observation, the detection limit for faint companions was determined. An $n \times n$ box around each pixel was selected, with n being set to match the image FWHM reported by the TCI pipeline. The mean and standard deviation of the counts within the box were computed, and the 5σ upper limit was found to correspond closely to the reliable detection limit of the automated detection algorithm. The 5σ flux limit was converted to a magnitude difference based on the counts in an $n \times n$ box centred on the target star. This process was repeated for each of the seven lucky imaging selection criteria used during the star detection process. For a given angular separation, the overall detection limit of the image was taken to be the best detection limit of any of the seven generated detection curves. These are tabulated at selected separations in the observation logs, located in Appendix A. Additionally, Figs. 3.16, 3.17, and 3.18 illustrate the sensitivity of the observations in each year. The median detection limit was ~ 5 mag. at $1''$, ~ 8 mag. at $2''$, and ~ 10 mag. beyond at $4''$.

3.7 Photometry and astrometry

For each confirmed companion star, fluxes and positions were measured relative to the target planet host star. For the 2014 data, stellar positions were measured only from the Red camera. For the 2015 and 2016 data, astrometry was measured from both the Red and Vis datasets, and reported separately.

3.7.1 2014 reduction

Measurements were performed on the 2014 data using the 90% selection of lucky imaging frames. Astrometry was derived for stars through a peakfinding method as follows: a 9×9 pixel region centred on the estimated position of the companion was supersampled by a factor of ten, and then summed along rows and columns separately; the row

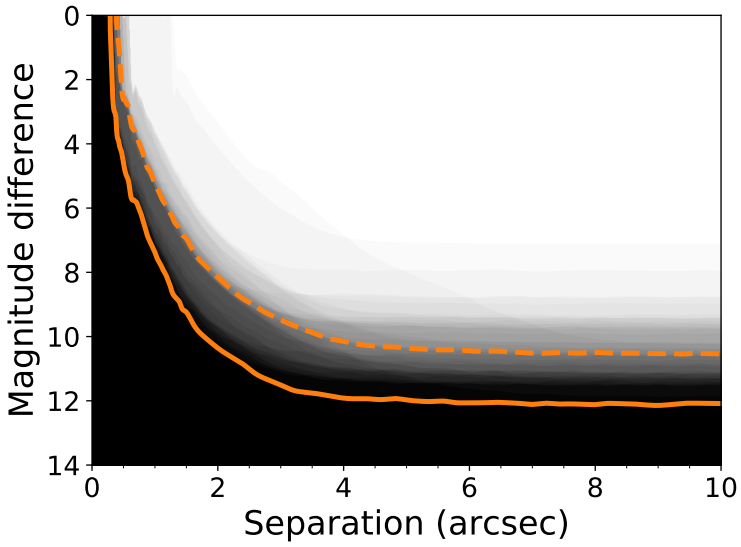

Figure 3.17: Detection limits for targets observed in 2015. Description as for Fig. 3.16

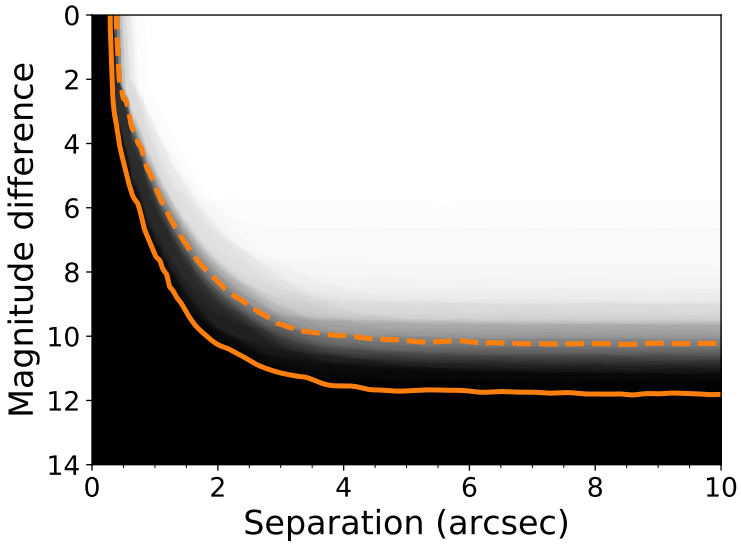

Figure 3.18: Detection limits for targets observed in 2016. Description as for Fig. 3.16

and column with the highest signal were taken as the stellar position. The method was tested using artificial stars, which resulted in the choice of the supersampling factor, due to no improvement in astrometric accuracy being found for higher factors. The method was accurate to better than 0.5px (0.044″) for stars with SNRs as low as 5. Photometry was performed using simple aperture photometry. The photometric aperture radius was set to 1.5 times the image FWHM reported by the TCI pipeline, with the inner and outer edges of the sky annulus set at twice and three times this value respectively. These values were again being chosen following tests, minimising the scatter in the derived photometry.

For the closest companion stars, these methods were not suitable due to the close proximity of the companions to the target star, leading to large offsets in both photometry and astrometry. Instead, these were fitted using the PSF modelling software `DAOPHOT` (Stetson 1987) via the `IRAF` software system (Tody 1986, Tody 1993). This process was not adopted for all targets due to the manual process required (at the time) for each image. The output of the `DAOPHOT` procedure includes the pixel coordinates and instrumental magnitudes of all stars on the image, which was converted to relative photometry and astrometry to match the results of other targets.

3.7.2 2015/2016 reduction

As noted above, the methods of aperture photometry and simple peak finding were not always adequate for objects close to the target star, but additionally are not necessarily reliable for pairs of companions close to one another, of which an increasing number were identified in the 2015 and 2016 data. Furthermore, it was deemed desirable to use a single reduction method for all targets, rather than combining separate methods with potentially different systematic errors. The `DAOPHOT` reduction method was therefore adopted for all stars, following the development of an automated reduction procedure utilising the `PyRAF` software. `DAOPHOT` was provided with an input list of coordinates of the target and companion stars, from which suitable PSF reference objects were automatically selected, and PSF photometry was then performed on all objects. This

process was repeated for all TCI lucky imaging selections from 1% to 90%, using both the Red and Vis camera data.

The DAOPHOT output data did not necessarily contain results for each input star. Some companions would be rejected automatically by DAOPHOT when they were too faint to detect using a low fraction of the lucky imaging exposures, whilst others would become indistinguishable from nearby brighter stars when using a large fraction of the lucky imaging exposures. For each star, the lucky imaging selection with the smallest photometric uncertainty was chosen, having excluded those with undetermined photometric/astrometric uncertainties, indicating an error in the fitting process.

3.7.3 Colour-flux ratio-distance comparison

Provided that the measured colour of a companion was within the range of the calibration in Table 3.1, the temperature of the companion could then be determined. The flux ratio of the companion to the target star was then compared to the flux ratio predicted from Table 3.1 for two equidistant stars with the corresponding temperatures, with the target star's temperature being adopted from TEPCat. For example, a cooler, less massive binary companion is expected to appear fainter than the planet host star, whilst a hotter companion star would be brighter, under the assumption that none of the stars have evolved significantly. By comparing the observed flux ratio to that expected for the equidistant stars hypothesis, and taking into account the uncertainty on the photometric measurements, the probability that the observed companion star is equidistant (and hence a plausible binary companion) was computed. This was performed separately for v_{TCI} and r_{TCI} flux ratios, though the results for each were often in good agreement. Companion stars with photometric distances consistent with the planet host stars were selected for further investigation, including a search for archival photometry or proper motion measurements further supporting the hypothesis that the two stars form a wide binary system.

4 Results of the lucky imaging survey

This chapter describes the results of the companion search described in Chapter 3, covering in particular those stars which were suspected of being bound binary companions to the targeted exoplanet host stars. The full photometric and astrometric results tables are not included in this thesis due to their length, and instead have been made available in digital format at the Strasbourg Astronomical Data Centre (CDS). These catalogues also contain digital versions of the observing logs, as well as the distances estimated through the K-band surface brightness–temperature relation. The 2014 results are stored in catalogue `J/A+A/589/A58`, available at:
`http://cdsarc.u-strasbg.fr/viz-bin/qcat?J/A+A/589/A58`
The 2015 and 2016 results are in catalogue `J/A+A/610/A20`, available at:
`http://cdsarc.u-strasbg.fr/viz-bin/qcat?J/A+A/610/A20`

Table 4.1 contains those companion stars which have been found to be probable bound companions. After describing the initial selection of companions for further study (Section 4.1, and the literature search and analysis of catalogue data available for those companions (Section 4.2), this chapter then discusses the plausible bound companions listed in Table 4.1, as well as those companions for which evidence against physical association was found (Section 4.3). The discovery of archival astrometry suggesting measurable orbital motion for some exoplanet-hosting binaries led to a detailed investigation of the orbits of these systems, which is detailed in Section 4.4, with a discussion of the results for the successful fits to WASP-77AB and WASP-85AB. Finally, Section 4.5 considers the results of this survey in the context of other, similar works, and the properties of the discovered companions.

4.1 Selection of targets for follow-up

The TCI has a much larger field of view than many similar surveys, resulting in a vast number of companion stars being detected, with 499 from the 2014 data, 317 from the

Table 4.1: Probable bound companions to exoplanet host stars found by lucky imaging over the three years (2014-2016) of the TCI lucky imaging survey. The properties given below are from the most recent observation, with the exception of HAT-P-35 companion 1, where the 2014 results are adopted. The 'ID' column indicates the unified companion ID used throughout this work. The 'Gaia' column indicates supporting evidence from the Gaia DR2 catalogue, with the codes being defined as follows: **C** - common proper motion; **D** - common distance (parallax); **I** - inconsistent astrometry. The reasons for retaining each of the 'inconsistent' companions are given in the text; in general, these systems either have underestimated uncertainties, have very faint companions, or have companions that appear to themselves be binaries.

					Obs. Years				
Target	ID	Separation (″)	Pos. Angle (°)	$\Delta r_{\,TCI}$ (mag.)	'14	'15	'16	Gaia	Notes
CoRoT-02	1	4.0691 ± 0.0012	208.61 ± 0.07	3.73 ± 0.06	X		X	C	
CoRoT-09	4	11.960 ± 0.040	47.1 ± 0.2	3.92 ± 0.06	X			CD	
CoRoT-11	1	2.537 ± 0.009	307.0 ± 0.2	1.99 ± 0.06	X			I	
CoRoT-19	1	13.942 ± 0.049	233.4 ± 0.2	6.92 ± 0.39	X				
CoRoT-20	1	6.460 ± 0.020	76.9 ± 0.2	5.70 ± 0.30	X				
HAT-P-30	1	3.8544 ± 0.0018	3.94 ± 0.07	5.42 ± 0.07	X	X	X	CD	
HAT-P-35	1	1.016 ± 0.011	149.4 ± 0.2	3.81 ± 0.13	X		X		
HAT-P-35	2	9.0198 ± 0.0016	214.44 ± 0.07	5.95 ± 0.07	X	X	X	CD	
HAT-P-41	1	3.6053 ± 0.0016	184.10 ± 0.07	3.96 ± 0.06	X	X	X	CD	
HATS-10	2	11.6121 ± 0.2067	140.41 ± 0.82	9.71 ± 0.30		X			
HATS-10	6	20.7614 ± 0.3053	237.95 ± 0.92	9.21 ± 0.21		X			
HATS-14	1	7.7518 ± 0.0583	86.50 ± 0.30	8.42 ± 0.35			X		
K2-02	1	8.3969 ± 0.0600	236.19 ± 0.87	6.89 ± 0.13			X	CD	White dwarf
K2-27	1	2.8836 ± 0.0179	177.54 ± 0.10	6.97 ± 0.13			X	CD	
K2-31	1	8.4295 ± 0.0363	127.75 ± 0.39	9.49 ± 0.43			X	CD	
KELT-15	1	6.1340 ± 0.0064	283.28 ± 0.08	7.74 ± 0.10			X	CD	

Continued on next page

Target	ID	Separation (″)	Pos. Angle (°)	Δr_{TCI} (mag.)	Obs. Years '14	'15	'16	Gaia	Notes
OGLE-TR-211	12	9.817 ± 0.023	246.4 ± 0.2	5.30 ± 0.15	X			C	Crowded Field
WASP-02	1	0.709 ± 0.010	103.4 ± 0.2	4.94 ± 0.15	X				
WASP-08	1	4.499 ± 0.0064	171.04 ± 0.10	4.78 ± 0.06	X		X	CD	
WASP-24	1	16.6479 ± 0.0380	166.34 ± 0.11	9.57 ± 0.28	X	X	X	CD	Eclipsing binary
WASP-26	1	15.3751 ± 0.0050	143.65 ± 0.07	3.12 ± 0.06	X		X	CD	
WASP-36	1	4.8627 ± 0.0054	66.67 ± 0.07	5.83 ± 0.07	X	X	X	CD	
WASP-45	1	4.3507 ± 0.0553	317.73 ± 0.23	8.21 ± 0.20	X		X	I	
WASP-49	1	2.2128 ± 0.0020	178.56 ± 0.06	6.68 ± 0.14	X		X	CD	
WASP-54	1	5.7065 ± 0.0241	115.68 ± 0.16	10.14 ± 0.24	X	X	X		
WASP-55	1	4.3464 ± 0.0037	163.90 ± 0.07	6.85 ± 0.10	X	X	X	CD	
WASP-66	1	12.9928 ± 0.0201	60.63 ± 0.28	9.83 ± 0.41	X	X	X		
WASP-70	1	3.1723 ± 0.0073	167.87 ± 0.11	2.51 ± 0.06	X		X	CD	
WASP-77	1	3.2702 ± 0.0082	154.03 ± 0.07	1.90 ± 0.05	X	X		CD	
WASP-85	1	1.4548 ± 0.0038	99.60 ± 0.08	1.15 ± 0.11		X	X	C	
WASP-87	4	8.0921 ± 0.0027	141.30 ± 0.06	2.12 ± 0.06		X	X	I	
WASP-94	1	15.0774 ± 0.0018	89.61 ± 0.06	0.38 ± 0.06			X	CD	
WASP-98	1	12.242 ± 0.019	225.2 ± 0.2	7.47 ± 0.13	X			CD	White dwarf
WASP-100	1	3.982 ± 0.012	186.3 ± 0.2	6.15 ± 0.06	X			CD	
WASP-104	1	6.7798 ± 0.0076	176.95 ± 0.12	8.05 ± 0.18		X	X	CD	
WASP-108	4	8.7906 ± 0.0224	41.21 ± 0.14	9.23 ± 0.39		X	X	CD	
WASP-111	1	5.0151 ± 0.0091	100.05 ± 0.14	5.61 ± 0.08		X	X	D	
WASP-121	1	7.6386 ± 0.0351	221.78 ± 0.14	9.62 ± 0.23			X	I	Suspected binary
WASP-123	1	4.7970 ± 0.0030	205.16 ± 0.06	6.77 ± 0.10			X	I	Suspected binary
WASP-133	4	16.6448 ± 0.1819	354.37 ± 0.15	9.78 ± 0.56			X		

2015 data, and 482 from the 2016 data.[1] It was therefore not feasible to perform a detailed search of the literature and archival datasets for information on each detected companion to determine whether or not it is physically associated with the relevant target star.

In the 2014 dataset, photometry was obtained in only a single band for most targets – hence photometric distances could not be determined – and astrometry covered a time period of a few months at best – too short for common proper motion to be measurable. It was therefore not possible to select stars through either photometric distance or common proper motion without archival data, which is difficult to find due to the faintness of many companions and the poor angular resolution of many surveys. Instead, only the closest companion stars, separated by less than 5″ from the target stars, were chosen for follow-up.

As the 2015 and 2016 dataset included two-band photometry for all observations, and photometric distances were determined for most companion stars as detailed in Chapter 3. Therefore, only those companions with distances consistent (i.e. within 2σ) with the distance to the relevant target star were selected for further analysis. An exception to these selection criteria was the white dwarf companion to K2-02, previously discovered by Vanderburg et al. (2015), which did not have a photometric distance determination due to its high temperature. However, even if this companion did have a photometric distance determined, the value would be incorrect due to the assumption that all companion stars are on the main sequence. The data were inspected for evidence of other hot white dwarf companions – very blue, faint objects near to the target stars – but no plausible candidates were identified.

4.2 Archival and literature data

A variety of different measurements can be used to investigate whether two stars form a bound binary. The use of TCI photometry, and hence photometric distances, has

[1]The 2015 and 2016 counts include repeat observations of previously detected companions.

already been discussed in detail in Chapter 3; this technique can also be applied to other photometric data. Proper motion measurements can be used to determine if two stars are moving together across the sky – i.e. they show common proper motion – or instead to show that the two stars are moving in entirely independent directions, and hence are unrelated. Relative astrometry over several years, measuring the separation and position angle between the target star and companion, can also be used to show that a pair of stars exhibit common proper motion. Spectroscopic measurements can provide precise estimates of the atmospheric properties of stars – from which distances can be estimated – or instead can be used to measure the radial velocities of stars – which should be very similar for the components of a wide binary, much like proper motions.

4.2.1 Photometry

Many of the companion stars are either unresolved or too faint to be detected in large photometric catalogues such as 2MASS, APASS, or Tycho-2. However, when such data are available, it provided a useful check of the photometric properties and distances derived from the TCI. In cases where TCI photometry was obtained in one band only, such additional data was necessary to characterise the companion star. A second source of photometry for companion stars are targeted observations in the literature. The 'Friends of Hot Jupiters' (Ngo et al. 2015, Ngo et al. 2016) survey obtained multiband near infrared (NIR) photometry for their detected companions, and derived stellar temperatures and masses from the companion stars using this data. The AstraLux Norte lucky imaging survey (Wöllert et al. 2015, Wöllert & Brandner 2015) obtained dual band photometry for the majority of detected companion stars, although no analysis of this data was presented. Other photometric measurements were also found on a case-by-case basis for companion stars, with some planet discovery or characterisation papers including photometry of companions, and some smaller high resolution imaging surveys covering a handful of targets observed in this work.

4.2.2 Catalogue astrometry

During the course of this PhD, the precision, accuracy, and coverage of proper motion catalogues has significantly improved. Initially, the NOMAD, PPMXL, and UCAC4 catalogues were used for the bulk of proper motion data, although the provenance of the data in these catalogues is not always clear, and in many cases the same archival photographic plates have been used in multiple surveys. Furthermore, these catalogues (in particular NOMAD) contain a relatively high fraction of spurious sources, often caused by incomplete matching of observations from multiple epochs, or confusion caused by diffraction spikes or other optical features. The accuracy of the data are difficult to judge from the quoted uncertainties alone, and in several cases the proper motions for a star would be highly discrepant between the three catalogues.

The ground-based URAT1 catalogue was released after the analysis of the 2014 data was concluded, and provided a new, independent source of astrometry, without any reliance on earlier data, input data for this catalogue being derived from a single instrument. Very few spurious sources were found in the data, and common proper motion was reliably indicated for confirmed wide binaries in the TCI sample. However, in some cases, it appears that the URAT1 proper motions differ systematically from other catalogues. This was discovered through investigations of bright, well-resolved common proper motion pairs, which are consistently shown as moving in one direction in the NOMAD, PPMXL, and UCAC4 catalogues, but are recorded with very different (but still common) proper motions in URAT1; this effect also applies to other nearby stars. For example, in the region of K2-27, the URAT1 motions are systematically offset by approximately +15mas/yr in RA and +12mas/yr in Declination. The URAT1 team has been made aware of this issue and intend to investigate further (N. Zacharias, priv. comm.).

The *Gaia* satellite was launched in late 2013 as the successor to the *Hipparcos* satellite, with the aim of providing proper motions and parallaxes for approximately 1 billion stars. The number of stars for which proper motions are now available is an order of magnitude higher than from ground-based catalogues, and the *Gaia* has so far

determined parallaxes for over 10,000 times as many stars as the *Hipparcos* mission was able to provide. This wealth of data, coupled with the good angular resolution of *Gaia*, will make it an excellent tool for the discovery and characterisation of wide binaries. In the context of this thesis, Data Release 1 (DR1) was released following the analysis of the 2014 data; this initial release did not contain enough data from *Gaia* alone to provide proper motion or parallax measurements, but for brighter stars included in the Tycho catalogue (which consisted of those stars observed by Hipparcos without sufficient data to determine astrometric solutions), the joint Tycho-Gaia Astrometric Solution (TGAS) was presented. The faint limit of the TGAS catalogue is similar to the brightnesses of most TEP host stars, and hence even where the target star itself was included in TGAS, companion stars often were not. However, DR1 did include position measurements for many fainter companions, from which relative separations and position angles could be determined.

At the time of writing, *Gaia* Data Release 2 has very recently been released, and many suspected companions may now be confirmed through analysis of their proper motions, parallaxes, and for the brightest companion stars, even through their radial velocities. The release of Data Release 2 (DR2) post-dates much of the work described in this thesis, but relevant measurements and results are mentioned briefly in the discussions on individual system. The future prospects for finding, confirming, and characterising wide binary companions in DR2 and subsequent data releases are discussed in the Conclusions chapter.

In this thesis, and in most literature sources, the proper motions μ of stars are expressed as separate components aligned to the axes of the equatorial system, right ascension and declination. One notable feature of the equatorial coordinate system is that lines of parallel right ascension become closer together towards the poles, and hence the absolute proper motion does not correspond to the Pythagorean combination of μ_α and μ_δ. Instead, the relation $\mu^2 = \mu_\alpha^2 \cdot \cos^2\delta + \mu_\delta^2$ must be used. To avoid confusion due to this subtlety, it is custom for proper motion catalogues to instead include the value $\mu_{\alpha*} = \mu_\alpha \cdot \cos\delta$; this is the case for all of the astrometric catalogues used in this thesis – Gaia DR1/TGAS, Gaia DR2, NOMAD, PPMXL, UCAC4, and URAT1. Units of

milli-arcseconds per year (mas/yr) are used throughout this thesis, and proper motions will be quoted in vector format, i.e. $\boldsymbol{\mu} = (a \pm \epsilon_{\rm a}, b \pm \epsilon_{\rm b})$ mas/yr, where $\boldsymbol{\mu}_1 = \mu_{\alpha *}$ and $\boldsymbol{\mu}_2 = \mu_\delta$.

Parallaxes from Gaia DR2 are used for a number of objects, with values expressed in units of milli-arcseconds (mas). These measurements are considered in their native form, rather than converting them to distances, avoiding some of the difficulties inherent in interpreting parallaxes and propogating the correlated uncertainties in the astrometric solution (Luri et al. 2018). The vast majority of target stars are sufficiently close and bright that their fractional parallax uncertainties are small, and companion stars with highly uncertain astrometric solutions were not analysed through parallax measurements.

The parallaxes and proper motions quoted from Gaia data releases 1 and 2 do not include the additional systematic uncertainties that are known or suspected to exist within the results. In DR2, systematic uncertainties of up to 0.1 mas in parallax and 0.1 mas/yr in proper motion are thought to exist (Luri et al. 2018). Significant offsets, as determined from the published uncertainties, have been noted in parallax or proper motion for several wide binaries, perhaps caused by underestimated uncertainties in some cases, although the proper motion 'discrepancies' are shown to be consistent with orbital motion in several cases.

4.2.3 Literature astrometry

As with photometry, a number of similar surveys for companions to known TEPs have provided astrometric measurements over recent years. Additionally, companions are occasionally studied in detail during the characterisation of planetary systems, particularly when they are unusually close or bright, although precise astrometry is not always available. With sufficient time coverage, it is possible to determine whether two stars are moving together (and hence their relative positions do not change), or instead that they are slowly drifting apart due to different proper motions. The time coverage needed depends on both the proper motions of the stars, and also the accuracy

of the astrometry – if a binary system has a low proper motion, it is difficult to confirm that the stars are indeed co-moving, especially if data quality is poor.

A number of exoplanets have been discovered in previously known or suspected wide binaries, and astrometric measurements predating the discovery of the exoplanet exists. In this work, the Washington Double Star catalogue (WDS, Mason et al. 2001) was used to search for data outside the exoplanet literature. This catalogue provides a large collection of astrometric (and photometric) data, including references and other pertinent details of each individual measurement, with data extending as far back as the 18th century in some cases. For two wide binaries, WASP-77 and WASP-85, the data in the WDS was found to map out a significant fraction of the orbit, allowing the orbital parameters of these systems to be determined.

4.2.4 Radial velocity measurements

For some wide binaries with stellar components of similar brightness, the initial discovery light curve from surveys such as WASP or HAT did not have sufficient angular resolution to determine which star was the planet host. In some cases, the exoplanet host star was identified by obtaining radial velocity measurements of both stars to determine which star exhibits the radial velocity variation due to the detected transiting planet. These measurements have also usefully shown that the radial velocities of the stars are consistent with bound orbits, and place constraints on the orbital motion of the system, which was combined with the historic astrometry from the WDS for WASP-77 and WASP-85. Such radial velocity measurements can also have other benefits, allowing the discovery of additional non-transiting planets, with the WASP-94AB system having a detected hot Jupiter around both stars (Neveu-VanMalle et al. 2014). Starting with DR2, the *Gaia* mission also provides radial velocity measurements, albeit only for the brightest stars, and with greater uncertainties than planet-hunting spectrographs. As with the DR2 astrometric results, these are briefly mentioned where relevant, but were released after the main part of the analysis in this work.

4.3 Notes on individual systems

The following short sections discuss those companions that were considered to be 'of interest', primarily those which were consistent with binary companions. These notes include any relevant data found in the literature or catalogues, and the implications of those data. These notes closely follow the discussion sections in Evans et al. (2016) and Evans et al. (2018), although a number of results from the first paper are reconsidered in light of additional data from 2015/2016, or the improved TCI calibrations presented in the second paper. Additionally, notes have been added or updated where new insights are available from Gaia DR2 and other recently published results. The majority of suspected binary companions have been confirmed by the precise parallaxes and proper motions in Gaia DR2, while a small number of false positives – mainly luminous background stars masquerading as foreground objects – and false negatives – including white dwarfs and unresolved binaries – have been identified.

4.3.1 CoRoT-2

A binary companion located 4.1″ from CoRoT-2A was initially discovered during CoRoT follow-up observations (Alonso et al. 2008), with subsequent spectroscopic observations confirming the two objects have radial velocities consistent with a bound orbit (Schröter et al. 2011). The companion has subsequently been observed by numerous high resolution imaging surveys (Faedi et al. 2013, Wöllert et al. 2015, Wöllert & Brandner 2015). TCI data were obtained in 2014 (red camera only) and 2016, with its temperature determined to be 3660 ± 90 K and its flux found to be consistent with a bound companion. The TCI photometric temperature is somewhat lower than the 4000 ± 100 K (2σ uncertainty) determined by Schröter et al. (2011) from spectroscopy, but is in good agreement with the Gaia DR2 determination of 3660^{+210}_{-100} K. Gaia DR2 shows common proper motion between the stars, although the determined parallaxes are discrepant at 3σ, with $\pi = 4.66 \pm 0.05$ mas for CoRoT-2 and $\pi = 4.90 \pm 0.06$ mas for the companion. The cause of the parallax discrepancy is unclear.

4.3.2 CoRoT-3

Two relatively bright companions were discovered during initial follow-up work (Deleuil et al. 2008), both located approximately 5″ away, with the brighter located to the south ($\Delta \mathrm{r}_{\mathrm{TCI}} = 2.6\,\mathrm{mag}$) and the fainter to the east ($\Delta \mathrm{r}_{\mathrm{TCI}} = 4.8\,\mathrm{mag}$.). Both have been imaged by high resolution imaging surveys (Faedi et al. 2013, Wöllert & Brandner 2015), and data were obtained with the TCI red camera in 2014. The available photometry was insufficient to determine photometric distances, and difficulty was found in determining whether either companion showed common proper motion, due to the very low proper motion of CoRoT-3 itself. Gaia DR2 includes parallax and proper motion measurements for all three stars, and neither companion is consistent with being physically associated with CoRoT-3. The TCI data revealed three fainter companion stars within 5″ of CoRoT-3, but additional photometry or astrometry is not yet available for these objects.

4.3.3 CoRoT-7

Due to the very small measured radius and mass of CoRoT-7b, and hence the potential faintness of any blended eclipsing binary if the system was a false positive, near infrared AO observations were obtained by the CoRoT team to confirm the nature of the system. Three faint stars were detected, all with separations of approximately 5″ and approximately 8 mag fainter in the J band (Léger et al. 2009). All three were detected in single band TCI data in 2014, approximately 9 mag fainter than CoRoT-7 in $\mathrm{r}_{\mathrm{TCI}}$, and two-band photometry was obtained in 2016. In 2014, it was concluded that all three were too faint to be bound stellar objects. For two companions, two-colour photometry was obtained in 2016, revealing that neither was consistent with a bound object. One of these companions has a full astrometric solution in Gaia DR2, but the parallax and proper motion are too uncertain to constrain its nature.

4.3.4 CoRoT-8

Two-colour photometry was obtained of CoRoT-8 in 2014, although temperatures and photometric distances could only be derived for one of the three stars within 5″ due to the faintness of these stars. For companion 3, it was concluded that the companion was an unassociated background star, and Gaia DR2 parallaxes and proper motions support this conclusion.

4.3.5 CoRoT-9

CoRoT-9 was observed in r_{TCI} only in 2014, with no companions being sufficiently close to be deemed of interest. However, examination of the Gaia DR2 results reveal that companion 4, located 12″ to the northeast and 3.9 mag fainter in r_{TCI}, exhibits common proper motion and has a parallax consistent with that of CoRoT-9. Based on the magnitude difference measured from the TCI red camera, an effective temperature of 5613K for CoRoT-9 (Mortier et al. 2013), and the TCI colour-flux-temperature calibration, the companion has an effective temperature of approximately 3500K if it is a main sequence object.

4.3.6 CoRoT-11

A companion star exists 2″ from CoRoT-11, approximately 2 mag fainter in the optical. Due to its brightness, on-off photometry was obtained for this star during the initial characterisation of the system to determine whether it or CoRoT-11 were the source of the planetary signal. Following the confirmation that CoRoT-11 was the planet host, the companion star was not analysed in any further detail (Gandolfi et al. 2010). Observations have since been obtained with the AstraLux Norte lucky imager (Wöllert et al. 2015, Wöllert & Brandner 2015) and with the TCI red camera in 2014. Based on proper motion measurements of CoRoT-11 recorded in the NOMAD, PPMXL, and UCAC4 catalogues, it was expected that changes in separation and position angle

would be detectable if the companion was stationary on the sky. No such change was seen, although the expected change was uncertain due to the highly discrepant proper motions between the three named catalogues.

Gaia DR2 shows similar but discrepant values for the parallaxes and proper motions of these two stars, with parallax measurements of $\pi = 1.50 \pm 0.06$ mas for CoRoT-11 and $\pi = 1.07 \pm 0.09$ mas for the companion, and proper motions of $\boldsymbol{\mu} = (1.92 \pm 0.07, -5.24 \pm 0.08)$ mas/yr for CoRoT-11 and $\boldsymbol{\mu} = (2.53 \pm 0.11, -5.10 \pm 0.12)$ mas/yr for the companion. However, the companion's astrometry has a poor fit, with an astrometric goodness-of-fit statistic[2] of 14.5. Interestingly, a third, fainter star at $4''$, denoted companion 3, also has a similar proper motion to these stars, with $\boldsymbol{\mu} = (2.70 \pm 1.25, -6.28 \pm 1.48)$ mas/yr, suggesting that the CoRoT-11 system contains at least three stars. However, the parallax determination for companion 3 is very uncertain, and caution is advisable in interpreting the results for this potential third component.

4.3.7 CoRoT-18

Companions 2, 3, and 5 to CoRoT-18 were found to have consistent photometric distances in 2014. All three are included in Gaia DR2, and while the uncertainties on all are relatively high, none appear to have a common parallax or proper motion with CoRoT-18.

4.3.8 CoRoT-19

The closer of the two companions to CoRoT-19 detected in 2014 was found to have a consistent photometric distance. It is too faint to be included in Gaia DR2, and no further data has been located.

[2]The Goodness of Fit is designed to be normally distributed with mean zero and standard deviation 1. Values greater than three or so indicate poor astrometric solutions.

4.3.9 CoRoT-20

Two of the five companion stars were found to have consistent photometric distances from two colour photometry in 2014. Gaia DR2 indicates that companion 3 is not physically associated; the fainter companion 1 is not included in the catalogue.

4.3.10 CoRoT-22

As with CoRoT-7, near infrared AO observations were obtained to rule out faint contaminating sources due to the small size of CoRoT-22b, with the closest star detected being 3″ north (Moutou et al. 2014). Two-band photometry was obtained with the TCI in 2015, with the photometry ruling out this closest companion as a bound object, but many other stars in the crowded field were found to be at least marginally consistent with bound objects. Companion 8, located 8.4″ to the west, was noted as having a photometric distance differing from CoRoT-22 by only 0.2σ. Gaia DR2 gives a parallax of $\pi = 1.57 \pm 0.03$ mas for CoRoT-22 but a much smaller value of $\pi = 0.56 \pm 0.19$ mas for the companion, in addition to a significantly different proper motion, indicating that the companion is a luminous background star.

4.3.11 CoRoT-24

Two band TCI photometry was obtained in 2016, with a number of well separated stars being observed. Most were found to have photometric distances that are discrepant with the distance to CoRoT-24 at the 3σ level, although the closest companion differed by only 0.9σ. The Gaia DR2 astrometry for these companion stars is too uncertain to draw any meaningful conclusions from; whilst the parallax measured for companion 5 ($\pi = 1.65 \pm 0.82$ mas) is very similar to that of CoRoT-24 ($\pi = 1.66 \pm 0.04$ mas), the parallax value differs from zero at only 2σ, and the TCI photometric distance is discrepant at 3σ for this companion.

4.3.12 CoRoT-28

Photometry was obtained in 2015, with only a single companion, number 37, having a distance consistent with CoRoT-28. However, all available proper motion measurements for the pair showed that they did not exhibit common proper motion. Gaia DR2 includes a temperature determination of 4000^{+500}_{-240}K from photometry, consistent with the TCI measurement of 4030 ± 140K. However, the companion's parallax of $\pi = 0.14 \pm 0.04$ mas corresponds to a distance of several thousand parsecs, much more distant than CoRoT-28 with $\pi = 1.28 \pm 0.02$ mas, and hence this companion is an unassociated high luminosity background star. This case clearly illustrates that photometric distances alone are not sufficient to confirm a binary star system.

4.3.13 HAT-P-30

A bright companion to HAT-P-30 was discovered during follow-up observations (Enoch et al. 2011), with several subsequent AO observations (Adams et al. 2013, Ginski et al. 2013, Ngo et al. 2015). Despite the flux ratio of the stars being consistent with a bound binary, Ginski et al. (2013) found that the stars did not exhibit common proper motion. This conclusion was refuted by later reanalyses, both by Ngo et al. (2015) and in the 2014 TCI paper, which found that the stars did show common proper motion. TCI photometry was obtained in all three years, with the two-colour photometry from 2015 and 2016 giving matching photometric distances for the two stars. Gaia DR2 also supports the conclusion that the stars are a bound system, with consistent parallaxes and similar proper motions.

During the analysis of the 2014 data, it was noted that the WDS contained an entry for a faint 'C' component to the system, located 10″ to the northeast. At this point, only a single TCI photometric band was available, and the star was instead characterised by its 2MASS J−H photometry. These data indicated that the companion is an A- or F-type star, based on the Straižys & Lazauskaitė (2009) calibration, and hence the object is much to faint to be a bound main sequence star. An alternative

hypothesis that was examined was that the companion was a hot, but faint, white dwarf companion. The synthetic white dwarf photometry from Althaus et al. (2007) was used to evaluate this, with the TCI red camera photometry assumed to be similar to I-band photometry. Based on the 2MASS J − H colour, the companion was found to be too bright in all three photometric bands (I, J, and H) for a bound white dwarf companion.

Two-colour photometry from the 2015 and 2016 observations supported the previous results, with a derived temperature of 5700 ± 500K, and discrepant proper motions in the newly released URAT1 catalogue. Gaia DR2 confirms that the star is a distant background object with very low proper motion, compared to the 30 mas/yr motion of HAT-P-30.

4.3.14 HAT-P-35

A companion only 0.93″ from HAT-P-35 was discovered through lucky imaging by Wöllert & Brandner (2015), and subsequently reobserved with AO by Ngo et al. (2016), who found the companion to show common proper motion. The system was observed with the TCI in all three years, but the companion was poorly resolved in all three datasets, and good astrometry was not obtained. However, the 2015 data was sufficient to derive a photometric temperature of 3730 ± 180 K, similar to the value of approximately 3550 K derived by Ngo et al. (2016).

A second companion at 9″ was also observed, and also found to have a consistent photometric distance with HAT-P-35. Further photometry was available in the SDSS and 2MASS surveys, which was combined with the BT-Settl models (Allard, Homeier & Freytag 2012) and the estimated age and distance of HAT-P-35A from Bakos et al. (2012), and the companion was again found to have a consistent distance. TCI, 2MASS, and Gaia DR1 astrometry indicated no change in relative position over a 16-year period. The companion was therefore tentatively considered as a teritary stellar component in the system; whilst a few planet-hosting triple systems are known, the 'B' and 'C' components almost always form tight binary orbiting the 'A' at much greater distance.

Denoting the 0.9″ star as 'B' and the 9″star as 'C', Gaia DR2 includes good astrometry for the A and C components, whilst the data for the B component was rejected as a duplicate detection of A. The A and C components clearly exhibit common proper motion and have consistent parallaxes, further supporting the conclusion that HAT-P-35 is a triple stellar system.

4.3.15 HAT-P-41

A close companion was noted during the initial characterisation of the HAT-P-41 system (Hartman et al. 2012). Located 3.5″ from the planet host star, the companion has been imaged by several surveys, including the AstraLux survey (Wöllert et al. 2015, Wöllert & Brandner 2015), the Friends of Hot Jupiters survey (Ngo et al. 2016), and the TCI in 2014, 2015, and 2016. The analysis of the two band TCI imaging supports the two stars being equidistant, matching the conclusion of Ngo et al. (2016), although their proper motion analysis was not conclusive. Gaia DR2 confirms that the two stars exhibit common proper motion and have consistent parallaxes.

In the 2014 results, an optical ghost in the TCI data was sufficiently distant from HAT-P-41 to be incorrectly classed as a true companion – see Section 3.6.3 for further details on the optical ghosts present in the TCI data. It was realised that this was not a true companion when analysing the subsequent 2015 and 2016 data, in conjunction with the lack of any detection in the higher resolution AO data presented in Ngo et al. (2016).

4.3.16 HAT-P-45

Two band photometry obtained for HAT-P-45 in 2015 indicated a number of potential companion stars, based on consistent photometric distances. However, in such a crowded field, it was considered likely that most of these would be spurious chance alignments, either with foreground stars at similar distances to HAT-P-45, or with

distant background red giants. Of those stars with successful astrometric fits in Gaia DR2, none are consistent with being physically associated companions.

4.3.17 HATS-1

Two potential companions were identified observations taken in 2014 and 2015, with a closer, faint companion at 6″ having poor photometry due to falling on a diffraction spike, and a more distant companion at 12″ having a photometric distance marginally consistent (1.6σ) with being physically associated. Gaia DR2 shows that the more distant companion is more distant with a significantly different proper motion.

A much more distant common proper motion companion was claimed by Mugrauer, Ginski & Seeliger (2014), at a separation of 229″, based on the UCAC4 catalogue proper motions and 2MASS photometry. Based on the data in Gaia DR2, these stars do not appear to have any physical association. While the two stars have similar proper motions and parallaxes, the values of these parameters differ by much more than the very small uncertainties on such bright stars.

4.3.18 HATS-2

A close companion at 1.1″ was noted in all three years. However, despite this small separation, the photometric distance of the companion is inconsistent with HATS-1 at 4σ. Given the high (46 mas/yr) proper motion of HATS-2, a drift in relative astrometry should be noticeable in future data.

4.3.19 HATS-10

Two companions were identified as having consistent photometric distances. No further supporting data are yet available, with neither having parallaxes or proper motions in Gaia DR2.

4.3.20 HATS-11

As with HAT-P-45, several stars in the crowded field around HATS-11 have consistent photometric distances. None of those included in Gaia DR2 match the parallax or proper motion of HATS-11.

4.3.21 HATS-12

Four stars were found to have photometric distances consistent within 2σ of HATS-12. All four are included in Gaia DR2, and have parallaxes and proper motions inconsistent with HATS-11.

4.3.22 HATS-14

Two-band photometry from 2016 included a companion at $8''$ with a photometric distance consistent (1.1σ) with HATS-14. Due to the faintness of this companion, there is not yet sufficient data to confirm the hypothesis that it is physically associated.

4.3.23 HATS-26

This planetary system is one of several for which a background galaxy was detected in the TCI data, which in this case appears to be an edge-on spiral galaxy. This example is notable due to the small angular separation between the galaxy and the target star, with the disc of the galaxy passing within $2''$ of HATS-26, and hence is close enough to potentially cause contamination, although the galaxy's extended emission is much fainter than HATS-26 itself.

4.3.24 HATS-27

Observed in 2016, the relatively bright companion 5 was identified as having a photometric distance marginally consistent (1.9σ) with that of HATS-27. However, ad-

ditional photometry available in the APASS and 2MASS catalogues indicate that the companion is a mid-K spectral type, whilst HATS-27 is a mid-F dwarf. From these estimates, the companion should appear 3 mag fainter in the V band, compared to the much smaller difference of 0.90 ± 0.06 mag recorded in the APASS catalogue. Proper motion catalogues available at the time of the 2016 data analysis did not give consistent results for the proper motions of either HATS-27 or companion 5, but none indicated common proper motion. The Gaia DR2 data show that the two stars have inconsistent parallaxes, proper motions, and radial velocities.

4.3.25 K2-02 (HIP 116454/EPIC 60021410)

A faint common proper motion companion to this system was discovered by Vanderburg et al. (2015); due to the very high proper motion of K2-02 (299 mas/yr), common proper motion alone is sufficient to conclude that this companion is physically associated. Unusually for a bound companion, the fainter star is much bluer than the planet host star, indicating that it is in fact a hot white dwarf. This conclusion is supported by the two band TCI photometry obtained in 2016, which gives a temperature of 7300 ± 200K, compared to 5089 ± 50K for the planet host star (Vanderburg et al. 2015). Unsurprisingly, Gaia DR2 astrometry supports the conclusion that two objects forming a bound system.

4.3.26 K2-21 (EPIC 206011691)

Two band photometry was obtained in 2016, with a faint companion detected at $3''$ in the red camera data only. The detection limits for the vis camera data did not place any useful constraints on the properties of the companion. However, it was noted that the companion was not mentioned by Petigura et al. (2015), who presented K band AO observations of the system. While the detection limit data presented in Petigura et al. (2015) extended out to $2''$ only, it was confirmed that the companion was within the field of view of the data, and was not detectable (D. Ciardi, priv. comm.), and hence

the companion must be at least 7.5 mag fainter in the K band. Assuming the TCI red camera passband is similar to the Cousins I band, a limit of $I_c - K < 2.5$ mag was placed on the companion's colour, based on the Baraffe et al. (2015) isochrones and an assumed $I_c - K$ colour of 1.8 mag for the primary, determined from the isochrones for a star with $T_{eff} = 4043 \pm 375$ K (Petigura et al. 2015). The colour constraint for the companion corresponds to a temperature of 3000 K or higher, and hence it is too faint to be physically associated with K2-21.

4.3.27 K2-27 (EPIC 201546283)

A companion 3″ from K2-27 was detected through AO imaging during the initial followup of the system, with the companion being 3.7 mag fainter in the K band (Montet et al. 2015; B. Montet, priv. comm.). Two band TCI photometry in 2016 resulted in a photometric temperature determination of 3150 ± 80 K and a photometric distance consistent with K2-27. The K band magnitude difference was also found to be consistent with these conclusions, based on the Baraffe et al. (2015) isochrones and a temperature of 5248 ± 60K for K2-27 (Van Eylen et al. 2016).

During the analysis of this companion and the inspection of archival imagery, a star of similar brightness and colour to K2-27 was noted approximately 30″ to the west. Despite being outside the TCI field of view, this star was further investigated, and the PPMXL, NOMAD1, UCAC4, and URAT1 catalogues all show proper motions that are consistent at the 2σ level or better, although the actual direction of motion differed significantly between these catalogues. Catalogue photometry for these two bright stars was found in several catalogues, which was used to determine the temperatures and distances of the two stars by fitting the photometry to ATLAS9 model atmospheres (Castelli & Kurucz 2004). The stellar $\log g$ values were both fixed as 4.5, and no correction was made for extinction, reddening, or the contribution of the closer companion at 3″. Photometry was adopted from: GALEX – near UV (Bianchi et al. 2012); APASS – B, V, r, and i (Henden et al. 2016); 2MASS – J, H, and Ks (Skrutskie et al. 2006); and WISE – W1 and W2 (Cutri & et al. 2012). Temperatures of 5250 ± 130 K and

5880 ± 140 K were found for K2-27 and the 30″ companion respectively, with consistent distances of 236 ± 19 pc and 220 ± 15 pc for the two components.

Gaia DR2 gives consistent parallaxes and proper motions for K2-27 and the 30″ companion. Based on the quoted uncertainties, the astrometry for the 3″ companion is inconsistent at the 2σ level. However, the fractional difference in the proper motion values is small, and hence it seems likely that the companion is indeed physically associated, and that the Gaia astrometry for this close, faint companion is affected by contaminating light from K2-27.

4.3.28 K2-31 (EPIC 204129699)

TCI observations in 2016 revealed a single companion at 8″, with a photometric distance consistent with K2-31. Whilst not included in proper motion catalogues, positional data for the companion was found in the 2MASS and Gaia DR1 catalogues. Separations were measured from these positions, with 8.19 ± 0.09″ from 2MASS observations dated 1999-04-28, and 8.404 ± 0.011″ from Gaia DR1 observations with a mean epoch of 2015-01-01, giving a separation change of 13 ± 6 mas per year. This rate was also found to be consistent with the change from Gaia DR1 to the TCI observations of 26 mas, although this is within the position uncertainty on the TCI data. From these results, it was therefore concluded that the companion was physically unassociated.

The astrometric solution in Gaia DR2 refutes this earlier conclusion, showing common proper motion and parallaxes that are consistent at 1.3σ, with a separation of 8.4015 ± 0.0003″ at 2015-06-01. It therefore appears that the stellar positions recorded in 2MASS were offset, and that caution should be applied when using 2MASS astrometry to determine the motions of faint companion stars. Gaia DR2 also includes an additional source at a separation of 6.23″, located between K2-31 and the companion detected in the TCI data. A full astrometric solution was not derived for this companion, but photometry is available, showing it to be 1.75 ± 0.02 mag fainter in the Gaia G band than the companion detected in the TCI. This would correspond to a TCI red camera magnitude difference of approximately 9.6 mag, very close to the quoted

detection limit of 9.7 mag. With prior knowledge of the position of this star, it is just discernible on visual inspection of the full combination of all red camera exposures.

4.3.29 K2-38 (EPIC 204221263)

The closest detected companion to this star was marginally consistent with being physically associated (1.4σ). However, Gaia DR2 shows it as being a distant background object, with parallax and proper motion inconsistent with K2-38.

4.3.30 KELT-15

A cool, faint companion located $6''$ from KELT-15 was detected in 2016, with the companion's photometric distance consistent with that of KELT-15 at 0.8σ. Gaia DR2 finds the stars to have consistent parallaxes and proper motions.

4.3.31 OGLE-TR-211

Single band photometry was obtained in 2014, and hence no companion stars could be confirmed as being physically associated. However, Gaia DR2 astrometry suggests that companion 12, located $9.9''$ away at a position angle of 246°, may be a binary companion, with consistent – but uncertain – proper motions compared to OGLE-TR-211. However, given the very crowded field in which OGLE-TR-211 resides, further data are required before these two stars can confidently be classed as a binary.

4.3.32 WASP-2

AO imaging was obtained during the initial follow-up of the WASP-2 system, revealing a companion star at $0.7''$, 2.7 mag fainter in the H band (Collier Cameron et al. 2007). Due to the length of time since the discovery of the WASP-2 system, the companion has been imaged many times subsequently, with lucky imaging observations by Daemgen

et al. (2009), Bergfors et al. (2013), and Wöllert et al. (2015), with NIR AO observations by Adams et al. (2013) and Ngo et al. (2015). Common proper motion was preferred in separate analyses by Bergfors et al. (2013) and Wöllert et al. (2015).

Observations were obtained with the TCI red camera in 2014. It was noted at the time that the TCI astrometry, in conjunction with previous measures, showed the separation of the two stars reducing over time, at a rate of approximately 7 mas per year. This corresponds to a transverse motion of approximately 1.1au per year at WASP-2's distance of 140pc (Collier Cameron et al. 2007), which was compared to the expected orbital motion of an edge-on binary with an orbital separation a of approximately 100au, the projected separation of the two stars. The expected period P of the system was then determined through Kepler's third law,

$$P^2 = \frac{4\pi^2 a^3}{G(M_1 + M_2)}, \tag{4.1}$$

where G is the gravitational constant, and M_1 and M_2 are the masses of the two stars in the system. Values for the masses were adopted from Southworth (2012) (primary) and Ngo et al. (2015) (secondary), giving $M_1 = 0.85\mathrm{M}_\odot$ and $M_2 = 0.39\mathrm{M}_\odot$; with these parameters, the expected period of the binary is 898 years. Assuming a circular orbit – and hence that the orbital velocity is constant – the rate of motion is simply given by the circumference of the orbit divided by the period, and is 0.7 au/year. This is of the same order of magnitude as the observed relative motion, and the higher observed velocity may be explained by an eccentric orbit, an underestimate for the total mass for the system, or an overestimate of the apparent motion due to uncertainties or calibration errors in some astrometry.

Given the relatively short orbital period predicted in the previous paragraph, and the fast motion observed, continued precise astrometry of the system may allow the orbit of the system to be determined in the next few years. Results from Gaia may be of assistance, with the mission being sensitive enough to measure the difference in proper motions between the two stars; however, in Gaia DR2, the data for WASP-2B were discarded as a duplicate detection of WASP-2A.

4.3.33 WASP-8

The WASP-8 system was recorded in the WDS as a double star before the discovery of the planet around WASP-8A, with measurements of the binary dating back to 1930. AO observations obtained by Ngo et al. (2015) and TCI photometry taken in both 2014 and 2016 indicate that the two stars have consistent photometric distances, and no detectable change in separation or position angle. Gaia DR2 results support the conclusion that the two stars forming a bound system.

In the analysis of the 2014 data, it was noted that the temperature derived from TCI photometry for WASP-8A was significantly higher than the spectroscopic determination presented in Queloz et al. (2010), whilst the determination for the B component agreed with previous values, with the cause being unknown – a contaminating star nearer to WASP-8A that was bright enough to offset the photometry was deemed unlikely, given the null detection by Ngo et al. (2015). This issue was resolved by the improved photometric calibration that was produced during the analysis of the 2015 and 2016 observations.

4.3.34 WASP-19

Two companions, both at approximately $17''$ have photometric distances consistent with WASP-19 in both 2015 and 2016. With WASP-19's high proper motion, Gaia DR2 clearly shows that these companion stars are not physically associated.

4.3.35 WASP-24

Observations were obtained of WASP-24 in all three years of the TCI survey, and in 2016 the pointing of the observations allowed a relatively bright companion located $22''$ away to be detected. The photometric distance of this star was found to be inconsistent with that of WASP-24 at 2.2σ, with the companion appearing too bright, and hence the star was not considered in further detail. However, the Gaia DR2 data clearly show

that the two stars have consistent parallaxes and proper motions, calling into question the accuracy of the TCI photometric distance determination.

The solution to the discrepancy between the TCI and Gaia DR2 results is that the companion is not a single star, but two – the TCI analysis explicitly assumes that all companion objects are single stars. The binary nature of the companion was revealed during the initial follow-up of the system by Street et al. (2010), who discovered that the companion exhibits deep eclipses. The period of the eclipsing binary was not uniquely determined, due to the lack of good phase coverage, but periods of 1.156 days or 2.312 days were suggested. Further light curve data on the EB was presented in Southworth et al. (2014). However, the companion was not analysed in any further detail in either Street et al. (2010) or Southworth et al. (2014), and its nature as a bound component of the system remained unknown.

4.3.36 WASP-26

Smalley et al. (2010) presented an analysis of a companion star at 15″, with a comprehensive consideration of archival images and catalogue photometry. It was noted that no significant change in separation or position angle had occurred since images obtained by the POSS-I survey in the 1950s, and visible and NIR photometry indicated a consistent distance for the two stars, and hence it was concluded that the two stars are physically associated. The TCI data support this conclusion, as does Gaia DR2.

4.3.37 WASP-31

While no physically associated companions were identified in TCI observations from 2014 and 2015, Gaia DR2 results reveal a binary companion 34.6″ away (DR2 source ID 3545873567346193920), well outside the TCI field of view. The companion is located to the south, and is approximately 3.5 mag fainter in the Gaia G band.

4.3.38 WASP-35

Two colour photometry in 2014 indicated that companion 2, located 20″to the west, had a consistent photometric distance. Gaia DR2 shows the star to be significantly more distant than WASP-35.

4.3.39 WASP-36

A companion at 4″ was noted during the initial follow-up of the system (Smith et al. 2012), and subsequently observed with lucky imaging (Wöllert & Brandner 2015). These brightness measurements presented in these two papers disagree significantly, with Smith et al. (2012) measuring a magnitude difference of 4.8 mag with a Gunn r filter, while Wöllert & Brandner (2015) reported the companion to be much dimmer, approximately 8.5 mag fainter in the i' band, with the measurement marked as being highly uncertain. The TCI photometry obtained in all three years is in agreement with the initial results of Smith et al. (2012), with the 2016 data giving a magnitude difference of 4.55 ± 0.04 mag in the red camera passband. It is unclear why the photometry in Wöllert & Brandner (2015) indicated the star was so much fainter; the astrometry presented in that work agrees with other measurements, and hence it does seem the correct star was identified.

Smith et al. (2012) investigated the proper motion of the 4″ companion, in addition to three more distant companions; it was concluded that none of the companions were consistent with being physically associated. However, ground-based proper motion catalogues give highly discrepant proper motions for the three more distant stars, and for the 4″ companion, no proper motion measurements could be located at all in the catalogues available at the time of the Smith et al. (2012) analysis. The TCI data resulted in consistent photometric distances both the 4″ companion and a more distant one at 13″, but confirmation of common proper motion for either star was not possible. The Gaia DR2 results show that the 4″ companion has consistent parallax and proper motion measurements (at the 2σ level). The 13″ companion has a similar parallax but

a very different proper motion, indicating that it is an unassociated foreground star.

4.3.40 WASP-45

A companion at 4.4″ was observed in 2014 and 2016, with its photometric distance found to be consistent with that of WASP-45 in the 2016 analysis. At that time, the Tycho-Gaia Astrometric Solution gave a precise proper motion for WASP-45, but did not include the companion. However, it was noted that if the companion was a background star with negligible motion, WASP-45's high proper motion of 70 mas/yr should have resulted in a measurable change in separation or position angle between the two observations; the measured differences of $-0.013 \pm 0.058''$ in separation and $0.03 \pm 0.30°$ indicated that the stars very likely showed common proper motion. The Gaia DR2 astrometric solution for the companion is poorly constrained, but even with the large uncertainties quoted for the companion, the parallaxes and proper motions for the two stars are inconsistent; however, the relative differences between the values are small, with both stars having a proper motion of approximately 70 mas/yr, and hence appear to form a true binary system.

4.3.41 WASP-49

Lendl et al. (2016) resolved a companion at 2.2″, obtaining spectrophotometric measurements of the companion from observations of three planetary transits. The companion was characterised only as being 'redder'. From TCI photometry in 2016, the companion's photometric distance was found to be consistent with WASP-49 at the 1.2σ level, the companion being slightly brighter than expected. The astrometric data were analysed for evidence of common proper motion, and while a trends of increasing separation and position angle were found, the results were not conclusive. Gaia DR2 results show that the two stars have consistent parallaxes and exhibit common proper motion. Unusually, the Gaia temperature estimate is in significant disagreement with the TCI, with the Gaia estimate of 5100^{+1800}_{-800} K being significantly higher than the

TCI measurement of 3220 ± 90 K. However, the Gaia blue photometer measurement of BP $= 15.90 \pm 0.19$ is highly uncertain, with error bars of this size more typical of stars fainter than 20th magnitude, suggesting that the photometry and temperature estimate are not to be trusted.

4.3.42 WASP-54

A star located 5.7″ from WASP-54 was observed in all three years of the TCI survey, with two band photometry in 2015 and 2016 giving a photometric distance consistent with WASP-54. However, common proper motion could not be confirmed from these data. While the star is resolved in Gaia DR2, it does not have a full astrometric solution.

4.3.43 WASP-55

Similar to the companion to WASP-54, a nearby companion was found 4.3″ from WASP-55, with a consistent photometric distance but no confirmation of common proper motion. Gaia DR2 shows the stars have consistent parallaxes and proper motions.

4.3.44 WASP-64

Imaged in 2014 with the red camera only, Gaia DR2 shows that neither of the two detected companions are physically associated. Visible just at the eastern edge of the TCI field of view was an additional star, close to companion 2, for which astrometry and photometry could not be derived; Gaia DR2 shows this companion, 24″ from WASP-64, to have a consistent parallax and proper motion.

4.3.45 WASP-66

A star located 13″to the northeast was found to have a consistent photometric distance in 2015 (1.2σ), but with a 2016 reobservation disagreeing, with a 2.2σ inconsistency. Approximately 8.7 mag. fainter than WASP-66 in r_{TCI}, star is too faint to be included in Gaia DR2 or other astrometric or photometric catalogues.

4.3.46 WASP-68

Companion 2 to WASP-68, located 21″ to the south, was found to have a consistent photometric distance from observations in 2015 and 2016. The star is included in Gaia DR2, which supports the conclusion that the stars are at the same distance, but with completely independent proper motions, and hence are simply passing near to one another along the line of sight.

4.3.47 WASP-70

The WASP-70 system consists of a hot Jupiter orbiting the brighter A component, with the B component being located 3.3″ away to the southeast. Anderson et al. (2014b) obtained radial velocity measurements of both stars in order to determine the planet host star, with the data also confirming that the two stars have radial velocities consistent with a bound orbit. In addition to TCI observations in 2014 and 2016, the system was also observed by Wöllert & Brandner (2015) in 2014. The photometric distances of the stars were found to be consistent, and common proper motion was confirmed in the 2014 analysis, given the system's high proper motion of 54 mas/yr.

4.3.48 WASP-77

This system was recorded as a double star in the WDS before the discovery of the planet around WASP-77A, with measurements dating back to 1903. Given the long

timespan of the observations without any significant change in relative separation, and the high proper motion of the system (94 mas/yr), the two stars clearly exhibit common proper motion. In addition to TCI observations in 2014 and 2015, Wöllert & Brandner (2015) presented measurements from 2014. Two band photometry gives consistent photometric distances for the two stars, and consistent radial velocities were found in Maxted et al. (2013). The Gaia DR2 catalogue includes further supporting evidence, with consistent parallaxes and proper motions.

4.3.49 WASP-85

WASP-85 is historically known as a wide binary, with measurements in the WDS from 1881 onwards, despite a separation of only 1.5″. In addition to TCI observations in 2015 and 2016, lucky imaging was obtained by Wöllert & Brandner (2015), and speckle interferometry results were presented in Tokovinin et al. (2016) and Schmitt et al. (2016), although the results in the latter two works appear to be derived from the same observations. The TCI data gives consistent photometric distances for the two stars, and the lack of any significant change in separation since 1881 despite a proper motion of 78 mas/yr shows the two stars must exhibit common proper motion.

The WDS data clearly shows a large change in position angle between the stars, from approximately 114° in 1881 to 100° today, which may be evidence of orbital motion. As with WASP-2, Kepler's Third Law can be used to determine whether the motion is plausible for an orbit. From a simple inversion of the Gaia DR2 parallax of WASP-85B (the A component lacks a full astrometric solution) of 7.0197 ± 0.0601 mas, the distance to the system is 142.5 ± 1.2 pc. The angular separation of the two stars in 2016 was $1.455 \pm 0.004''$, giving a projected separation of 207.3 ± 1.8 au. Assuming this to be the semi major axis of the system, and adopting masses of $1.04 \pm 0.07\,M_\odot$ and $0.88 \pm 0.07\,M_\odot$ for the two components (Brown 2015), the orbital period of the system is a mere 2000 years. For a face-on orbit, the expected annual change in position angle is 0.18°, or 24° between the first (1881) and last (2016) measurements. The actual change is less than this, which can plausibly be explained by situations such as an

inclined orbit, the projected separation being an underestimate of the true semi major axis, the orbit being eccentric, or an incorrect determination of the total mass of the system.

4.3.50 WASP-87

Anderson et al. (2014a) noted a bright star located 9″ to the southeast of WASP-87, and through analysis of 2MASS photometry of the star, concluded it was a plausible binary companion. A proper motion analysis was also performed, based on the UCAC4 catalogue, with the conclusion that the motions are 'similar'. However, the motions for the two stars in this catalogue are in fact highly inconsistent based on the published uncertainties, and different in both magnitude (3.2 ± 2.0 mas/yr vs. 14.3 ± 2.0 mas/yr) and direction (northwest vs. southeast). The motions in the NOMAD catalogue are more consistent, whilst the PPMXL catalogue lacks an entry for the companion star.

Two band TCI photometry in 2015 and 2016 indicated that the star had a somewhat inconsistent photometric distance, being 1.2σ too faint for a bound star. However, it was noted that the analysis of Anderson et al. (2014a) showed WASP-87A to be somewhat evolved, rather than being on the main sequence as is assumed in the TCI analysis, and hence the flux ratio between WASP-87A and a bound main sequence companion would be greater than predicted. As a result, the companion was tentatively classed as a bound component of the system. The Gaia DR2 results show the stars to have similar but not entirely consistent parallaxes and proper motions, with a 2.2σ difference in parallax, and differences greater than 5σ in both components of the proper motion. Both stars are indicated as having relatively poor astrometric solutions, with goodness-of-fit statistics of 13.2 and 9.6 (values are expected to be normally distributed around zero with mean one), perhaps explaining the discrepancies.

4.3.51 WASP-94

This system forms a striking visual double star, with the two components being of almost identical brightness and colour. A transiting planet was discovered around the slightly hotter A component, but chance radial velocity observations of the B component revealed that it, too, hosts a close-in hot Jupiter (Neveu-VanMalle et al. 2014). A search for transits on the B component did not reveal any detectable signal, and hence it was concluded that the orbital planes of the two planets must be inclined relative to one another by at least 9°. Neveu-VanMalle et al. (2014) presented a variety of observations confirming that the two stars are physically associated, including observations since 1834 in the WDS that show no change in relative position, consistent radial velocity measurements, and matching catalogue proper motions. TCI photometry from 2016 also produces consistent photometric distances for the two stars, and Gaia DR2 gives consistent parallaxes and similar proper motions.

Stellar binaries consisting of stars with very similar properties, often dubbed 'twins', have been of particular interest for finding and studying correlations between the existence of planets and the elemental abundances in the host star. It has been known for some time that the presence (and hence formation) of giant planets is correlated with host star metallicity (e.g. Santos, Israelian & Mayor 2004, Fischer & Valenti 2005), and there is evidence that elemental abundances in stars can be altered by planet formation (e.g. Meléndez et al. 2009, Ramírez et al. 2015). In this context, Teske, Khanal & Ramírez (2016) performed an investigation of the stellar elemental abundances in the WASP-94 system, which provides an interesting contrast to many other wide binaries due to the presence of similar planets around both stars. Their results were unexpected and difficult to explain, with WASP-94A – hosting the less massive planet – having a lower overall metallicity, and also being depleted in 'volatile' elements (those with lower condensation temperatures). Various hypotheses to explain these observations were put forward, including the presence of additional, unresolved stellar components altering the dynamics of the system, and hence the early formation and evolution of the protoplanetary disc and planets. No evidence of such companions

was found in the TCI data.

4.3.52 WASP-98

An faint ($\Delta \mathrm{r}_{\mathrm{TCI}} \simeq 7\,\mathrm{mag}$) companion was detected 12″ from WASP-98 in 2014. Two band photometry was obtained, showing the companion to be bluer and hence hotter than WASP-98. The companion was therefore determined to be a distant background star, and was not analysed in any great detail. However, the release of Gaia DR2 reveals that this star is, in fact, physically associated with WASP-98, with the stars having consistent parallaxes and proper motions. The Gaia BP and RP photometry confirm that this star is much bluer than WASP-98 itself, and the companion is undetectable in near infrared 2MASS images. Given its high effective temperature but low luminosity, this companion must therefore be a white dwarf. Future observations of the white dwarf companion may allow a more stringent age constraint to be placed on the WASP-98 system, as was previously done for the similar K2-02 system (Vanderburg et al. 2015). Further study of WASP-98 is of particular interest due to the planet host star's exceptionally low metallicity, which poses difficulties for planet formation theory (Hellier et al. 2014, Mancini et al. 2016).

4.3.53 WASP-100

A companion 4″ from WASP-100 was detected in 2014, with two band imaging obtained. The star was found to have a similar colour to WASP-100, being approximately 6.2 mag fainter in both cameras, and hence was classified as a background star. However, Gaia DR2 results show the two stars to have consistent parallaxes and proper motions. Furthermore, the Gaia BP-RP colour indicates it is significantly redder than WASP-100, in line with the expectation for a low mass companion. Inspection of the original TCI data shows that the magnitude difference reported for the vis camera observations appears to be to small, with the difference being on the order of 7 mag, giving the companion a revised temperature of approximately 3500 K, and a photometric dis-

tance consistent with WASP-100. The companion falls near to the diffraction spikes from WASP-100, and contaminating light from these may explain why the companion's flux was overestimated by a factor of two in the vis camera data.

4.3.54 WASP-103

A companion only 0.24″ from WASP-103 was detected by Wöllert & Brandner (2015) with lucky imaging, and subsequently reobserved by Ngo et al. (2016) in the near infrared. This companion was not detectable in TCI red camera data obtained in 2014, being much closer than any companion detected with the instrument, and far below the detection limit. Astrometry recorded by the Gaia mission is confused due to the two barely resolved stars, with various goodness-of-fit indicators showing that DR2 astrometric fit is very poor, and it is therefore not possible to check for additional common proper motion companions.

4.3.55 WASP-104

This system was observed in both 2015 and 2016, but two band photometry was only obtained in the latter year due to a technical fault in 2015. A companion star approximately 7″ to the south was detected in both years, with photometry of the companion being affected by a diffraction spike from WASP-104, particularly the vis camera measurement. The companion was found to have a photometric distance consistent with WASP-104 at 1σ, but this result was considered questionable due to the diffraction spike contamination. Additional resolved photometry in r, i, and z was located in the SDSS catalogue, and the BT-Settl isochrones (Allard, Homeier & Freytag 2012) were used to show that the two stars have consistent distances. Proper motions in the URAT1 catalogue also support the hypothesis that the two stars are physically associated, although the data are quite uncertain. The Gaia DR2 results clearly show common proper motion between the two stars, and their parallaxes are consistent at 2σ, with the companion's astrometry being relatively uncertain due to its faintness.

4.3.56 WASP-106

A companion located 18″to the southeast was imaged in 2015 and 2016, with the latter observations indicating a consistent photometric distance. Gaia DR2 shows the star to have a much smaller parallax than WASP-106, with a negligible proper motion, indicating that it is likely a background giant star.

4.3.57 WASP-108

Two companion stars with photometric distances consistent with WASP-108 were identified from 2 band photometry in 2015 and 2016. Companion 4, 9″ away to the north east, is 7.6 mag fainter in r_{TCI}. Companion 10 is relatively bright, being only 2.2 mag fainter in r_{TCI}, and is located 19″ away, again to the north east. As WASP-108 is located in a relatively crowded field, it was considered likely that at least one of these stars is a chance alignment. The more distant companion 10 is bright enough to have been included in ground-based proper motion catalogues, with the NOMAD, PPMXL, and UCAC4 catalogues all indicating that it does not exhibit common proper motion with WASP-108. This is further supported by the results in Gaia DR2, which indicate that it is a background giant star, due to its very small parallax of 0.18 ± 0.03 mas., corresponding to a distance of several kiloparsecs. For the closer companion 4, no additional photometry or astrometry was located during the initial analysis, but Gaia DR2 now confirms that this companion has common proper motion with WASP-108, with parallax values consistent at 2σ, the companion's astrometry being quite uncertain due to its faintness.

4.3.58 WASP-109

An extremely faint ($\Delta r_{TCI} = 8$ mag) companion was detected at 20.5″, having a photometric distance consistent with WASP-109. Due to its faintness, and close proximity to a brighter star, no additional data was available from ground based catalogues. Gaia

DR2 reveals that while the companion does have a parallax consistent with WASP-109, the proper motions of the two stars are not at all similar, and hence the companion is an unassociated star simply passing close to the WASP-109 system.

4.3.59 WASP-110

A relatively bright companion located 4.6″ from WASP-110 was noted by Anderson et al. (2014a), who measured a separation of $4.589 \pm 0.016''$ and a magnitude difference of 2.872 ± 0.012 mag in the I filter, but lacked enough data to determine whether the companion was physically associated with WASP-110. TCI photometry in 2015 gave a similar magnitude difference in r_{TCI} of 2.82 ± 0.04 mag, but a smaller difference in v_{TCI} of 2.29 ± 0.05 mag, revealing the companion to be significantly bluer – and hence hotter – than WASP-110. The companion's colour falls outside the limits of the TCI colour–temperature relation, and hence a photometric distance could not be determined. The two stars were poorly resolved in ground based astrometric catalogues, although the UCAC4 catalogue shows the two stars as having highly dissimilar proper motions, predicting that the separation should increase and position angle decrease with time. A trend of increasing separation was indeed seen, with measurements of $4.589 \pm 0.016''$ on 2013-08-16 (Anderson et al. 2014a), $4.62506 \pm 0.00013''$ at a mean epoch of 2015-01-01 (Gaia DR1), and $4.628 \pm 0.006''$ on 2015-05-29 (TCI). Position angle measurements similarly show the expected increase, although measurements were only available from Gaia DR1 ($114.6165 \pm 0.0018°$) and the TCI ($114.152 \pm 0.068°$). Gaia DR2 resolves the two stars, with the proper motions being similar to those in the UCAC4 catalogue, and hence the two stars do not exhibit common proper motion. The companion's parallax of only 0.16 ± 0.05 mas indicates that it is a highly luminous star located several kiloparsecs beyond WASP-110.

4.3.60 WASP-111

A companion star located 5″ from WASP-111 was detected in TCI data from 2015 and 2016, with a photometric distance consistent with that of WASP-111. The NOMAD catalogue was the only ground based catalogue found to contain a proper motion determination for the companion, with the stars having consistent proper motions, although the measurements for the companion are relatively uncertain. Additional astrometric measurements were derived from 2MASS ($4.97 \pm 0.09''$ at $100.0 \pm 1.1°$ on 1998-07-10) and Gaia DR1 ($5.0273 \pm 0.0004''$ at $100.161 \pm 0.003°$ at a mean date of 2015-01-01), revealing no clear trend in either separation or position angle over a period of 18 years. Gaia DR2 confirms the stars have consistent parallaxes, though whilst the proper motions are similar (within 1 mas/yr in both axes), they are significantly different (3.3σ in RA, 5.8σ in Dec.), which may be an indication of detectable orbital motion.

4.3.61 WASP-121

TCI observations in 2016 included a faint, red companion star located 7.6″ to the southwest of WASP-121 with a consistent photometric distance. The position recorded in the 2MASS catalogue (7.40 ± 0.09 on 1997-03-03) gives a change of only $0.24 \pm 0.10''$, although this is similarly consistent with common proper motion (no change) and the expected motion of WASP-121 over 20 years ($0.5178 \pm 0.0012''$, based on Gaia DR2 proper motions). Gaia DR2 resolves the stars, but does not include a full astrometric solution for the companion, which has a poor goodness of fit and is indicated as having had an ignored 'duplicate' detection, which may indicate the presence of a third star unresolved in the TCI data, as with WASP-24. The TCI photometry indicates the companion is slightly brighter than expected (0.7σ), is consistent with this idea.

4.3.62 WASP-123

This system was observed in 2016, with a companion star detected 4.8″ from WASP-123, 5.1 mag fainter in r_{TCI}. The companion's photometric distance is consistent with that of WASP-123 at 1.2σ, the companion being somewhat brighter than expected. 2MASS position measurements give a separation of $4.64 \pm 0.12''$ on 1998-07-25, showing that the two stars have not moved significantly relative to one another in the last 20 years. As with the potentially bound companion to WASP-121, Gaia DR2 does not have a full astrometric solution despite the companion being relatively bright and sufficiently far away to be well resolved. The companion's restricted astrometric solution is indicated as having a poor goodness of fit, although no duplicate detection is noted as being present. Once again, the poor astrometric solution and overluminosity of the companion suggest that may be an unresolved binary.

4.3.63 WASP-129

Companion 2, located 5.9″ from WASP-129 and imaged in 2016, was found to have a photometric distance consistent with WASP-129 itself. 2MASS astrometry gives a separation of $5.59 \pm 0.09''$ on 1999-05-04, and at the time this was stated as consistent with no change; however, this does differ from the TCI measurement at the 4σ level. Gaia DR2 shows that companion 2 has a parallax and proper motion inconsistent with those of WASP-129; these conclusions also apply to companion 1, a very blue object for which no photometric distance was derived.

4.3.64 WASP-133

The faintest companion star, number 4, was identified as having a consistent photometric distance. Due to its faintness, it is not included in catalogues such as Gaia DR2.

4.4 Orbits of planet-hosting wide binaries

For most suspected or confirmed wide binaries studied in this work, the only constraints on the binary orbit are the projected separation at the time of observation and the estimated total mass of the system, based on the photometric or spectroscopic properties of the two stars. The projected separation places a lower limit on the actual separation of the two stars, and in conjunction with the total mass, a lower limit on the orbital period of the system. However, the true semi-major axis and period remain unknown, as do the alignment and eccentricity of the binary orbit. Knowledge of these parameters is of interest for models of hot Jupiter formation, as migration mechanisms such as the Lidov-Kozai effect are strongly dependent on these parameters, in particular the alignment of the binary orbit relative to the planetary orbit.

4.4.1 Target selection and initial inspection

During the analysis of detected companions, several systems – in particular WASP-85 – were noted as having noticeable changes in separation or position angle over time, typically where the WDS includes historical measurements dating back to at least the early 20th century. The WDS was searched for entries relating to any transiting exoplanet system contained within the TEPCat catalogue. The online version of the WDS only shows summaries of the oldest and most recent entries in the catalogue for a given system, with the full data available only on request. Those systems for which the summary line showed a change in separation of more than an arcsecond or so, or a change in position angle greater than a couple of degrees, were selected and the full WDS records obtained. These systems are as follows:

HAT-P-01 – a change in position angle of 4° and separation of 3″ was shown by the WDS summary between 1828 and 2010. However, the 1828 measurement appears to be in error, as repeated measurements since 1904 show no clear trend in either value.

HAT-P-20 – a small change in position angle was shown since 1909, but only six independent measurements (and only 2 predating 1998) are recorded, which were

insufficient to constrain the orbit.

HAT-P-34 – a change of 4° in position angle and 2.5″ in separation was shown between 1895 and 2015. However, apart from the 1892 entry, the position angle measurements are consistent. The separation measurements before 2000 are highly scattered.

K2-02 (HIP 116454) – although only 3 measurements were shown in the WDS, the existence of high precision astrometry from Keck/NIRC2 and the TCI, combined with a change of 2° in position angle and 0.4″ in the WDS entries, gave hope that orbital motion might be detectable. However, the measurements show significant scatter between the separate datasets, indicating that systematic errors likely dominate over the orbital motion.

KELT-8 – a large change of 2.5″ in separation and 4° in position angle was recorded in the WDS, once again suggestive of orbital motion. However, when trying to model these data, the motion was found to be much too rapid to be explained as orbital motion. Fulton et al. (2015) analysed the companion in some detail, finding a low surface gravity indicative of the companion being a luminous background giant, in addition to a radial velocity entirely inconsistent with a bound orbit, differing from KELT-8 by 65 km/s. The WDS entry is therefore a spurious matching of two unrelated stars.

WASP-2 – a clear trend of reducing separation is seen since the companion's discovery, although position angle measurements are scattered. The data were found to be insufficient to meaningfully constrain the orbit.

WASP-8 – a large change of 10° in position angle and 0.5″ in separation are indicated between 1930 and 2014 in the WDS. However, it appears that the 1930 measurement is in error, as no clear trend in either variable is seen.

WASP-77 – a change of 4° in position angle is seen since 1903, with dense observational coverage of the system by several observers between 1903 and 1933 giving a good constraint on the astrometry in the early 20th century.

WASP-85 – this system is by far the best observed of all binaries investigated, with a change of 15° in position angle between 1881 and the current day. Measurements

are recorded in the WDS for almost every decade until the 1980s, and these alone clearly show orbital motion.

WASP-94 – the earliest measurement of this system dates back to 1834, indicating little change in separation but a change of 3° in position angle. However, 20th century position angle measurements are highly consistent, with all observations since 1913 giving $89.6 \pm 0.5°$.

For all systems, an attempt was made at fitting the orbits using the method outlined in the following sections. For some, such as the non-binary KELT-8, no reasonable orbital fit could be derived. For others, the data was insufficient in either phase coverage or quality to meaningfully restrict the orbit. Only the results for WASP-77 and WASP-85 were considered to be sufficiently well constrained to be of interest, and only these systems will be considered from this point on.

4.4.2 Orbital mechanics – a brief introduction

The orbit of wide binaries, as well as many other two-body systems systems, can be described by a Keplerian orbit, an idealised case which considers the motion of one body relative to the other body, ignoring various possible perturbations such as other bodies, tidal interactions, and relativistic effects. The orbit is described by an ellipse if the bodies are bound (i.e. the orbit repeats), or by a parabola or a hyperbola if the bodies are not bound. For bound orbits, which are those being studied in this thesis, the size of the orbit ellipse is defined by the semi-major axis a, which is half the longest diameter across the ellipse (the major axis), while the shape of the ellipse is determined by the eccentricity e, which is defined as

$$b = a\sqrt{1 - e^2} \tag{4.2}$$

where b is the semi-minor axis, half the shortest diameter across the ellipse (the minor axis). For bound orbits, e takes a value in the range $[0, 1)$, with an eccentricity of zero corresponding to a completely circular orbit.

The binary orbit is defined in the $\mathbf{x}^K$ coordinate system, with axes XYZ, with the primary star being fixed at the origin. The orbit occurs in the X-Y plane, with the $+X$ direction towards periastron, the point in the orbit at which the two stars are closest. However, in general the observer is using a different coordinate system $\mathbf{x}^k$ that is not aligned with the $\mathbf{x}^K$ system, with axes xyz. The observer's coordinate system is commonly the equatorial coordinate system, with x and y being right ascension and declination respectively, and z the radial direction. In order to transform from one system to the other, three rotations are required, with the angles denoted Ω, i, and ω, which take values in the ranges $[0, 2\pi)$, $[0, \pi]$, and $[0, 2\pi)$ respectively. The transformation from the $\mathbf{x}^K$ to the $\mathbf{x}^k$ is given by

$$\mathbf{x}^k = R_Z(\Omega)R_X(i)R_Z(\omega)\mathbf{x}^K, \tag{4.3}$$

where R_Z denotes a rotation around the Z axis and R_X denotes a rotation around the X axis. The angles can be described as follows: i, the inclination of the system, gives the tilt of the orbital plane relative to the line of sight, and hence $i = \pi$ defines a face-on orbit. Ω, the position angle of the ascending node, is the angle relative to true north at which the ascending node – the point at which the orbit passes through the x-y plane moving away from the observer – is located. ω, the argument of periapsis, defines the angle between the ascending node and periapsis.

The shape and orientation of the orbit are now defined, but the position of the secondary body at a given moment in time is not yet defined. For wide binaries, this is typically done by determining T_0, the time of periastron passage. Alternatively, the position of the body at a specified time can be determined. Finally, either the period P or the total mass M_{Tot} of the system must be defined; only one of these is necessary, as the other can be calculated using Kepler's third law in conjunction with a. For problems such as the orbits of satellites around the Earth, or the orbits of planets around the Sun, this is rarely considered as an additional variable, as the total mass of the system is well known. However, for wide binaries, the total mass is not measured, and in many cases a complete orbit has not been observed, and hence the period is also unknown. In this thesis, the total mass of the system is used, as some constraints

can be placed on it through information on the properties of the two stars.

4.4.3 Fitting orbits to observations

Despite being one of the oldest and best studied problems in astronomy, determining the orbit of a binary star system remains a difficult problem to tackle. The seven-dimensional parameter space (a, e, i, Ω, ω, T_0, and either $M_{\rm Tot}$ or P) is large and has relatively few intrinsic constraints. From population studies of wide binaries there exists some prior knowledge on the distributions of a and e, which are determined by the processes through which binary stars form and govern their subsequent evolution. For a given system, $M_{\rm Tot}$ may be constrained by photometric and spectroscopic analyses of the component stars. For the other parameters, the three rotation angles – i, Ω, and ω – and T_0, there is no prior constraint, and these must be determined from the observed astrometric or radial velocity measurements of the system.

As presented, the orbital elements are not ideally suited for use with optimisation algorithms. Because a full rotation of 2π in any axis gives identical results to the unrotated system, an infinite number of degenerate solutions exist if the optimisation algorithm is not constrained to limits such as $0 \leq \Omega < 2\pi$. However, such constraints do not reflect the continuous nature of these variables, and an iteration within a given algorithm that proposes a new trial value $\Omega' = \Omega + \delta\Omega$ will be rejected if Ω' falls outside these limits, rather than accepting the proposal as $\Omega' = (\Omega + \delta\Omega) \mod 2\pi$, which is the desired result. In the best case, such a restriction biases parameters and uncertainties; in other cases, the optimisation algorithm may fail to find an optimal solution at all. To overcome these problems, it is instead typical to use the sines or cosines of the rotation angles, which have a well defined range of valid values ($-1 \leq \cos\Omega \leq 1$, etc.) and do not provide degenerate solutions.

A further difficulty is the correlations and degeneracies that occur between several groups of parameters when fitting to data. For example, with only a small part of the orbit observed, it may be difficult to distinguish between a circular orbit, a tight eccentric orbit that is currently at apoapsis, or a wide eccentric orbit that is currently

at periapsis. These different scenarios are characterised by specific combinations of a, e, ω, and T_0. Many optimisation algorithms encounter difficulty in exploring such tightly correlated parameter spaces, leading to problems related to both finding good solutions for the orbital parameters, and also to characterising the uncertainty in the resulting optimal solutions. A well-known example of degeneracies is the argument of periapsis, w, which is poorly constrained for low eccentricity systems and undefined for circular systems. It is therefore common to consider arithmetic combinations of orbital elements that exhibit better numerical stability and reduce the effect of correlations, such as $e\cos\omega$ and $e\sin\omega$ in place of e and ω. Discussions on the choices of such combinations in the context of Markov Chain Monte Carlo methods can be found in Ford (2006) and Appendix A of Chauvin et al. (2012).

For WASP-77 and WASP-85, the relatively short portions of their orbits that have been observed were found to make Markov Chain Monte Carlo (MCMC) methods perform poorly – too little prior information was available to meaningfully constrain the fits, and as outlined above, difficulties were encountered in exploring the full range of possible solutions. Instead, the Bayesian rejection sampling algorithm presented in Blunt et al. (2017), dubbed 'Orbits for the Impatient' (OFTI), was adopted. As suggested by its name, this algorithm is aimed at systems where waiting for the full orbit to be be observed is impractical, as is the case for the two systems being studied. The OFTI algorithm operates similarly to an MCMC algorithm, generating an orbit based on prior probability distributions for the various parameters, and then accepting or rejecting the orbit probabilistically, based on the goodness-of-fit between the orbit and the observed data; however, unlike MCMC, each iteration is independent of all others, avoiding the possibility of the fitting algorithm becoming 'trapped' in a certain region of parameter space.

The OFTI implementation used was coded in C++, based on the description of the algorithm in Blunt et al. (2017), with some minor alterations.[3] The initial step involves the generation of orbit parameters, with e, a, $\cos i$, Ω, ω, $M_{\rm Tot}$, and ϕ_0 (the

[3]The author thanks S. Blunt and E. Nielsen for their advice on implementing the algorithm.

phase at time of observation) being the parameters used – note that the implementation of Blunt et al. (2017) uses P and T_0 in place of $M_{\rm Tot}$ and ϕ_0. e, $\cos i$, ω, and ϕ_0 are chosen from uniform distributions, with $0 \leq e < 1$, $-1 \leq \cos i \leq 1$, $0 \leq \omega < 2\pi$, and $0 \leq \phi < 1$. The choice of eccentricity prior differs from that used by Blunt et al. (2017), which is based on observations of exoplanets; for wide binaries with periods longer than 100 days, the distribution of eccentricity is reasonably close to uniform, albeit with some evidence of a deficit at very high eccentricity (Raghavan et al. 2010). $M_{\rm Tot}$ was derived from a normal distribution based on the quoted masses of the two individual components in each system, with values taken from Maxted et al. (2013) for WASP-77, and from Brown (2015) for WASP-85. The derived masses for the two stellar components in each system were assumed to be uncorrelated,

In order to improve the acceptance fraction, OFTI introduces an additional 'scale-and-rotate' step, in order to set values for a and Ω. If these values were set freely, many generated orbits would not pass near to any of the observed positions, and hence a high fraction of iterations would be rejected. However, as already discussed, prior distributions for a and Ω are likely to be complex and difficult to model. OFTI tackles this problem by generating each orbit with initial values of $a = 1\,{\rm au}$ and $\Omega = 0$, calculating the expected position of the two bodies at a given epoch, and comparing this to the observed data. The value of a is then increased or decreased to match the observed separation (scale), and the value of Ω is changed to match the observed position angle (rotate). In each iteration, the observed data point is perturbed within its uncertainties, assuming a normal distribution. In the original OFTI algorithm, the 'observed' data point is the true observation that provides the highest acceptance fraction; in this implementation, the mean and standard deviation of all observed data points is used.

The final stage is to calculate the goodness-of-fit of each generated orbit, as determined by its χ^2 value, and to accept orbits based on $p_{\rm accept} \propto e^{\frac{-\chi^2}{2}}$. An initial step in the algorithm determines a χ^2 offset, as a further step to increase the fraction of accepted orbits (Blunt et al. 2017). The program was run until 1,000,000 orbits had been accepted, in order to generate smooth posterior probability distributions.

In the original algorithm, an intermediate step was introduced to restrict the values of $\cos i$ and $M_{\rm Tot}$, based on the distribution results of the first 100 accepted orbits. Once again, the intention of this step was to increase the acceptance fraction. However, these steps were not used in the implementation described here. For $M_{\rm Tot}$, the combination of an existing prior and the relatively insensitivity of the acceptance fraction to the value of $M_{\rm Tot}$ meant that this restriction did not meaningfully alter the results. For $\cos i$, it was found that the inclusion of this extra restriction noticeably biased the results compared to an un-restricted run of the program, due to the wide range of plausible $\cos i$ values.

4.4.3.1 Radial velocity data

For wide binaries, orbits are commonly fitted using measurements of separation and position angle only. However, for both WASP-77 and WASP-85, radial velocity measurements of both stars are available, and hence the radial velocity difference between the two stars can be determined. In both cases, the measurements were obtained with the HARPS instrument, which has a sufficiently small aperture to resolve the stellar components and hence allowed the planet host star to be confidently identified.

For the planet-hosting A components, the individual radial velocity measurements include the effect of the orbiting planets ($322 \pm 4\,$km/s for WASP-77A and $173 \pm 5\,$km/s for WASP-85A), and hence the systemic radial velocity determined during the planet orbital analysis was adopted. For the B components, the weighted mean of all observations was used. The difference between these measurements was taken as the radial velocity difference between the two stars, giving a single measurement for each system. The mean date of all HARPS radial velocity measurements for each system was assigned to this measurement, with the range of observing dates being insignificant compared to the orbital period – under two months for WASP-77, and less than two weeks for WASP-85, compared to orbital periods that exceed a century.

Although the radial velocities of all stars are measured precisely, the true radial motions of the stars are less well known, due to convective blueshift and gravitational

redshift. The former is an apparent net blueshift in the spectrum of a star, caused by hotter material rising in convective cells (i.e. approaching the observer) accounting for a larger fraction of the star's overall flux than the cooler, falling material. Gravitational redshift is a general relativistic effect, with light losing some energy as it escapes from the star's gravitational potential. These two effects are similar in magnitude, with a net radial velocity shift of a few hundred m/s. With sufficient radial velocity measurements over the orbit of a system, it is possible to directly measure and correct for the overall radial velocity shift; this is commonly done for eclipsing binaries, and has also been achieved for the α Cen AB system (Pourbaix & Boffin 2016, Kervella, Thévenin & Lovis 2017). However, as noted above, the time span over which radial velocities were obtained for WASP-77 and WASP-85 is insignificant compared to the orbital period. While gravitational redshift can be estimated reasonably well, convective blueshift is difficult model, varying on a line-by-line basis and requiring full 3D hydrodynamical modelling to capture the effects of convection, in addition to dependence on both the spectrograph used and the reduction procedure (Allende Prieto et al. 2013). It was instead decided to assume a conservative uncertainty of 0.5 km/s on the measured radial velocity difference between the stars.

4.4.4 Orbit fitting results

The resulting parameter distributions for the orbits of WASP-77 and WASP-85 are complex, with the marginal distributions poorly represented by normal distributions, and with parameters being highly correlated with one another. Table 4.2 quotes several measures of the marginal distributions, and Figs. 4.1 and 4.2 display corner plots for the parameter distributions. In both cases, the distribution of M_{Tot} is dominated by the prior on the masses, as it is not meaningfully constrained by the available data.

Table 4.2: Distributions of parameters for the orbits of WASP-77AB and WASP-85AB. The 16th, 50th, and 84th percentiles are denoted by P_{16}, P_{50} and P_{84}. For WASP-85, two degenerate solutions exist for Ω and ω, and these values are quoted separately the solution that lies in the range 0–180°.

Parameter	Symbol	Median	Mode	P_{84}	P_{16}	$P_{84} - P_{50}$	$P_{50} - P_{16}$
WASP-77AB							
Semi-major axis (au)	a	420	310	660	290	250	130
Eccentricity	e	0.60	0.95	0.88	0.34	0.28	0.26
Inclination (°)	i	75	79	81	60	6	15
Long. of the asc. node	Ω	339	340	346	299	7	40
Arg. of periapsis	ω	226	211	278	197	51	30
WASP-85AB							
Semi-major axis (au)	a	148	123	200	125	52	23
Eccentricity	e	0.43	0.55	0.56	0.18	0.13	0.25
Inclination (°)	i	140	136	157	128	16	12
Long. of the asc. node	Ω	112	108	290	64	177	49
Arg. of periapsis	ω	209	329	319	54	110	156
WASP-85AB: Ω and ω restricted to the range 0–180°							
Long. of the asc. node	Ω	108	109	137	50	29	57
Arg. of periapsis	ω	81	36	154	24	73	57

4.4.4.1 WASP-77

The radial velocity data are sufficient to constrain the binary orbit in one of the two possible degenerate solutions. The stellar orbit is close to edge-on, with $i = 75^{+6}_{-15}$ (1σ confidence interval). While the planetary orbit is also known to be edge on by virtue of it being transiting ($i = 89.4^{+0.4}_{-0.7}$, Maxted et al. 2013), the longitude of the ascending node of the planet's orbit is unknown, and hence the degree of (mis)alignment between the planetary and stellar orbits is not certain. The fitting algorithm prefers orbits that are at least moderately eccentric, although with only a small fraction of the orbit observed, it is advisable to avoid placing too much emphasis on this result.

4.4.4.2 WASP-85

Neither of the two degenerate solutions in Ω and ω is strongly preferred by the fit, with the radial velocity measurement being too uncertain to constrain these values. With a good fraction of the orbit covered by astrometry with very little change in separation, it is certain that WASP-85AB is not in an edge-on configuration, and hence the stellar and planetary orbits are at least moderately inclined relative to one another. The same measurements also exclude high eccentricity solutions, with very few samples exceeding $e = 0.7$. The highest eccentricity solutions correspond to the smallest semi major axes of approximately 120 au, giving a periastron distance $a(1 - e) = 35$ au.

With the relatively detailed constraints on the orbit, and the finding that the stellar orbit is inclined relative to the planetary one, it is interesting to compare the system to the predictions of eccentric Lidov-Kozai migration models in the literature. The parameters of most interest are $a = 148^{+52}_{-23}$ au, an upper eccentricity bound of $e = 0.7$, and a minimum mutual inclination of $50^{+16\circ}_{-12}$ (based on $i_p = 89.69^{+0.11}_{-0.03}$, Močnik et al. 2016). Stellar and planetary masses are adopted from (Brown 2015).

Equation 35 of Fabrycky & Tremaine (2007) provides an expression for the maximum eccentricity reached for an inner body (in this case, the planet), from which the minimum pericenter distance reached by a hypothetical migrating planet can be

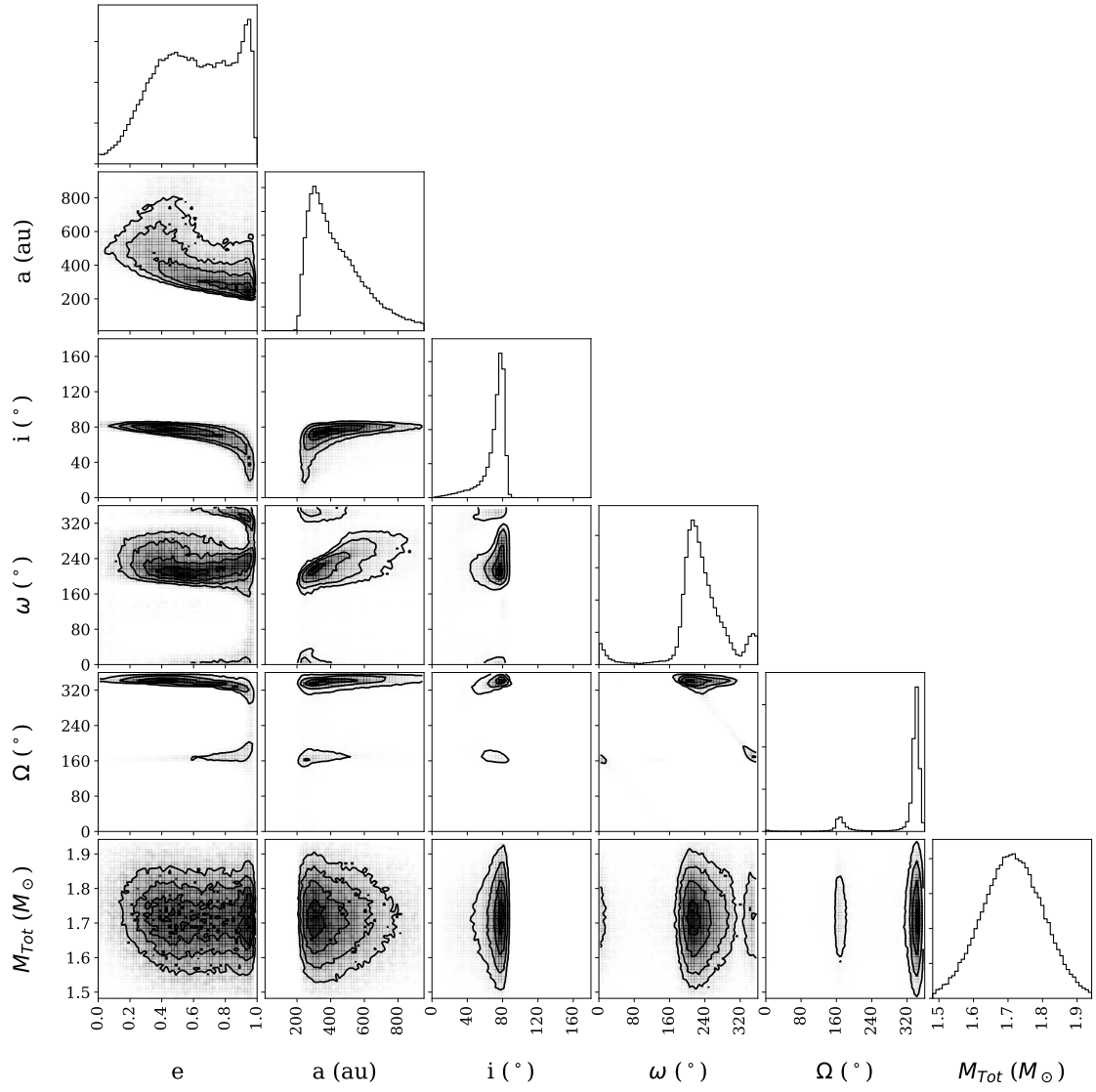

Figure 4.1: Distributions of parameters for the orbit of WASP-77AB. Shading indicates the density of accepted samples, with successive contours enclosing 68.3%, 95.5%, 99.7%, and 99.9% of the accepted samples. Evans et al., A&A, 610, A20, 2018, reproduced with permission © ESO

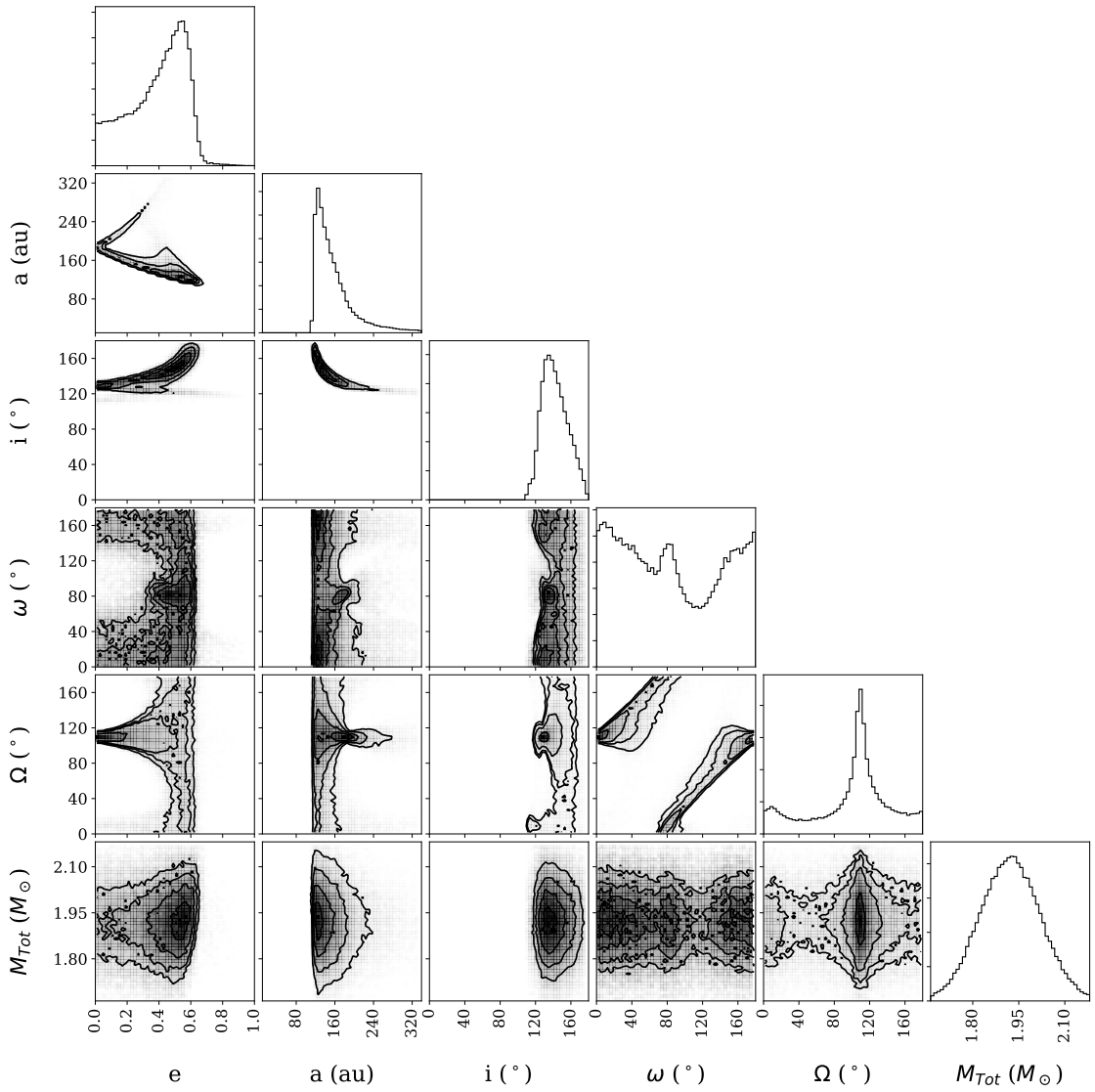

Figure 4.2: Distributions of parameters for the orbit of WASP-85AB. Shading indicates the density of accepted samples, with successive contours enclosing 68.3%, 95.5%, 99.7%, and 99.9% of the accepted samples. As two degenerate solutions exist for Ω and ω, the plot restricts the ranges of these to 0–180°. Evans et al., A&A, 610, A20, 2018, reproduced with permission © ESO

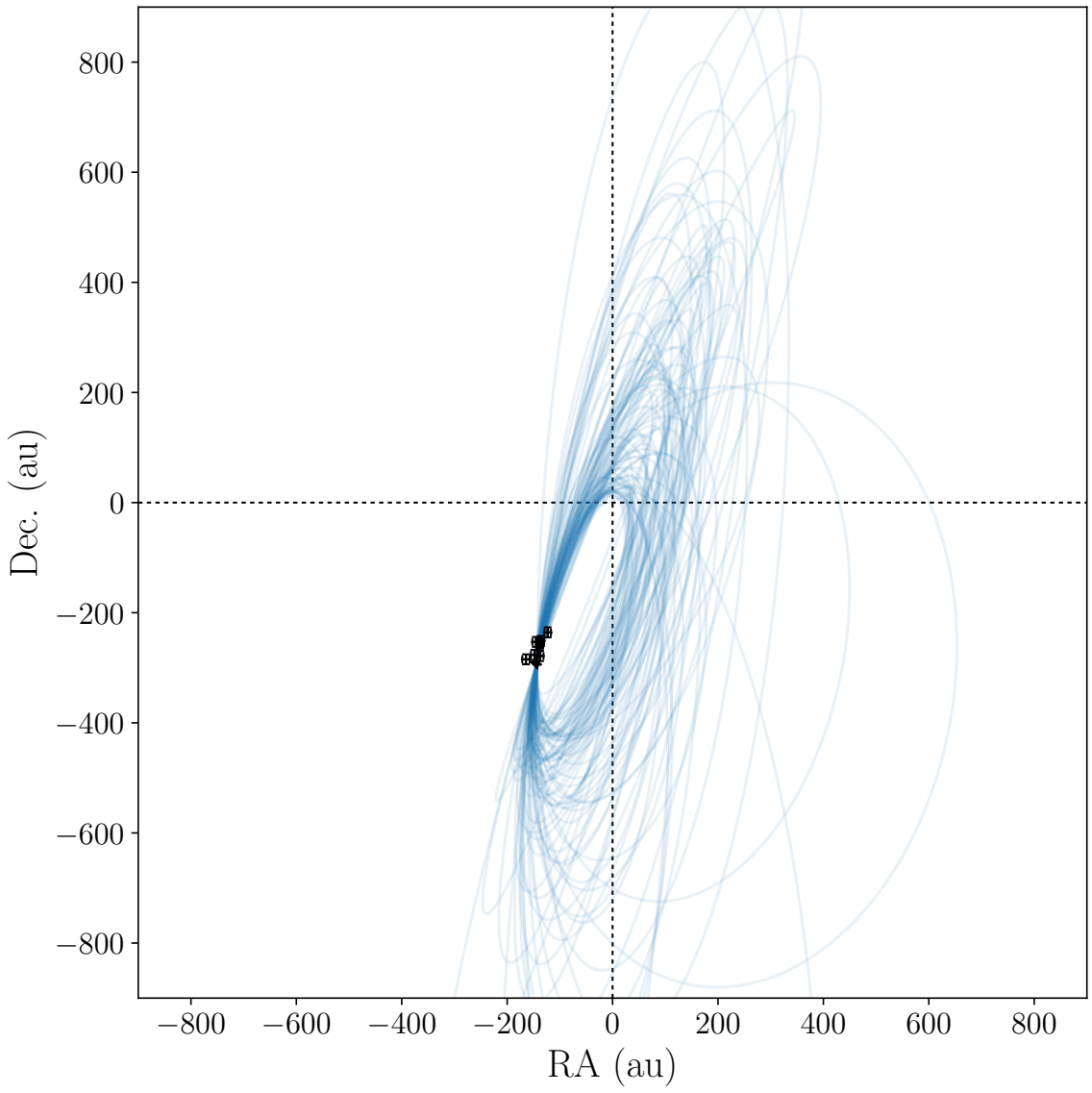

Figure 4.3: Visualisation of the orbit of WASP-77, using 100 randomly chosen samples from the full 1,000,000 accepted samples. Dashed black lines indicate the position of WASP-77A, while black data points indicate relative astrometry of WASP-77B. The binary orbit is close to edge on ($i = 77^{+6}_{-15}{}^{\circ}$), and may be relatively closely aligned with the planetary orbit. An O-C plot of the same 100 samples can be found in Fig. 4.5. Evans et al., A&A, 610, A20, 2018, reproduced with permission © ESO

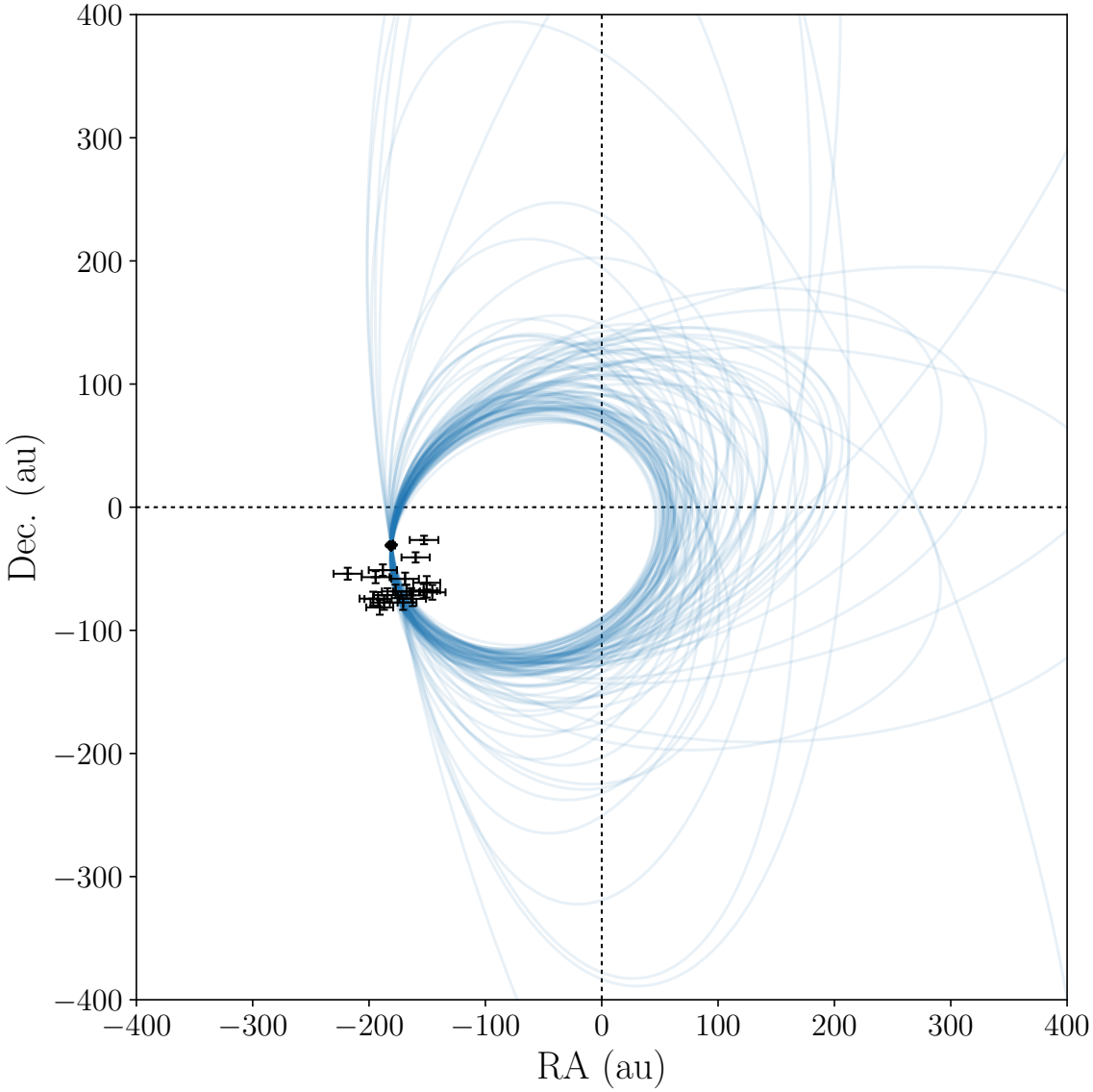

Figure 4.4: Visualisation of the orbit of WASP-85, using 100 randomly chosen samples from the full 1,000,000 accepted samples. Dashed black lines indicate the position of WASP-85A, while black data points indicate relative astrometry of WASP-85B. The binary orbit is approximately halfway between edge-on and face-on ($i = 140^{+16}_{-12}{}^{\circ}$), and hence is misaligned relative to the planetary orbit. An O-C plot of the same 100 samples can be found in Fig. 4.6. Evans et al., A&A, 610, A20, 2018, reproduced with permission © ESO

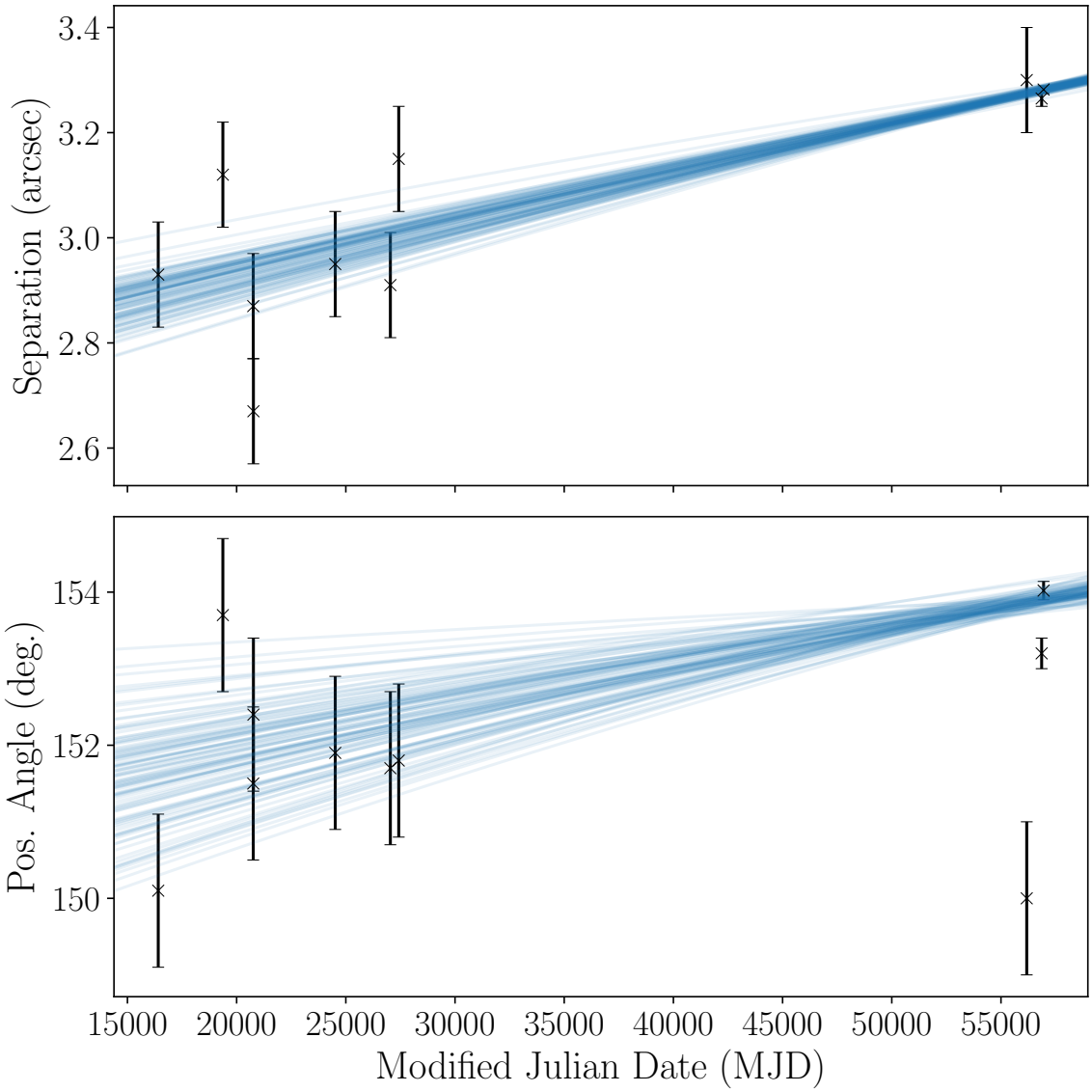

Figure 4.5: O-C plot for the orbit of WASP-77, using 100 randomly chosen samples from the full 1,000,000 accepted samples. A visualisation of the same 100 samples in the plane of the sky can be found in Fig. 4.3. Evans et al., A&A, 610, A20, 2018, reproduced with permission © ESO

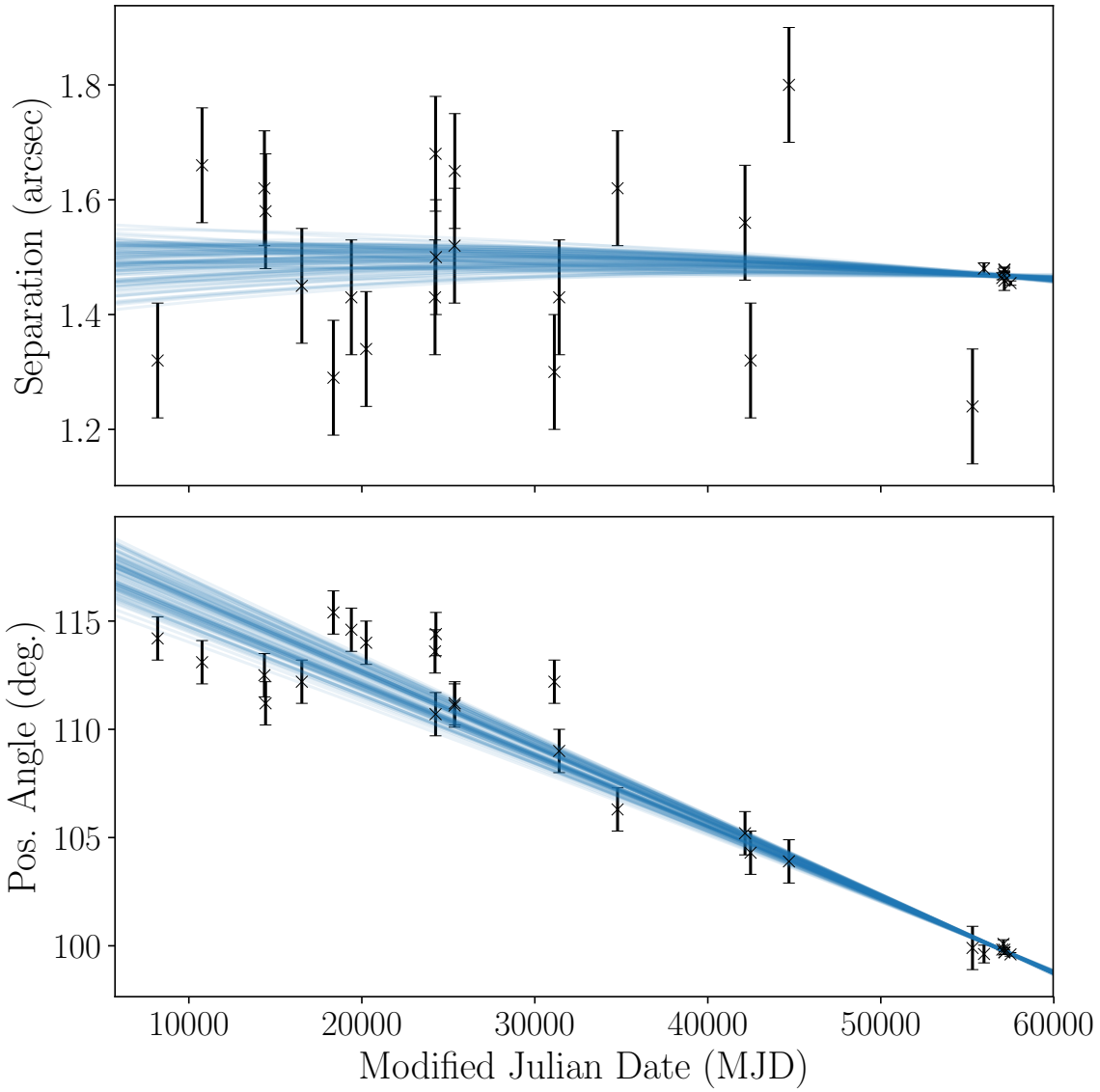

Figure 4.6: O-C plot for the orbit of WASP-85, using 100 randomly chosen samples from the full 1,000,000 accepted samples. A visualisation of the same 100 samples in the plane of the sky can be found in Fig. 4.4. Evans et al., A&A, 610, A20, 2018, reproduced with permission © ESO

determined. Assuming the planet is on an initially circular orbit, a formation distance of 6 au is sufficient to result in a minimum pericenter distance of 0.01 au if the binary eccentricity is $e = 0.7$ and 0.08 au if it is not, sufficiently close that tidal interactions could occur and a hot Jupiter could be formed. However, the initial formation locations of hot Jupiters are not strongly constrained – in a similar analysis of hot Jupiters with known stellar companions, Ngo et al. (2016) considered initial planetary orbits of 1 au, 2.5 au, and 5 au, concluding that very few binary companions were capable of creating hot Jupiters from planets originating at those distances. Ngo et al. (2016) separately note that additional planetary or low-mass stellar components in the system can act to stabilise the inner system (e.g. Wu & Murray 2003, Batygin, Morbidelli & Tsiganis 2011), with earlier radial velocity observations indicating that half od hot Jupiters have a companion within 20 au (Knutson et al. 2014).

Naoz, Farr & Rasio (2012) present simulations with two stars of mass $1\mathrm{M}_{\odot}$ each, and a planet of mass $1\mathrm{M}_{\mathrm{Jup}}$, reasonably similar to the WASP-85 system's masses of $m_{\mathrm{A}} = 1.04 \pm 0.07\mathrm{M}_{\odot}$, $m_{\mathrm{B}} = 0.88 \pm 0.07\mathrm{M}_{\odot}$, and $m_{\mathrm{p}} = 1.22 \pm 0.05\mathrm{M}_{\mathrm{Jup}}$ (Brown 2015). Panel b of their Fig. 2 shows the results of a simulation with a binary semi-major axis of 100 au, showing that migration is indeed possible across a range of separations, and that above $e = 0.5$, this can occur for a very wide range of mutual inclinations. However, their results also indicate that most of those planets that migrate fail to produce a hot Jupiter; instead, the majority are destroyed by collisions with their host star. Instead, they find that hot Jupiter formation by the eccentric Lidov-Kozai mechanism only becomes favourable for binary orbits that are three or four times wider than WASP-85. It is still possible that a hot Jupiter could form by other mechanisms in such a system, perhaps through interactions with an external planet, although there is currently no evidence of such a companion (Brown 2015, Močnik et al. 2016).

4.5 Discussion

Of the 156 systems observed, 40 were found to have plausible binary companions.[4] The majority of these were identified directly from the two band lucky imaging, and vetted through the use of catalogue photometry and astrometry. A small number of stars were initially rejected as being too luminous or faint given their colour, but were later found to have parallaxes and proper motions consistent with the planet host stars through inspection of the Gaia DR2 catalogue.

Without correction for detection limits, and assuming uncertainties described by Poisson statistics, this survey a stellar multiplicity rate of $26 \pm 4\%$ for transiting hot Jupiters. This is similar to the values found by other surveys of the multiplicity of transiting hot Jupiters. Ngo et al. (2016) found a raw multiplicity rate of $35 \pm 7\%$ from AO observations of 77 systems, with the majority of those companions confirmed to exhibit common proper motion. After correction for survey incompleteness, and assuming the distribution of orbits and binary companion masses matches those of field stars, they quote a final multiplicity rate between 50 and 2000 au of $47 \pm 12\%$. Wöllert et al. (2015) observed 12 companions to 49 transiting hot Jupiter host stars with lucky imaging, corresponding to a multiplicity rate of $24 \pm 7\%$. Further observations presented in Wöllert & Brandner (2015) resulted in 30 companions being detected to 74 targets, or $41 \pm 7\%$ multiplicity. No vetting was done of these companion stars, with all detected stars within the 12×12 arcsec. field of view being reported; however, the more restricted field of view compared to this survey reduces the probability of chance alignments.

Surveys focusing on planets found by the radial velocity method (or a combination of both RV and transiting detections) show significant disagreement with the above results for transiting hot Jupiters, with multiplicity rates being at least a factor of two lower. However, many such surveys do not focus on hot Jupiters alone, and

[4]This total includes companions to K2-27, WASP-31, and WASP-64 that were outside the LI FOV, but were identified as companions through catalogue inspection; it excludes unresolved companion stars found by other surveys, such as WASP-20B and WASP-103B.

hence the differences may indeed be real. Roell et al. (2012) provided a comprehensive review of companions to all known exoplanets at the time, mostly dominated by radial velocity results, finding a multiplicity rate of 12%. Mugrauer & Ginski (2015) obtained AO observations of 33 systems discovered by radial velocity measurements, finding only three companion stars consistent with being physically associated, corresponding to a multiplicity rate of 9%. A survey of 128 systems was detailed in Ginski et al. (2012) and Ginski et al. (2016), of which 12 targets were transiting systems, and only seven systems were confirmed to have multiple stars, leading Ginski et al. (2016) to quote a multiplicity rate of only 5.5%. However, it was noted that their survey included several further detected companions with unconfirmed status, which would bring the multiplicity rate to approximately 10% if confirmed. Although not considered separately, it is interesting to note the differences between the transiting and radial velocity sub-samples: 7 of the 12 transiting systems studied had plausible or confirmed companions ($58 \pm 22\%$), compared to 11 out of 116 for the radial sample ($9 \pm 3\%$), a difference that is significant at 2.2σ.

Studies of the multiplicity of transiting planets in the Kepler survey have been carried out by numerous groups. The majority of planets found by Kepler are not hot Jupiters, but instead are on wider orbits; many of Kepler's planets are also smaller and located in systems with multiple planets. Due to the larger distance to many Kepler systems compared to ground-based hot Jupiter discoveries, combined with the higher stellar density in the Kepler field, a companion star at only a few arcseconds is more likely to be physically unassociated. However, the faintness, low proper motions, and large number of these companions mean that very few have been analysed in sufficient detail to confirm their status. Furlan et al. (2017) considered the results from several different techniques, which generally showed that approximately 10% of Kepler Objects of Interest (KOIs, confirmed and suspected planetary systems) have at least one star within $1''$, and approximately 30% have companions within $4''$. Ziegler et al. (2018) is the latest in a series of papers by the Robo-AO collaboration, which had provided homogeneous imaging of 3857 KOIs at the time of that paper. Along with several other findings, they considered the multiplicity fraction as a function of both

planet size (divided into 'giant' and 'small', with the division at $3.9\,R_{\oplus}$) and orbital period. For periods beyond three days, no difference between the two planet types was found; however, short period giant planets were found to have a significantly higher multiplicity fraction (12.8%) small planets in the same period range (2.4%). While the multiplicity rate is lower than those found for hot Jupiters from ground-based surveys, this is likely to be at least partly due to the increased distance of the Kepler systems, and hence reduced angular separation and detection probability for any given companion.

4.5.1 Properties of companions

A noticeable theme among the companions detected by lucky imaging in this survey is that all are fainter and most are redder than the star that hosts the transiting planet, and hence the companions are the less massive component in the system. The exceptions to this trend are the white dwarf companions to K2-02 and WASP-98, which likely originated as brighter, more massive binary companions that evolved more quickly than the planet host stars. The theme of faint, less massive companions is also seen in other surveys of hot Jupiter host star multiplicity. The directly imaged companions observed by the Friends of Hot Jupiters survey (Ngo et al. 2015, Ngo et al. 2016) were all at least 2.4 mag. fainter than the planet host stars in the J band, corresponding to mass ratios below 0.6. The convinced results of Wöllert et al. (2015) and Wöllert & Brandner (2015) include 35 companions, of which only three were within 2 mag. of the transiting planet host star in the i band, and none were brighter.

For those companions observed in 2015 and 2016, and those observed in two bands in 2014, effective temperatures were previously determined from the TCI colour. Using these in conjunction with temperature-mass relation presented in Chapter 3 and literature values for the mass of the planet host star in each system, the mass ratio of each system was calculated. This was also performed for the primary and companion masses quoted in the Friends of Hot Jupiter direct imaging survey, and also for the high resolution imaging study of 382 Kepler planet host stars by Kraus et al. (2016),

which did not focus on hot Jupiters. The distributions of companion mass ratios are shown in Fig 4.7. The cutoff at high mass ratios for hot Jupiter companion stars is obvious, but is not present in the KOI sample – in fact, there is a noticeable clustering of companions above a mass ratio of 0.9 in the Kraus et al. (2016) sample.

The reason for the apparent lack of high mass companions to hot Jupiters is not clear. As higher mass companions are brighter relative to the planet host star, they are more favourable to detection through high resolution imaging; the deficit is in fact likely to be even greater than observed, due to additional low mass companions remaining undetected. One possible explanation is that higher mass stellar companions are unfavourable to the formation of hot Jupiters. This idea is in conflict with high eccentricity migration theories, which predict that closer, more massive companion stars are required to excite the high eccentricities required for tidal dissipation. However, numerical models of the mechanism have often struggled to cope with the high fraction of planets that are predicted to be destroyed by migration (e.g. Anderson, Storch & Lai 2016, Muñoz, Lai & Liu 2016), which is perhaps the effect that is being observed here.

An alternative explanation is a bias in the detection of transiting hot Jupiters, and a subsequent bias in the selection of candidates for follow-up. As detailed in Chapter 1, contaminating light from unresolved stars reduces the likelihood of detecting both the photometric and spectroscopic signature of a planet, and so the presence of a bright, high-mass stellar companion reduces the chance that a given hot Jupiter will be detected. Furthermore, surveys of transiting exoplanets are known to be plagued by false positives, of which blended eclipsing binaries can be particularly troublesome. The presence of two stars ar small separation, or of multiple sets of spectral lines in the spectrum of the system, may be enough to discourage further follow-up of wide binaries in favour of more promising targets – a similar selection bias has affected hot Jupiters orbiting hotter stars until recently, due to the difficulty of obtaining accurate radial velocity measurements (Temple et al. 2017).

While numerical models could be used to estimate the effect of dilution on the detection of planets in wide binaries (e.g. Ciardi et al. 2015), the latter hypothesis is

f

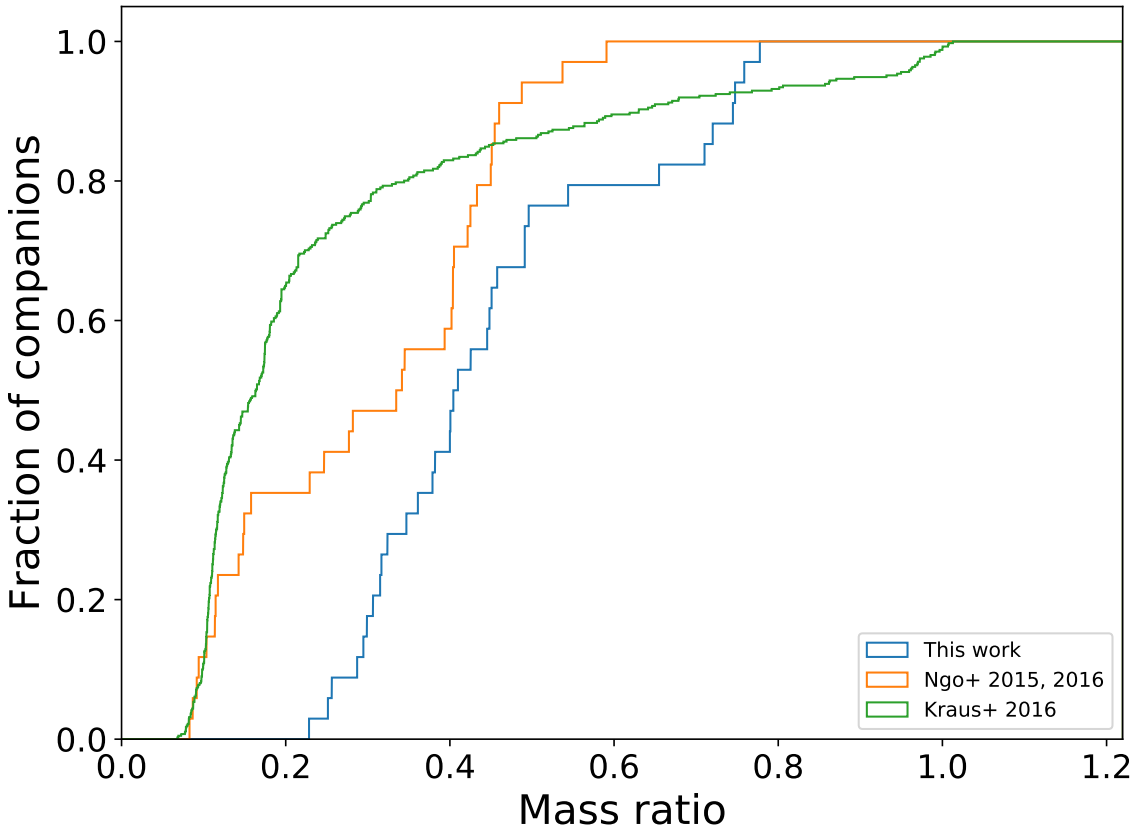

Figure 4.7: Mass ratios of planet-hosting binaries from different surveys. The blue line shows companions declared as 'plausibly bound' in this work (excluding those for which no temperature was determined). The orange line shows the Friends of Hot Jupiters direct imaging survey, a similar survey with similar target selection criteria. The green line shows the survey of Kepler Objects of Interest by Kraus et al. (2016), which covers a variety of planetary system architectures.

more difficult to test. Ground-based transiting exoplanet surveys, which are responsible for the vast majority of discovered hot Jupiters, do not generally publish planet candidates, due to the strong competition between groups in the field. In comparison, the Kepler mission team has routinely published all detected planet candidates (KOIs), allowing a much better understanding of the fraction of transit-like events that turn out to be false positives; however, due to its small field of view and a main mission consisting of only a single field of view, Kepler is not ideal for an investigation of hot Jupiter detection. The TESS mission (Ricker et al. 2014) will provide a better opportunity for such an investigation, with a follow-up programme that will be very open about candidate planets, and the expectation that it will detect over 1000 planets greater than 4 $R_\oplus$ with at least 3 transits and an SNR greater than 10 (Barclay, Pepper & Quintana 2018).

A further possibility is that the lack of distant, massive companions is not so unusual after all. Raghavan et al. (2010) presented a large survey of stellar multiplicity of Sun-like stars, and while one of the findings was that binaries are most likely to have components that are similar in mass, the massive companions tend to exist in shorter orbital periods. Raghavan et al. (2010) noted that despite the survey covering orbital periods into the millions of years, 78% of surveyed binaries with a mass ratio above 0.95 have orbital periods below 200 years, and all below 1000 years, with the widest having an orbital separation of 115 au. This work and the Friends of Hot Jupiters direct imaging survey both generally probe much wider orbital separations, with the distribution of projected separations of companions shown in Fig. 4.8, and so such close companions would not be detected. However, the results of the radial velocity search by Knutson et al. (2014) do not indicate that a large fraction of systems harbour such companions, and the interferometric results from Kraus et al. (2016) indicate that KOIs are rarely found in binaries with separations below 50au.

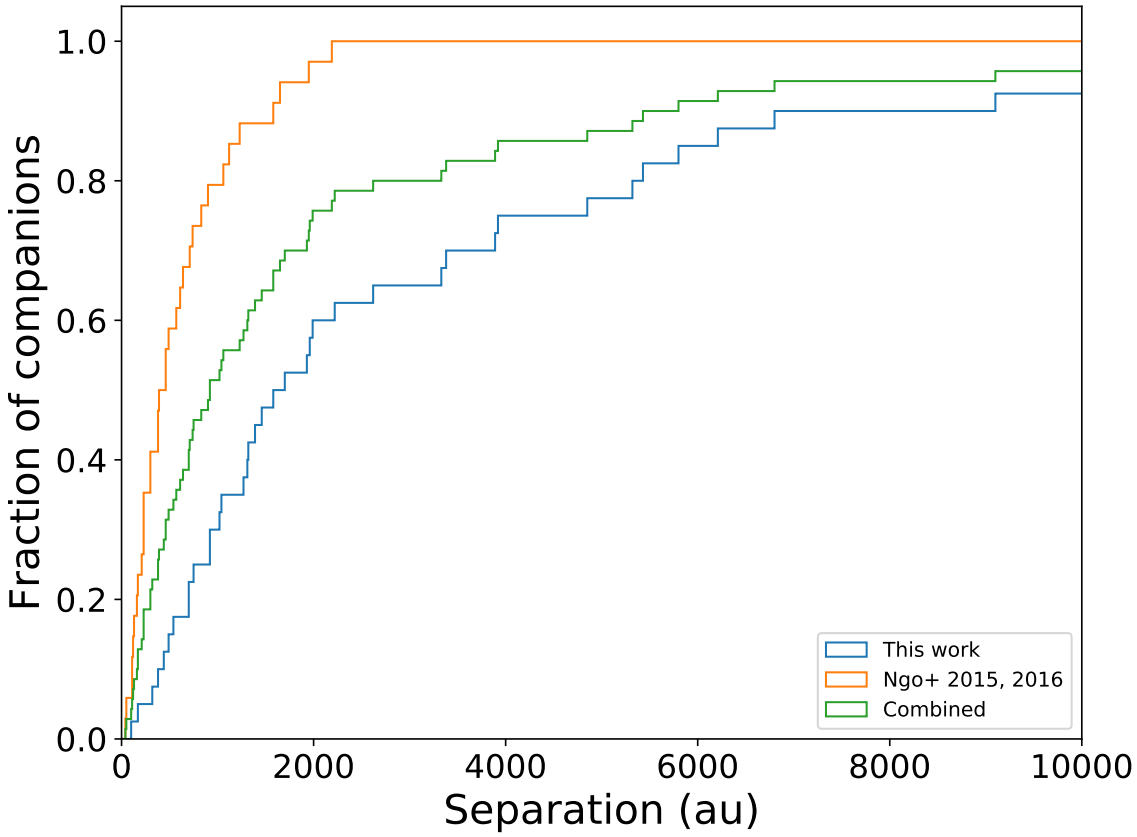

Figure 4.8: Distribution of projected separations of probable companions from this work (blue) and the Friends of Hot Jupiters direct imaging survey (orange). A combined histogram is also shown in green, after the removal of systems duplicated in both surveys by adopting the separation from this survey.

4.5.2 Contaminating stars and false positives

The lucky imaging survey did not reveal any new companion stars which are both sufficiently close and bright enough for the lack of correction for contamination to have significantly altered the properties of the detected transiting planets. Furthermore, no companions were identified as likely sources of false positive signals. The closest companion star with a magnitude difference of less than 2.5 mag., WASP-85B, was identified during the initial follow-up of the system (Močnik et al. 2016), as well as being a historically known wide binary. Fig. 4.9 shows a magnitude-separation plot of all detected stars within 20″ of a target star, illustrating the lack of close, bright companions.

As shown in this chapter, many of the companions detectable with lucky imaging are also resolved in Gaia DR2, which may prove a useful alternative to dedicated lucky imaging observations in future. Even where the stars are not resolved in Gaia DR2, there is often evidence present that the planet host star is not single, either through direct indications in the catalogue that multiple sources were merged, or through poor or noisy astrometric fits to planet host stars that would otherwise be expected to result in high quality fits, due to their brightness and distances of only a few hundred parsecs. In particular, the 'astrometric goodness of fit' and 'astrometric excess noise' values have been found to be correlated with the presence of binary companions, as detailed in a brief investigation in Evans (2018).

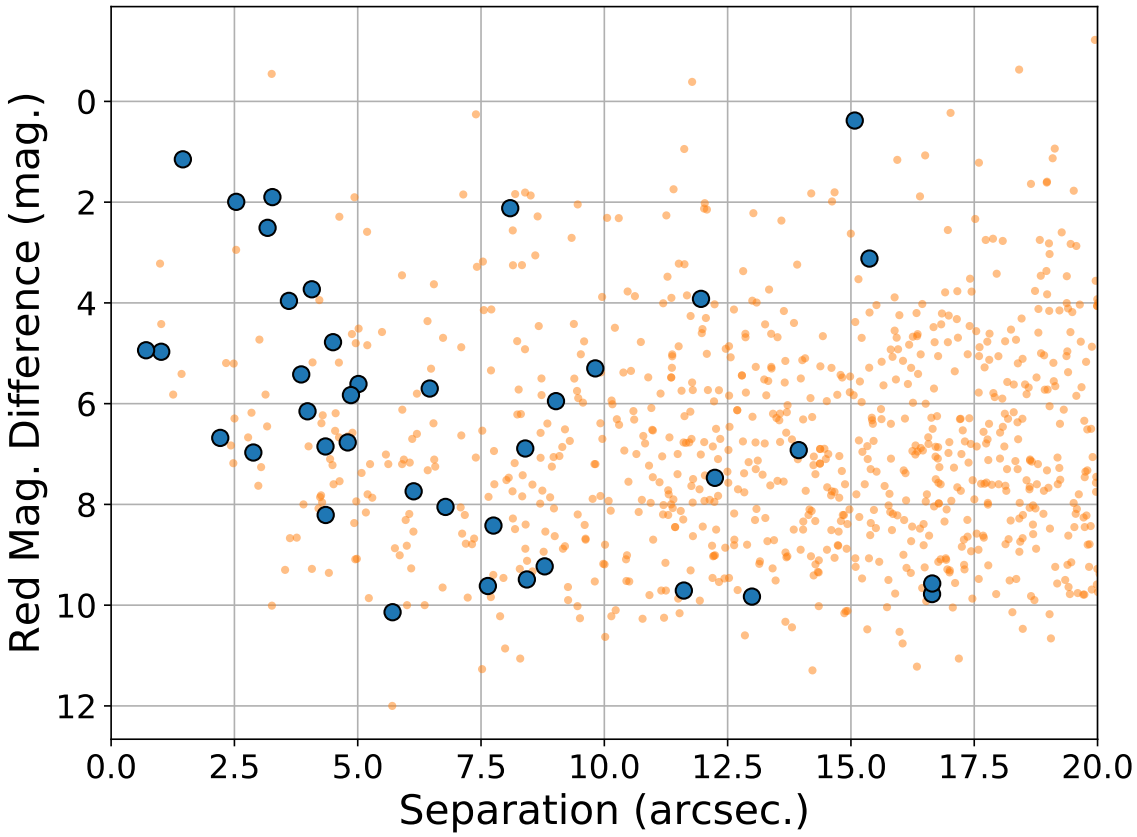

Figure 4.9: Magnitude and angular separation of detected companions within 20 arcsec., with companions considered to be 'plausibly bound' shown with large blue markers, and all others shown with small orange markers.

5 Adaptive optics survey with SPHERE

Between September 2016 and September 2017, 46 bright (R $<$ 11) exoplanet host stars were observed with VLT/SPHERE, an adaptive optics instrument capable of both imaging and spectroscopy in the visible and near infrared. This survey utilised SPHERE's IRDIS and IFS sub-instruments, which simultaneously provided imaging data in the K band and integral field spectroscopy across the Y, J, and H bands. The spectroscopic data from the IFS is particularly valuable, allowing a much more precise characterisation of companion stars than a wide-band imaging, whilst making efficient use of telescope time.

5.1 The SPHERE instrument

SPHERE is an extreme adaptive optics instrument, designed for the direct imaging of exoplanets (Beuzit et al. 2008). Several factors combine to make direct detection difficult – not only are planets many orders of magnitudes fainter than their host stars, even in the thermal infrared, but they are found at small angular separations from their stars, which makes distinguishing planetary and stellar photons difficult. Imaging of these objects therefore requires adaptive optics (or space-based telescopes), a method to ensure rejection of as much starlight as possible whilst retaining the planetary signal, and the development of methods to distinguish between residual starlight and the light from planets. SPHERE combines extreme adaptive optics with coronographic capabilities to meet the first and second requirements, whilst the three subinstruments and the variety of available observing modes are designed to achieve the third requirement.

SPHERE is made up of three sub-instruments: IRDIS (Dohlen et al. 2008), IFS (Claudi et al. 2008), and ZIMPOL (Thalmann et al. 2008). Capabilities such as adaptive optics correction, coronographs, and field derotation are common to all three instruments, being handled by the Common Path Instrument (CPI). IRDIS provides near-infrared imaging, polarimetry, and long slit spectroscopy. The IFS is an inte-

gral field spectrograph, also operating in the near-infrared, providing spatially resolved spectra across a $1.73'' \times 1.73''$ field of view. ZIMPOL provides imaging and polarimetry in the optical. In order to increase the observing efficiency of SPHERE, it is possible to utilise both IRDIS and the IFS simultaneously, obtaining both integral field spectroscopy and imaging data in at different wavelengths. This is the instrumental setup that was chosen for this work. The ZIMPOL subinstrument was not used in this observing campaign, and hence is not discussed further.

The following sub-instrument descriptions are based on the SPHERE user manual, in which further details can be found (Girard et al. 2017).

5.1.1 IRDIS

The Infrared Dual-band Imager and Spectrograph (IRDIS) operates in the near infrared between the Y and K bands (0.95–2.32μm). As suggested by the name, it is capable of both imaging – either 'classical', 'dual band', or 'dual polarisation' – and long slit spectroscopy. For imaging, the incoming light is split to form two separate images, each placed on one half of the detector. The detector has a plate scale of 12.25 mas/px, corresponding to a field of view of $11'' \times 12.5''$. IRDIS is capable of coronographic observations in all modes.

The two separate images permit the 'dual band' and 'dual polarisation' modes, both of which are aimed at the direct detection of planets or protoplanetary disks, where the main limiting factor is discrimination between residual starlight (in the form of slowly varying speckles) and the very faint light from a planet. The Dual Band Imaging (DBI) mode permits the Spectral Differential Imaging (SDI) technique, which highlights differences in the spectra of stars and planets in order to discriminate between speckles and true planetary signals. Different filters are used for the two images, with the filters chosen to highlight spectral features in planetary atmospheres (Vigan et al. 2010). Dual Polarisation Imaging (DPI) utilises the fact that starlight is unpolarised, whilst light from a planet or disk is likely to be polarised, especially in the case of reflected light. In this mode, the two separate polarisation directions are

imaged simultaneously, allowing the identification of polarised sources (Langlois et al. 2014).

5.1.2 IFS

The Integral Field Spectrograph (IFS) produces a series of spatially resolved spectra, covering a field of $1.73'' \times 1.73''$. The spectra are arranged on a hexagonal grid with a spacing of 12.25 mas, which is interpolated onto a square grid at 7.4 mas/px during the reduction process. The instrument can operate in either Y–J mode, with the spectra covering 0.95–1.35μm at a spectral resolution of R = 50, or in Y–H mode, covering 0.95–1.65μm at R = 30. The IFS is capable of using coronographs in either mode, and can be used in conjunction with IRDIS, which simultaneously produces images in either the H (Y–J mode only) or K bands.

A hexagonal grid of 'lenslets' are used to sample the field of view, with the light from each lenslet used to create one of the 21,000 spectra visible on the detector. The instrument pipeline extracts the individual spectra, corrects for flat fielding effects, and determines the wavelength calibration. The pipeline then extracts flux measurements at 39 points along each spectrum, providing a data cube with dimensions (x,y,λ). For final analysis, the pipeline resamples the data from the original hexagonal grid onto a square grid with a spatial resolution 7.4mas/px, with the final result being a series of 39 monochromatic images of the target field.

The main advantage of the IFS for direct imaging of planets relies on the wavelength dependence on speckles. Like the PSF of a star, speckles scale with increasing wavelength, moving further from the star. However, a point source such as planet will remain stationary on the image, and hence the two can be distinguished. In addition, the spectra contain valuable information about the planet. These advantages also apply to the detection of stellar companions, with the spectra obtained providing more information than wide band photometry alone.

5.2 Observations

Observations of 46 exoplanet host stars we taken in service mode between September 2016 and September 2017 (ESO Periods 98 and 99). The observations are detailed in Table 5.1. The selected targets are all confirmed transiting exoplanet host stars, observable from Paranal observatory, with R-band magnitudes brighter than 11. This magnitude limit corresponds to the minimum flux required for reliable AO correction with SPHERE, with the target stars used as the AO guide star in all cases. As the contrast requirements for this programme were less stringent than for direct imaging of exoplanets, due to stellar companions having much more favourable flux ratios relative to the target stars, we permitted observations during mediocre weather conditions, requiring only that seeing was better than 1.2″ and that thick cloud was not present.

SPHERE can be operated either in the visible (ZIMPOL) or near infrared (IRDIS and the IFS). For low mass stellar companions to planet host stars of spectral types F, G, and K, the flux ratios are more favourable at longer wavelengths, and hence observations were performed in the near infrared. In addition, the ability to observe simultaneously with both IRDIS and the IFS significantly increases the efficiency of the observations. Typically, stellar companions are characterised by separate imaging observations in two or three bands; however, the IFS has the capability to cover two or three of the typical photometric bands (Y, J and H) with improved wavelength resolution, with IRDIS extending the observations to a fourth photometric band.

The IFS can either be operated in Y–J mode (with $R = 50$) or Y–H mode ($R = 30$). It was not expected that the higher spectral resolution of Y–J mode would improve results, as stellar spectra are relatively featureless at such low resolution. The Y–H mode covers a larger fraction of the stellar spectrum, providing a better constraint on companion properties, and also has the advantage of collecting more photons from the targets due to its wider wavelength range. The IFS was therefore operated in Y–H mode, with a broadband K_S filter used for IRDIS. In order to increase sensitivity to close companion stars, a coronograph in the Common Path Instrument was used to block light from the target star.

IRDIS offers a variety of observing modes, both imaging and spectroscopy. The long slit spectroscopy mode does not have any direct application to a high resolution imaging survey, as the location of any potential companion star is unknown. The dual band imaging (i.e. the spectral differential imaging technique, SDI) and dual polarisation imaging modes are useful for discriminating between the target and companion object when large differences in spectral features or polarisation properties are expected. However, both objects would be stars in these observations, and hence are expected to be unpolarised black body sources, negating the benefit of these observing modes. As a result, IRDIS was operated in Classical Imaging (CI) mode, in which a single filter is used for imaging.

SPHERE is also capable of implementing the angular differential imaging (ADI) technique. As the VLT consists of Alt-Az telescopes, the sky rotates relative to the orientation of the telescope and attached instruments. Many instruments therefore receive light from the telescope through a derotator, a rotating optical element that corrects for this effect. When using the ADI mode, the instrument's derotator is disabled, and the field of view is allowed to rotate through the observing sequence. Whilst astrophysical sources such as stars and planets are seen to rotate around the optical axis (usually aligned to the target star), residual PSF aberrations originating from static optical components remain fixed, and it is therefore possible to discriminate between point-source-like speckles and true astrophysical objects (Marois et al. 2006).

However, the scheduling of ADI observations is significantly less flexible than non-ADI observations. Field rotation is maximised when a star is crossing the meridian, and falls off sharply with increasing hour angle, limiting possible observing times. Additionally, only targets within a few degrees of the zenith exceed maximum field rotation rates of 1 degree/minute, meaning that ADI observing sequences typically require tens of minutes to achieve a meaningful amount of field rotation. It was therefore clear that ADI was not compatible with the intention of the observations to act as a flexible series of short observations, and hence ADI was not used.

Table 5.1: Log of observations carried out with SPHERE.

Target	Date	Note	Target	Date	Note
EPIC 204221263	2017-03-05		WASP-73	2016-10-08	
EPIC 212803289	2017-08-28		WASP-74	2017-06-21	
HAT-P-41	2016-10-24		WASP-76	2016-11-07	
HAT-P-57	2016-10-08		WASP-80	2017-06-21	
–	2017-05-14		WASP-87	2017-04-01	
K2-02	2017-05-14	1	WASP-88	2017-05-14	
K2-24	2017-06-22		WASP-94	2016-10-08	
K2-38	2017-06-22	2	WASP-95	2016-10-20	
K2-39	2017-05-14		WASP-97	2016-10-08	
KELT-10	2017-05-14		WASP-99	2017-06-23	5
WASP-02	2017-05-14		–	2017-07-05	
WASP-07	2016-10-05		WASP-108	2017-03-04	
WASP-08	2016-10-05		WASP-109	2017-07-22	
WASP-16	2017-03-05		WASP-111	2017-05-14	
WASP-20	2016-10-05		WASP-117	2016-10-20	
WASP-21	2016-10-23		WASP-118	2017-07-05	
WASP-29	2016-10-08		WASP-120	2016-12-19	
WASP-30	2017-05-14		WASP-121	2016-12-24	
WASP-54	2017-03-04		WASP-122	2016-10-21	
WASP-68	2017-06-28	2, 3	WASP-123	2016-10-21	
WASP-69	2016-10-05		WASP-130	2017-03-10	
WASP-70	2017-05-14		WASP-131	2017-07-04	
WASP-71	2016-11-07		WASP-136	2016-10-24	6
WASP-72	2017-06-16	4	J0143	2016-10-31	3, 7
–	2017-07-04	5			
–	2017-07-05				

[1] K2-02 was not centred behind the coronograph, and is near the edge of the IFS field of view.

[2] Other datasets were obtained, but the target was not centred correctly.

[3] Other partial datasets were obtained, but observations were aborted due to weather or technical issues.

[4] Taken through thick cloud.

[5] Taken in poor seeing.

[6] Observations are archived under the name ‘J0001’.

[7] J0143 is currently unpublished; a public WASP-nnn identifier will be announced in future.

5.2.1 Observing sequence

The observations followed the typical SPHERE observing sequence, which comprises 'Flux', 'Centre', and 'Science' frames. In Period 98, the observing sequence was Flux-Centre-Science; in Period 99 a Flux-Centre-Science-Centre-Flux sequence was used.

'Flux' observations consist of an image of the target field, with the target star offset from the coronograph. This observation provides a reference for the stellar PSF, and was also used to measure the flux of the primary star, allowing relative flux measurements to be derived for any detected companion.

'Centre' observations are obtained once the target star is placed behind the coronograph. As this significantly reduces the signal from the primary, it can be difficult to accurately determine the position of the primary for the purposes of astrometry. For SPHERE, the solution is to intentionally introduce an aberration into the adaptive optics correction which produces four off-axis ghosts of the target star's PSF, located at the four points of a cross centred on the target star. Through the measurement of the points in this 'waffle pattern', it is possible to accurately locate the primary star after it is placed behind the coronograph.

Finally, 'Science' observations are a series of coronographic exposures with both IRDIS and the IFS to obtain enough signal to detect faint companions. The total exposure time with both instruments was 256s, chosen to allow the detection of companions at the hydrogen burning limit for the most distant target stars.

5.3 Data reduction

In this work, the process of data reduction for SPHERE was mainly handled by the SPHERE pipeline, provided by ESO. Some additional modifications and improvements to the IFS reduction process were included, based on the `VLTPF` package[1], which implements the additional reduction steps outlined in Vigan et al. (2015). The following

[1]Available at `https://github.com/avigan/VLTPF/`

information is mainly derived from the SPHERE Pipeline Manual (Möller-Nilsson et al. 2016) and the tutorials for data reduction with IRDIS (Moehler & Lundin 2017a) and the IFS (Moehler & Lundin 2017b).

5.3.1 IRDIS

IRDIS is fitted with a HAWAII HgCdTe infrared detector (Girard et al. 2017). As with standard CCD detectors, the individual pixels on the detector are read out to create an image, and the data reduction process generally follows the standard procedure for CCD photometry. As previously mentioned, IRDIS' optics produce two separate images of the target field on the detector, one on each half; the entire detector is read out as a single frame, including the two illuminated areas and the remaining unilluminated areas.

5.3.1.1 Dark frame subtraction

A set of dark frames are obtained for subtraction from each observation. As IRDIS has essentially zero dark current, the dark frames are mainly used to capture structured noise due to the detector readout electronics, which vary with exposure time and readout mode (Möller-Nilsson et al. 2016). By far the most noticeable effect in the dark frames is the contribution of bad pixels, with a large number of hot pixels (i.e. those with high dark current) across the detector array. Pixels with abnormally low, high, or variable counts are recorded as 'bad' pixels.

5.3.1.2 Flat field correction

A series of flat frames are obtained with a calibration lamp internal to IRDIS. Pixels with abnormally low or high response are marked as bad, in addition to any pixels with high variability between each frame. The flat frames are also used to determine

the regions of the detector which are illuminated, and hence the positions of the 'left' and 'right' images.

5.3.1.3 Instrumental background correction

IRDIS science exposures show a clear, complex background structure, mainly consisting of a curved feature (perhaps due to a curved optical element) and a background gradient in each of the illuminated regions, causing the background to vary by a factor of two across each region. These features originate at a stage in the SPHERE optical path before the IRDIS shutter, and hence are not seen in IRDIS internal flat fields using the calibration lamps. A series of images are taken with the shutter open, with the instrument set in the same optical configuration as observations, as the background varies significantly with different filters, beamsplitters, and so forth.

5.3.1.4 Bad pixel interpolation

As previously mentioned, bad pixels on the IRDIS detector are identified using the dark and flat frames. Bad pixels are interpolated from the adjacent 8 pixels, excluding any that are also marked as bad (Möller-Nilsson et al. 2016). Interpolation is applied to both the calibration frames (master dark, master flat, etc.) and the science frames.

5.3.2 IFS

The IFS is fitted with a HAWAII HgCdTe detector that is nominally identical to that fitted to IRDIS (Girard et al. 2017), although the IFS detector suffers from a higher fraction of bad pixels. Observations with the IFS produce frames filled with thousands of low-resolution spectra in a geometric pattern, which must be individually identified, extracted and wavelength-calibrated. After each spectrum has been reduced, the SPHERE pipeline extracts flux values at 39 points along each spectrum, and uses this

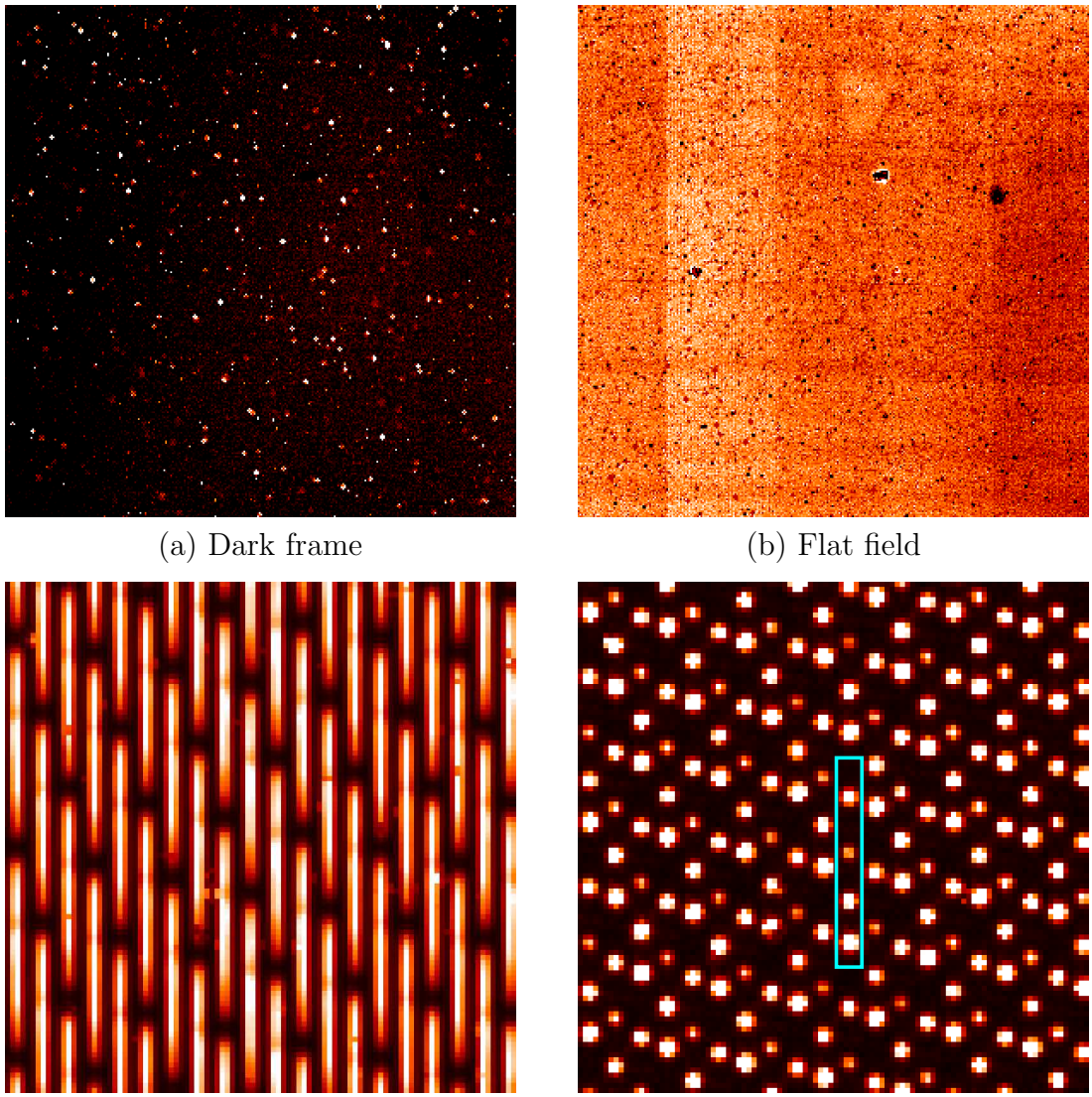

(a) Dark frame

(b) Flat field

(c) Spectra positions

(d) Wavelength calibration

Figure 5.1: Examples of calibration frames used to reduce SPHERE/IRDIS or SPHERE/IFS data; steps (c) and (d) apply to the IFS only. (a) Master dark frame, showing the presence of numerous hot pixels. (b) Detector flat field using the broad-band calibration lamp. The vertical striping effect due to the detector pre-amplifiers is visible. (c) Spectra positions calibration frame, with each lenslet brightly illuminated. Small variations in the brightness of different slits may be noticeable, caused by variations in lenslet throughput which are later corrected using the IFU flat field. (d) Wavelength calibration frame, with four monochromatic lasers illuminating each slit. The blue box indicates the position of a single slit. All images are shown with a linear colour scale, with the parameters set to highlight pertinent features; images (a) and (b) cover 300 pixels per side; (c) and (d) cover 100 pixels per side.

information to create a set of 39 monochromatic images. Examples of dark, detector flat, spectra position, and wavelength calibration frames are shown in Figure 5.1.

5.3.2.1 Dark frame subtraction

The dark frame subtraction process for the IFS is identical to that outlined for IRDIS in Section 5.3.1.1.

5.3.2.2 Spectrum position determination

The position of each individual spectrum on the detector must be known in order to permit each spectrum to be extracted and wavelength calibrated. A calibration frame is taken with the slits brightly illuminated, and their measured positions are used to offset and rotate a model predicting their positions. In addition, the pipeline can also attempt to correct for distortion, by fitting a 2D 4th-order polynomial to the x and y positions of the spectra (Möller-Nilsson et al. 2016).

5.3.2.3 Wavelength calibration

Each individual spectrum is wavelength calibrated by illuminating the IFS with four monochromatic lasers of known wavelength (0.988μm, 1.124μm, 1.309μm, and 1.545μm). For each spectrum, the positions of the four spectral lines are measured, and a polynomial is fitted to determine the observed wavelength in each pixel. The predicted wavelength calibration, based on the instrument model adopted in the previous section, is then updated.

5.3.2.4 Detector flat field correction

The IFS detector flat field corresponds to the normal flat fielding technique, correcting for pixel-to-pixel variations in detector response and linearity. However, the IFS covers a much wider spectral range than normal imaging techniques, and so it is expected

that the wavelength dependence of the flat field will be non-negligible – the detector response at 0.95μm may be very different to that at 1.65μm.

Four monochromatic lamps are used to determine the wavelength dependence of the IFS detector. For each pixel, a polynomial is fitted to the response as a function of flat field lamp wavelength, and the final flat field value is determined based on the expected wavelength of light reaching the pixel, following the calibrations detailed in the previous two sections. The resulting calibration is referred to as the 'super flat frame'.

In addition, a fifth flat field is obtained using a 'white' broadband lamp. This frame is firstly intended to correct for a vertical striping effect seen on the IFS, caused by the detector pre-amplifiers. In addition, the SPHERE Pipeline Manual states that the detector flat field is variable over short timescales (being stable at the level of 0.1% for only an hour); it is therefore suggested that broadband flat fields are taken during the night to correct for short term variability. However, accuracy at the 0.1% level was not required for the observations, and night time flat frames are not provided by default; therefore no correction was made for such short-term variability.

5.3.2.5 IFU flat field correction

In addition to pixel-to-pixel response variations, the IFS also shows lens-to-lens variations within the lenslet array – i.e. throughput is higher for some of the lenslets than others. These variations are determined by illuminating the lenslet array and measuring the average flux in each of the resulting spectra, and an integral field unit flat (IFU flat) is created to correct for these variations. This is the same calibration as the 'lenslet flat' used by some other IFS pipelines (e.g. Brandt et al. 2017).

5.3.2.6 Wavelength cube creation

At this stage, the science images are corrected using the master dark and super flat frame, and bad pixels are interpolated. The bad pixel interpolation routine from the

`VLTPF` package is used, which interpolates based on vertically adjacent pixels only. This accounts for the fact that the spectra on the IFS are orientated vertically, and hence horizontally adjacent pixels are likely to be unilluminated regions of the detector. In addition, `VLTPF` undertakes a search for bad pixels in the science data itself rather than relying only on the calibration frames, identifying numerous temporary hot pixels that are not present in calibration frames taken several hours before or after.

The individual spectra are now extracted, and corrected for the IFU flat field. Flux values are then extracted from the spectra at 39 points, resulting in a hexagonal grid of flux measurements for each of the 39 wavelengths. The final step is to interpolate from the hexagonal grid onto a square grid of pixels, allowing the data to be analysed with standard astronomy and image manipulation software, producing a datacube with dimensions (x,y,λ).

5.3.3 SPHERE Data Centre reductions

The SPHERE Data Centre (DC) was set up to support the operation of the SPHERE instrument, providing a dedicated source of data reduction expertise (Delorme et al. 2017). Since September 2017, the DC has offered reduction services to all instrument users. The DC uses a modified and updated data reduction pipeline, which includes a number of upgrades not available in the public version. These include corrections for instrument anamorphism (Maire et al. 2016) and the application of numerous PSF removal algorithms.

Comparisons were made between my reductions of IRDIS and IFS data and those of the DC (i.e. between the public and DC versions of the pipeline). No noticeable improvement was noticed for IRDIS data, but the DC reductions of the IFS were found to be of better quality. Subsequent introduction of the `VLTPF` routines and careful consideration of pipeline options has greatly improved the quality of my own reductions, and these are used throughout this work.

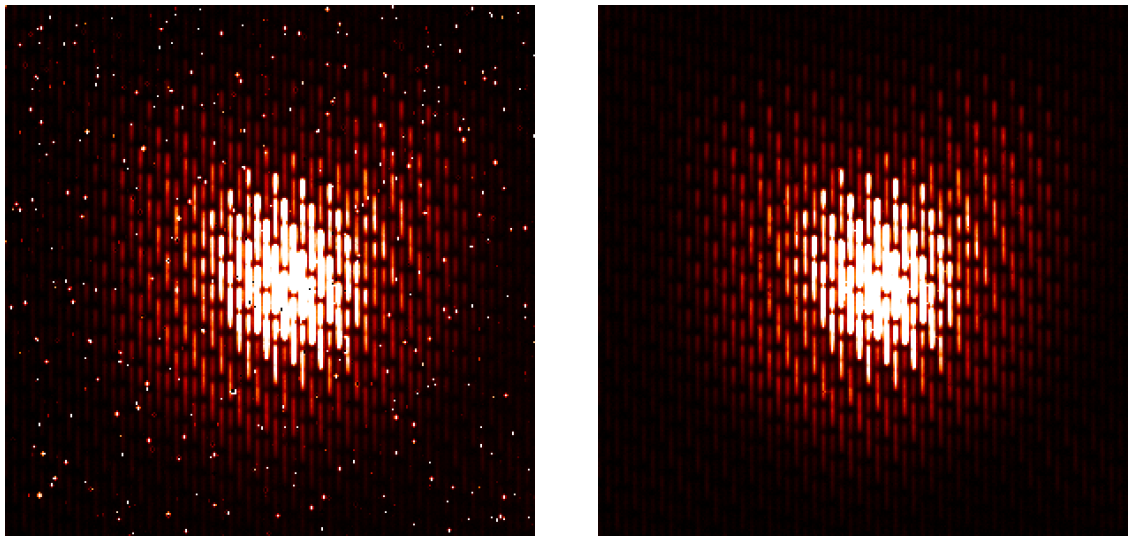

(a) Raw frame

(b) Corrected for detector response

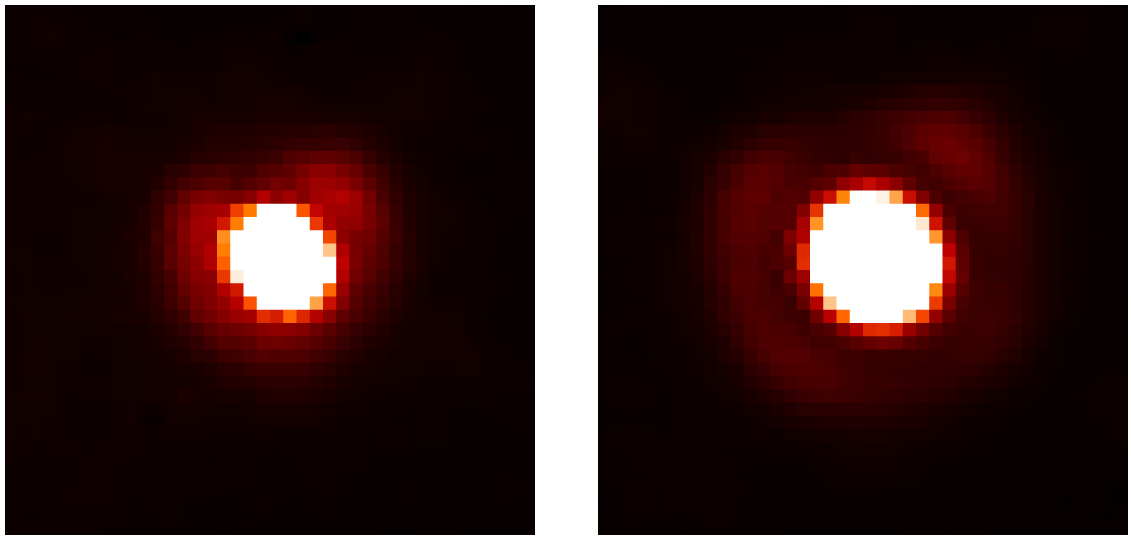

(c) Extracted image at $\lambda = 1.017\mu$m

(d) Extracted image at $\lambda = 1.589\mu$m

Figure 5.2: Reduction of IFS science data frames. (a) Raw science frame with a star visible, with the top of each spectrum being the long wavelength end. Numerous bad pixels are visible, which would severely impact the extracted spectra if not corrected for. (b) Science frame after correction for dark current, detector flat frames, and correction of all bad pixels identified in the calibration process. The dark gap visible in each spectrum is due to poor atmospheric transmission between the J and H bands; a second, lesser gap can also be seen between Y and J. (c) Final extracted image at a wavelength of 1.017μm. (d) Final extracted image at a wavelength of 1.589μm. Note the increased size of the PSF in (d) compared to (c), as a result of increased wavelength. Some PSF imperfections are visible, due to incomplete correction by the AO system.

5.4 Data analysis

The reduced IRDIS and IFS data were inspected by eye to identify stellar companions to the target star. At a later date, it is intended that an automated detection algorithm will be developed, allowing the survey's detection limits to be more easily quantified.

5.4.1 Astrometry

Plate scale and detector orientation values were adopted from Maire et al. (2016). For IRDIS using the K_S filter, the plate scale[2] is 12.265 ± 0.009 mas/px with a true north offset of $-1.75 \pm 0.08°$. The reduced IFS data has a scale of 7.42 ± 0.02 mas/px, and is rotated relative to the IRDIS detector by $+100.48 \pm 0.10°$.

The optical distortion in SPHERE is dominated by a relative compression $0.60 \pm 0.02\%$ along one axis, aligned to the vertical direction in IRDIS, and rotated by 100.48° for the IFS. Higher order optical distortions are neglected, and Maire et al. (2016) estimates that these are below 1 mas in amplitude.

The observations presented here are not affected by the time-variable derotation error noted by Maire et al. (2016), as they were taken after SPHERE's clock synchronisation issues were solved in July 2016.

The published results in Evans, Southworth & Smalley (2016) contained an error in the calculation of the position angle of WASP-20B, which is incorrect by several tens of degrees. This issue occurred due to the formula for calculating the true North angle for field-stabilised data being incorrectly applied to pupil-stabilised data. The error is corrected in this work, with the correct formula selected for each dataset based on data stored in the FITS file headers.

[2]The error bar of 0.009 mas/px quoted for the H2 filter in Maire et al. (2016) applies to all filters (A.-L. Maire, priv. comm.)

5.4.2 Photometry

All photometric measurements of companion stars are determined relative to the flux of the brightest star, facilitated by obtaining additional 'flux' (i.e. non-coronographic) observations of the target field. Relative photometry avoids the complication (and additional telescope time) required for calibration using standard stars. In addition, observations were permitted in conditions of thin cloud due to relaxed requirements compared to exoplanet direct imaging; in some observations, relatively poor atmospheric transmission due to cloud is noticeable. Calibrated near-infrared photometry of all targets is present in the 2MASS survey, with some well separated companions ($\gtrsim 4''$) being resolved in this survey. For closer companions, measurement of the flux ratio from SPHERE data allows the unresolved 2MASS photometry to be split between the two stars.

In order to prevent saturation, 'flux' observations were taken with a neutral density filter, which has significant variations in transmission. The 'flux' observations were corrected for the transmission of the neutral density filter[3] as well as for the difference in exposure time. In some cases, relative fluxes can be determined directly from the 'flux' frame alone, measuring both target and companion star on these images; however, for all but the brightest companion stars, the short exposure time and low transmission would lead to large uncertainties on the flux ratio.

5.4.3 Poor instrument background subtraction

As mentioned in Section 5.3.1.3, IRDIS shows a significant and highly structured background pattern. Examples of this pattern from science and calibration frames are shown in Figure 5.3. Whilst the calibrations show the same overall structure as the science frames, the fine detail within the circular structure is significantly different, in addition to differences in background gradient and offset. Other instrument users

[3]Transmission curves are available at `http://www.eso.org/sci/facilities/paranal/instruments/sphere/inst/filters.html`

have also noted the issue, likely caused by differences in the optical setup between observations and daytime calibrations – for example, coronographs are not typically placed into the optical path during daytime calibrations, and on-sky calibration frames taken immediately after observations provide good correction (C. Ginski, priv. comm). However, on-sky calibrations were not scheduled for these observations, and hence are not available.

The background pattern of the science frames is not well fitted by simple linear transformations of the calibration frame. Figure 5.4 shows the best possible match between the two frames using additive and multiplicative operations, but the curved structure is clearly of a different form and cannot be matched. If left uncorrected, the complex background structure will complicate automated detection of faint companion stars with a signal comparable to the variation in background level, although bright companions can more easily be identified.

Further work is needed to determine the best method to correct or subtract this background. Preliminary investigations have indicated that the background pattern seen in science frames is relatively consistent, with simple multiplicative and additive transformations of the background derived from other science datasets providing much better agreement than is possible with the calibration frames. By masking out the areas in each dataset with stars visible and normalising the background, it may be possible to use the observations to calibrate one another, either by selecting the best-matching comparison image, or instead through the combination several reference images. Similar techniques have already been used to good effect for PSF subtraction, especially for exoplanet direct imaging (e.g. Lafrenière et al. 2007, Amara & Quanz 2012, Soummer, Pueyo & Larkin 2012).

5.4.4 Detector persistence

Infrared detectors of many types suffer from an effect known as ‘detector persistence’, ‘charge persistence’, or ‘latent charge’. Bright illumination of the detector results in increased counts from the previously illuminated pixels in subsequent readouts, which

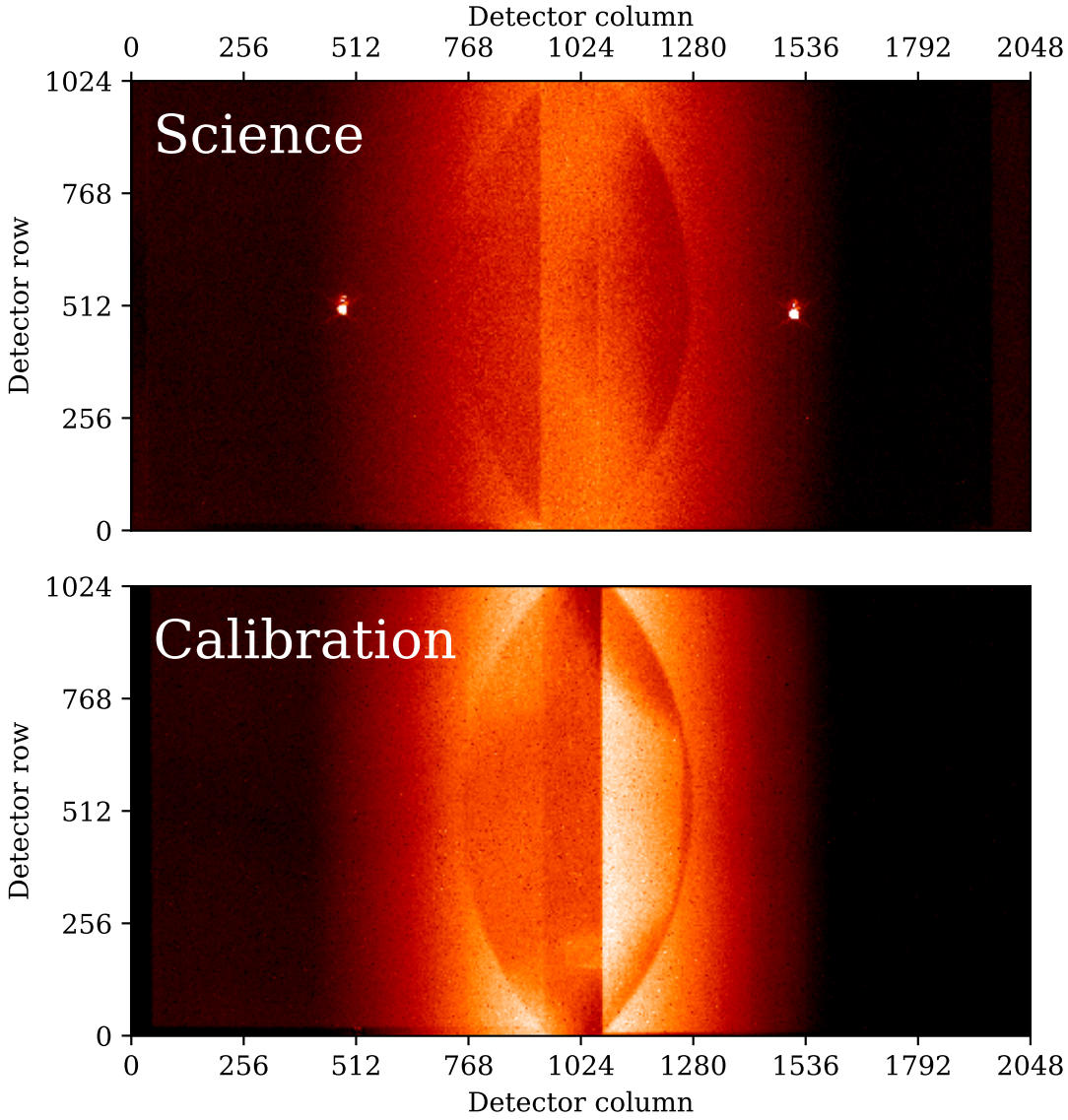

Figure 5.3: The instrument background for SPHERE/IRDIS, comparing an on-sky observation (top, with stars visible) and the corresponding calibration frame (bottom). Both images are displayed with the same linear colour scale, after the correction of an offset in base background level. There is an overall resemblance between the two images, with the illuminated regions showing a gradient and a curved feature. However, the amplitude and detailed structure of the background signal differ significantly, particularly inside the curved feature.

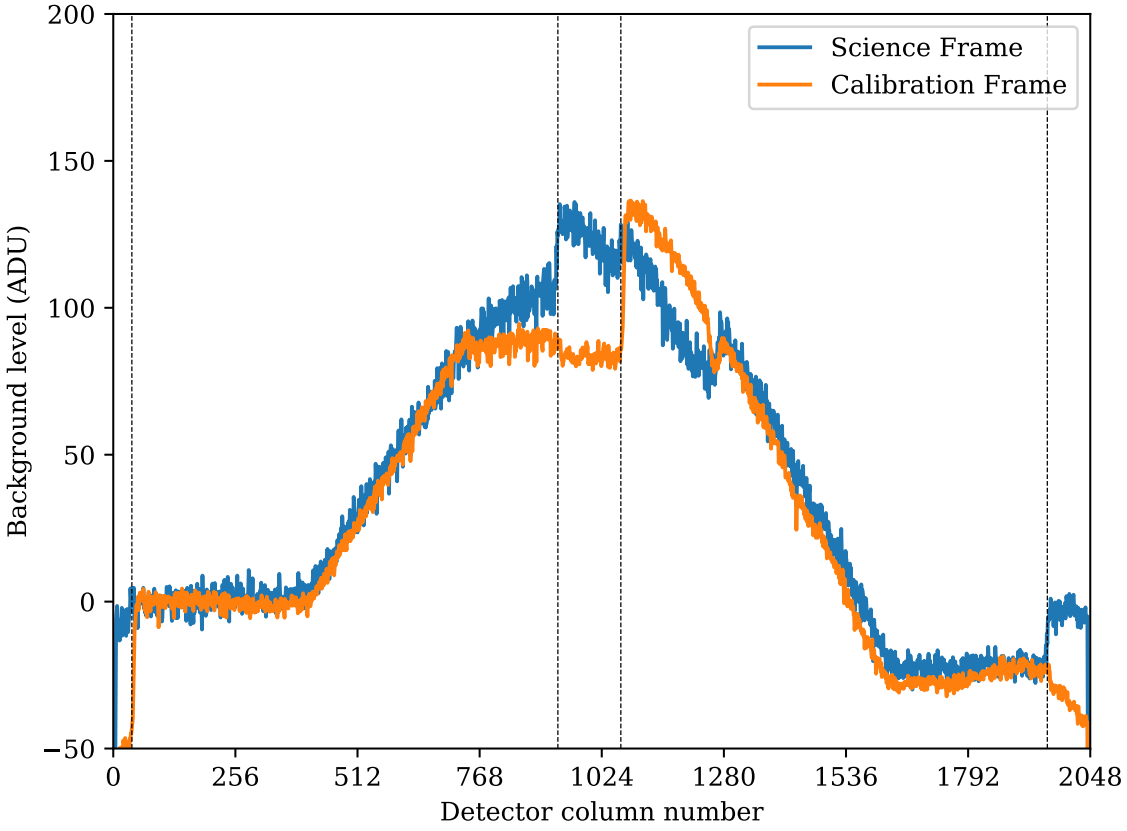

Figure 5.4: Cuts at pixel row 440 of the two images previously shown in Figure 5.3, showing the background levels of the science observation in blue and calibration observation in orange. The black dashed lines show the limits of the two illuminated regions on the detector. The calibration observation has been scaled to best match the science observation, but there are clear differences in the structure of the background pattern for detector columns 700∼1300, corresponding to the curved feature visible on the images.

can remain detectable for several hours (Campbell & Thompson 2006). The effect is caused by photoelectrons becoming trapped in defects in the detector structure and later released, with those released during a subsequent exposure being measured at detector readout (e.g. Smith et al. 2008). The counts generated by persistence typically depend on the flux of the illuminating source (bright sources generate more persistence than long exposures of faint sources) and the time since illumination. There have been sporadic reports (often anecdotal) that persistence can be reduced by repeatedly reading out the detector to 'flush out' the trapped photoelectrons, but such an effect was not verified in laboratory tests by Campbell & Thompson (2006). Whilst persistence remains an issue, developments in detector manufacturing have allowed modern HgCdTe detectors to achieve less than 0.01% persistence below 80% full well depth (Blank et al. 2011), with persistence below 100ppm specified for the SPHERE/IFS detector (Claudi et al. 2008).

The observations obtained with IRDIS show no identifiable evidence of persistence, as would be expected from the detector specification. This is confirmed by an observation of K2-02 on 2017-05-04, in which an error in the coronograph centring process resulted in the unobscured target star being imaged without a neutral density filter, significantly overexposing the images in the following 256s exposure. However, the corresponding IFS data show persistence that is clearly visible by visual inspection, with the subsequent off-axis flux frame showing a residual level of approximately 30 counts/px/frame in the most heavily overexposed region (the detector being saturated at 40,000 counts in the science exposure). Table 5.2 shows measurements made in the next frame obtained after the overexposed observation, approximately 90 seconds later, taking the mean and RMS of the counts in 25×25 pixel regions. On each detector, one region was centred on the previously overexposed pixels, whilst two regions were placed in nearby, unilluminated regions (70 pixels away for IRDIS, 140 pixels for the IFS). While IRDIS does not show any increase in counts above the background, the IFS clearly shows elevated counts in the previously overexposed region. The effect is clearly visible in the raw frames, shown in Figure 5.5.

Persistence has also been detected in several cases where images were not overex-

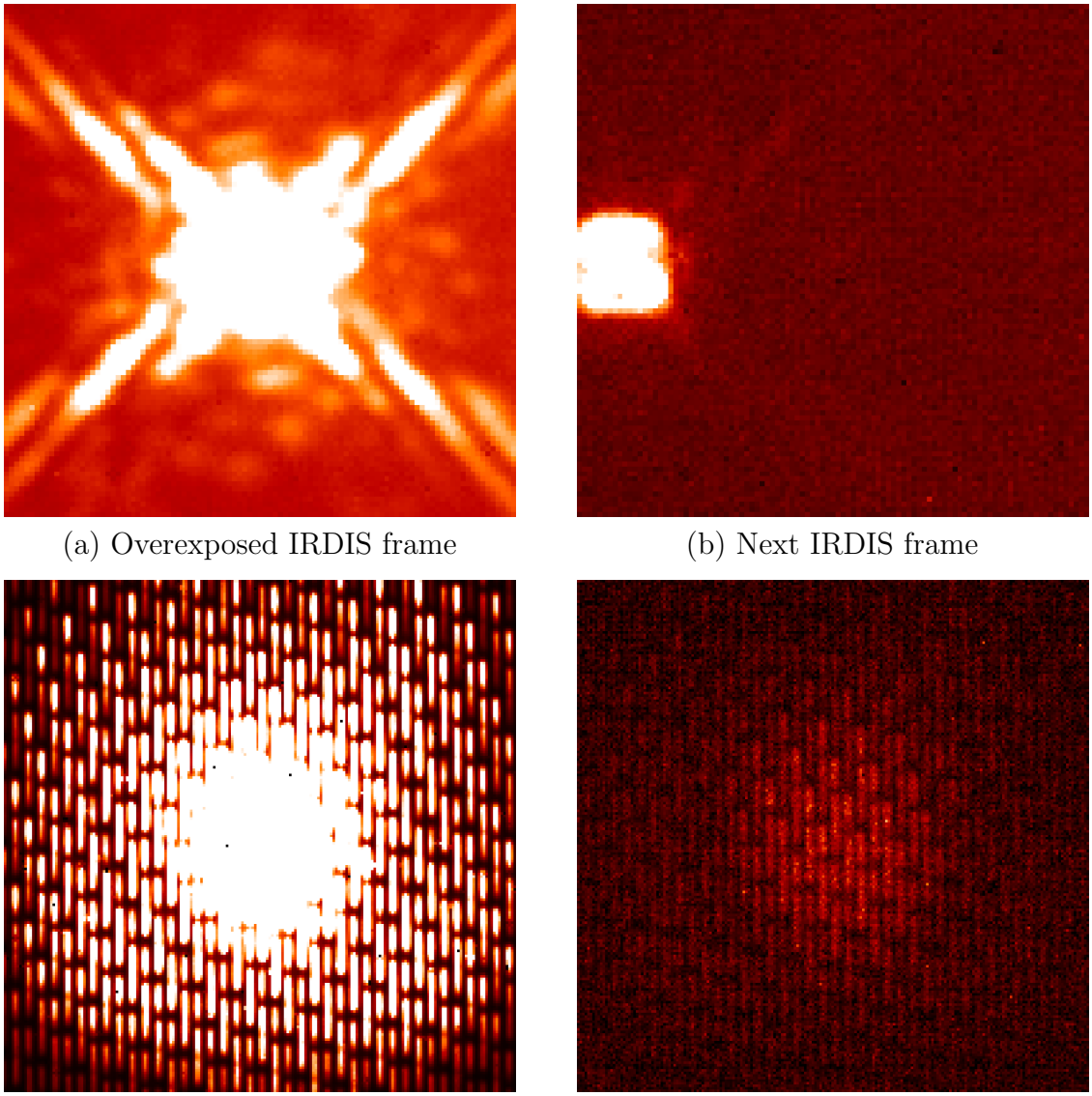

(a) Overexposed IRDIS frame

(b) Next IRDIS frame

(c) Overexposed IFS frame

(d) Next IFS frame

Figure 5.5: The effect of detector persistence in SPHERE/IFS. In the left hand column, panels (a) and (c) show overexposed images from IRDIS (a) and the IFS (c). The next frames read from each detector are shown in the right hand column in panels (b) and (d); these were flux calibration observations during which the telescope was offset, and so the original detector location was unilluminated. No residual effects are visible in IRDIS, but a clear afterimage is visible in the IFS data. The star visible in image (b) is the offset target star, and is not important for the purposes of persistence.

Table 5.2: Measurements of detector persistence in IRDIS and the IFS. These measurements were taken from the first frame obtained after an overexposed observation. 'Illuminated' indicates a region where an overexposed star was previously located (but is no longer illuminated), whilst 'Background' denotes an unaffected region that did not contain any stars. IRDIS shows no significant difference between the regions, whilst the IFS shows elevated counts due to persistence.

Detector	Region	Mean counts	RMS deviation
IRDIS	Illuminated	80.7	9.4
IRDIS	Background 1	75.7	8.9
IRDIS	Background 2	79.1	9.0
IFS	Illuminated	29.7	13.9
IFS	Background 1	4.2	7.3
IFS	Background 2	2.6	7.5

posed, leading to several false detections when other survey targets were subsequently observed. These mainly consist of residual images at the 1% level from previously observed bright companion stars such as WASP-2B and WASP-76B, and technical issues that resulted in incorrect placement of stars behind the coronograph during science exposures. However, there is at least one case where persistence is visible from a previous observation from a separate, unrelated project.

False detections due to persistence can be identified by comparison of the 'flux' and 'science' frames. In order to obtain the 'flux' observation, the field of view is offset slightly to move the target star away from the coronograph. Whilst real companions will move with the target star, false positives will remain stationary on the detector, and the two can be easily distinguished through visual inspection of the two frames. Table 5.3 lists the false positive detections identified through this method.

It is unclear why there is such a large difference in the persistence properties of detectors fitted to IRDIS and the IFS, given that they are the same model of detector from the same manufacturer, used in relatively similar instruments. Possible hypotheses include differences in the arrangement of the detector electronics, or a difference originating during the manufacturing process, and investigations by the instrument

Table 5.3: False positive detections of companions with SPHERE/IFS due to detector persistence. The listed coordinates are taken from the final reconstructed images.

Target	Coordinates	Source
WASP-30	(195, 63)	Overexposure in previous data due to technical issue.
WASP-71	(178, 194)	Persistence due to the companion to WASP-76.
WASP-109	(86, 69)	Overexposure in previous data due to technical issue.
WASP-131	(124, 158)	Persistence from a previous, unassociated observation.

team are ongoing (H. Boffin, priv. comm).

5.4.5 IFS wavelength recalibration

During the reduction of IFS observations of WASP-20, it was noted that atmospheric absorption features were systematically redshifted compared to their expected wavelengths. A similar effect was noted by Vigan et al. (2015), who found discrepancies between the size of the diffraction patterns and the reported wavelengths. These effects both indicate an error in the wavelength calibration performed by the data reduction pipeline. This issue was reported as fixed in version 0.31.0 of the pipeline, released on 2017-12-22; however, the reduction and analysis outlined in this chapter were performed prior to this date.

Vigan et al. (2015) outlined two methods to correct the wavelength calibration: a custom reduction of the wavelength calibration data, or a method based on the size of the 'waffle' pattern in the 'centre' frames, which scales with wavelength like a normal PSF. The former procedure was adopted in this work, which treats the wavelength calibration frames as science data. In these frames, the entire array is illuminated with four monochromatic calibration lamps simultaneously. Reducing these frames as if they were science data to create an (x,y,λ) datacube, Each slice is collapsed in the x and y spatial directions to give a single measurement of the spectrum across the entire detector, which clearly shows four emission lines corresponding to the calibration lamps.

The spectrum is plotted as flux against slice number, and the centres of the four lines fitted simultaneously using Gaussian profiles. A third order polynomial is used to match the wavelengths of these peaks to the known line wavelengths of 0.9877μm, 1.1237μm, 1.3094μm, and 1.5451μm (Möller-Nilsson et al. 2016). The original and corrected wavelength solutions are shown in Figure 5.6.

5.4.6 Detection limits

Detection limits for both IRDIS and the IFS were determined using the same method as for the lucky imaging, described in Sect. 3.6.4. The mean μ and standard deviation σ of pixel counts within an $n \times n$ pixel box were taken, with n set to equal the FWHM of the target PSF. A companion was assumed to be detected if it had $\mu + 5 \cdot \sigma$ counts, and this number of counts was converted to a magnitude difference by taking the counts in an $n \times n$ box centred on the target star in the 'Flux' (i.e. non-coronographic) calibration image, scaled to the exposure time as necessary. For the IFS, all wavelength bands were combined into a single image.

Figs. 5.7 and 5.8 show the detection limits for IRDIS and the IFS respectively. The inner working angle of the `N_ALC_YJH_S` coronograph used during these observations is approximately 0.15″ (Girard et al. 2017), below which the contrast limit is no longer reliable, as any companion would also begin to be attenuated by the coronograph. The structure in the detection limit at and just below this point is due to starlight from the target leaking past the edge of the coronograph.

Compared to the lucky imaging contrast ratios shown in Sect. 3.6.4, the main advantage of SPHERE is obvious: while the lucky imaging detection limit is noticeably affected by the target star out to 4″, both SPHERE instruments are background limited before reaching an angular separation of 0.4″. While the magnitude limits of the lucky imaging and SPHERE appear similar (and in the case of IRDIS, somewhat worse), it should be noted that cool, red companion stars have a much more favourable magnitude ratio in the NIR.

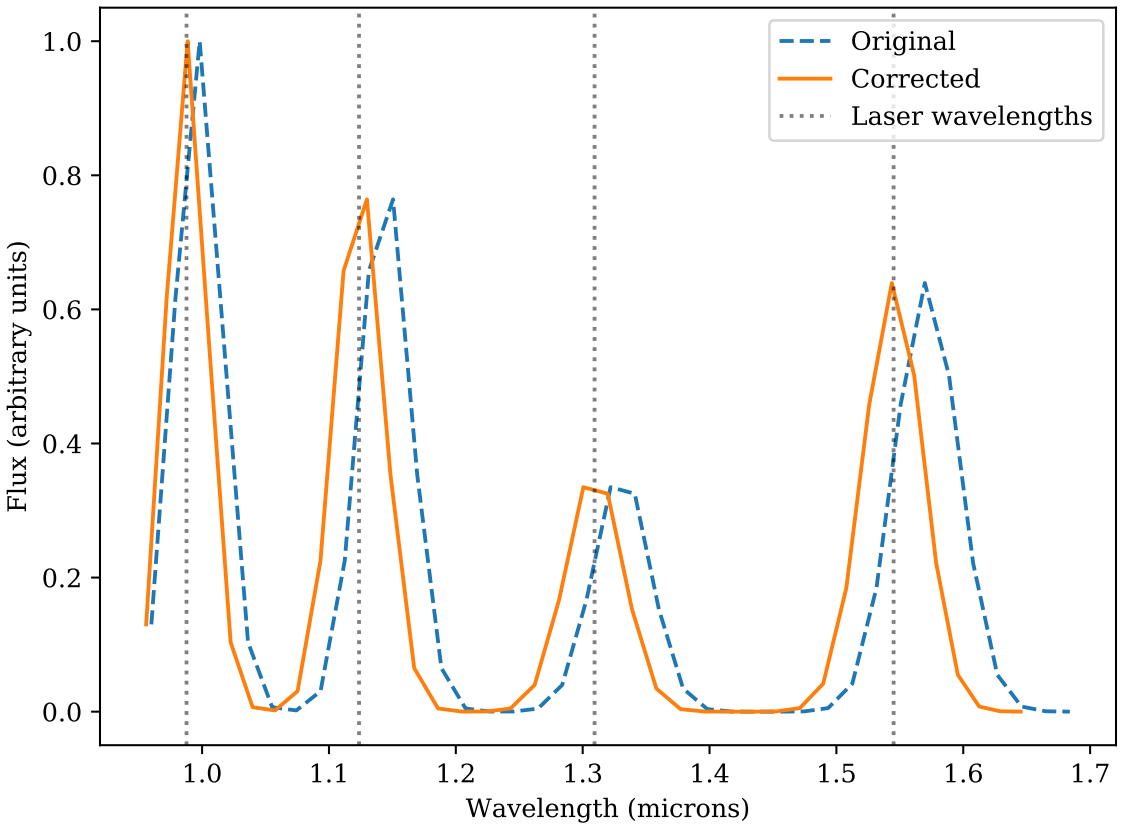

Figure 5.6: Recalibration of the SPHERE/IFS wavelength solution. Plotted is the measured flux in the IFS wavelength calibration frame, where the detector is illuminated by four monochromatic lasers, with wavelengths indicated by vertical dotted lines. The SPHERE reduction pipeline wavelength solution (dashed blue) is clearly discrepant, producing redshifts for all four lines, whilst the recalibrated solution (solid orange) gives the correct positions for these lines.

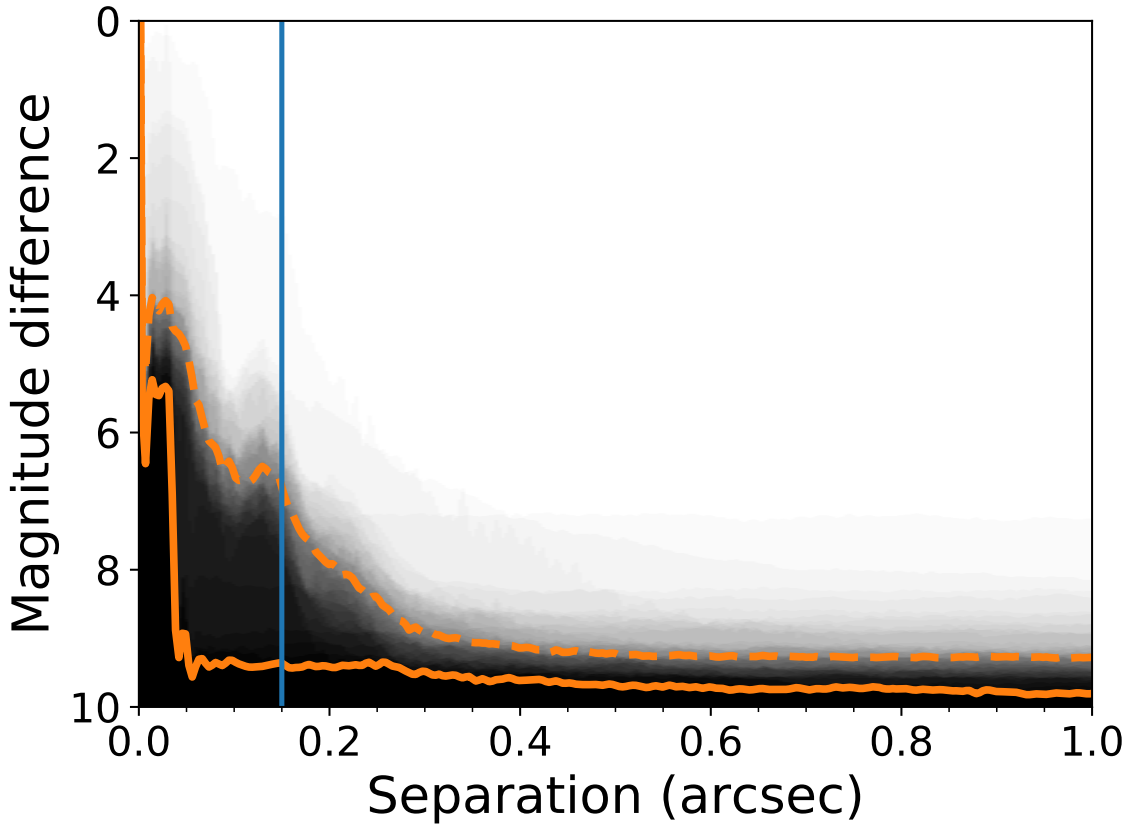

Figure 5.7: Detection limits for IRDIS. Shading on the image indicates the fraction of observations for which a given contrast was achieved, with white indicating 100%, and black 0%. The dashed line indicates the median contrast across all targets. The solid line indicates the contrast of the best observation. The vertical blue line indicates the approximate inner working angle of 0.15″.

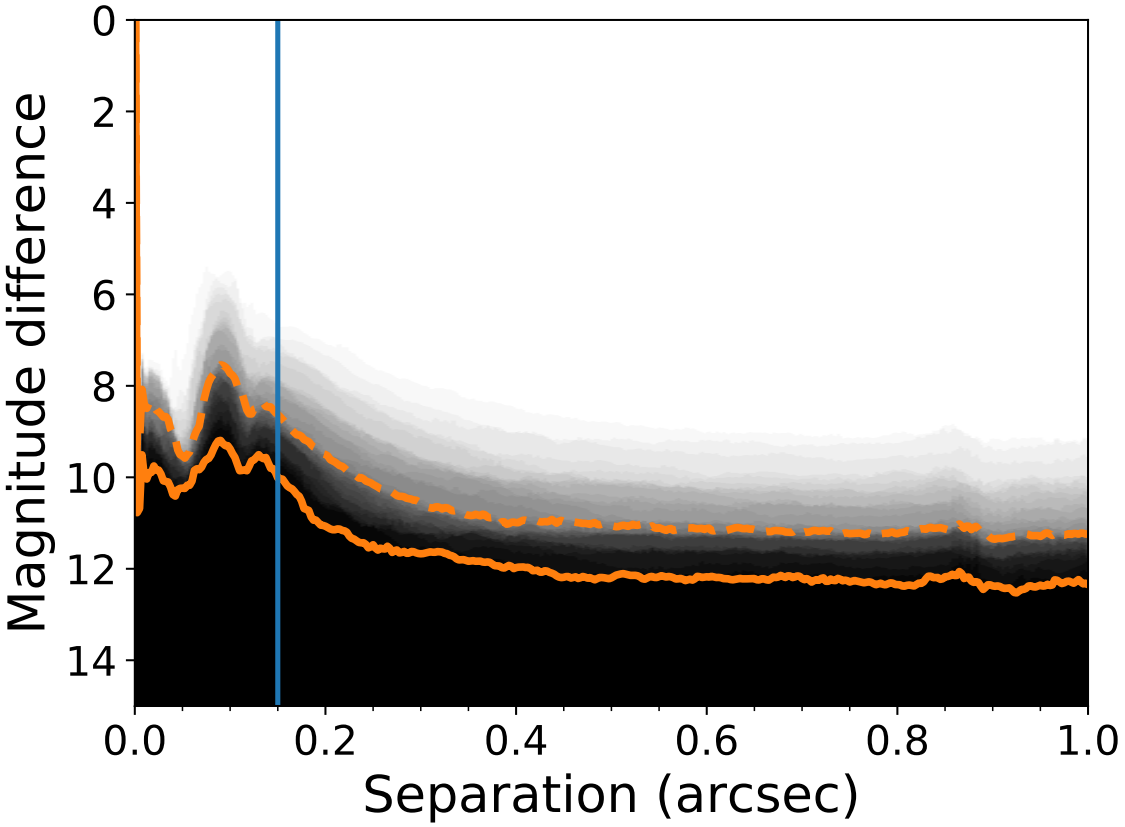

Figure 5.8: Detection limits for IFS. Description as for Fig. 5.7

5.5 Results

Of the 46 targets observed, additional point sources were identified for 26 targets, with HAT-P-57, WASP-108 and WASP-120 each having two detected companions. Eight of the detected companion stars are detected in IFS data. A further two systems have objects detected in IRDIS that are within the IFS field of view, but have not been detected in the IFS. Preliminary astrometric and photometric results from the IFS are presented in Table 5.4, and preliminary astrometry from IRDIS is presented in Table 5.5.

When comparing Tables 5.4 and 5.5, there is a noticeable systematic difference in separation between the IFS and IRDIS astrometry, with the IFS producing smaller separations. It is not yet known which detector's astrometric solution is in error, although there is tentative evidence that the IRDIS separations are a better match to literature values. In addition, IRDIS position angles occasionally show significant offsets to literature values, but without any clear trend. It is intended that archival SPHERE observations of astrometric calibration targets will be reduced using the same reduction process as the science data, in order to better understand the astrometric properties of the data.

With the exception of WASP-20, detailed characterisation has not taken place for newly detected companions. This process will involve determination of their stellar parameters, using additional archival or future observations where required, and investigation of whether the companions are physically associated with the target stars. This could come through confirmation of common proper motion, or by comparison of the colours and relative brightness of the target and companion stars.

Information about the detected companions, including the results of previous searches for companions to these systems (successful or otherwise), is summarised in the following brief notes on each target.

HAT-P-41: The stellar companion is well known, having been detected in the TCI survey in 2014, 2015 and 2016, and independently by Wöllert et al. (2015), Wöllert & Brandner (2015), and Ngo et al. (2016). Analysis of the companions colours in both

Table 5.4: Properties of companion stars detected by SPHERE/IFS. Position angles (P.A.) are measured in degrees eastwards of North. Differential magnitudes in Y, J, and H are calculated from binned IFS photometry.

Target	Sep. (mas)	P.A. (°)	ΔY (mag.)	ΔJ (mag.)	ΔH (mag.)
WASP-2	710.4 ± 2.0	103.61 ± 0.19	3.051 ± 0.010	2.850 ± 0.008	2.845 ± 0.006
WASP-20	245.4 ± 0.9	210.00 ± 0.25	1.036 ± 0.007	0.891 ± 0.006	0.881 ± 0.005
WASP-72	640.0 ± 1.8	333.85 ± 0.20	4.134 ± 0.009	3.814 ± 0.007	3.579 ± 0.005
WASP-76	413.3 ± 1.3	213.07 ± 0.21	2.753 ± 0.008	2.531 ± 0.011	2.369 ± 0.006
WASP-108	146.1 ± 1.2	201.43 ± 0.46	4.503 ± 0.019	4.165 ± 0.012	4.069 ± 0.008
WASP-122	798.6 ± 2.8	348.51 ± 0.21	6.152 ± 0.047	5.707 ± 0.022	5.552 ± 0.018
WASP-130	628.9 ± 3.5	98.29 ± 0.34	4.200 ± 0.019	4.084 ± 0.017	3.988 ± 0.011
WASP-131	193.7 ± 0.9	108.39 ± 0.39	3.578 ± 0.010	3.247 ± 0.008	3.066 ± 0.006

Table 5.5: Properties of companion stars detected by SPHERE/IRDIS. Position angles are measured in degrees eastwards of North.

Target	Sep. (mas)	Pos. Angle (°)
HAT-P-41	3590.2 ± 2.9	186.01 ± 0.14
HAT-P-57	2649.9 ± 2.0	232.40 ± 0.14
	2769.5 ± 2.1	227.42 ± 0.14
K2-38	1403.3 ± 3.8	184.45 ± 0.21
WASP-2*	725.4 ± 1.1	105.41 ± 0.11
WASP-7	4441.6 ± 3.9	231.31 ± 0.14
WASP-8	4513.0 ± 4.0	168.74 ± 0.14
WASP-20*	254.7 ± 0.8	209.42 ± 1.22
WASP-54	5701.1 ± 4.5	116.38 ± 0.14
WASP-70	3168.9 ± 2.6	167.22 ± 0.08
WASP-72*	629.4 ± 0.8	334.86 ± 0.10
WASP-76*	434.2 ± 0.7	211.49 ± 0.16
WASP-80	2090.9 ± 2.5	275.30 ± 0.10
WASP-87	4120.1 ± 4.4	202.50 ± 0.09
WASP-87	5556.3 ± 4.3	240.90 ± 0.08
WASP-88	3291.9 ± 2.8	355.57 ± 0.08
WASP-94†	351.5 ± 2.5	178.45 ± 0.43
WASP-97	5920.3 ± 4.7	269.48 ± 0.14
WASP-99†	410.3 ± 2.2	344.56 ± 0.33
WASP-108*	186.1 ± 0.8	196.77 ± 0.27
	5041.6 ± 5.3	173.16 ± 0.14
WASP-111	5075.0 ± 3.8	100.26 ± 0.08
WASP-118	1237.7 ± 1.4	244.71 ± 0.10
WASP-120	2096.4 ± 2.3	91.29 ± 0.14
	2192.3 ± 2.5	89.17 ± 0.15
WASP-122*	822.8 ± 1.5	346.22 ± 0.17
WASP-123	4741.5 ± 3.7	204.58 ± 0.14
WASP-130*	638.7 ± 1.4	99.14 ± 0.18
WASP-131*	178.7 ± 1.3	122.27 ± 0.41
WASP-137	1679.9 ± 1.4	176.13 ± 0.14

* Also observed in IFS data.

† Within IFS field of view, but not detected.

the visible (TCI survey) and NIR (Ngo et al. 2016) suggest it is a bound companion. The IRDIS position angle is $\sim 2^\circ$ higher than previous measures, which was been stable to better than 0.5° between June 2013 and April 2016; the cause of this difference is unclear. The separation measurement is in better agreement, and the combined dataset is suggestive of reducing separation.

HAT-P-57: The pair of companions was previously detected by Hartman et al. (2015), with their H and L′ photometry supporting the two stars being physically associated M dwarfs. Due to the small separation of the B and C components, it is likely that the system is a hierarchical triple, with the BC binary orbiting the planet-hosting A component. Hartman et al. (2015) gives only a single separation value between A and BC (2667 ± 1mas), and the separation between the B and C components (225 ± 2mas). The comparable measures from the IRDIS data are 2709.7 ± 1.5mas for the mean position of the BC binary, and 264.4 ± 0.5mas for the B-C separation. Both are significantly larger than the previous measures, and the differences are much too large to be attributed to orbital motion, given the estimated orbital periods of 500 years (B-C) and 14,000 years (A-BC). Further investigation is needed to determine why these measurements are so different.

K2-38: Sinukoff et al. (2016) reported Keck/NIRC2 AO observations of K2-38 using a Br-γ filter[4], with no detections down to a 5σ sensitivity limit of $\sim$8 magnitudes fainter over the $10''$ field of view. This target was also observed in the TCI lucky imaging campaign, with no detections within 10 arcseconds. The IRDIS detection is of a very faint source that is likely below the sensitivity limits of both surveys.

WASP-2: The binary companion to this system is well studied, with repeated measurements since 2007 (Collier Cameron et al. 2007, Daemgen et al. 2009, Bergfors et al. 2013, Wöllert et al. 2015, Adams et al. 2013, Ngo et al. 2015, TCI survey in 2014). The IRDIS astrometry agrees well with previous data, supporting the trend of

[4]Keck/NIRC2 observations routinely use a Brackett Gamma (Br-γ or BrG) filter in place of a K_S filter for bright stars. Compared to the K_S filter, the Br-γ has a similar effective wavelength, but a smaller passband, increasing the possible exposure time before saturation (see e.g. Sinukoff et al. 2016).

reducing separation noted during the analysis of the 2014 TCI data. There may also be a trend of increasing position angle, though the scatter in the measurements is high.

WASP-7: The faint companion was previously identified in the TCI survey, but was not detected by the NIR AO survey of Ngo et al. (2015). The IRDIS separation agrees with the TCI survey, but gives a larger position angle, perhaps indicative of the two stars being unbound and hence having different proper motions.

WASP-8: The close companion star was noted during the initial characterisation of the system, in addition to an astrometric measurement from 1930 recorded in the WDS (Queloz et al. 2010). The lack of any large change in separation or position angle, despite WASP-8's high proper motion, was taken as good evidence of common proper motion. Additional astrometry and photometry have since been obtained by Cubillos et al. (2013), Ngo et al. (2015), and the TCI survey in 2014 and 2016. The IRDIS separation agrees well with previous data, but has a significantly discrepant position angle (2°).

WASP-20: A close, bright companion was identified in the IRDIS and IFS data, and it is by far the brightest companion found within the IFS field of view in our observations. The companion was not detected during the verification and characterisation of the system by Anderson et al. (2015). A detailed analysis of this system is presented later in this thesis, and has been published in Evans, Southworth & Smalley (2016).

WASP-54: A very faint companion star was detected in the IRDIS data. The TCI survey previously identified a separate companion star, which was determined to be bound from optical photometry; this companion was just outside the IRDIS field of view.

WASP-70: Both stars were analysed by Anderson et al. (2014b), with the stars showing no relative motion over 13 years, matching spectroscopic distances, and similar radial velocities. Further observations were obtained by Wöllert & Brandner (2015) and the TCI survey. Position angle measurements for the system show significant scatter (approx. 2°), whilst the separation measured by Anderson et al. (2014b) is much larger than later measurements.

WASP-72: A companion star was discovered in the IRDIS and IFS data. Assuming a primary star with a temperature of 6250K and an age of 3 Gyr in conjunction with the Baraffe et al. (2015) isochrones, the YJH flux ratios measured from the IFS indicate that the companion is consistent with being a bound companion with $M{\sim}0.55\mathrm{M}_{\odot}$. Whilst the companion is just bright enough to produce the 0.4% depth transit signal in the optical, a factor of two difference in observed transit depth would be expected between the R band (5.6 mag. fainter) and I band (4.7 mag. fainter). This is not seen in the multicolour photometry presented in Gillon et al. (2013), indicating the brighter star is the source of the transit signal.

WASP-76: Wöllert & Brandner (2015) initially identified the companion from optical lucky imaging data, with further LI observations presented in Ginski et al. (2016) and NIR AO observations by Ngo et al. (2015), with the latter two works suggesting the companion shows common proper motion and is bound.

WASP-80: A single faint star was detected in IRDIS, which is not visible in any of the TCI survey observations over 3 years. Given WASP-80's low temperature of 4145K (Triaud et al. 2013a) and the extreme brightness ratio, the companion would have to be an extremely cool, faint object in order for it to be bound.

WASP-87: Both companions were previously identified in the TCI survey, and the optical photometry does not strongly favour either being a bound companion. The inner companion shows a trend of increasing separation and position angle, indicative of it being an unassociated background star with differing proper motion. The likely bound companion, noted in Anderson et al. (2014a) and the TCI survey, is located outside the IRDIS field of view.

WASP-88: No companion was detected at the same location in the TCI survey, with a $\mathrm{r}_{\mathrm{TCI}}$ detection limit of 8 mag. in the red optical.

WASP-94: A faint star-like is seen in the IRDIS data within the IFS field of view, but there is no evidence for a matching source in the IFS data, which may be due to the detected source being below the contrast limits of the IFS data. However, the source is similar in flux and separation to several static speckles visible in the target star's PSF, and is orientated along the direction of the telescope's diffraction spikes;

further investigation is required to confirm whether or not the source is a false positive.

WASP-97: The companion was previously detected in the TCI survey during 2014 and 2015, with two-colour data in 2015 suggesting the star was a background object. The combined dataset shows the separation increasing at ∼100 mas/yr, very similar to WASP-97's proper motion of 98 mas/yr (Gaia Collaboration et al. 2016b), as would be expected if the companion were a distant background source with negligible proper motion.

WASP-99: As with the source near WASP-94, this detection is within the IFS field of view but not detected in IFS data. In this case the source is not aligned with the diffraction spikes, but WASP-99's brightness (V = 9.5) leads to a highly visible speckle pattern. The source shows strong fluctuations in brightness during the series of exposures, mimicking the behaviour of other speckles visible on the image.

WASP-108: This system has the closest companion detected in the IFS data, with the companion being significantly fainter and redder. Using the Baraffe et al. (2015) isochrones, a system age of 4 Gyr, and a primary star temperature of 6400K (Anderson et al. 2014a), the companion is consistent with being a bound $\sim 0.4 M_{\odot}$ companion. The more distant companion, detected in the TCI survey in 2016, shows a very large separation difference of 150 mas between the two datasets; this may be due to incorrect determination of the target star's position due to the close companion.

WASP-111: The companion was previously identified in the TCI survey in 2015 and 2016, and was found to have flux ratios consistent with being physically associated. In isolation, the TCI and IRDIS data indicate a strong trend of increasing separation at a rate of ∼40 mas/yr, inconsistent with a bound orbit. However, archival data does not support any clear long-term separation trend, with 2MASS data corresponding to a separation of 4969 ± 91 mas on 1997-07-10, and Gaia DR1 data giving 5027.3 ± 0.4 mas on an effective date of 2015-01-01.

WASP-118: A faint companion is detected in the IRDIS data. No other high resolution imaging observations of the source are known, and the companion is not resolved in catalogues such as 2MASS or Gaia DR1.

WASP-120: As with other systems such as HAT-P-8, HAT-P-57, and WASP-12,

the WASP-120 system appears to be a hierarchical triple, with the two detected companions being very close to one another. Unlike previous examples, the two companions have rather unequal brightnesses, with the more northerly source being approximately three times as bright. The companions are included in the Gaia DR1 catalogue as a single, unresolved source.

WASP-122: The faint, red companion star is consistent with a bound $\sim$0.16$M_{\odot}$ companion, based on the Baraffe et al. (2015) isochrones, a system age of 5 Gyr, and a primary temperature of 5720K (Turner et al. 2016). The companion was not detected in the TCI survey in 2016, but with an estimated magnitude difference of 7 mag. in the optical, the companion would be far below the detection limit at its separation.

WASP-123: The TCI survey identified a companion marginally consistent with being an associated companion, with no large change in position angle since 2MASS observations in 1997. The IRDIS position angle and separation differ quite significantly from the TCI measurements, but are consistent with the 2MASS data.

WASP-130: The close companion is consistent with a bound $\sim$0.3$M_{\odot}$ dwarf, based on the Baraffe et al. (2015) isochrones, a system age of 2 Gyr, and a primary temperature of 5600K (Hellier et al. 2017). The star was below the detection limit of the TCI survey.

WASP-131: The second-closest detection in the survey, the companion was unsurprisingly not resolved in the TCI observations. Again using the Baraffe et al. (2015) isochrones, a system age of 5 Gyr, and a temperature of 5950K for the primary (Hellier et al. 2017), the companion is found to be consistent with a bound $\sim$0.55$M_{\odot}$ star.

WASP-137: A faint companion was found in the IRDIS data, but is too close and faint to be located in any catalogue data, and no other high resolution imaging data exists to date.

5.6 WASP-20

This section details the follow-up to the discovery of WASP-20B, a previously unknown bright binary companion to a transiting exoplanet system, published in Evans, Southworth & Smalley (2016). Various modifications and improvements on the IRDIS and IFS data reduction have been made since Evans, Southworth & Smalley (2016), and hence the published flux measurements and separation vary slightly from those presented in Tables 5.4 and 5.5. As previously mentioned, an error was made in the calculation of the position angle in the published paper, which has been corrected in the data presented in this thesis. For consistency with the published work, the original photometry and measured separation are quoted in this section.

The companion to WASP-20 was identified as being of special interest due to the combination of its brightness, small angular separation from WASP-20 ($0.2578 \pm 0.0007''$), and lack of any prior detection. Whilst several transiting planetary systems with similarly bright companions are known, in all cases the companion star was identified during the initial characterisation, and in all but a few cases the binary stars have an angular separation of over an arcsecond (a notable exception is Kepler-14AB, Buchhave et al. 2011). In contrast, the binary nature of WASP-20 was entirely undetected during the follow-up process, and was treated as a single star throughout (Anderson et al. 2015).

5.6.1 Physical association of the companion

Flux ratios were measured from both the IFS and IRDIS data, with broadband magnitude differences of $\Delta J = 1.07 \pm 0.04$ mag., $\Delta H = 0.93 \pm 0.03$ mag., and $\Delta K = 0.834 \pm 0.004$ mag., clearly indicating that the companion star is redder than WASP-20A, as would be expected of a fainter main sequence companion. However, it is also possible that the two stars could be physically unrelated, perhaps due to the companion being an unassociated main sequence star at a similar distance, or instead a luminous red giant star located significantly further away. These two competing hypotheses were

compared using statistical models.

The probability of a chance alignment was computed through version 1.6 of the TRILEGAL galactic stellar population model (Girardi et al. 2005), which simulates the Milky Way stellar population along a given line of sight from the Earth, including important features such as of unresolved binary stars. A 1° field of view was simulated at the galactic coordinates of WASP-20 ($l = 55.9, b = -82.4$). The synthetic population was then binned by K_S magnitude, with a bin size of 0.001 mag., giving the integrated number of stars at each magnitude.

The K_S magnitude of the companion star, along with its uncertainty, were derived from the unresolved 2MASS K_S flux measurement and the IRDIS flux ratio. The resulting K_S magnitude probability distribution was convolved with the synthetic stellar population K_S distribution, to determine the number of matching background stars across the whole 1° field of view, and then divided by the sky area simulated to give the number of contaminators per unit area. This was then multiplied by the sky area contained within the companion's measured separation, allowing the calculation of the probability that an unassociated star with the correct K_S magnitude would be found within 257.8mas of WASP-20A.

The probability that the two stars form a binary was derived from a Monte Carlo model of binary stars, again used to determine the chance that a star of matching brightness would be found at the correct projected separation. The properties of the binary population model were based on the results of Raghavan et al. (2010).

46% of stellar systems were assumed to be binary, with higher order multiplicity neglected. The mass ratio q was parameterised in three regimes – low mass ratio ($0 < q \leq 0.20$), intermediate mass ratio ($0.20 < q \leq 0.95$), and high mass ratio ($0.95 < q \leq 1.0$). Solar-type stars are preferentially found in binaries with stars of similar masses, with extreme mass ratios being rare; for each generated system, the mass ratio regime was assigned to either low, intermediate, or high mass ratio with probabilities of 0.132, 0.750, and 0.118 respectively, and the actual value of q determined from a uniform distribution within the regime's bounds. The mass of the primary was fixed at that derived for WASP-20A, and the secondary constrained to lie above the

canonical brown dwarf limit of $0.08 M_{\odot}$, below which mass-radius-temperature relations are highly uncertain.

Raghavan et al. (2010) found the period distribution of binaries to be log-normal, with $\mu = 5.03$ and $\sigma = 2.28$ when the period is expressed in days. It was assumed that stars with periods below 10 years would have been identified through radial velocity monitoring or by their influence on the planetary orbit (e.g. via transit timing variations), and so shorter orbital periods were rejected. Orbital eccentricities were characterised as a uniform distribution with $0.00 \leq e \leq 0.95$, with wide binary stars having no clear preference for any value of eccentricity. Other orbital parameters, such as inclination and phase at time of observation, were randomised uniformly.

For each generated binary system, the projected separation and K_S magnitude difference were determined, the former assuming a distance of 210 ± 20pc (Anderson et al. 2015), and the latter derived through the isochrones of An et al. (2009) assuming $[Fe/H] = -0.01$ and an age of 7 Gyr (Anderson et al. 2015). In total, 1,000,000 binary systems were generated, and the probability of each matching the true properties of the detected companion was determined. The fraction of matching systems was then reduced to match the binary star fraction of 0.46, giving the final probability of a star like WASP-20 having a binary companion of the correct K_S brightness at a separation below 257.8mas.

The simulations strongly preferred the companion being physically associated, with $p = 2.0 \times 10^{-9}$ for the background star scenario and $p = 2.6 \times 10^{-4}$ for the binary companion scenario, and hence it was concluded that the two objects do form a binary system.

5.6.2 Properties of WASP-20B

Spectra were previously obtained with the HARPS and CORALIE spectrographs for the measurement of radial velocity signals induced by the planet (Anderson et al. 2015), and the available data were reinspected in light of the SPHERE detection. The two stars are sufficiently close together to be spatially unresolved by either CORALIE

or HARPS (2″ and 1″ sky aperture, respectively; Queloz et al. 2001). The reduced HARPS spectra were inspected by eye for duplicated spectral lines, but no such evidence was found. Analysis of the computed cross-correlation functions for the reduced HARPS data did not reveal any clear radial velocity signature from a second star. This evidence indicates that the two stars have very similar radial velocities, supporting the hypothesis that they are gravitationally bound, but direct characterisation of the fainter secondary star is therefore complicated due to the lack of resolved spectroscopic information.

The measured IFS narrowband and IRDIS K_S flux ratios were used to determine the stellar properties of the second star. In order to constrain the system, the temperature of 6000 ± 100K derived by Anderson et al. (2015) was adopted for the primary star, under the assumption that the brighter, hotter star would dominate the spectra and that the temperature was only slightly biased by the secondary. The `atlas9` model atmospheres (Castelli & Kurucz 2004) were used in conjunction with the temperature-radius relation presented in the first HITEP lucky imaging paper to calculate the flux ratios for a given secondary temperature. The best-fitting temperature was determined using the least squares method, giving a secondary temperature of 5060 ± 250K.

5.6.3 Planet properties

The two stellar components in the WASP-20 system are completely unresolved in seeing-limited observations, and hence all of the photometric and spectroscopic measurements analysed in Anderson et al. (2015) are affected by contaminating light, biasing the properties of the planet. In order to improve these values, corrections must be made for the dilution of transit photometry, and for the reduction in radial velocity semi-amplitude due to the blending of multiple stellar lines.

Determining the true properties of the planet is further complicated by the lack of knowledge about which star is orbited by the planet, with the SPHERE data being insufficient to determine which star hosts the planet. It was therefore decided to consider two different scenarios during the data reduction, allowing the planet to transit

the primary star in one scenario ('planet transits A'), and the secondary star in the other ('planet transits B'). Additionally, a control test was performed by re-reducing the data without any correction for binarity ('ignoring binarity'), in order to highlight differences caused solely by the impact of binarity, rather than differences between the modelling techniques used in this work and those in Anderson et al. (2015).

5.6.3.1 Photometry

Of the data presented in Anderson et al. (2015), only the Gunn-r data were used, due to the high scatter and incomplete coverage of the other data presented. The flux ratio models derived using the `atlas9` model atmospheres in Section 5.6.2 were convolved with a Gunn-r filter profile[5] to determine the effect of dilution for each star, and the transit depths corrected accordingly.

5.6.3.2 Radial velocities

Anderson et al. (2015) presented radial velocity (RV) measurements derived from the CORALIE and HARPS observations. The radial velocities were measured in the standard way for these instruments, with the spectra being cross-correlated with a synthetic spectrum representing a G2V star, and the RV determined from the offset in the cross-correlation peak. The amplitude of the RV dilution is non-trivial to determine, with no linear relationship between flux ratio and RV, due to the changing amplitudes of spectral lines with temperature (e.g. Santerne et al. 2015). The RV dilution effect was instead determined by combining pairs of spectra with a specified radial velocity offset, and measuring the resulting offset on the cross-correlation peak.

Spectra were generated to represent each star using the `iSpec` software package (Blanco-Cuaresma et al. 2014), with a spectral resolution of $R = 120000$ and wavelength range of 380–690 nm, representing the properties of the more precise HARPS instrument. The stellar effective temperatures derived above were used, with $[\mathrm{Fe/H}] = -0.01$,

[5] `http://www.not.iac.es/instruments/filters/filters.php`

$\log g = 4.5$, and a projected surface rotation of $v \sin i = 2$ km/s for both stars. A 'reference' G2 template was also generated with a temperature of 5770K, [Fe/H] $= 0.0$, $\log g = 4.5$, and $v \sin i = 2$ km/s.

The spectra of either the A or B component were shifted by a specified radial velocity offset, and the two spectra combined, weighted by the flux ratio at each wavelength. The combined spectrum was then cross-correlated with the unmodified G2 reference spectrum, and the effective radial velocity shift was measured. The process was iterated for both components until the measured RV shift matched the semi-amplitude of 32.8 m/s determined by Anderson et al. (2015), with the input value them being taken as the corrected RV amplitude. The final resulting RV amplitudes were 44.0 ± 2.3 m/s for 'planet transits A', and 177 ± 21 m/s for 'planet transits B'.

Anderson et al. (2015) also presented a measurement of the Rossiter-McLaughlin (RM) effect from HARPS data, but these measurements were not re-analysed. Correct treatment of the RM effect would require detailed knowledge of the spectroscopic line profiles of each star, in particular their rotational velocities (Santerne et al. 2015).

5.6.3.3 Planetary system modelling

Analysis of the lightcurve and radial velocity data was carried out by Dr. J. Southworth following the methodology outlined in Southworth (2012) and references therein. The `JKTEBOP` modelling code (Southworth 2013) was used to rederive the properties of the system after correction for dilution (or, in the 'ignoring binarity' case, using the original data). The photometric and radial velocity data were fitted simultaneously to determine the orbital parameters (period P, time of mid-transit T_0, inclination i, and RV semi-amplitude of the star K_A) and relative physical properties of the system (fractional radii of the star, $\frac{R_A}{a}$, and planet, $\frac{R_b}{a}$).

The stellar temperature, metallicity, and results from the `JKTEBOP` code were then used as inputs to the `JKTABSDIM` code, in order to determine the absolute dimensions of star and planet. The code begins with a stellar model at the zero-age main sequence, and interpolates the model in metallicity and mass to match the measured temperature.

The planetary orbital velocity is then modified to best match the observed system parameters at this stellar age. The stellar models are iterated through in age steps of 0.01 Gyr, until the star is determined to have become evolved ($\log g < 3.5$) or an age of 20 Gyr is reached. The best-fitting stellar age is then chosen, and the statistical uncertainties in the output parameters values are determined by perturbing the input parameters within their error bars and re-calculating the output parameters. Due to the poorly constrained uncertainties in stellar modelling, the entire process is repeated for five different sets of stellar models (see Southworth 2010 for further details on the choice of models). The unweighted mean of the five different results is taken as the final result, adopting the largest statistical error from any of the five models, and taking the standard deviation of the results as a systematic error.

The final results are shown in Table 5.6, showing the three modelled scenarios, in addition to the original results presented in Anderson et al. (2015).

5.6.4 Bisector span analysis

Planet follow-up studies are usually very cautious to avoid false positives, in particular those caused by blended systems along the line of sight. One method routinely used to identify such systems is line bisector span analysis, which searches for correlations between the shape of the spectral lines and the measured RV signal. If the received spectrum consists of only a single star with a real orbiting planet, the entire spectrum should be shifted uniformly in the logarithm of wavelength, with no change in spectral line profile. However, if the spectrum consists of multiple blended stars, of which one or more show a radial velocity shift, the blended spectral line profiles will change as the individual stellar spectra are shifted relative to one another. This results in a varying asymmetry in the blended line profile, correlated with orbital phase.

The line bisector determined by measuring the midpoints of the spectral line (or, more commonly, the derived cross-correlation function for the entire spectrum) as a function of depth throughout the line. The bisector span is then computed by subtracting the mean velocity of the 'bottom' part of the line from that of the 'top',

Table 5.6: Derived physical properties of WASP-20 for the three scenarios considered – ignoring binarity, the planet orbiting star A, and the planet orbiting star B. The original results of Anderson et al. (2015) are provided for comparison. Where two sets of errorbars are given, the first is the statistical uncertainty and the second is the systematic uncertainty.

Parameter	Symbol	Ignoring binarity	Planet transits A Adopted solution	Planet transits B	A15
Linear limb darkening coefficient	$u_{\rm A}$	0.57 ± 0.15	0.59 ± 0.15	0.55 ± 0.14	
Quadratic limb darkening coefficient	$u_{\rm A}$	0.35 (fixed)	0.35 (fixed)	0.21 (fixed)	
Sum of the fractional radii	$r_{\rm A} + r_{\rm b}$	0.1076 ± 0.0081	0.1019 ± 0.0080	0.0957 ± 0.0043	
Ratio of the radii	$k = R_{\rm b}/R_{\rm A}$	0.1006 ± 0.0047	0.1148 ± 0.0057	0.1922 ± 0.0078	0.1079 ± 0.0011
Inclination (°)	i	86.77 ± 0.78	87.46 ± 0.88	88.96 ± 0.88	85.56 ± 0.22
Fractional radius of the star	$r_{\rm A} = R_{\rm A}/a$	0.0977 ± 0.0070	0.0914 ± 0.0068	0.0803 ± 0.0033	0.1078 ± 0.0027
Fractional radius of the star	$r_{\rm b} = R_{\rm b}/a$	0.0098 ± 0.0011	0.0091 ± 0.0013	0.0154 ± 0.0011	
Stellar mass ($\rm M_\odot$)	$M_{\rm A}$	$1.090 \pm 0.048 \pm 0.017$	$1.089 \pm 0.047 \pm 0.017$	$0.792 \pm 0.058 \pm 0.280$	1.200 ± 0.041
Stellar radius ($\rm R_\odot$)	$R_{\rm A}$	$1.221 \pm 0.090 \pm 0.006$	$1.142 \pm 0.085 \pm 0.006$	$0.903 \pm 0.046 \pm 0.011$	1.392 ± 0.044
Stellar surface gravity (cgs)	$\log g_{\rm A}$	$4.302 \pm 0.063 \pm 0.002$	$4.360 \pm 0.066 \pm 0.002$	$4.426 \pm 0.037 \pm 0.005$	4.231 ± 0.020
Stellar density ($\rho_\odot$)	$\rho_{\rm A}$	0.60 ± 0.13	0.73 ± 0.17	1.08 ± 0.13	0.447 ± 0.033
Age (Gyr)	τ	$5.0\,^{+0.8\ +0.6}_{-1.6\ -0.8}$	$3.6\,^{+1.9\ +0.8}_{-2.9\ -2.2}$	$16.1\,^{+1.1\ +3.9}_{-5.2\ -5.7}$	7^{+2}_{-1}
Planet mass ($\rm M_{Jup}$)	$M_{\rm b}$	$0.291 \pm 0.017 \pm 0.003$	$0.378 \pm 0.022 \pm 0.004$	$1.30 \pm 0.19 \pm 0.03$	0.311 ± 0.017
Planet radius ($\rm R_{Jup}$)	$R_{\rm b}$	$1.20 \pm 0.14 \pm 0.01$	$1.28 \pm 0.15 \pm 0.01$	$1.69 \pm 0.12 \pm 0.02$	1.462 ± 0.059
Planet surface gravity ($\rm m\,s^{-2}$)	$g_{\rm b}$	5.0 ± 1.2	5.8 ± 1.5	11.3 ± 2.2	2.530 ± 0.036
Planet density ($\rho_{\rm Jup}$)	$\rho_{\rm b}$	$0.159 \pm 0.059 \pm 0.001$	$0.170 \pm 0.065 \pm 0.001$	$0.252 \pm 0.064 \pm 0.003$	0.099 ± 0.012
Equilibrium temperature (K)	$\rm T'_{eq}$	1326 ± 52	1282 ± 52	1013 ± 54	1379 ± 31
Orbital semimajor axis (AU)	a	$0.0581 \pm 0.0009 \pm 0.0003$	$0.0581 \pm 0.0008 \pm 0.0003$	$0.0523 \pm 0.0013 \pm 0.0006$	0.0600 ± 0.0007

with the some variation between authors as to the exact definition of the 'top' and 'bottom' regions (Santerne et al. 2015). Whilst the bisector span will usually identify an asymmetry even for a single star, as a result of stellar granulation (Gray 1989), it is correlated changes in the bisector span that are of interest, which would indicate a relative shift of the 'top' of a spectral line compared to the 'bottom'.

For stars with differing spectra – due to differences in rotational broadening, for example – the relative contributions of each star to the 'top' and 'bottom' of the line profile will differ – the star with broader spectral lines will have little influence at the core, or bottom, of the spectral line. Therefore, radial velocity changes in one of the spectra will modify the asymmetry of the line, hence changing the bisector span in phase with its radial velocity changes. The bisector span method may also be used to identify apparent RV shifts originating from stellar activity, which result solely from changes in spectral line profiles; however, such false positives are not a significant concern for transiting exoplanets, as the existence of an orbiting body is confirmed by the transits, and orbital periods are typically much shorter than the timescales for stellar activity.

As is routine for the WASP survey, Anderson et al. (2015) included an analysis of the line bisector spans from CORALIE and HARPS spectra, with the conclusion that no significant correlation existed between RV amplitude and bisector span for WASP-20, although no quantification is given for the significance of this result. However, visual inspection of the RV–bisector span data suggested that such a correlation did exist, albeit obscured by the highly scattered CORALIE measurements and a systematic offset between the bisector spans measured from the two instruments.

We re-analysed the line bisector–RV correlation by determining the Pearson correlation coefficient, r, both for the HARPS and CORALIE datasets separately, and for the combined dataset. The confidence intervals on r were determined through a Monte Carlo method, permuting the measurements based on their uncertainties and recalculating r for each test. Both datasets show significant positive correlations, as expected of a blended system, with the CORALIE data having $r = 0.24$, the correlation being greater than zero at 2.7σ. The higher quality HARPS data were found to have a

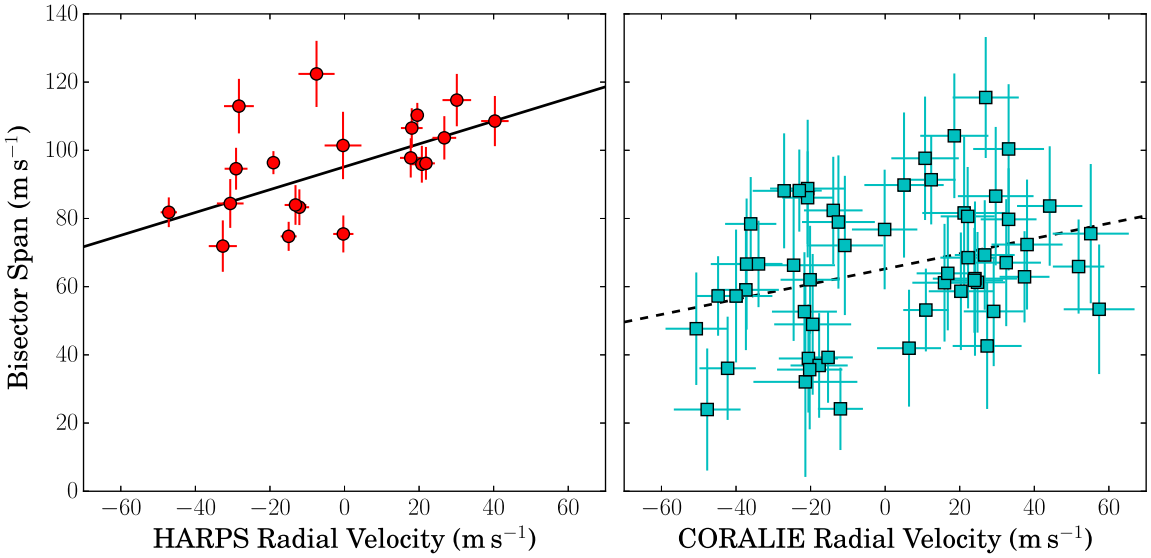

Figure 5.9: Measurements of the radial velocity and line bisector spans from spectra of the WASP-20 system, obtained by Anderson et al. (2015) using the HARPS (left) and CORALIE (right) spectrographs. Both show a highly significant positive trend, indicated by lines, as would be expected of a blended stellar system.

correlation coefficient of $r = 0.47$, significant at 5.3σ. Linear fits to both datasets are shown in Figure 5.9, with a gradient of 0.22 ± 0.09 for CORALIE and 0.34 ± 0.09 for HARPS.

The combined dataset was also found to have a significant correlation with this method, with $r = 0.31$, significant at 4.8σ. The significance is similar to the HARPS-only dataset, despite the inclusion of the lower quality CORALIE data. It is not clear why this correlation remained undetected in Anderson et al. (2015), although the method used to determine the correlation (or lack thereof) in that work is not stated.

5.6.5 Status of the planet WASP-20b

Considering the final results for the planetary system shown in Table 5.6, the 'ignoring binarity' scenario is similar to, although not in exact agreement with, the results of Anderson et al. (2015), finding both the host star and planet to be somewhat smaller. In the 'planet transits A' scenario, correcting for the dilution of RVs results in a 30% (4σ) increase in the planet's mass, but there little change is made to the planet's radius, and its density still remains low. As such, it would continue to be an attractive target for atmospheric characterisation.

Somewhat unexpectedly, the 'planet transits B' scenario was also found to be consistent with a planetary mass object, with relatively normal properties for a Jupiter-sized planet. As before, it is the planet's mass which changes the most, increasing by a factor of four. The planetary radius is less affected, partly due to the smaller host star requiring a less inflated planet to produce the same relative transit depth.

However, despite the 'planet transits B' scenario corresponding to a realistic planet, its prediction for the stellar properties is more questionable. For star B, there is a tension between the relatively long measured transit time and the relatively small predicted radius of the star. In order to match these properties, `JKTABSDIM` finds a solution where the star has begun to evolve off the main sequence, and hence has increased in radius. However, due to the low mass of star B, it is not expected to have reached such an evolved state within the current age of the universe, and the system's near-solar metallicity indicates that the stars were not formed in the early universe. In addition, given the relatively large difference in mass between the A and B components, it would be expected that the more massive star would have finished its stellar evolution long before the less massive star; it is difficult to envision a scenario in which the less massive star in such a wide binary system has started its post-main-sequence evolution first. For these reasons, the 'planet transits A' scenario was adopted as the preferred solution.

Further observations of the system during a planetary transit could more directly determine which star hosts the planet. If precise resolved photometric observations

Table 5.7: Predicted transit depths for WASP-20 in various filters for the 'planet transits A' and 'planet transits B' scenarios, based on the r-band transit depth and the dilution as a function of wavelength.

Filter	λeff (nm)	Depth transiting A (%)	Depth transiting B (%)
u	354	1.324	0.569
U	366	1.323	0.574
B	436	1.263	0.795
g	477	1.227	0.930
V	545	1.199	1.035
r	623	1.164	1.164
R_J	641	1.158	1.189
i	763	1.132	1.285
I_J	798	1.124	1.316
z	913	1.105	1.385
J	1235	1.066	1.532
H	1662	1.016	1.718
K_S	2159	1.005	1.757

could be made, it would be immediately obvious which star shows a dimming due to the planet. Alternatively, unresolved multi-band photometry of the system could determine which star hosts the planet through the colour-dependence of the transit depth. As the two stars have differing temperatures and hence spectral energy distributions, the dilution effect is wavelength-dependent, especially towards the blue optical where the flux of the B component drops off rapidly with wavelength. The expected apparent transit depths for a variety of filters in the optical[6] and near infrared[7] are given in Table 5.7, indicating that variations on the order of 50% in transit depth are expected in the optical alone if the B component is being transited.

[6]UBVRI and ugriz filter passbands taken from Nordic Optical Telescope filters 1-5 and 82-86, `http://www.not.iac.es/instruments/filters/filters.php`

[7]JHK filter passbands taken from SPHERE/IRDIS, `https://www.eso.org/sci/facilities/paranal/instruments/sphere/inst/filters.html`

5.7 Discussion

The SPHERE survey has been highly successful in detecting companion stars, obtaining additional spectrophotometry and astrometry for 12 known companions, identifying 12 definite companion stars, and providing tentative evidence for two more. Particularly interesting are the eight sub-arcsecond detections with the IFS, all of which are consistent with bound objects, and only two of which were previously known. As expected, the spectrophotometric capabilities of the IFS have been shown to greatly benefit the project in comparison to more typical broadband imaging observations, allowing all eight IFS detections to be given detailed characterisation from a single epoch only.

The discovery of the binary nature of WASP-20 illustrates how difficult it can be to detect even relatively bright stellar companions from unresolved imaging and spectroscopic data. The only evidence was the existence of a correlation between radial velocity and spectroscopic line bisector span, but it is also important to caution against rejecting planet candidates based solely on such an indicator. However, WASP-20 is the only such close, bright detection in this survey, and the remaining IFS detections are all much fainter companions. As with the TCI survey, there is still a notable lack of high mass binary companions to hot Jupiters – but what is still unclear is whether this is a deficit that exists in the real planetary population, or representative of a sampling bias.

If planetary candidates such as WASP-20 are falsely rejected, the population of known planetary systems would clearly be biased towards single stellar systems. Whilst WASP-20 was difficult to identify from low spatial resolution data, was it merely 'the one that got away', due to the two stars having velocities nearly perpendicular to the line of sight (i.e. negligible RV offset)? Planetary candidate systems which are found to have multiple sets of spectral lines (i.e. additional stars within approximately 1∼2 arcsec.) are routinely rejected by the WASP group, without further searching for a real planetary RV signal (Triaud et al. 2017).

It may be a worthwhile investigation to re-analyse certain rejected planetary candidates which may plausibly be planets in a wide binary system, in order to better

understand the selection biases present in the observed transiting exoplanet population. Additional high resolution imaging observations could be obtained to search for evidence of a wide binaries, unresolved by seeing-limited observations but detectable as multiple sets of superimposed stellar spectra. Alternatively, a small amount of additional spectroscopic observations could be performed to determine if the RV variation of the system is consistent with a planetary-mass object. For example, if both stellar components have varying RV shifts, the system is likely a (grazing) eclipsing binary; if only one of the spectra shows velocity variations of several km/s, the plausible explanation is it is orbited by a third, unseen stellar component (e.g. Triaud et al. 2013b).[8]

[8]Even if a large RV amplitude is seen, one could still envision a hierarchical triple system in which a tight spectroscopic binary is orbited by a wide tertiary component, with this single star hosting a transiting exoplanet.

6 Conclusions

Over three observing seasons between 2014 and 2016, lucky imaging observations were obtained for a total of 156 transiting exoplanet systems. Using the photometric distances derived from two band photometry, and with the assistance of catalogue photometry and astrometry, 39 of those systems have been identified as probable multiple star systems. Three new companions that show evidence of being multiples themselves (WASP-24B, which is an eclipsing binary (Southworth et al. 2014), WASP-121B, and WASP-123B). WASP-98 has a white dwarf companion, joining the previously discovered white dwarf companion to K2-02 (Vanderburg et al. 2015) as a rare example of such companions. The highlighted results were enabled through the use of Gaia DR2 parallaxes and proper motions, as the photometric distances derived from lucky imaging assumed that all companions would be single main sequence stars.

The combination of modern astrometric results with the historic data in the Washington Double Star Catalog allowed the orbits of two hot-Jupiter-hosting binaries, WASP-77 and WASP-85, to be fitted. For WASP-85, the stellar orbit is clearly misaligned with the planetary orbit, while for WASP-77 the situation remains ambiguous, with the stellar orbit being edge-on to the observer, like the planetary orbit, but the two may still be inclined relative to one another in this configuration. These results offer one of the first chances to test for theories of planet formation that require highly inclined planetary companions, and obtaining further data and results for other systems is strongly encouraged – hints of orbital motion can already be seen in other systems such as WASP-2.

While the lucky imaging survey did not result in the discovery of any previously unknown companions with the capability to significantly alter the derived properties of the known transiting planets, the SPHERE survey resulted in the discovery of WASP-20B, a close companion located only $0.26''$ from the primary star. As the two stars remained completely unresolved during the characterisation of the planet, it remains unclear which star is the source of the planetary signal, and updated solutions for the

transiting planet were provided for both the 'planet transits A' and 'planet transits B' scenarios. The analysis of previously available data in the case of WASP-20 highlighted that evidence of companion stars may already exist – in particular, the bisector spans from the radial velocity measurements of WASP-20 hinted at the presence of a second star within the spectroscopic aperture.

In all observations carried out by this survey and others, there is a noticeable lack of bright, high mass companions to hot Jupiter host stars. Of all transiting systems considered in this survey, only two contain components that are likely more massive than the planet host stars, and in both cases – K2-02 and WASP-98 – the likely higher mass companion is a white dwarf. Excluding these two cases, all other planet-hosting binaries in this survey have a mass ratio below 0.8, in contrast to the expectation that solar type stars commonly have binary companions with similar masses (Raghavan et al. 2010). The reason for this deficit is unclear; one certainty is that there is no observational bias against detecting more massive companions – in fact, due to the brightness of such companions, they are more likely to be detected. It is possible that surveys searching for transiting planets are biased against finding planets in such binaries, due to the increased influence of contaminating light. There may be an additional bias against selecting such systems for follow-up even when the planets are detected, due to the difficulties of characterising planets correctly when there is a bright contaminant nearby, in addition to concerns about potential false positives from blended eclipsing binaries. An alternative hypothesis that the deficit is real – it is possible that more massive stellar companions tend to disrupt the formation and migration of hot Jupiters, explaining the observed deficit. This may be further supported by the results of Raghavan et al. (2010), which indicate that binaries with near-equal-mass components tend to have tighter orbits, which would increase the probability that hot Jupiter formation (and planet formation in general) is less likely to succeed.

6.1 Future work

The analysis of results from the Gaia satellite, which became available towards the end of this Ph.D., have shown that it is competitive with lucky imaging for the detection of close stellar components. In future data releases from the Gaia mission, the inclusion of additional data and more in-depth processing of marginally resolved objects are likely to reveal additional close companions. Future exoplanet surveys would be well advised to routinely check the results of the Gaia mission as a first step when checking for contaminating stars. Even where the companion stars barely resolved and the Gaia data analysis does not explicitly state that two stars are present, the influence of companions on the astrometric data can still be seen in the form of poor astrometric results with large amounts of excess noise. These poor fits may prove a useful selection tool for valuable high-resolution imaging using AO or interferometry, both for systems known (or suspected) to contain exoplanets, and also for the general discovery and study of binary stars. The availability of high quality measurements of parallax and proper motion in the Gaia catalogue has also significantly improved our ability to confirm which stars are physically associated, and a widespread analysis of the Gaia catalogue to detect binary companions through common parallaxes and proper motions should be done – again, both for the study of exoplanets in multiple stellar systems, as well as the many other fields in which multiple stars play an important role.

Some further work is required to complete the reduction and analysis of the SPHERE survey detailed in this paper. The issues with background subtraction on the IRDIS instrument may be related to flat-fielding issues: as broadband K sky flats are not routinely taken, lamp flats were used instead, which result in poorer quality reduced data. It has instead been suggested that sky flats from SPHERE's dual K1/K2 filters could be used as a substitute to produce better results.[1] Additionally, the astrometric scale offsets between the IRDIS and IFS results, noted in Sect. 5.5, require

[1]Flat field issue diagnosis and suggestions from discussion with A. Vigan, C. Ginski, B. Macintosh, and others.

further investigation; it is unclear why the results from the two instruments disagree on the angular separation of several companions, nor why the offset is not consistent between different targets. The potential stellar companions to WASP-94 and WASP-99 also require further investigation; both were detected solely with IRDIS, and appear visually similar to static speckles elsewhere on the image.

6.1.1 Completeness correction and statistical analysis

In order to fully understand the results of the survey, and to derive meaningful statistical results, correction must be made for the detection limits of the surveys. Due to the inability to detect companions at small angular separation, direct imaging surveys are biased against faint companions and companions on tighter orbits. This could be achieved by creating a synthetic population of binary companions to each target star, with a range of orbital parameters and physical properties (in particular, mass and luminosity). For each synthetic companion, the angular separation at the time of observation and magnitude ratio in the relevant band would be used to class the companion as either detected or undetected – such a calculation would take into account the distance to, and properties of, the planet host star. By generating a sufficiently large number of synthetic companions, the completeness of the survey can be estimated, and hence the true multiplicity fraction estimated.

A further correction is needed for false positive companion stars – stars at small angular separation of approximately the right apparent luminosity and colour to mimic a bound companion, but which are in fact physically unassociated. This problem is reduced somewhat for the lucky imaging survey by the supporting evidence identified in the Gaia DR2 catalogue, which led to both the confirmation and rejection of numerous stars, but many fainter companions still lack further supporting data. Estimates for the number of background stars of a given magnitude and colour can be obtained from galactic stellar population models, with the TRILEGAL (Vanhollebeke, Groenewegen & Girardi 2009) and Besançon (Robin et al. 2003) models having readily available interfaces for producing synthetic populations at a given galactic latitude and longitude.

The probability of a background companion being found at a given separation can then be compared to that of a bound companion, using the model of binary systems described above, and stars that are much more likely to be background objects can be rejected.

A key part of these corrections are the assumptions that go into the binary model. While detailed statistics on a variety of binary system properties are available in works such as Raghavan et al. (2010), adopting these without modification would be highly misleading. Firstly, a significant fraction of binary stars are close binaries, with approximately half of the systems identified by Raghavan et al. (2010) having orbital separations below 30 au. Radial velocity analyses of transiting planet systems such as Knutson et al. (2014) have found that while a number of giant planets and brown dwarf companions exist in this range of orbital separations, the high amplitude radial velocity signals expected of stellar companions are not seen, unless many are on orbits highly inclined to the planetary system. Similarly, both this work and others have found that the vast majority of stellar companions to hot Jupiters are much less massive than the planet host stars, again in contrast to the results of Raghavan et al. (2010), which find that companions of similar mass to the primary are most common.

Given the number of observations in this work, it is instead possible to begin investigating properties of the binaries by varying the properties used to generate the synthetic binary systems. For example, Kraus et al. (2016) found a lack of close-in companion stars, and adopted a model based on the Raghavan et al. (2010) distributions, but with a reduction in the number of companions by some factor $S_{\rm bin}$ within an orbital separation $a_{\rm cut}$, fitting these two parameters to their data. While the exact values were not determined with great accuracy, the authors point out that the null hypothesis (no reduction of close in companions) was strongly rejected by their data, hence concluding that close-in stellar companions are very efficient at suppressing planet formation. It would be particularly interesting to perform a similar experiment with the dataset presented in this thesis, modelling not only orbital separation, but properties such as companion mass ratio as well.

With regard to the Lidov-Kozai mechanism of hot Jupiter formation, the key

question to investigate is whether a sufficiently high proportion of systems have stellar companions capable of exciting planetary migration. This requires a companion being sufficiently massive and close to have excited the hot Jupiter in its initial orbit at several au, both of which are properties that could be investigated in the observed sample. The inclination of the binary orbit relative to the planetary orbit, as well as the eccentricity of the binary, are also important; however, placing limits on these in addition to projected separation becomes difficult, as degeneracies exist between these parameters and orbital separation, in addition to the alignment of the planetary orbit (other than the fact it is edge-on to us as observers) being unknown.

With limits on some or all of the orbital parameters of hot Jupiter companions, it is then possible to compare to the results of theoretical studies of Lidov-Kozai migration. These works often provide formulae that predict whether migration is likely to happen (e.g. Fabrycky & Tremaine 2007), or instead investigate regions of parameter space in which migration is likely to occur (e.g. Anderson, Storch & Lai 2016). One example of such a comparison is shown in Fig. 5 of Ngo et al. (2015), where the projected separations of several detected companions are compared to the minimum orbital separation a proto-hot-Jupiter would require in order for migration to occur. However, knowledge of all orbital parameters is necessary to fully test the models; the encouraging results of Anderson, Storch & Lai (2016) rely on the assumption of $e = 0.8$. To do this, follow-up studies of discovered binaries are required to better understand their orbits.

In future studies of the orbits of wide, planet-hosting binaries, the high astrometric precision of instruments such as SPHERE will prove crucial in determining the orbits of these systems, which will significantly improve our ability to compare to theoretical studies of migration. Due to the long orbital systems of these wide binaries, such as WASP-77 and WASP-85, the apparent rates of motion are very slow, and so even with decades of conventional seeing-limited observations recorded in catalogues such as the WDS, orbital motion still remains challenging to detect; the milli-arcsecond precision that the latest generation of AO instruments are designed to achieve will allow their orbits to be mapped out much more quickly. Increasing the sample of systems

for which the orbits of the binary – and in particular, the orbital separation, eccentricity, and inclination – are known will provide a crucial test of the predictions of high eccentricity migration theories for hot Jupiters.

Publications

- Evans D. F., Southworth J., Maxted P. F. L., et al., 2016, A&A, 589, 58, *High-resolution Imaging of Transiting Extrasolar Planetary systems (HITEP). I. Lucky imaging observations of 101 systems in the southern hemisphere.*
- Evans D. F., Southworth J., and Smalley B., 2016, ApJ, 833, L19, *WASP-20 Is a Close Visual Binary with a Transiting Hot Jupiter.*
- Evans D. F., Southworth J., and Smalley B., 2018, A&A, 610, 20, *High-resolution Imaging of Transiting Extrasolar Planetary systems (HITEP). II. Lucky Imaging results from 2015 and 2016.*
- Evans D.F., 2018, RNAAS, 2, 20, *Evidence for Unresolved Exoplanet-hosting Binaries in Gaia DR2.*

A Lucky imaging observing logs

This appendix contains the lists of targets for the lucky imaging campaigns in 2014, 2015, and 2016. These include the date and time of all observations used in the final data analysis. The total exposure time in seconds is stated, with all scientific observations performed at a framerate of 10Hz, although a small fraction (below 1%) of exposures were rejected by the TCI pipeline due to poor quality. For each observation, the pipeline-determined PSF FWHM for the best 1% of exposures is noted, in addition to the limiting magnitude for the detection of companions with the Red camera images for several angular separations.

Table A.1: **Observations with the TCI in 2014.**

				Detection limit (mag)						
Target	Date	Exp. time (s)	1% FWHM (″)	0.5″	0.8″	1.5″	2.5″	5.0″	10.0″	20.0″
CoRoT-1	2014-04-21 23:41:17	600	0.42	4.72	6.61	9.11	10.94	11.21	11.23	11.14
CoRoT-2	2014-04-25 09:55:20	440	0.39	4.69	6.35	8.94	11.07	12.03	12.13	12.07
CoRoT-2	2014-05-06 09:43:45	440	0.44	4.29	6.29	8.89	11.13	11.94	11.97	11.92
CoRoT-3	2014-05-10 10:03:15	890	0.42	4.44	6.44	8.99	10.98	11.28	11.30	11.24
CoRoT-4	2014-04-21 23:52:41	600	0.36	4.62	6.51	8.92	10.72	11.02	11.02	10.94
CoRoT-6	2014-05-07 08:18:26	600	0.57	0.00	5.30	8.02	10.12	10.53	10.57	10.51
CoRoT-6	2014-05-09 08:35:08	899	0.43	4.77	6.61	9.18	10.84	11.08	11.07	11.02
CoRoT-7	2014-04-21 23:15:19	54	0.83	0.00	0.00	6.96	8.91	9.07	9.06	9.00
CoRoT-7	2014-04-21 23:37:10	190	0.36	4.66	6.68	9.37	11.63	12.58	12.68	12.63
CoRoT-8	2014-05-15 07:38:08	899	0.51	4.11	5.97	8.56	10.21	10.37	10.38	10.37
CoRoT-8	2014-05-17 07:55:54	900	0.66	0.00	5.17	8.03	10.04	10.22	10.21	10.19
CoRoT-8	2014-07-25 04:05:09	900	0.56	0.00	5.32	7.88	10.18	10.74	10.78	10.69
CoRoT-8	2014-08-19 03:26:28	899	0.40	4.88	6.80	9.49	11.00	11.21	11.22	11.14
CoRoT-9	2014-05-06 09:26:30	600	0.43	4.34	6.24	8.80	10.41	10.60	10.63	10.56
CoRoT-11	2014-04-25 09:44:28	550	0.50	4.30	5.95	8.41	10.24	11.07	11.13	11.05
CoRoT-11	2014-05-06 09:12:47	550	0.43	4.51	6.33	8.99	10.85	11.17	11.20	11.15
CoRoT-18	2014-09-24 09:35:56	900	0.94	0.00	0.00	6.53	8.86	8.94	8.94	8.91
CoRoT-19	2014-09-27 09:16:44	900	0.65	0.00	5.13	7.74	9.69	9.94	9.90	9.85
CoRoT-20	2014-09-24 09:16:20	900	0.62	0.00	5.26	8.04	10.02	10.32	10.29	10.22
CoRoT-20	2014-09-27 09:41:34	898	0.96	0.00	0.00	6.53	8.26	8.31	8.31	8.29
CoRoT-25	2014-05-10 07:59:56	590	0.73	0.00	5.06	5.06	5.07	5.05	5.04	4.98
CoRoT-25	2014-05-15 08:00:45	686	0.81	0.00	4.41	7.12	9.30	9.49	9.48	9.44
CoRoT-25	2014-05-16 07:53:20	900	0.76	0.00	4.51	7.55	9.31	9.34	9.37	9.30
GJ 1214	2014-05-07 05:53:46	900	0.44	4.30	6.13	8.67	10.83	12.10	12.14	12.10
HAT-P-26	2014-04-18 06:09:13	190	1.12	0.00	0.00	6.12	9.37	11.60	11.73	11.70

Continued on next page

Table A.1 – continued from previous page

				Detection limit (mag)						
Target	Date	Exp. time (s)	1% FWHM (″)	0.5″	0.8″	1.5″	2.5″	5.0″	10.0″	20.0″
HAT-P-26	2014-05-06 04:05:23	190	0.44	4.35	6.12	8.65	10.86	12.04	12.19	12.11
HAT-P-27	2014-04-18 06:39:59	290	1.16	0.00	0.00	5.90	9.05	11.10	11.19	11.14
HAT-P-27	2014-05-07 03:32:08	290	0.51	4.21	5.74	8.31	10.39	11.68	11.78	11.71
HAT-P-27	2014-05-08 03:11:03	290	0.42	4.64	6.52	9.13	11.34	12.22	12.28	12.23
HAT-P-30	2014-04-22 23:23:25	120	0.40	4.55	6.43	9.14	11.41	13.11	13.28	13.27
HAT-P-35	2014-04-22 00:04:05	390	0.33	5.53	7.20	9.78	11.62	12.02	12.05	12.02
HAT-P-41	2014-04-21 09:56:15	130	0.35	5.74	7.42	10.18	11.91	12.50	12.66	12.62
HAT-P-42	2014-04-22 23:58:56	300	0.34	5.49	7.14	9.36	11.29	12.04	12.05	12.01
HAT-P-45	2014-04-21 09:45:07	540	0.34	5.54	7.57	10.01	11.92	12.41	12.43	12.37
HAT-P-46	2014-04-21 09:39:05	240	0.35	5.49	7.28	9.74	11.75	12.44	12.48	12.41
HATS-1	2014-04-25 00:03:38	260	0.43	4.30	5.92	8.63	10.83	11.79	11.85	11.80
HATS-1	2014-04-25 23:18:50	260	0.62	0.00	4.90	7.32	9.62	11.15	11.21	11.16
HATS-1	2014-04-27 22:56:45	260	0.59	0.00	5.13	7.59	9.78	10.52	10.54	10.54
HATS-1	2014-04-27 23:27:53	260	0.51	4.17	5.56	7.80	10.11	11.35	11.41	11.36
HATS-1	2014-04-28 23:20:48	260	0.57	0.00	5.05	7.52	9.84	11.38	11.50	11.46
HATS-1	2014-04-30 22:53:35	260	0.46	4.24	5.92	8.43	10.58	10.99	11.04	11.01
HATS-1	2014-05-06 00:17:45	260	0.44	4.15	6.02	8.69	10.99	11.79	11.83	11.78
HATS-1	2014-05-06 01:07:53	260	0.44	4.25	6.04	8.45	10.67	11.69	11.76	11.71
HATS-2	2014-04-25 00:09:50	600	0.37	4.60	6.11	8.44	10.47	11.06	11.04	11.00
HATS-2	2014-04-25 23:24:40	656	1.08	0.00	0.00	5.57	8.23	10.29	10.39	10.32
HATS-2	2014-04-27 23:02:18	900	0.94	0.00	0.00	6.29	9.03	10.58	10.60	10.55
HATS-2	2014-04-27 23:33:43	899	0.77	0.00	4.39	6.84	9.45	10.92	10.95	10.88
HATS-2	2014-04-30 22:58:56	900	0.42	4.42	6.08	8.56	10.65	11.15	11.15	11.08
HATS-2	2014-05-06 00:49:30	900	0.46	4.29	6.04	8.52	10.69	11.24	11.28	11.21
HATS-2	2014-05-06 01:20:46	900	0.44	4.25	6.01	8.30	10.42	11.19	11.18	11.12
HATS-3	2014-04-21 10:01:00	390	0.34	5.45	7.55	9.87	11.71	12.14	12.17	12.14

Continued on next page

Table A.1 – continued from previous page

Target	Date	Exp. time (s)	1% FWHM (″)	Detection limit (mag) 0.5″	0.8″	1.5″	2.5″	5.0″	10.0″	20.0″
HATS-4	2014-04-21 22:50:32	598	0.71	0.00	4.46	7.49	9.25	9.36	9.33	9.32
HATS-4	2014-04-22 22:57:54	600	0.35	5.47	7.28	9.59	10.25	10.35	10.30	10.33
HATS-5	2014-08-10 09:52:57	460	0.64	0.00	5.15	7.89	10.32	11.39	11.44	11.39
HATS-5	2014-08-12 08:27:00	460	0.54	0.00	5.27	7.82	10.22	11.44	11.50	11.46
HATS-5	2014-08-19 08:12:17	458	0.43	4.49	6.02	8.52	10.82	11.74	11.82	11.75
OGLE-TR-113	2014-05-07 00:13:54	724	0.71	0.00	5.01	8.02	9.68	9.79	9.74	9.66
OGLE-TR-113	2014-05-07 23:39:34	664	0.50	4.37	6.18	8.57	9.72	9.81	9.80	9.73
OGLE-TR-113	2014-05-08 00:55:10	900	0.58	0.00	5.25	7.72	9.47	9.68	9.66	9.60
OGLE-TR-113	2014-05-08 23:48:49	323	0.80	0.00	4.54	7.63	9.37	9.46	9.43	9.35
OGLE-TR-211	2014-05-06 23:33:53	900	0.75	0.00	4.55	7.47	8.48	8.56	8.53	8.47
OGLE-TR-211	2014-05-06 23:51:42	900	0.52	4.09	5.73	8.26	9.17	9.20	9.16	9.13
OGLE-TR-211	2014-05-07 23:13:26	900	0.38	4.43	6.60	9.01	9.69	9.73	9.71	9.68
OGLE-TR-211	2014-05-08 23:32:39	900	0.49	3.98	5.91	8.42	9.39	9.41	9.40	9.29
OGLE-TR-L9	2014-05-07 00:41:43	900	0.51	4.22	5.88	8.25	9.58	9.77	9.73	9.68
OGLE-TR-L9	2014-05-08 00:00:44	900	0.43	4.48	6.12	8.33	9.58	9.70	9.65	9.66
OGLE-TR-L9	2014-05-08 01:18:57	900	0.42	4.35	6.09	8.30	9.56	9.78	9.72	9.69
OGLE-TR-L9	2014-05-09 00:43:56	900	0.48	4.19	6.00	8.46	9.70	9.90	9.86	9.80
OGLE-TR-L9	2014-05-09 01:24:32	900	0.39	4.54	6.19	8.72	10.02	10.13	10.09	10.05
Qatar-2	2014-04-18 05:49:16	600	1.36	0.00	0.00	5.32	8.70	10.54	10.58	10.54
Qatar-2	2014-05-06 02:40:07	900	0.45	4.33	5.93	8.48	10.56	11.34	11.39	11.31
WASP-2	2014-04-25 10:09:06	250	0.47	4.33	5.81	8.57	10.72	11.88	12.00	11.95
WASP-2	2014-04-29 10:21:29	250	0.64	0.00	4.96	7.35	9.83	11.52	11.61	11.56
WASP-2	2014-05-10 10:20:49	250	0.35	5.47	6.95	9.58	11.36	11.63	11.69	11.64
WASP-4	2014-07-25 09:51:47	390	0.58	0.00	5.16	7.44	9.88	11.44	11.52	11.45
WASP-4	2014-08-09 06:35:45	390	0.64	0.00	4.80	7.06	9.37	10.99	11.08	10.99
WASP-4	2014-08-11 06:37:38	390	0.57	0.00	5.04	7.55	10.02	11.20	11.24	11.21

Continued on next page

Table A.1 – continued from previous page

				Detection limit (mag)						
Target	Date	Exp. time (s)	1% FWHM (″)	0.5″	0.8″	1.5″	2.5″	5.0″	10.0″	20.0″
WASP-4	2014-08-19 08:50:21	390	0.33	5.60	7.19	9.69	11.45	12.09	12.16	12.05
WASP-5	2014-08-09 06:29:02	290	0.64	0.00	4.68	4.63	4.66	4.67	4.64	4.57
WASP-5	2014-08-11 07:17:06	290	0.52	4.06	5.64	8.19	10.41	11.34	11.37	11.35
WASP-5	2014-08-19 09:24:56	290	0.37	4.49	6.09	8.74	11.01	12.10	12.19	12.12
WASP-6	2014-07-25 09:37:42	230	0.52	4.13	5.37	7.70	9.97	11.37	11.46	11.40
WASP-6	2014-08-09 06:19:25	230	0.71	0.00	4.76	6.80	8.96	10.68	10.80	10.78
WASP-6	2014-08-11 06:16:15	230	0.50	4.23	5.71	8.28	10.62	11.31	11.37	11.33
WASP-6	2014-08-19 03:44:00	230	0.30	5.99	7.66	10.15	11.95	12.37	12.38	12.35
WASP-7	2014-04-25 10:16:34	120	0.60	0.00	5.30	8.16	10.79	13.07	13.47	13.44
WASP-7	2014-05-09 09:49:54	120	0.59	0.00	5.63	8.33	10.78	13.43	13.99	13.98
WASP-7	2014-05-16 08:53:26	120	0.40	4.43	6.55	9.37	11.74	13.57	13.80	13.79
WASP-8	2014-07-25 10:17:46	60	0.62	0.00	5.18	7.45	10.01	12.35	12.75	12.74
WASP-8	2014-08-09 06:47:04	60	0.75	0.00	4.47	6.38	8.92	11.50	12.48	12.51
WASP-8	2014-08-11 07:22:56	59	0.65	0.00	4.88	7.45	10.14	12.51	12.92	12.91
WASP-8	2014-08-11 07:25:19	60	0.58	0.00	5.05	7.63	10.23	12.44	12.73	12.73
WASP-8	2014-08-19 09:30:55	60	0.52	4.09	5.87	8.47	10.94	12.99	13.47	13.45
WASP-8	2014-08-19 09:32:44	20	0.53	0.00	5.93	8.34	10.65	12.40	12.83	12.80
WASP-8	2014-09-21 04:54:31	60	0.37	4.55	6.68	9.44	11.75	13.36	13.65	13.62
WASP-15	2014-04-18 06:03:31	120	0.92	0.00	0.00	6.64	9.43	11.66	11.89	11.86
WASP-15	2014-05-06 02:57:03	120	0.46	4.18	5.85	8.44	10.61	12.02	12.20	12.16
WASP-16	2014-04-18 06:15:36	130	0.88	0.00	0.00	7.30	9.75	11.61	11.76	11.74
WASP-16	2014-05-06 04:10:15	130	0.37	4.50	6.42	9.03	11.30	12.48	12.57	12.53
WASP-17	2014-04-25 09:37:35	160	0.51	4.15	5.67	8.00	10.03	11.28	11.49	11.43
WASP-17	2014-04-29 09:02:20	160	0.59	0.00	5.03	7.37	9.91	11.66	11.80	11.78
WASP-17	2014-05-07 02:48:13	160	0.43	4.50	6.14	8.71	11.00	12.10	12.21	12.16
WASP-18	2014-07-09 10:11:04	60	0.63	0.00	5.41	8.44	10.93	13.26	13.80	13.80

Continued on next page

Table A.1 – continued from previous page

Target	Date	Exp. time (s)	1% FWHM (″)	Detection limit (mag) 0.5″	0.8″	1.5″	2.5″	5.0″	10.0″	20.0″
WASP-18	2014-08-09 08:58:07	60	0.89	0.00	0.00	6.00	8.43	11.20	12.24	12.23
WASP-18	2014-08-10 08:53:27	60	0.57	0.00	4.99	7.78	10.42	12.65	13.00	12.99
WASP-18	2014-08-19 07:17:16	60	0.62	0.00	5.30	8.31	10.83	13.27	13.79	13.76
WASP-18	2014-08-19 07:19:51	20	0.61	0.00	5.04	8.25	10.68	12.68	13.10	13.09
WASP-18	2014-09-21 05:34:04	60	0.40	4.69	6.57	9.40	11.70	13.60	13.87	13.88
WASP-19	2014-04-19 04:41:50	340	0.43	4.31	6.18	8.83	10.92	11.82	11.89	11.82
WASP-19	2014-04-23 00:05:51	340	0.40	4.46	6.24	8.75	10.91	12.02	12.09	12.05
WASP-20	2014-07-09 09:14:59	70	0.42	4.75	6.58	9.18	11.31	12.64	12.82	12.76
WASP-22	2014-07-25 09:22:05	190	0.54	0.00	5.10	7.50	9.83	11.58	11.73	11.64
WASP-22	2014-08-09 09:49:32	190	0.85	0.00	0.00	6.24	8.48	10.83	11.08	11.02
WASP-22	2014-08-10 09:22:00	190	0.52	4.19	5.61	8.22	10.60	11.56	11.60	11.55
WASP-22	2014-08-12 08:00:04	190	0.61	0.00	5.01	7.39	9.75	11.38	11.48	11.46
WASP-22	2014-08-19 07:42:52	190	0.36	4.64	6.45	9.16	11.30	12.36	12.45	12.37
WASP-22	2014-08-19 09:51:30	190	0.43	4.28	6.11	8.65	10.79	12.07	12.18	12.13
WASP-23	2014-04-21 03:10:21	490	0.63	0.00	4.99	7.60	9.93	11.32	11.41	11.34
WASP-23	2014-04-21 23:27:06	490	0.36	4.47	6.38	9.00	11.36	12.21	12.29	12.20
WASP-24	2014-05-07 03:26:48	120	0.52	4.09	5.81	8.17	10.45	11.66	11.79	11.72
WASP-24	2014-05-08 03:08:04	120	0.38	4.66	6.46	9.12	11.36	12.25	12.33	12.28
WASP-25	2014-04-18 05:30:22	220	1.28	0.00	0.00	5.57	8.97	11.32	11.45	11.41
WASP-25	2014-05-06 00:38:54	220	0.39	4.42	6.42	9.06	11.27	12.20	12.30	12.20
WASP-25	2014-05-06 01:55:11	220	0.43	4.30	6.13	8.66	10.86	12.04	12.12	12.09
WASP-26	2014-05-07 10:37:10	130	1.26	0.00	0.00	5.13	8.00	9.35	9.36	9.35
WASP-26	2014-05-08 10:36:25	130	0.61	0.00	5.15	7.93	9.81	10.09	10.09	10.10
WASP-26	2014-07-09 09:24:28	100	0.35	5.69	6.97	9.54	11.57	12.50	12.59	12.53
WASP-26	2014-07-09 09:41:42	100	0.38	4.50	6.61	9.12	11.36	12.58	12.67	12.63
WASP-28	2014-07-25 10:00:29	290	0.51	4.29	5.71	7.98	10.31	11.44	11.56	11.49

Continued on next page

Table A.1 – continued from previous page

				Detection limit (mag)						
Target	Date	Exp. time (s)	1% FWHM (″)	0.5″	0.8″	1.5″	2.5″	5.0″	10.0″	20.0″
WASP-28	2014-08-09 05:56:10	290	0.82	0.00	4.37	6.25	8.32	10.43	10.62	10.59
WASP-28	2014-08-11 06:49:53	290	0.57	0.00	5.10	7.67	10.10	11.24	11.23	11.22
WASP-28	2014-08-19 09:06:35	289	0.42	4.41	6.13	8.50	10.71	11.84	11.92	11.86
WASP-29	2014-08-09 06:56:53	120	0.65	0.00	4.48	6.30	8.61	10.67	11.19	11.16
WASP-29	2014-08-11 06:58:11	120	0.58	0.00	5.05	7.66	10.23	12.09	12.24	12.20
WASP-29	2014-08-19 09:13:42	120	0.39	4.55	6.40	8.94	11.16	12.80	13.02	12.95
WASP-30	2014-07-25 10:11:15	230	0.58	0.00	5.05	7.40	9.82	11.88	12.05	11.99
WASP-30	2014-08-09 06:04:49	230	0.85	0.00	0.00	6.13	8.49	10.93	11.28	11.22
WASP-30	2014-08-11 07:02:28	230	0.60	0.00	5.07	7.64	10.18	11.75	11.84	11.78
WASP-30	2014-08-19 09:18:59	230	0.38	4.60	6.32	8.63	10.93	12.40	12.51	12.45
WASP-31	2014-04-24 23:57:40	240	0.38	4.49	6.14	8.62	10.84	11.85	11.90	11.82
WASP-31	2014-04-25 23:13:31	240	0.60	0.00	4.98	7.53	9.70	11.15	11.22	11.17
WASP-31	2014-06-16 23:51:39	240	0.33	5.51	7.19	9.74	11.60	12.10	12.20	12.12
WASP-32	2014-07-09 10:06:49	120	0.35	5.78	7.34	9.82	11.72	12.34	12.44	12.38
WASP-34	2014-04-24 23:18:29	120	0.47	4.62	6.02	8.73	11.06	12.85	13.08	13.05
WASP-34	2014-04-25 23:09:57	120	0.63	0.00	4.86	7.26	9.68	11.91	12.25	12.24
WASP-34	2014-04-27 22:52:27	120	0.54	0.00	5.18	7.81	10.30	11.54	11.59	11.57
WASP-34	2014-04-27 23:24:47	120	0.59	0.00	4.98	7.46	10.02	12.30	12.79	12.77
WASP-34	2014-04-28 23:17:50	120	0.57	0.00	5.06	7.68	10.19	12.50	12.92	12.90
WASP-34	2014-04-30 22:50:02	120	0.50	4.12	5.86	8.34	10.61	11.73	11.82	11.82
WASP-34	2014-06-17 00:10:52	120	0.45	4.47	6.21	9.07	11.46	13.21	13.46	13.43
WASP-35	2014-09-21 08:39:13	90	0.42	4.36	6.24	8.91	11.00	12.32	12.47	12.45
WASP-36	2014-04-22 23:43:02	490	0.32	5.53	7.21	9.57	11.27	11.69	11.73	11.71
WASP-37	2014-04-18 06:28:58	500	0.89	0.00	0.00	6.13	9.16	10.80	10.80	10.78
WASP-37	2014-05-06 05:44:42	500	0.36	4.69	6.63	9.28	11.39	12.00	12.06	11.99
WASP-39	2014-04-18 06:20:13	280	0.98	0.00	0.00	6.63	9.53	11.43	11.48	11.46

Continued on next page

Table A.1 – continued from previous page

Target	Date	Exp. time (s)	1% FWHM (″)	Detection limit (mag) 0.5″	0.8″	1.5″	2.5″	5.0″	10.0″	20.0″
WASP-39	2014-05-06 05:38:32	280	0.34	5.58	7.27	9.77	11.64	12.30	12.36	12.32
WASP-41	2014-04-21 06:08:41	180	0.37	4.52	6.41	9.04	11.19	12.55	12.64	12.62
WASP-41	2014-04-25 23:41:26	180	0.69	0.00	4.75	7.02	9.35	11.34	11.59	11.55
WASP-41	2014-04-25 23:46:04	180	0.68	0.00	4.77	7.02	9.35	11.26	11.49	11.44
WASP-41	2014-04-28 00:01:13	180	0.51	4.11	5.63	8.03	10.44	11.93	12.07	12.02
WASP-41	2014-04-28 23:28:00	180	0.63	0.00	4.83	7.38	9.83	11.70	11.87	11.82
WASP-41	2014-04-30 23:15:11	180	0.47	4.18	5.94	8.42	10.84	12.23	12.33	12.32
WASP-41	2014-05-06 00:24:17	180	0.41	4.40	6.36	8.97	11.22	12.43	12.48	12.41
WASP-41	2014-05-06 01:38:42	180	0.55	0.00	5.11	7.53	9.98	11.87	12.09	12.03
WASP-42	2014-04-21 06:35:29	440	0.34	5.45	7.20	9.70	11.69	12.45	12.53	12.49
WASP-42	2014-05-06 01:45:30	440	0.47	4.30	5.83	8.32	10.35	11.73	11.86	11.80
WASP-42	2014-05-07 01:30:30	440	0.45	4.28	5.95	8.29	10.55	12.02	12.15	12.07
WASP-43	2014-04-19 04:52:16	360	0.50	4.14	5.89	8.55	10.63	11.94	12.00	11.99
WASP-43	2014-04-24 22:39:12	359	0.69	0.00	4.99	7.66	9.17	9.26	9.19	9.20
WASP-43	2014-04-24 22:48:59	359	0.42	4.46	6.20	8.90	10.76	10.96	10.97	10.93
WASP-43	2014-04-24 22:57:33	358	0.46	4.27	6.09	8.59	10.86	11.44	11.45	11.43
WASP-43	2014-04-25 22:58:11	358	0.98	0.00	0.00	6.03	8.97	10.99	11.07	11.05
WASP-44	2014-07-09 09:28:46	590	0.36	4.62	6.58	9.20	11.22	11.82	11.88	11.81
WASP-45	2014-07-09 09:17:49	250	0.32	5.44	7.05	9.49	11.37	12.09	12.15	12.11
WASP-46	2014-07-09 09:46:36	619	0.59	0.00	5.04	7.66	9.97	11.19	11.23	11.17
WASP-47	2014-05-09 10:25:30	230	0.32	5.88	7.72	9.99	11.43	11.57	11.62	11.63
WASP-49	2014-04-20 23:57:06	129	0.72	0.00	4.83	7.15	7.43	7.42	7.42	7.35
WASP-49	2014-04-21 22:47:26	130	0.45	4.27	6.09	8.68	9.77	9.86	9.85	9.83
WASP-50	2014-07-25 09:17:43	150	0.57	0.00	5.20	7.67	9.81	11.54	11.69	11.64
WASP-50	2014-08-09 09:41:36	150	0.91	0.00	0.00	5.85	8.13	10.65	11.04	10.99
WASP-50	2014-08-10 09:18:28	150	0.53	0.00	5.09	7.77	10.30	11.62	11.69	11.64

Continued on next page

Table A.1 – continued from previous page

				Detection limit (mag)						
Target	Date	Exp. time (s)	1% FWHM (″)	0.5″	0.8″	1.5″	2.5″	5.0″	10.0″	20.0″
WASP-50	2014-08-12 07:56:08	150	0.54	0.00	5.15	7.67	10.17	11.60	11.72	11.67
WASP-50	2014-08-19 07:35:53	150	0.36	4.57	6.44	9.13	11.34	12.31	12.39	12.34
WASP-50	2014-08-19 09:42:26	150	0.40	4.44	6.20	8.80	11.02	12.15	12.24	12.21
WASP-52	2014-07-25 09:44:06	300	0.58	0.00	5.14	7.53	9.93	11.69	11.84	11.76
WASP-52	2014-08-09 06:13:02	300	1.20	0.00	0.00	5.29	7.48	10.07	10.63	10.60
WASP-52	2014-08-11 06:22:06	300	0.64	0.00	5.01	7.47	9.85	11.11	11.12	11.11
WASP-52	2014-08-19 08:38:48	300	0.53	0.00	5.83	8.29	10.41	11.68	11.74	11.69
WASP-52	2014-09-21 04:43:20	300	0.41	4.36	6.37	8.99	11.05	12.27	12.34	12.28
WASP-54	2014-04-18 05:44:08	120	1.12	0.00	0.00	6.07	9.20	11.99	12.42	12.40
WASP-54	2014-05-06 02:36:40	120	0.51	4.14	5.72	8.34	10.71	12.51	12.77	12.75
WASP-54	2014-05-07 01:41:35	120	0.53	0.00	5.68	8.12	10.38	12.45	12.76	12.73
WASP-54	2014-05-08 01:43:29	120	0.42	4.47	6.15	8.62	10.83	12.66	12.91	12.87
WASP-54	2014-05-08 03:04:27	120	0.43	4.43	6.34	8.75	11.17	13.00	13.28	13.23
WASP-55	2014-04-18 05:37:42	200	0.74	0.00	4.19	7.09	9.77	11.10	11.17	11.13
WASP-55	2014-05-06 00:44:36	200	0.43	4.28	6.07	8.70	10.84	11.84	11.92	11.85
WASP-55	2014-05-06 02:00:44	200	0.48	4.31	5.83	8.32	10.43	11.55	11.67	11.61
WASP-57	2014-05-06 05:55:25	700	0.35	5.50	7.29	9.73	11.46	11.83	11.89	11.82
WASP-61	2014-08-10 10:04:26	410	0.62	0.00	5.29	7.87	10.21	11.47	11.51	11.48
WASP-61	2014-08-19 08:24:41	409	0.43	4.37	6.03	8.58	10.63	11.79	11.84	11.76
WASP-62	2014-09-24 09:55:37	60	0.43	4.34	6.05	8.58	10.61	11.03	11.03	11.02
WASP-63	2014-04-21 23:03:15	120	0.37	4.51	6.40	8.96	11.23	11.94	11.98	11.96
WASP-63	2014-04-22 23:09:33	120	0.35	5.57	7.26	9.72	11.60	12.22	12.27	12.24
WASP-64	2014-04-21 23:20:07	330	0.41	4.33	6.22	8.81	10.94	11.59	11.63	11.57
WASP-64	2014-04-22 23:16:18	330	0.30	5.65	7.32	9.67	11.24	11.60	11.59	11.55
WASP-65	2014-04-22 23:54:13	230	0.35	5.42	7.04	9.37	11.25	12.03	12.06	12.00
WASP-66	2014-04-19 05:17:00	170	0.40	4.50	6.58	8.93	11.06	12.00	12.05	12.02

Continued on next page

Table A.1 – continued from previous page

Target	Date	Exp. time (s)	1% FWHM (″)	Detection limit (mag) 0.5″	0.8″	1.5″	2.5″	5.0″	10.0″	20.0″
WASP-66	2014-04-24 23:10:13	170	0.36	4.49	6.07	8.67	10.96	11.72	11.80	11.76
WASP-66	2014-04-24 23:14:05	170	0.36	4.63	6.29	8.73	11.00	11.86	11.98	11.92
WASP-66	2014-04-25 23:05:44	170	0.67	0.00	4.82	7.26	9.51	10.76	10.83	10.78
WASP-67	2014-04-21 09:29:24	430	0.35	5.34	7.26	9.71	11.32	11.57	11.64	11.63
WASP-69	2014-04-25 10:25:00	120	0.68	0.00	5.12	8.01	10.48	12.48	12.66	12.65
WASP-69	2014-05-09 09:53:35	120	0.63	0.00	5.38	8.32	10.76	13.41	14.03	14.02
WASP-69	2014-05-16 09:01:17	120	0.42	4.52	6.55	9.28	11.57	13.45	13.71	13.73
WASP-70	2014-04-21 10:09:31	120	0.36	4.60	6.79	9.52	11.59	12.41	12.51	12.48
WASP-71	2014-07-25 09:08:24	60	0.47	4.23	5.84	8.24	10.43	12.01	12.20	12.20
WASP-71	2014-08-09 09:16:58	60	0.74	0.00	4.34	5.87	8.12	10.70	11.19	11.16
WASP-71	2014-08-09 09:18:54	60	1.05	0.00	0.00	5.69	7.95	10.50	11.20	11.15
WASP-71	2014-08-10 09:03:22	60	0.50	4.09	5.65	8.38	10.49	11.85	11.98	11.93
WASP-71	2014-08-12 07:38:33	60	0.55	0.00	5.24	7.82	10.32	11.95	12.10	12.06
WASP-71	2014-08-19 07:26:18	60	0.40	4.63	6.43	9.03	11.25	12.57	12.75	12.70
WASP-71	2014-08-19 09:49:12	60	0.38	4.78	6.24	8.67	10.87	12.46	12.66	12.61
WASP-72	2014-07-25 09:13:21	80	0.56	0.00	5.22	7.77	10.08	11.89	12.05	12.04
WASP-72	2014-08-09 09:29:15	80	0.88	0.00	0.00	6.02	8.43	10.86	11.24	11.18
WASP-72	2014-08-10 09:08:54	80	0.75	0.00	4.17	7.27	10.20	11.85	11.97	11.91
WASP-72	2014-08-12 07:53:12	80	0.54	0.00	5.30	7.77	10.31	11.92	12.07	12.01
WASP-72	2014-08-19 07:32:38	80	0.36	4.66	6.34	9.16	11.35	12.60	12.74	12.64
WASP-72	2014-08-19 09:39:27	80	0.39	4.43	6.13	8.74	11.01	12.37	12.54	12.50
WASP-73	2014-05-09 10:06:02	120	0.44	4.50	6.27	9.07	11.43	13.10	13.32	13.29
WASP-75	2014-05-09 10:30:50	150	0.36	4.74	6.73	9.34	10.96	11.21	11.22	11.20
WASP-76	2014-07-25 09:05:19	60	0.53	0.00	5.66	8.06	10.46	12.49	12.81	12.84
WASP-76	2014-08-09 09:09:56	60	0.75	0.00	4.27	6.20	8.62	11.33	12.11	12.13
WASP-76	2014-08-10 08:59:15	60	0.47	4.26	6.20	8.80	11.05	12.72	12.93	12.93

Continued on next page

Table A.1 – continued from previous page

				Detection limit (mag)						
Target	Date	Exp. time (s)	1% FWHM (″)	0.5″	0.8″	1.5″	2.5″	5.0″	10.0″	20.0″
WASP-76	2014-08-19 07:22:44	60	0.60	0.00	5.11	8.19	10.78	13.15	13.63	13.63
WASP-76	2014-08-19 07:24:17	20	0.59	0.00	5.59	8.42	10.77	12.69	13.02	13.00
WASP-77	2014-07-25 08:53:28	60	0.61	0.00	4.88	7.32	9.56	11.61	12.31	12.32
WASP-77	2014-07-25 08:55:28	60	0.61	0.00	5.18	7.69	9.63	11.74	12.41	12.41
WASP-77	2014-07-25 08:57:10	59	0.60	0.00	5.12	7.75	9.75	11.76	12.43	12.44
WASP-77	2014-07-25 08:58:44	60	0.53	0.00	5.58	8.08	10.01	11.98	12.44	12.45
WASP-77	2014-08-09 09:25:32	60	0.66	0.00	4.48	6.32	8.57	11.02	11.69	11.68
WASP-77	2014-08-10 09:06:18	60	0.53	0.00	6.03	8.68	10.87	12.42	12.71	12.68
WASP-77	2014-08-12 07:49:56	60	0.55	0.00	5.28	8.12	10.57	12.48	12.81	12.82
WASP-77	2014-08-19 07:29:04	60	0.43	4.33	6.36	9.07	11.07	12.76	13.12	13.10
WASP-77	2014-08-19 09:37:04	60	0.47	4.32	6.12	8.63	10.89	12.67	13.08	13.02
WASP-78	2014-08-10 09:40:50	240	0.58	0.00	5.15	7.79	10.22	11.16	11.20	11.16
WASP-78	2014-08-12 08:18:39	240	0.60	0.00	4.99	7.37	9.69	10.90	10.96	10.92
WASP-78	2014-08-19 08:01:20	240	0.44	4.31	5.97	8.43	10.47	11.39	11.43	11.38
WASP-79	2014-07-25 09:27:11	60	0.53	0.00	5.64	8.14	10.47	12.38	12.66	12.63
WASP-79	2014-08-10 09:49:16	60	0.61	0.00	5.44	8.05	10.59	12.41	12.63	12.58
WASP-79	2014-08-12 08:24:42	60	0.55	0.00	5.17	7.73	10.20	12.30	12.56	12.51
WASP-79	2014-08-19 08:06:38	60	0.49	4.09	5.93	8.46	10.78	12.60	12.86	12.83
WASP-79	2014-08-19 08:08:24	60	0.49	4.27	5.86	8.60	10.84	12.59	12.88	12.87
WASP-79	2014-09-21 06:25:05	60	0.40	4.34	6.24	8.71	10.88	12.44	12.62	12.58
WASP-79	2014-09-21 07:43:29	60	0.36	4.73	6.65	9.29	11.42	12.72	12.86	12.83
WASP-80	2014-04-25 10:04:28	220	0.41	4.50	6.32	9.12	11.31	12.77	12.93	12.92
WASP-82	2014-09-21 08:35:23	60	0.40	4.38	6.36	8.97	11.07	12.47	12.65	12.62
WASP-84	2014-04-22 23:28:32	120	0.40	4.53	6.40	9.07	11.18	12.95	13.12	13.06
WASP-88	2014-04-24 10:24:39	140	0.33	5.48	6.87	9.08	10.48	10.71	10.76	10.75
WASP-90	2014-05-09 09:57:29	190	0.48	4.38	6.30	8.84	10.91	11.99	12.08	12.06

Continued on next page

Table A.1 – continued from previous page

				Detection limit (mag)						
Target	Date	Exp. time (s)	1% FWHM (″)	0.5″	0.8″	1.5″	2.5″	5.0″	10.0″	20.0″
WASP-95	2014-07-25 09:33:13	60	0.60	0.00	5.25	7.60	10.08	12.43	12.83	12.81
WASP-95	2014-08-11 06:11:25	60	0.59	0.00	5.11	7.78	10.40	12.41	12.62	12.61
WASP-95	2014-08-19 08:35:36	60	0.50	4.07	6.03	8.67	11.05	12.90	13.20	13.14
WASP-95	2014-09-21 04:50:30	60	0.35	5.36	7.10	9.83	11.77	12.87	13.07	13.05
WASP-96	2014-07-09 09:03:55	300	0.34	5.34	6.96	9.28	11.07	11.57	11.66	11.60
WASP-97	2014-07-09 10:14:02	60	0.43	4.38	6.22	8.86	11.08	12.55	12.83	12.77
WASP-98	2014-08-09 09:56:27	660	0.86	0.00	0.00	6.55	8.89	10.62	10.74	10.65
WASP-98	2014-08-10 09:26:45	660	0.59	0.00	5.04	7.71	10.14	11.10	11.11	11.06
WASP-98	2014-08-12 08:05:17	660	0.50	4.14	5.73	8.19	10.41	11.13	11.18	11.14
WASP-98	2014-08-19 07:48:36	660	0.40	4.59	6.19	8.74	10.86	11.66	11.69	11.60
WASP-98	2014-08-19 09:58:10	660	0.37	4.60	6.51	9.02	11.15	11.80	11.83	11.76
WASP-99	2014-08-09 09:34:00	60	0.95	0.00	0.00	5.61	8.07	10.81	12.01	12.01
WASP-99	2014-08-10 09:14:56	60	0.79	0.00	4.59	7.34	9.80	12.46	13.07	13.06
WASP-99	2014-09-21 06:22:15	60	0.41	4.49	6.19	8.95	11.30	13.27	13.52	13.50
WASP-100	2014-09-21 08:13:30	80	0.43	4.40	6.11	8.72	11.05	12.35	12.56	12.49
WASP-100	2014-09-21 08:15:17	80	0.43	4.39	6.18	8.67	11.07	12.36	12.52	12.47
WASP-101	2014-04-21 23:06:45	120	0.45	4.34	6.31	9.01	11.38	12.72	12.81	12.80
WASP-101	2014-04-22 23:13:14	120	0.43	4.52	6.31	9.05	11.45	12.97	13.13	13.10
WASP-103	2014-04-29 08:11:23	410	0.55	0.00	5.14	7.69	10.07	11.58	11.65	11.58
WASP-103	2014-05-07 05:31:37	410	0.49	4.08	5.94	8.41	10.56	11.65	11.73	11.65

Table A.2: **Observations with the TCI in 2015.**

				Detection limit (mag)						
Target	Date	Exp. time (s)	1% FWHM (″)	0.5″	0.8″	1.5″	2.5″	5.0″	10.0″	20.0″
CoRoT-22	2015-09-12 23:50	900	0.57	0.00	3.29	5.84	8.08	8.77	8.75	8.70
CoRoT-28	2015-09-12 23:32	900	0.53	0.00	4.06	6.53	8.77	9.48	9.52	9.47
HAT-P-27	2015-05-12 04:47	300	0.33	4.64	6.16	8.84	10.71	11.43	11.46	11.41
HAT-P-30	2015-04-28 01:30	60	0.52	2.32	3.84	6.25	8.43	9.64	9.76	9.74
HAT-P-35	2015-04-28 01:15	400	0.47	2.43	4.21	6.68	8.59	9.39	9.39	9.37
HAT-P-41	2015-05-29 07:57	140	0.46	2.61	4.25	6.72	8.95	9.63	9.67	9.64
HAT-P-45	2015-05-29 07:45	560	0.45	2.49	4.32	6.87	8.94	9.36	9.41	9.36
HAT-P-46	2015-05-29 07:40	240	0.44	2.51	4.23	6.63	8.85	9.54	9.58	9.52
HATS-1	2015-04-29 02:01	270	0.30	4.49	6.22	8.51	10.34	11.05	11.09	11.06
HATS-2	2015-04-29 00:50	900	0.28	4.69	6.32	8.69	10.23	10.52	10.53	10.49
HATS-9	2015-09-27 01:03	900	0.58	0.00	3.16	5.76	8.05	8.93	8.96	8.90
HATS-10	2015-09-12 03:42	770	0.59	0.00	2.94	5.42	7.83	9.26	9.31	9.24
HATS-13	2015-09-27 01:23	900	1.23	0.00	0.00	2.68	5.40	7.05	7.10	7.06
K2-02	2015-09-13 06:04	60	0.45	2.50	4.43	7.01	9.31	11.07	11.25	11.26
WASP-16	2015-04-29 03:28	130	0.37	2.69	4.63	7.11	9.26	10.75	10.93	10.86
WASP-17	2015-05-15 02:52	160	0.35	4.39	6.01	8.54	10.55	11.34	11.41	11.38
WASP-19	2015-04-28 01:40	350	0.40	2.71	4.51	6.84	8.86	9.56	9.60	9.55
WASP-24	2015-05-12 04:20	120	0.32	4.85	6.33	8.97	10.51	11.09	11.16	11.10
WASP-25	2015-04-29 03:06	220	0.38	2.81	4.47	6.81	9.00	10.30	10.38	10.34
WASP-28	2015-08-31 04:56	300	0.61	0.00	2.94	5.50	7.53	7.91	7.94	7.93
WASP-31	2015-04-29 01:32	240	0.32	4.37	6.16	8.65	10.35	11.02	11.08	11.03
WASP-36	2015-04-29 01:12	510	0.41	2.88	4.57	7.18	9.10	9.87	9.88	9.85
WASP-37	2015-05-12 04:35	530	0.29	4.90	6.43	9.17	10.86	11.31	11.37	11.33
WASP-39	2015-04-29 03:33	280	0.35	4.09	5.65	7.98	9.84	10.77	10.87	10.83
WASP-41	2015-05-15 02:17	180	0.34	4.75	6.51	9.21	11.16	11.97	12.09	12.00

Continued on next page

Table A.2 – continued from previous page

				Detection limit (mag)						
Target	Date	Exp. time (s)	1% FWHM (″)	0.5″	0.8″	1.5″	2.5″	5.0″	10.0″	20.0″
WASP-42	2015-04-29 02:55	450	0.37	2.73	4.46	7.04	9.18	10.61	10.71	10.68
WASP-54	2015-04-29 03:25	60	0.43	2.46	4.22	6.21	8.65	10.34	10.46	10.44
WASP-55	2015-04-29 03:18	210	0.36	3.92	5.48	7.61	9.58	10.51	10.57	10.57
WASP-66	2015-04-29 01:26	180	0.30	4.54	6.19	8.67	10.43	11.21	11.28	11.22
WASP-68	2015-05-11 07:21	70	0.46	2.63	4.59	7.24	9.28	10.69	10.81	10.80
WASP-74	2015-05-11 07:26	60	0.48	2.48	4.34	6.92	9.19	10.90	11.12	11.11
WASP-77	2015-09-26 09:21	60	0.58	0.00	2.93	5.46	7.90	10.07	10.35	10.33
WASP-80	2015-05-29 08:02	230	0.44	2.65	4.37	7.00	9.17	10.11	10.15	10.14
WASP-83	2015-04-29 02:33	600	0.33	4.16	5.86	8.20	10.13	11.11	11.20	11.10
WASP-85	2015-04-29 02:12	120	0.36	2.98	4.80	7.07	9.12	10.88	11.11	11.10
WASP-87	2015-04-29 02:29	80	0.33	4.11	5.57	8.17	10.04	11.15	11.31	11.33
WASP-97	2015-09-26 08:59	900	0.56	0.00	3.07	5.74	8.40	11.25	11.85	11.84
WASP-104	2015-06-04 23:30	110	0.61	0.00	2.91	5.23	7.70	9.29	9.40	9.35
WASP-106	2015-05-15 02:06	120	0.33	4.71	6.32	8.98	10.76	11.42	11.51	11.43
WASP-108	2015-04-29 03:13	120	0.40	2.67	4.20	6.70	8.88	10.32	10.53	10.45
WASP-109	2015-05-15 02:36	150	0.35	4.47	5.99	8.71	10.58	11.40	11.44	11.39
WASP-110	2015-05-29 08:08	340	0.40	2.66	4.41	6.89	8.55	8.72	8.74	8.68
WASP-111	2015-09-13 05:59	60	0.51	2.34	3.98	6.42	8.74	10.39	10.55	10.55
WASP-112	2015-09-13 06:08	900	0.46	2.47	4.15	6.57	8.80	9.63	9.72	9.63
WASP-117	2015-09-26 09:17	60	0.58	0.00	2.92	5.35	7.85	9.99	10.18	10.21

Table A.3: **Observations with the TCI in 2016.**

				Detection limit (mag)						
Target	Date	Exp. time (s)	1% FWHM (″)	0.5″	0.8″	1.5″	2.5″	5.0″	10.0″	20.0″
CoRoT-02	2016-04-30 10:01	450	0.34	4.45	6.11	8.65	10.43	10.98	11.03	10.96
CoRoT-04	2016-04-21 00:51	900	0.70	0.00	2.90	5.43	7.56	8.19	8.19	8.14
CoRoT-07	2016-04-21 00:08	200	0.42	2.57	4.68	7.33	9.64	10.44	10.47	10.43
CoRoT-24	2016-04-21 00:35	850	0.86	0.00	0.00	4.49	6.53	6.65	6.65	6.60
GJ 1132	2016-04-21 02:21	900	0.33	4.19	6.08	8.46	10.46	11.70	11.81	11.76
HAT-P-26	2016-06-18 23:21	203	0.36	2.90	5.00	7.82	9.87	10.71	10.79	10.73
HAT-P-27	2016-05-03 04:05	300	0.36	2.84	4.83	7.54	9.77	10.76	10.76	10.73
HAT-P-30	2016-04-21 01:09	60	0.43	2.56	4.63	7.24	9.47	10.44	10.51	10.49
HAT-P-35	2016-04-21 01:13	400	0.45	2.56	4.38	6.88	8.92	9.67	9.63	9.61
HAT-P-41	2016-04-30 10:11	140	0.36	3.06	4.90	7.52	9.63	10.78	10.94	10.89
HATS-02	2016-06-18 23:37	900	0.30	4.58	6.64	9.03	10.19	10.28	10.34	10.20
HATS-03	2016-06-11 09:17	390	0.47	2.50	4.21	6.90	8.76	10.18	10.23	10.19
HATS-04	2016-04-20 23:46	900	0.40	2.86	4.82	7.28	9.16	9.54	9.51	9.47
HATS-07	2016-05-03 02:16	900	0.31	4.46	6.36	8.91	10.55	10.89	10.87	10.82
HATS-09	2016-07-30 03:48	900	0.67	0.00	3.44	5.63	5.79	5.79	5.80	5.71
HATS-11	2016-04-30 09:22	900	0.31	4.53	6.32	8.54	9.67	9.78	9.82	9.70
HATS-12	2016-04-30 09:45	550	0.36	4.16	6.24	8.76	10.24	10.49	10.57	10.52
HATS-13	2016-06-11 08:22	900	0.48	2.41	4.11	6.61	8.57	8.97	8.96	8.93
HATS-14	2016-06-11 08:40	900	0.47	2.52	4.23	6.69	8.49	8.86	8.86	8.82
HATS-16	2016-06-19 10:17	900	0.34	4.19	5.95	8.30	9.35	9.48	9.41	9.37
HATS-17	2016-04-21 03:15	380	0.38	2.80	4.69	7.33	9.39	10.01	10.06	10.01
HATS-18	2016-06-18 00:43	900	0.47	2.43	4.19	6.53	8.31	8.65	8.69	8.62
HATS-25	2016-06-19 00:03	770	0.37	2.72	4.80	7.54	9.26	9.46	9.49	9.44
HATS-26	2016-06-19 23:56	660	0.53	0.00	3.99	6.40	8.21	8.93	8.99	8.94
HATS-27	2016-06-21 00:24	560	0.49	2.40	4.08	6.40	8.49	9.29	9.32	9.25

Continued on next page

Table A.3 – continued from previous page

Target	Date	Exp. time (s)	1% FWHM (″)	Detection limit (mag) 0.5″	0.8″	1.5″	2.5″	5.0″	10.0″	20.0″
HATS-29	2016-07-30 03:36	480	0.46	2.51	4.24	7.00	9.22	10.17	10.21	10.11
K2-02	2016-06-09 10:50	60	0.54	0.00	3.10	5.90	8.04	8.49	8.54	8.48
K2-03	2016-04-21 03:08	310	0.37	2.91	4.86	7.51	9.78	10.95	11.04	11.00
K2-10	2016-04-30 00:26	380	0.35	4.11	5.36	7.53	9.48	10.32	10.38	10.33
K2-19	2016-04-21 03:25	668	0.43	2.57	4.32	6.74	8.82	9.37	9.38	9.33
K2-21	2016-06-19 10:40	600	0.36	2.85	4.71	7.36	9.40	9.97	10.00	9.95
K2-24	2016-06-21 00:44	140	0.46	2.53	4.41	6.88	9.16	10.34	10.39	10.35
K2-27	2016-04-30 00:16	480	0.40	2.72	4.39	6.64	8.62	9.80	9.88	9.82
K2-31	2016-06-19 00:46	90	0.44	2.55	4.41	7.12	9.11	9.74	9.78	9.75
K2-38	2016-06-21 00:38	150	0.47	2.46	4.17	6.67	8.93	10.01	10.09	10.06
K2-39	2016-07-30 06:12	90	0.46	2.52	4.18	6.87	9.12	10.91	11.18	11.12
K2-44	2016-06-18 23:29	320	0.30	4.82	6.39	9.18	10.73	11.07	11.13	11.05
KELT-15	2016-04-21 01:29	150	0.42	2.59	4.41	6.69	8.95	10.26	10.37	10.31
WASP-08	2016-06-28 10:39	60	0.63	0.00	2.79	5.37	7.92	9.91	10.33	10.35
WASP-17	2016-06-19 00:40	158	0.39	2.78	4.61	7.25	9.06	9.58	9.60	9.62
WASP-19	2016-04-21 01:52	350	0.40	2.59	4.41	7.07	9.34	10.07	10.11	10.06
WASP-23	2016-04-21 00:23	500	0.35	4.18	6.18	8.60	10.42	10.78	10.83	10.79
WASP-24	2016-05-03 04:11	120	0.39	2.86	4.53	7.26	9.51	10.51	10.60	10.54
WASP-26	2016-06-28 10:26	120	0.62	0.00	2.81	5.30	7.65	9.46	9.64	9.59
WASP-28	2016-06-19 10:08	310	0.35	4.18	5.91	8.28	9.74	9.97	9.99	9.92
WASP-32	2016-06-28 10:19	140	0.69	0.00	2.66	4.92	7.31	8.79	8.89	8.86
WASP-36	2016-04-21 01:35	508	0.41	2.76	4.38	6.86	8.87	9.54	9.56	9.53
WASP-44	2016-07-01 09:28	620	0.51	2.38	3.96	6.48	8.52	9.17	9.21	9.13
WASP-45	2016-06-20 10:38	260	0.58	0.00	2.84	5.29	7.60	8.95	9.03	8.90
WASP-49	2016-04-20 23:40	140	0.38	2.81	4.70	7.42	9.48	10.48	10.57	10.52
WASP-54	2016-05-03 02:33	60	0.42	2.78	4.74	7.38	9.63	10.83	10.93	10.90

Continued on next page

Table A.3 – continued from previous page

				Detection limit (mag)						
Target	Date	Exp. time (s)	1% FWHM (″)	0.5″	0.8″	1.5″	2.5″	5.0″	10.0″	20.0″
WASP-55	2016-04-21 03:46	210	0.41	2.63	4.39	6.77	8.92	9.51	9.55	9.53
WASP-64	2016-04-21 00:15	340	0.37	2.77	4.92	7.47	9.54	9.88	9.94	9.86
WASP-66	2016-04-21 02:38	180	0.37	2.71	4.62	7.07	9.13	10.00	10.09	10.03
WASP-67	2016-06-09 09:03	430	0.65	0.00	2.78	5.11	7.67	9.50	9.62	9.55
WASP-68	2016-04-30 10:16	70	0.41	2.84	4.77	7.57	9.67	10.76	10.86	10.82
WASP-70	2016-06-09 10:41	80	0.54	0.00	3.17	5.65	7.45	7.78	7.80	7.75
WASP-74	2016-04-30 10:14	60	0.55	0.00	3.44	6.35	8.72	10.92	11.14	11.12
WASP-80	2016-04-30 10:19	230	0.36	2.89	4.83	7.66	9.62	10.69	10.73	10.74
WASP-83	2016-04-30 00:02	556	0.46	2.42	4.18	6.44	8.60	10.14	10.23	10.17
WASP-85	2016-04-21 03:37	120	0.44	2.49	4.36	6.58	8.70	10.26	10.45	10.43
WASP-87	2016-04-21 03:03	80	0.37	3.01	4.73	7.35	9.63	10.64	10.74	10.71
WASP-94	2016-06-11 08:56	60	0.50	2.43	3.99	6.57	8.85	10.63	10.91	10.86
WASP-101	2016-04-21 00:03	60	0.43	2.65	4.38	7.14	9.38	10.48	10.63	10.57
WASP-104	2016-04-21 01:46	110	0.44	2.64	4.26	6.78	8.75	9.59	9.63	9.60
WASP-106	2016-04-21 03:00	120	0.37	2.75	4.64	7.16	9.34	10.04	10.10	10.07
WASP-108	2016-04-21 03:42	120	0.43	2.57	4.47	6.93	9.18	10.15	10.27	10.23
WASP-109	2016-05-03 04:14	150	0.39	2.66	4.61	7.34	9.61	10.59	10.66	10.61
WASP-111	2016-06-11 09:25	60	0.52	2.27	3.89	6.47	8.76	10.50	10.74	10.72
WASP-112	2016-07-30 06:17	900	0.45	2.50	4.25	6.78	8.94	9.57	9.67	9.55
WASP-121	2016-04-21 01:23	60	0.45	2.49	4.36	6.88	9.18	10.48	10.63	10.58
WASP-122	2016-04-21 01:26	100	0.45	2.51	4.49	7.01	9.20	10.44	10.52	10.50
WASP-123	2016-04-30 09:57	100	0.36	2.99	5.12	7.81	9.97	11.01	11.16	11.09
WASP-124	2016-06-11 09:31	510	0.52	2.35	4.03	6.55	8.65	9.47	9.51	9.46
WASP-129	2016-05-03 01:55	350	0.31	4.50	6.37	8.97	10.71	11.28	11.37	11.29
WASP-130	2016-06-18 23:57	120	0.34	4.21	6.25	8.65	10.32	10.60	10.63	10.62
WASP-131	2016-06-19 00:19	60	0.41	2.55	4.94	7.70	9.90	10.93	11.00	10.98

Continued on next page

Table A.3 – continued from previous page

				Detection limit (mag)						
Target	Date	Exp. time (s)	1% FWHM (″)	0.5″	0.8″	1.5″	2.5″	5.0″	10.0″	20.0″
WASP-132	2016-06-19 00:25	390	0.40	2.62	4.70	7.32	9.51	10.54	10.58	10.56
WASP-133	2016-06-11 08:59	620	0.51	2.34	3.98	6.53	8.56	9.56	9.61	9.53
WASP-157	2016-05-03 02:03	620	0.30	4.69	6.41	9.04	10.86	11.43	11.39	11.35

Bibliography

Adams E. R., Dupree A. K., Kulesa C., McCarthy D., 2013, AJ, 146, 9

Airy G. B., 1834, Transactions of the Cambridge Philosophical Society, 5, 283

Albrecht S., Winn J. N., Johnson J. A., Howard A. W., Marcy G. W., Butler R. P., Arriagada P., Crane J. D., Shectman S. A., Thompson I. B., Hirano T., Bakos G., Hartman J. D., 2012, ApJ, 757, 18

Allard F., Homeier D., Freytag B., 2012, Philosophical Transactions of the Royal Society of London Series A, 370, 2765

Allende Prieto C., Koesterke L., Ludwig H.-G., Freytag B., Caffau E., 2013, A&A, 550, A103

Almenara J. M., Deeg H. J., Aigrain S., Alonso R., Auvergne M., Baglin A., Barbieri M., Barge P., Bordé P., Bouchy F., Bruntt H., Cabrera J., Carone L., Carpano S., Catala C., Csizmadia S., de La Reza R., Deleuil M., Dvorak R., Erikson A., Fridlund M., Gandolfi D., Gillon M., Gondoin P., Guenther E., Guillot T., Hatzes A., Hébrard G., Jorda L., Lammer H., Léger A., Llebaria A., Loeillet B., Magain P., Mayor M., Mazeh T., Moutou C., Ollivier M., Pätzold M., Pont F., Queloz D., Rauer H., Régulo C., Renner S., Rouan D., Samuel B., Schneider J., Shporer A., Wuchterl G., Zucker S., 2009, A&A, 506, 337

Alonso R., Brown T. M., Torres G., Latham D. W., Sozzetti A., Mandushev G., Belmonte J. A., Charbonneau D., Deeg H. J., Dunham E. W., O'Donovan F. T., Stefanik R. P., 2004, ApJL, 613, L153

Alonso R., Brown T. M., Charbonneau D., Dunham E. W., Belmonte J. A., Deeg H. J., Fernández J. M., Latham D. W., Mandushev G., O'Donovan F. T., Rabus M., Torres G., 2007, in Afonso C., Weldrake D., Henning T., eds, Transiting Extrapolar

Planets Workshop, Astronomical Society of the Pacific Conference Series Vol. 366, p. 13

Alonso R., Auvergne M., Baglin A., Ollivier M., Moutou C., Rouan D., Deeg H. J., Aigrain S., Almenara J. M., Barbieri M., Barge P., Benz W., Bordé P., Bouchy F., de La Reza R., Deleuil M., Dvorak R., Erikson A., Fridlund M., Gillon M., Gondoin P., Guillot T., Hatzes A., Hébrard G., Kabath P., Jorda L., Lammer H., Léger A., Llebaria A., Loeillet B., Magain P., Mayor M., Mazeh T., Pätzold M., Pepe F., Pont F., Queloz D., Rauer H., Shporer A., Schneider J., Stecklum B., Udry S., Wuchterl G., 2008, A&A, 482, L21

Alonso R., Moutou C., Endl M., Almenara J.-M., Guenther E. W., Deleuil M., Hatzes A., Aigrain S., Auvergne M., Baglin A., Barge P., Bonomo A. S., Bordé P., Bouchy F., Cavarroc C., Cabrera J., Carpano S., Csizmadia S., Cochran W. D., Deeg H. J., Díaz R. F., Dvorak R., Erikson A., Ferraz-Mello S., Fridlund M., Fruth T., Gandolfi D., Gillon M., Grziwa S., Guillot T., Hébrard G., Jorda L., Léger A., Lammer H., Lovis C., MacQueen P. J., Mazeh T., Ofir A., Ollivier M., Pasternacki T., Pätzold M., Queloz D., Rauer H., Rouan D., Santerne A., Schneider J., Tadeu dos Santos M., Tingley B., Titz-Weider R., Weingrill J., Wuchterl G., 2014, A&A, 567, A112

Alsubai K. A., Parley N. R., Bramich D. M., Horne K., Collier Cameron A., West R. G., Sorensen P. M., Pollacco D., Smith J. C., Fors O., 2013, AcA, 63, 465

Alsubai K., Tsvetanov Z. I., Latham D. W., Bieryla A., Esquerdo G. A., Mislis D., Pyrzas S., Foxell E., McCormac J., Baranec C., Vilchez N. P. E., West R., Esamdin A., Dang Z., Dalee H. M., Al-Rajihi A. A., Al-Harbi A. K., 2018, AJ, 155, 52

Althaus L. G., García-Berro E., Isern J., Córsico A. H., Rohrmann R. D., 2007, A&A, 465, 249

Amara A., Quanz S. P., 2012, MNRAS, 427, 948

An D., Pinsonneault M. H., Masseron T., Delahaye F., Johnson J. A., Terndrup D. M., Beers T. C., Ivans I. I., Ivezić Ž., 2009, ApJ, 700, 523

Andersen J., 1991, A&A Rv, 3, 91

Andersen D. R., Jackson K. J., Blain C., Bradley C., Correia C., Ito M., Lardière O., Véran J.-P., 2012, PASP, 124, 469

Anderson J., van der Marel R. P., 2010, ApJ, 710, 1032

Anderson J. A., 1920, ApJ, 51, 263

Anderson J., Sarajedini A., Bedin L. R., King I. R., Piotto G., Reid I. N., Siegel M., Majewski S. R., Paust N. E. Q., Aparicio A., Milone A. P., Chaboyer B., Rosenberg A., 2008, AJ, 135, 2055

Anderson D. R., Collier Cameron A., Hellier C., Lendl M., Maxted P. F. L., Pollacco D., Queloz D., Smalley B., Smith A. M. S., Todd I., Triaud A. H. M. J., West R. G., Barros S. C. C., Enoch B., Gillon M., Lister T. A., Pepe F., Ségransan D., Street R. A., Udry S., 2011, ApJL, 726, L19

Anderson D. R., Brown D. J. A., Collier Cameron A., Delrez L., Fumel A., Gillon M., Hellier C., Jehin E., Lendl M., Maxted P. F. L., Neveu-VanMalle M., Pepe F., Pollacco D., Queloz D., Rojo P., Segransan D., Serenelli A. M., Smalley B., Smith A. M. S., Southworth J., Triaud A. H. M. J., Turner O. D., Udry S., West R. G., 2014a, ArXiv e-prints

Anderson D. R., Collier Cameron A., Delrez L., Doyle A. P., Faedi F., Fumel A., Gillon M., Gómez Maqueo Chew Y., Hellier C., Jehin E., Lendl M., Maxted P. F. L., Pepe F., Pollacco D., Queloz D., Ségransan D., Skillen I., Smalley B., Smith A. M. S., Southworth J., Triaud A. H. M. J., Turner O. D., Udry S., West R. G., 2014b, MNRAS, 445, 1114

Anderson D. R., Collier Cameron A., Hellier C., Lendl M., Lister T. A., Maxted P. F. L., Queloz D., Smalley B., Smith A. M. S., Triaud A. H. M. J., Brown D. J. A., Gillon

M., Neveu-VanMalle M., Pepe F., Pollacco D., Ségransan D., Udry S., West R. G., Wheatley P. J., 2015, A&A, 575, A61

Anderson K. R., Storch N. I., Lai D., 2016, MNRAS, 456, 3671

Apai D., Pascucci I., Brandner W., Henning T., Lenzen R., Potter D. E., Lagrange A.-M., Rousset G., 2004, A&A, 415, 671

Astraatmadja T. L., Bailer-Jones C. A. L., 2016, ApJ, 833, 119

Auvergne M., Bodin P., Boisnard L., Buey J.-T., Chaintreuil S., Epstein G., Jouret M., Lam-Trong T., Levacher P., Magnan A., Perez R., Plasson P., Plesseria J., Peter G., Steller M., Tiphène D., Baglin A., Agogué P., Appourchaux T., Barbet D., Beaufort T., Bellenger R., Berlin R., Bernardi P., Blouin D., Boumier P., Bonneau F., Briet R., Butler B., Cautain R., Chiavassa F., Costes V., Cuvilho J., Cunha-Parro V., de Oliveira Fialho F., Decaudin M., Defise J.-M., Djalal S., Docclo A., Drummond R., Dupuis O., Exil G., Fauré C., Gaboriaud A., Gamet P., Gavalda P., Grolleau E., Gueguen L., Guivarc'h V., Guterman P., Hasiba J., Huntzinger G., Hustaix H., Imbert C., Jeanville G., Johlander B., Jorda L., Journoud P., Karioty F., Kerjean L., Lafond L., Lapeyrere V., Landiech P., Larqué T., Laudet P., Le Merrer J., Leporati L., Leruyet B., Levieuge B., Llebaria A., Martin L., Mazy E., Mesnager J.-M., Michel J.-P., Moalic J.-P., Monjoin W., Naudet D., Neukirchner S., Nguyen-Kim K., Ollivier M., Orcesi J.-L., Ottacher H., Oulali A., Parisot J., Perruchot S., Piacentino A., Pinheiro da Silva L., Platzer J., Pontet B., Pradines A., Quentin C., Rohbeck U., Rolland G., Rollenhagen F., Romagnan R., Russ N., Samadi R., Schmidt R., Schwartz N., Sebbag I., Smit H., Sunter W., Tello M., Toulouse P., Ulmer B., Vandermarcq O., Vergnault E., Wallner R., Waultier G., Zanatta P., 2009, A&A, 506, 411

Bakos G. Á., 2018, ArXiv e-prints

Bakos G. Á., Lázár J., Papp I., Sári P., Green E. M., 2002, PASP, 114, 974

Bakos G., Noyes R. W., Kovács G., Stanek K. Z., Sasselov D. D., Domsa I., 2004, PASP, 116, 266

Bakos G. Á., Hartman J. D., Torres G., Béky B., Latham D. W., Buchhave L. A., Csubry Z., Kovács G., Bieryla A., Quinn S., Szklenár T., Esquerdo G. A., Shporer A., Noyes R. W., Fischer D. A., Johnson J. A., Howard A. W., Marcy G. W., Sato B., Penev K., Everett M., Sasselov D. D., Fűrész G., Stefanik R. P., Lázár J., Papp I., Sári P., 2012, AJ, 144, 19

Bakos G. Á., Csubry Z., Penev K., Bayliss D., Jordán A., Afonso C., Hartman J. D., Henning T., Kovács G., Noyes R. W., Béky B., Suc V., Csák B., Rabus M., Lázár J., Papp I., Sári P., Conroy P., Zhou G., Sackett P. D., Schmidt B., Mancini L., Sasselov D. D., Ueltzhoeffer K., 2013, PASP, 125, 154

Ballhaus W. B., Casani J., Dorfman S., Gallagher D., Illingworth G., Klineberg J., Schurr D., Lewis R., Lobbia M., 2010, Final Report, James Webb Space Telescope Independent Comprehensive Review Panel

Baraffe I., Homeier D., Allard F., Chabrier G., 2015, A&A, 577, A42

Baranec C., Ziegler C., Law N. M., Morton T., Riddle R., Atkinson D., Schonhut J., Crepp J., 2016, AJ, 152, 18

Barclay T., Pepper J., Quintana E. V., 2018, ArXiv e-prints

Baruteau C., Crida A., Paardekooper S.-J., Masset F., Guilet J., Bitsch B., Nelson R., Kley W., Papaloizou J., 2014, Protostars and Planets VI, , 667

Batalha N. M., Rowe J. F., Gilliland R. L., Jenkins J. J., Caldwell D., Borucki W. J., Koch D. G., Lissauer J. J., Dunham E. W., Gautier T. N., Howell S. B., Latham D. W., Marcy G. W., Prsa A., 2010, ApJL, 713, L103

Bates R. H. T., Cady F. M., 1980, Optics Communications, 32, 365

Batygin K., 2012, Nature, 491, 418

Batygin K., Bodenheimer P. H., Laughlin G. P., 2016, ApJ, 829, 114

Batygin K., Morbidelli A., Tsiganis K., 2011, A&A, 533, A7

Bayliss D. D. R., Sackett P. D., 2011, ApJ, 743, 103

Bayliss D. D. R., Weldrake D. T. F., Sackett P. D., Tingley B. W., Lewis K. M., 2009, AJ, 137, 4368

Bechter E. B., Crepp J. R., Ngo H., Knutson H. A., Batygin K., Hinkley S., Muirhead P. S., Johnson J. A., Howard A. W., Montet B. T., Matthews C. T., Morton T. D., 2014, ApJ, 788, 2

Beckers J. M., 1988, in Ulrich M.-H., ed., European Southern Observatory Conference and Workshop Proceedings, European Southern Observatory Conference and Workshop Proceedings Vol. 30, p. 693

Bedin L. R., Pourbaix D., Apai D., Burgasser A. J., Buenzli E., Boffin H. M. J., Libralato M., 2017, MNRAS, 470, 1140

Bellini A., Piotto G., Bedin L. R., King I. R., Anderson J., Milone A. P., Momany Y., 2009, A&A, 507, 1393

Bellini A., Bedin L. R., Piotto G., Milone A. P., Marino A. F., Villanova S., 2010, AJ, 140, 631

Bellini A., Anderson J., van der Marel R. P., Watkins L. L., King I. R., Bianchini P., Chanamé J., Chandar R., Cool A. M., Ferraro F. R., Ford H., Massari D., 2014, ApJ, 797, 115

Bento J., Schmidt B., Hartman J. D., Bakos G. Á., Ciceri S., Brahm R., Bayliss D., Espinoza N., Zhou G., Rabus M., Bhatti W., Penev K., Csubry Z., Jordán A., Mancini L., Henning T., de Val-Borro M., Tinney C. G., Wright D. J., Durkan S., Suc V., Noyes R., Lázár J., Papp I., Sári P., 2017, MNRAS, 468, 835

Bergfors C., Brandner W., Daemgen S., Biller B., Hippler S., Janson M., Kudryavtseva N., Geißler K., Henning T., Köhler R., 2013, MNRAS, 428, 182

Berry D. S., Warren-Smith R. F., Jenness T., 2016, Astronomy and Computing, 15, 33

Beuzit J.-L., Feldt M., Dohlen K., Mouillet D., Puget P., Wildi F., Abe L., Antichi J., Baruffolo A., Baudoz P., Boccaletti A., Carbillet M., Charton J., Claudi R., Downing M., Fabron C., Feautrier P., Fedrigo E., Fusco T., Gach J.-L., Gratton R., Henning T., Hubin N., Joos F., Kasper M., Langlois M., Lenzen R., Moutou C., Pavlov A., Petit C., Pragt J., Rabou P., Rigal F., Roelfsema R., Rousset G., Saisse M., Schmid H.-M., Stadler E., Thalmann C., Turatto M., Udry S., Vakili F., Waters R., 2008, Ground-based and Airborne Instrumentation for Astronomy II, Proc. SPIE, , Vol. 7014, p. 701418

Bhatti W., Bakos G. Á., Hartman J. D., Zhou G., Penev K., Bayliss D., Jordán A., Brahm R., Espinoza N., Rabus M., Mancini L., de Val-Borro M., Bento J., Ciceri S., Csubry Z., Henning T., Schmidt B., Arriagada P., Butler R. P., Crane J., Shectman S., Thompson I., Tan T. G., Suc V., Lázár J., Papp I., Sári P., 2016, ArXiv e-prints

Bianchi L., Herald J., Efremova B., Girardi L., Zabot A., Marigo P., Conti A., Shiao B., 2012, VizieR Online Data Catalog, 2312

Birkby J., Hodgkin S., Pinfield D., WTS Consortium, 2011, in Johns-Krull C., Browning M. K., West A. A., eds, 16th Cambridge Workshop on Cool Stars, Stellar Systems, and the Sun, Astronomical Society of the Pacific Conference Series Vol. 448, p. 803

Birkby J. L., Cappetta M., Cruz P., Koppenhoefer J., Ivanyuk O., Mustill A. J., Hodgkin S. T., Pinfield D. J., Sipőcz B., Kovács G., Saglia R., Pavlenko Y., Barrado D., Bayo A., Campbell D., Catalan S., Fossati L., Gálvez-Ortiz M.-C., Kenworthy M., Lillo-Box J., Martín E. L., Mislis D., de Mooij E. J. W., Nefs S. V., Snellen I. A. G., Stoev H., Zendejas J., del Burgo C., Barnes J., Goulding

N., Haswell C. A., Kuznetsov M., Lodieu N., Murgas F., Palle E., Solano E., Steele P., Tata R., 2014, MNRAS, 440, 1470

Blanco-Cuaresma S., Soubiran C., Heiter U., Jofré P., 2014, A&A, 569, A111

Blank R., Anglin S., Beletic J. W., Baia Y., Buck S., Bhargava S., Chen J., Cooper D., Eads M., Farris M., Hall D. N. B., Hodapp K. W., Lavelle W., Loose M., Luppino G., Piquette E., Ricardo R., Sprafke T., Starr B., Xu M., Zandian M., 2011, in Kuhn J. R., Harrington D. M., Lin H., Berdyugina S. V., Trujillo-Bueno J., Keil S. L., Rimmele T., eds, Solar Polarization 6, Astronomical Society of the Pacific Conference Series Vol. 437, p. 383

Blunt S., Nielsen E. L., De Rosa R. J., Konopacky Q. M., Ryan D., Wang J. J., Pueyo L., Rameau J., Marois C., Marchis F., Macintosh B., Graham J. R., Duchêne G., Schneider A. C., 2017, AJ, 153, 229

Boesgaard A. M., Stephens A., Deliyannis C. P., 2005, ApJ, 633, 398

Boley A. C., Granados Contreras A. P., Gladman B., 2016, ApJL, 817, L17

Boley A. C., Helled R., Payne M. J., 2011, ApJ, 735, 30

Borucki W. J., Koch D., Jenkins J., Sasselov D., Gilliland R., Batalha N., Latham D. W., Caldwell D., Basri G., Brown T., Christensen-Dalsgaard J., Cochran W. D., DeVore E., Dunham E., Dupree A. K., Gautier T., Geary J., Gould A., Howell S., Kjeldsen H., Lissauer J., Marcy G., Meibom S., Morrison D., Tarter J., 2009, Science, 325, 709

Borucki W. J., Koch D., Basri G., Batalha N., Brown T., Caldwell D., Caldwell J., Christensen-Dalsgaard J., Cochran W. D., DeVore E., Dunham E. W., Dupree A. K., Gautier T. N., Geary J. C., Gilliland R., Gould A., Howell S. B., Jenkins J. M., Kondo Y., Latham D. W., Marcy G. W., Meibom S., Kjeldsen H., Lissauer J. J., Monet D. G., Morrison D., Sasselov D., Tarter J., Boss A., Brownlee D., Owen T., Buzasi D., Charbonneau D., Doyle L., Fortney J., Ford E. B., Holman

M. J., Seager S., Steffen J. H., Welsh W. F., Rowe J., Anderson H., Buchhave L., Ciardi D., Walkowicz L., Sherry W., Horch E., Isaacson H., Everett M. E., Fischer D., Torres G., Johnson J. A., Endl M., MacQueen P., Bryson S. T., Dotson J., Haas M., Kolodziejczak J., Van Cleve J., Chandrasekaran H., Twicken J. D., Quintana E. V., Clarke B. D., Allen C., Li J., Wu H., Tenenbaum P., Verner E., Bruhweiler F., Barnes J., Prsa A., 2010, Science, 327, 977

Boss A. P., 1997, Science, 276, 1836

Bouchy F., Hebb L., Skillen I., Collier Cameron A., Smalley B., Udry S., Anderson D. R., Boisse I., Enoch B., Haswell C. A., Hébrard G., Hellier C., Joshi Y., Kane S. R., Maxted P. F. L., Mayor M., Moutou C., Pepe F., Pollacco D., Queloz D., Ségransan D., Simpson E. K., Smith A. M. S., Stempels H. C., Street R., Triaud A. H. M. J., West R. G., Wheatley P. J., 2010, A&A, 519, A98

Boué G., Laskar J., 2010, ApJL, 712, L44

Braga-Ribas F., Sicardy B., Ortiz J. L., Snodgrass C., Roques F., Vieira-Martins R., Camargo J. I. B., Assafin M., Duffard R., Jehin E., Pollock J., Leiva R., Emilio M., Machado D. I., Colazo C., Lellouch E., Skottfelt J., Gillon M., Ligier N., Maquet L., Benedetti-Rossi G., Gomes A. R., Kervella P., Monteiro H., Sfair R., El Moutamid M., Tancredi G., Spagnotto J., Maury A., Morales N., Gil-Hutton R., Roland S., Ceretta A., Gu S.-H., Wang X.-B., Harpsøe K., Rabus M., Manfroid J., Opitom C., Vanzi L., Mehret L., Lorenzini L., Schneiter E. M., Melia R., Lecacheux J., Colas F., Vachier F., Widemann T., Almenares L., Sandness R. G., Char F., Perez V., Lemos P., Martinez N., Jørgensen U. G., Dominik M., Roig F., Reichart D. E., Lacluyze A. P., Haislip J. B., Ivarsen K. M., Moore J. P., Frank N. R., Lambas D. G., 2014, Nature, 508, 72

Brahm R., Hartman J. D., Jordán A., Bakos G. Á., Espinoza N., Rabus M., Bhatti W., Penev K., Sarkis P., Suc V., Csubry Z., Bayliss D., Bento J., Zhou G., Mancini L., Henning T., Ciceri S., de Val-Borro M., Shectman S., Crane J. D., Arriagada P.,

Butler P., Teske J., Thompson I., Osip D., Díaz M., Schmidt B., Lázár J., Papp I., Sári P., 2018, AJ, 155, 112

Brandt T. D., Rizzo M., Groff T., Chilcote J., Greco J. P., Kasdin N. J., Limbach M. A., Galvin M., Loomis C., Knapp G., McElwain M. W., Jovanovic N., Currie T., Mede K., Tamura M., Takato N., Hayashi M., 2017, ArXiv e-prints

Brown D. J. A., 2015, European Planetary Science Congress, 10, EPSC2015

Bryan M. L., Alsubai K. A., Latham D. W., Parley N. R., Collier Cameron A., Quinn S. N., Carter J. A., Fulton B. J., Berlind P., Brown W. R., Buchhave L. A., Calkins M. L., Esquerdo G. A., Fűrész G., Gråe Jørgensen U., Horne K. D., Stefanik R. P., Street R. A., Torres G., West R. G., Dominik M., Harpsøe K. B. W., Liebig C., Calchi Novati S., Ricci D., Skottfelt J. F., 2012, ApJ, 750, 84

Buchhave L. A., Latham D. W., Carter J. A., Désert J.-M., Torres G., Adams E. R., Bryson S. T., Charbonneau D. B., Ciardi D. R., Kulesa C., Dupree A. K., Fischer D. A., Fressin F., Gautier, III T. N., Gilliland R. L., Howell S. B., Isaacson H., Jenkins J. M., Marcy G. W., McCarthy D. W., Rowe J. F., Batalha N. M., Borucki W. J., Brown T. M., Caldwell D. A., Christiansen J. L., Cochran W. D., Deming D., Dunham E. W., Everett M., Ford E. B., Fortney J. J., Geary J. C., Girouard F. R., Haas M. R., Holman M. J., Horch E., Klaus T. C., Knutson H. A., Koch D. G., Kolodziejczak J., Lissauer J. J., Machalek P., Mullally F., Still M. D., Quinn S. N., Seager S., Thompson S. E., Van Cleve J., 2011, ApJS, 197, 3

Buie M. W., Tholen D. J., Grundy W. M., 2012, AJ, 144, 15

Bush N., Stefanov K., Hall D., Jordan D., Holland A., 2014, Journal of Instrumentation, 9(12), C12042

Cabrera J., Barros S. C. C., Armstrong D., Hidalgo D., Santos N. C., Almenara J. M., Alonso R., Deleuil M., Demangeon O., Díaz R. F., Lendl M., Pfaff J., Rauer H., Santerne A., Serrano L. M., Zucker S., 2017, A&A, 606, A75

Calchi Novati S., Gould A., Udalski A., Menzies J. W., Bond I. A., Shvartzvald Y., Street R. A., Hundertmark M., Beichman C. A., Yee J. C., Carey S., Poleski R., Skowron J., Kozłowski S., Mróz P., Pietrukowicz P., Pietrzyński G., Szymański M. K., Soszyński I., Ulaczyk K., Wyrzykowski Ł., OGLE Collaboration, Albrow M., Beaulieu J. P., Caldwell J. A. R., Cassan A., Coutures C., Danielski C., Dominis Prester D., Donatowicz J., Lončarić K., McDougall A., Morales J. C., Ranc C., Zhu W., PLANET Collaboration, Abe F., Barry R. K., Bennett D. P., Bhattacharya A., Fukunaga D., Inayama K., Koshimoto N., Namba S., Sumi T., Suzuki D., Tristram P. J., Wakiyama Y., Yonehara A., MOA Collaboration, Maoz D., Kaspi S., Friedmann M., Wise Group, Bachelet E., Figuera Jaimes R., Bramich D. M., Tsapras Y., Horne K., Snodgrass C., Wambsganss J., Steele I. A., Kains N., RoboNet Collaboration, Bozza V., Dominik M., Jørgensen U. G., Alsubai K. A., Ciceri S., D'Ago G., Haugbølle T., Hessman F. V., Hinse T. C., Juncher D., Korhonen H., Mancini L., Popovas A., Rabus M., Rahvar S., Scarpetta G., Schmidt R. W., Skottfelt J., Southworth J., Starkey D., Surdej J., Wertz O., Zarucki M., MiNDSTEp Consortium, Gaudi B. S., Pogge R. W., DePoy D. L., μFUN Collaboration, 2015, ApJ, 804, 20

Cameron A. C., 2016, in Bozza V., Mancini L., Sozzetti A., eds, Methods of Detecting Exoplanets: 1st Advanced School on Exoplanetary Science, Springer, p. 89

Campbell R. D., Thompson D. J., 2006, in Beletic J. E., Beletic J. W., Amico P., eds, Astrophysics and Space Science Library, Astrophysics and Space Science Library Vol. 336, p. 507

Cardelli J. A., Clayton G. C., Mathis J. S., 1989, ApJ, 345, 245

Carpenter J. M., 2001, AJ, 121, 2851

Cassan A., Kubas D., Beaulieu J.-P., Dominik M., Horne K., Greenhill J., Wambsganss J., Menzies J., Williams A., Jørgensen U. G., Udalski A., Bennett D. P., Albrow M. D., Batista V., Brillant S., Caldwell J. A. R., Cole A., Coutures C., Cook

K. H., Dieters S., Dominis Prester D., Donatowicz J., Fouqué P., Hill K., Kains N., Kane S., Marquette J.-B., Martin R., Pollard K. R., Sahu K. C., Vinter C., Warren D., Watson B., Zub M., Sumi T., Szymański M. K., Kubiak M., Poleski R., Soszynski I., Ulaczyk K., Pietrzyński G., Wyrzykowski Ł., 2012, Nature, 481, 167

Castelli F., Kurucz R. L., 2004, ArXiv Astrophysics e-prints

Cegla H. M., Lovis C., Bourrier V., Beeck B., Watson C. A., Pepe F., 2016, A&A, 588, A127

Charbonneau D., Brown T. M., Latham D. W., Mayor M., 2000, ApJL, 529, L45

Charbonneau D., Berta Z. K., Irwin J., Burke C. J., Nutzman P., Buchhave L. A., Lovis C., Bonfils X., Latham D. W., Udry S., Murray-Clay R. A., Holman M. J., Falco E. E., Winn J. N., Queloz D., Pepe F., Mayor M., Delfosse X., Forveille T., 2009, Nature, 462, 891

Chatterjee S., Ford E. B., Matsumura S., Rasio F. A., 2008, ApJ, 686, 580

Chauvin G., Lagrange A.-M., Dumas C., Zuckerman B., Mouillet D., Song I., Beuzit J.-L., Lowrance P., 2004, A&A, 425, L29

Chauvin G., Lagrange A.-M., Udry S., Fusco T., Galland F., Naef D., Beuzit J.-L., Mayor M., 2006, A&A, 456, 1165

Chauvin G., Lagrange A.-M., Beust H., Bonnefoy M., Boccaletti A., Apai D., Allard F., Ehrenreich D., Girard J. H. V., Mouillet D., Rouan D., 2012, A&A, 542, A41

Ciardi D. R., Beichman C. A., Horch E. P., Howell S. B., 2015, ApJ, 805, 16

Claudi R. U., Turatto M., Gratton R. G., Antichi J., Bonavita M., Bruno P., Cascone E., De Caprio V., Desidera S., Giro E., Mesa D., Scuderi S., Dohlen K., Beuzit J. L., Puget P., 2008, Ground-based and Airborne Instrumentation for Astronomy II, Proc. SPIE, Vol. 7014, p. 70143E

Clénet Y., Rouan D., Gratadour D., Lacombe F., Gendron E., Genzel R., Ott T., Schödel R., Léna P., 2004, A&A, 424, L21

Close L. M., Siegler N., Freed M., Biller B., 2003, ApJ, 587, 407

Coleman G. A. L., Nelson R. P., 2016, MNRAS, 460, 2779

Collier Cameron A., Bouchy F., Hébrard G., Maxted P., Pollacco D., Pont F., Skillen I., Smalley B., Street R. A., West R. G., Wilson D. M., Aigrain S., Christian D. J., Clarkson W. I., Enoch B., Evans A., Fitzsimmons A., Fleenor M., Gillon M., Haswell C. A., Hebb L., Hellier C., Hodgkin S. T., Horne K., Irwin J., Kane S. R., Keenan F. P., Loeillet B., Lister T. A., Mayor M., Moutou C., Norton A. J., Osborne J., Parley N., Queloz D., Ryans R., Triaud A. H. M. J., Udry S., Wheatley P. J., 2007, MNRAS, 375, 951

Collier Cameron A., Bruce V. A., Miller G. R. M., Triaud A. H. M. J., Queloz D., 2010, MNRAS, 403, 151

Crass J., Aisher P., Femenia B., King D. L., Mackay C. D., Rebolo-López R., Labadie L., Pérez Garrido A., Balcells M., Díaz Sánchez A., Jimenez Fuensalida J., Lopez R. L., Oscoz A., Pérez Prieto J. A., Rodríguez-Ramos L. F., Villó I., 2012, Adaptive Optics Systems III, Proc. SPIE, Vol. 8447, p. 84470T

Crossfield I. J. M., Petigura E., Schlieder J. E., Howard A. W., Fulton B. J., Aller K. M., Ciardi D. R., Lépine S., Barclay T., de Pater I., de Kleer K., Quintana E. V., Christiansen J. L., Schlafly E., Kaltenegger L., Crepp J. R., Henning T., Obermeier C., Deacon N., Weiss L. M., Isaacson H. T., Hansen B. M. S., Liu M. C., Greene T., Howell S. B., Barman T., Mordasini C., 2015, ApJ, 804, 10

Crossfield I. J. M., Ciardi D. R., Petigura E. A., Sinukoff E., Schlieder J. E., Howard A. W., Beichman C. A., Isaacson H., Dressing C. D., Christiansen J. L., Fulton B. J., Lépine S., Weiss L., Hirsch L., Livingston J., Baranec C., Law N. M., Riddle R., Ziegler C., Howell S. B., Horch E., Everett M., Teske J., Martinez A. O.,

Obermeier C., Benneke B., Scott N., Deacon N., Aller K. M., Hansen B. M. S., Mancini L., Ciceri S., Brahm R., Jordán A., Knutson H. A., Henning T., Bonnefoy M., Liu M. C., Crepp J. R., Lothringer J., Hinz P., Bailey V., Skemer A., Defrere D., 2016, ApJS, 226, 7

Cubillos P., Harrington J., Madhusudhan N., Stevenson K. B., Hardy R. A., Blecic J., Anderson D. R., Hardin M., Campo C. J., 2013, ApJ, 768, 42

Cumming A., Butler R. P., Marcy G. W., Vogt S. S., Wright J. T., Fischer D. A., 2008, PASP, 120, 531

Currie M. J., Berry D. S., Jenness T., Gibb A. G., Bell G. S., Draper P. W., 2014, in Manset N., Forshay P., eds, Astronomical Data Analysis Software and Systems XXIII, Astronomical Society of the Pacific Conference Series Vol. 485, p. 391

Cutri R. M., et al., 2012, VizieR Online Data Catalog, 2311

Daemgen S., Hormuth F., Brandner W., Bergfors C., Janson M., Hippler S., Henning T., 2009, A&A, 498, 567

D'Angelo G., Weidenschilling S. J., Lissauer J. J., Bodenheimer P., 2014, Icarus, 241, 298

Dantowitz R., 1998, S&T, 96(2), 48

Dantowitz R. F., Teare S. W., Kozubal M. J., 2000, AJ, 119, 2455

Davies R. I., Thomas J., Genzel R., Müller Sánchez F., Tacconi L. J., Sternberg A., Eisenhauer F., Abuter R., Saglia R., Bender R., 2006, ApJ, 646, 754

Dawson R. I., Johnson J. A., 2018, ArXiv e-prints

de Pater I., Fletcher L. N., Pérez-Hoyos S., Hammel H. B., Orton G. S., Wong M. H., Luszcz-Cook S., Sánchez-Lavega A., Boslough M., 2010, Icarus, 210, 722

de Val-Borro M., Bakos G. Á., Brahm R., Hartman J. D., Espinoza N., Penev K., Ciceri S., Jordán A., Bhatti W., Csubry Z., Bayliss D., Bento J., Zhou G., Rabus M., Mancini L., Henning T., Schmidt B., Tan T. G., Tinney C. G., Wright D. J., Kedziora-Chudczer L., Bailey J., Suc V., Durkan S., Lázár J., Papp I., Sári P., 2016, AJ, 152, 161

Deeg H. J., Gillon M., Shporer A., Rouan D., Stecklum B., Aigrain S., Alapini A., Almenara J. M., Alonso R., Barbieri M., Bouchy F., Eislöffel J., Erikson A., Fridlund M., Eigmüller P., Handler G., Hatzes A., Kabath P., Lendl M., Mazeh T., Moutou C., Queloz D., Rauer H., Rabus M., Tingley B., Titz R., 2009, A&A, 506, 343

Deeg H. J., Moutou C., Erikson A., Csizmadia S., Tingley B., Barge P., Bruntt H., Havel M., Aigrain S., Almenara J. M., Alonso R., Auvergne M., Baglin A., Barbieri M., Benz W., Bonomo A. S., Bordé P., Bouchy F., Cabrera J., Carone L., Carpano S., Ciardi D., Deleuil M., Dvorak R., Ferraz-Mello S., Fridlund M., Gandolfi D., Gazzano J.-C., Gillon M., Gondoin P., Guenther E., Guillot T., Hartog R. D., Hatzes A., Hidas M., Hébrard G., Jorda L., Kabath P., Lammer H., Léger A., Lister T., Llebaria A., Lovis C., Mayor M., Mazeh T., Ollivier M., Pätzold M., Pepe F., Pont F., Queloz D., Rabus M., Rauer H., Rouan D., Samuel B., Schneider J., Shporer A., Stecklum B., Street R., Udry S., Weingrill J., Wuchterl G., 2010, Nature, 464, 384

Deleuil M., Deeg H. J., Alonso R., Bouchy F., Rouan D., Auvergne M., Baglin A., Aigrain S., Almenara J. M., Barbieri M., Barge P., Bruntt H., Bordé P., Collier Cameron A., Csizmadia S., de La Reza R., Dvorak R., Erikson A., Fridlund M., Gandolfi D., Gillon M., Guenther E., Guillot T., Hatzes A., Hébrard G., Jorda L., Lammer H., Léger A., Llebaria A., Loeillet B., Mayor M., Mazeh T., Moutou C., Ollivier M., Pätzold M., Pont F., Queloz D., Rauer H., Schneider J., Shporer A., Wuchterl G., Zucker S., 2008, A&A, 491, 889

Delorme P., Meunier N., Albert D., Lagadec E., Le Coroller H., Galicher R., Mouillet

D., Boccaletti A., Mesa D., Meunier J.-C., Beuzit. J.-L., Lagrange A.-M., Chauvin G., Sapone A., Langlois M., Maire A.-L., Montargès M., Gratton R., Vigan A., Surace C., Moreau C., Fenouillet T., 2017, ArXiv e-prints

Denker C., Tritschler A., Rimmele T. R., Richards K., Hegwer S. L., Wöger F., 2007, PASP, 119, 170

Descamps P., Marchis F., Berthier J., Emery J. P., Duchêne G., de Pater I., Wong M. H., Lim L., Hammel H. B., Vachier F., Wiggins P., Teng-Chuen-Yu J.-P., Peyrot A., Pollock J., Assafin M., Vieira-Martins R., Camargo J. I. B., Braga-Ribas F., Macomber B., 2011, Icarus, 211, 1022

Désert J.-M., Charbonneau D., Demory B.-O., Ballard S., Carter J. A., Fortney J. J., Cochran W. D., Endl M., Quinn S. N., Isaacson H. T., Fressin F., Buchhave L. A., Latham D. W., Knutson H. A., Bryson S. T., Torres G., Rowe J. F., Batalha N. M., Borucki W. J., Brown T. M., Caldwell D. A., Christiansen J. L., Deming D., Fabrycky D. C., Ford E. B., Gilliland R. L., Gillon M., Haas M. R., Jenkins J. M., Kinemuchi K., Koch D., Lissauer J. J., Lucas P., Mullally F., MacQueen P. J., Marcy G. W., Sasselov D. D., Seager S., Still M., Tenenbaum P., Uddin K., Winn J. N., 2011, ApJS, 197, 14

Dias-Oliveira A., Sicardy B., Lellouch E., Vieira-Martins R., Assafin M., Camargo J. I. B., Braga-Ribas F., Gomes-Júnior A. R., Benedetti-Rossi G., Colas F., Decock A., Doressoundiram A., Dumas C., Emilio M., Fabrega Polleri J., Gil-Hutton R., Gillon M., Girard J. H., Hau G. K. T., Ivanov V. D., Jehin E., Lecacheux J., Leiva R., Lopez-Sisterna C., Mancini L., Manfroid J., Maury A., Meza E., Morales N., Nagy L., Opitom C., Ortiz J. L., Pollock J., Roques F., Snodgrass C., Soulier J. F., Thirouin A., Vanzi L., Widemann T., Reichart D. E., LaCluyze A. P., Haislip J. B., Ivarsen K. M., Dominik M., Jørgensen U., Skottfelt J., 2015, ApJ, 811, 53

Díaz R. F., Almenara J. M., Santerne A., Moutou C., Lethuillier A., Deleuil M., 2014, MNRAS, 441, 983

Doel A. P., Dunlop C. N., Major J. V., Myers R. M., Purvis A., Thompson M. G., 1990, in Barr L. D., ed., Advanced Technology Optical Telescopes IV, Proc. SPIE, Vol. 1236, p. 179

Dohlen K., Langlois M., Saisse M., Hill L., Origne A., Jacquet M., Fabron C., Blanc J.-C., Llored M., Carle M., Moutou C., Vigan A., Boccaletti A., Carbillet M., Mouillet D., Beuzit J.-L., 2008, Ground-based and Airborne Instrumentation for Astronomy II, Proc. SPIE, Vol. 7014, p. 70143L

Donati J. F., Moutou C., Malo L., Baruteau C., Yu L., Hébrard E., Hussain G., Alencar S., Ménard F., Bouvier J., Petit P., Takami M., Doyon R., Cameron A. C., 2016, Nature, 534, 662

Dravins D., Lindegren L., Mezey E., Young A. T., 1998, PASP, 110, 610

Dressing C. D., Charbonneau D., 2013, ApJ, 767, 95

Dressing C. D., Vanderburg A., Schlieder J. E., Crossfield I. J. M., Knutson H. A., Newton E. R., Ciardi D. R., Fulton B. J., Gonzales E. J., Howard A. W., Isaacson H., Livingston J., Petigura E. A., Sinukoff E., Everett M., Horch E., Howell S. B., 2017, AJ, 154, 207

Eggenberger A., Udry S., Chauvin G., Beuzit J.-L., Lagrange A.-M., Ségransan D., Mayor M., 2007, A&A, 474, 273

Eisenhauer F., Perrin G., Brandner W., Straubmeier C., Perraut K., Amorim A., Schöller M., Gillessen S., Kervella P., Benisty M., Araujo-Hauck C., Jocou L., Lima J., Jakob G., Haug M., Clénet Y., Henning T., Eckart A., Berger J.-P., Garcia P., Abuter R., Kellner S., Paumard T., Hippler S., Fischer S., Moulin T., Villate J., Avila G., Gräter A., Lacour S., Huber A., Wiest M., Nolot A., Carvas P., Dorn R., Pfuhl O., Gendron E., Kendrew S., Yazici S., Anton S., Jung Y., Thiel M., Choquet É., Klein R., Teixeira P., Gitton P., Moch D., Vincent F., Kudryavtseva N., Ströbele S., Sturm S., Fédou P., Lenzen R., Jolley P., Kister

C., Lapeyrère V., Naranjo V., Lucuix C., Hofmann R., Chapron F., Neumann U., Mehrgan L., Hans O., Rousset G., Ramos J., Suarez M., Lederer R., Reess J.-M., Rohloff R.-R., Haguenauer P., Bartko H., Sevin A., Wagner K., Lizon J.-L., Rabien S., Collin C., Finger G., Davies R., Rouan D., Wittkowski M., Dodds-Eden K., Ziegler D., Cassaing F., Bonnet H., Casali M., Genzel R., Lena P., 2011, The Messenger, 143, 16

Enoch B., Anderson D. R., Barros S. C. C., Brown D. J. A., Collier Cameron A., Faedi F., Gillon M., Hébrard G., Lister T. A., Queloz D., Santerne A., Smalley B., Street R. A., Triaud A. H. M. J., West R. G., Bouchy F., Bento J., Butters O., Fossati L., Haswell C. A., Hellier C., Holmes S., Jehin E., Lendl M., Maxted P. F. L., McCormac J., Miller G. R. M., Moulds V., Moutou C., Norton A. J., Parley N., Pepe F., Pollacco D., Segransan D., Simpson E., Skillen I., Smith A. M. S., Udry S., Wheatley P. J., 2011, AJ, 142, 86

Espinoza N., Bayliss D., Hartman J. D., Bakos G. Á., Jordán A., Zhou G., Mancini L., Brahm R., Ciceri S., Bhatti W., Csubry Z., Rabus M., Penev K., Bento J., de Val-Borro M., Henning T., Schmidt B., Suc V., Wright D. J., Tinney C. G., Tan T. G., Noyes R., 2016, AJ, 152, 108

Evans D. F., 2018, Research Notes of the American Astronomical Society, 2(2), 20

Evans D. F., Southworth J., Maxted P. F. L., Skottfelt J., Hundertmark M., Jørgensen U. G., Dominik M., Alsubai K. A., Andersen M. I., Bozza V., Bramich D. M., Burgdorf M. J., Ciceri S., D'Ago G., Figuera Jaimes R., Gu S.-H., Haugbølle T., Hinse T. C., Juncher D., Kains N., Kerins E., Korhonen H., Kuffmeier M., Mancini L., Peixinho N., Popovas A., Rabus M., Rahvar S., Schmidt R. W., Snodgrass C., Starkey D., Surdej J., Tronsgaard R., von Essen C., Wang Y.-B., Wertz O., 2016, A&A, 589, A58

Evans D. F., Southworth J., Smalley B., Jørgensen U. G., Dominik M., Andersen M. I., Bozza V., Bramich D. M., Burgdorf M. J., Ciceri S., D'Ago G., Figuera Jaimes R.,

Gu S.-H., Hinse T. C., Henning T., Hundertmark M., Kains N., Kerins E., Korhonen H., Kokotanekova R., Kuffmeier M., Longa-Peña P., Mancini L., MacKenzie J., Popovas A., Rabus M., Rahvar S., Sajadian S., Snodgrass C., Skottfelt J., Surdej J., Tronsgaard R., Unda-Sanzana E., von Essen C., Wang Y.-B., Wertz O., 2018, A&A, 610, A20

Evans D. F., Southworth J., Smalley B., 2016, ApJL, 833, L19

Fabrycky D., Tremaine S., 2007, ApJ, 669, 1298

Faedi F., Staley T., Gómez Maqueo Chew Y., Pollacco D., Dhital S., Barros S. C. C., Skillen I., Hebb L., Mackay C., Watson C. A., 2013, MNRAS, 433, 2097

Faria J. P., Haywood R. D., Brewer B. J., Figueira P., Oshagh M., Santerne A., Santos N. C., 2016, A&A, 588, A31

Femenía B., Rebolo R., Pérez-Prieto J. A., Hildebrandt S. R., Labadie L., Pérez-Garrido A., Béjar V. J. S., Díaz-Sánchez A., Villó I., Oscoz A., López R., Rodríguez L. F., Piqueras J., 2011, MNRAS, 413, 1524

Figuera Jaimes R., Bramich D. M., Kains N., Skottfelt J., Jørgensen U. G., Horne K., Dominik M., Alsubai K. A., Bozza V., Burgdorf M. J., Calchi Novati S., Ciceri S., D'Ago G., Evans D. F., Galianni P., Gu S.-H., Harpsøe K. B. W., Haugbølle T., Hinse T. C., Hundertmark M., Juncher D., Kerins E., Korhonen H., Kuffmeier M., Mancini L., Peixinho N., Popovas A., Rabus M., Rahvar S., Scarpetta G., Schmidt R. W., Snodgrass C., Southworth J., Starkey D., Street R. A., Surdej J., Tronsgaard R., Unda-Sanzana E., von Essen C., Wang X.-B., Wertz O., 2016a, A&A, 592, A120

Figuera Jaimes R., Bramich D. M., Skottfelt J., Kains N., Jørgensen U. G., Horne K., Dominik M., Alsubai K. A., Bozza V., Calchi Novati S., Ciceri S., D'Ago G., Galianni P., Gu S.-H., Harpsøe K. B. W., Haugbølle T., Hinse T. C., Hundertmark M., Juncher D., Korhonen H., Mancini L., Popovas A., Rabus M., Rahvar S.,

Scarpetta G., Schmidt R. W., Snodgrass C., Southworth J., Starkey D., Street R. A., Surdej J., Wang X.-B., Wertz O., 2016b, A&A, 588, A128

Fischer D. A., Marcy G. W., 1992, ApJ, 396, 178

Fischer D. A., Valenti J., 2005, ApJ, 622, 1102

Ford E. B., 2006, ApJ, 642, 505

Foy R., Labeyrie A., 1985, A&A, 152, L29

Freedman W. L., Hughes S. M., Madore B. F., Mould J. R., Lee M. G., Stetson P., Kennicutt R. C., Turner A., Ferrarese L., Ford H., Graham J. A., Hill R., Hoessel J. G., Huchra J., Illingworth G. D., 1994, ApJ, 427, 628

Fressin F., Torres G., Charbonneau D., Bryson S. T., Christiansen J., Dressing C. D., Jenkins J. M., Walkowicz L. M., Batalha N. M., 2013, ApJ, 766, 81

Fridlund M., Baglin A., Lochard J., Conroy L., 2006, The CoRoT Mission Pre-Launch Status - Stellar Seismology and Planet Finding

Fried D. L., 1966, Journal of the Optical Society of America (1917-1983), 56, 1372

Fried D. L., 1978, Journal of the Optical Society of America (1917-1983), 68, 1651

Fulton B. J., Collins K. A., Gaudi B. S., Stassun K. G., Pepper J., Beatty T. G., Siverd R. J., Penev K., Howard A. W., Baranec C., Corfini G., Eastman J. D., Gregorio J., Law N. M., Lund M. B., Oberst T. E., Penny M. T., Riddle R., Rodriguez J. E., Stevens D. J., Zambelli R., Ziegler C., Bieryla A., D'Ago G., DePoy D. L., Jensen E. L. N., Kielkopf J. F., Latham D. W., Manner M., Marshall J., McLeod K. K., Reed P. A., 2015, ApJ, 810, 30

Furlan E., Ciardi D. R., Everett M. E., Saylors M., Teske J. K., Horch E. P., Howell S. B., van Belle G. T., Hirsch L. A., Gautier, III T. N., Adams E. R., Barrado D., Cartier K. M. S., Dressing C. D., Dupree A. K., Gilliland R. L., Lillo-Box J., Lucas P. W., Wang J., 2017, AJ, 153, 71

Gaia Collaboration, Brown A. G. A., Vallenari A., Prusti T., de Bruijne J. H. J., Mignard F., Drimmel R., Babusiaux C., Bailer-Jones C. A. L., Bastian U., et al., 2016a, A&A, 595, A2

Gaia Collaboration, Prusti T., de Bruijne J. H. J., Brown A. G. A., Vallenari A., Babusiaux C., Bailer-Jones C. A. L., Bastian U., Biermann M., Evans D. W., et al., 2016b, A&A, 595, A1

Gandolfi D., Hébrard G., Alonso R., Deleuil M., Guenther E. W., Fridlund M., Endl M., Eigmüller P., Csizmadia S., Havel M., Aigrain S., Auvergne M., Baglin A., Barge P., Bonomo A. S., Bordé P., Bouchy F., Bruntt H., Cabrera J., Carpano S., Carone L., Cochran W. D., Deeg H. J., Dvorak R., Eislöffel J., Erikson A., Ferraz-Mello S., Gazzano J.-C., Gibson N. B., Gillon M., Gondoin P., Guillot T., Hartmann M., Hatzes A., Jorda L., Kabath P., Léger A., Llebaria A., Lammer H., MacQueen P. J., Mayor M., Mazeh T., Moutou C., Ollivier M., Pätzold M., Pepe F., Queloz D., Rauer H., Rouan D., Samuel B., Schneider J., Stecklum B., Tingley B., Udry S., Wuchterl G., 2010, A&A, 524, A55

Gendron E., Coustenis A., Drossart P., Combes M., Hirtzig M., Lacombe F., Rouan D., Collin C., Pau S., Lagrange A.-M., Mouillet D., Rabou P., Fusco T., Zins G., 2004, A&A, 417, L21

Gendron E., Vidal F., Brangier M., Morris T., Hubert Z., Basden A., Rousset G., Myers R., Chemla F., Longmore A., Butterley T., Dipper N., Dunlop C., Geng D., Gratadour D., Henry D., Laporte P., Looker N., Perret D., Sevin A., Talbot G., Younger E., 2011, A&A, 529, L2

Gezari D. Y., Labeyrie A., Stachnik R. V., 1972, ApJL, 173, L1

Ghez A. M., Salim S., Weinberg N. N., Lu J. R., Do T., Dunn J. K., Matthews K., Morris M. R., Yelda S., Becklin E. E., Kremenek T., Milosavljevic M., Naiman J., 2008, ApJ, 689, 1044

Giacconi R., 1998, The Messenger, 93, 8

Gillessen S., Eisenhauer F., Trippe S., Alexander T., Genzel R., Martins F., Ott T., 2009, ApJ, 692, 1075

Gillon M., Anderson D. R., Collier-Cameron A., Doyle A. P., Fumel A., Hellier C., Jehin E., Lendl M., Maxted P. F. L., Montalbán J., Pepe F., Pollacco D., Queloz D., Ségransan D., Smith A. M. S., Smalley B., Southworth J., Triaud A. H. M. J., Udry S., West R. G., 2013, A&A, 552, A82

Gillon M., Triaud A. H. M. J., Demory B.-O., Jehin E., Agol E., Deck K. M., Lederer S. M., de Wit J., Burdanov A., Ingalls J. G., Bolmont E., Leconte J., Raymond S. N., Selsis F., Turbet M., Barkaoui K., Burgasser A., Burleigh M. R., Carey S. J., Chaushev A., Copperwheat C. M., Delrez L., Fernandes C. S., Holdsworth D. L., Kotze E. J., Van Grootel V., Almleaky Y., Benkhaldoun Z., Magain P., Queloz D., 2017, Nature, 542, 456

Ginski C., Mugrauer M., Seeliger M., Eisenbeiss T., 2012, MNRAS, 421, 2498

Ginski C., Mugrauer M., Seeliger M., Löhne T., 2013, A&A, 559, A71

Ginski C., Mugrauer M., Seeliger M., Buder S., Errmann R., Avenhaus H., Mouillet D., Maire A.-L., Raetz S., 2016, MNRAS, 457, 2173

Girard S., Wahhaj Z., Milli J., Vigan A., van den Ancker M., Boffin H., Mouillet D., Mawet D., Kasper M., Siebenmorgen R., The SPHERE Consortium, 2017, *SPHERE User Manual*

Girardi L., Groenewegen M. A. T., Hatziminaoglou E., da Costa L., 2005, A&A, 436, 895

Gonzalez R. C., Woods R. E., 2002, Digital image processing

Gould A., Dorsher S., Gaudi B. S., Udalski A., 2006, AcA, 56, 1

Gray D. F., 1976, The observation and analysis of stellar photospheres

Gray D. F., 1989, PASP, 101, 832

Green G. M., Schlafly E. F., Finkbeiner D. P., Rix H.-W., Martin N., Burgett W., Draper P. W., Flewelling H., Hodapp K., Kaiser N., Kudritzki R. P., Magnier E., Metcalfe N., Price P., Tonry J., Wainscoat R., 2015, ApJ, 810, 25

Grundahl F., Kjeldsen H., Christensen-Dalsgaard J., Arentoft T., Frandsen S., 2007, Communications in Asteroseismology, 150, 300

Grundahl F., Christensen-Dalsgaard J., Kjeldsen H., Jørgensen U. G., Arentoft T., Frandsen S., Kjærgaard P., 2009, in Dikpati M., Arentoft T., González Hernández I., Lindsey C., Hill F., eds, Solar-Stellar Dynamos as Revealed by Helio- and Asteroseismology: GONG 2008/SOHO 21, Astronomical Society of the Pacific Conference Series Vol. 416, p. 579

Gubler J., Tytler D., 1998, PASP, 110, 738

Guerra J. C., Brusa G., Christou J., Miller D., Ricardi A., Xompero M., Briguglio R., Wagner M., Lefebvre M., Sosa R., 2013, UV/Optical/IR Space Telescopes and Instruments: Innovative Technologies and Concepts VI, Proc. SPIE, , Vol. 8860, p. 886014

Guo X., Johnson J. A., Mann A. W., Kraus A. L., Curtis J. L., Latham D. W., 2017, ApJ, 838, 25

Guyon O., Pluzhnik E. A., Kuchner M. J., Collins B., Ridgway S. T., 2006, ApJS, 167, 81

Haisch, Jr. K. E., Lada E. A., Lada C. J., 2001, ApJL, 553, L153

Hamers A. S., Antonini F., Lithwick Y., Perets H. B., Portegies Zwart S. F., 2017, MNRAS, 464, 688

Harpsøe K. B. W., Jørgensen U. G., Andersen M. I., Grundahl F., 2012, A&A, 542, A23

Hartman J. D., Bakos G. Á., Béky B., Torres G., Latham D. W., Csubry Z., Penev K., Shporer A., Fulton B. J., Buchhave L. A., Johnson J. A., Howard A. W., Marcy G. W., Fischer D. A., Kovács G., Noyes R. W., Esquerdo G. A., Everett M., Szklenár T., Quinn S. N., Bieryla A., Knox R. P., Hinz P., Sasselov D. D., Fűrész G., Stefanik R. P., Lázár J., Papp I., Sári P., 2012, AJ, 144, 139

Hartman J. D., Bakos G. Á., Buchhave L. A., Torres G., Latham D. W., Kovács G., Bhatti W., Csubry Z., de Val-Borro M., Penev K., Huang C. X., Béky B., Bieryla A., Quinn S. N., Howard A. W., Marcy G. W., Johnson J. A., Isaacson H., Fischer D. A., Noyes R. W., Falco E., Esquerdo G. A., Knox R. P., Hinz P., Lázár J., Papp I., Sári P., 2015, AJ, 150, 197

Hartman J. D., Bakos G. Á., Bhatti W., Penev K., Bieryla A., Latham D. W., Kovács G., Torres G., Csubry Z., de Val-Borro M., Buchhave L., Kovács T., Quinn S., Howard A. W., Isaacson H., Fulton B. J., Everett M. E., Esquerdo G., Béky B., Szklenar T., Falco E., Santerne A., Boisse I., Hébrard G., Burrows A., Lázár J., Papp I., Sári P., 2016, AJ, 152, 182

Hay K. L., Collier-Cameron A., Doyle A. P., Hébrard G., Skillen I., Anderson D. R., Barros S. C. C., Brown D. J. A., Bouchy F., Busuttil R., Delorme P., Delrez L., Demangeon O., Díaz R. F., Gillon M., Gómez Maqueo Chew Y., Gonzàlez E., Hellier C., Holmes S., Jarvis J. F., Jehin E., Joshi Y. C., Kolb U., Lendl M., Maxted P. F. L., McCormac J., Miller G. R. M., Mortier A., Pallé E., Pollacco D., Prieto-Arranz J., Queloz D., Ségransan D., Simpson E. K., Smalley B., Southworth J., Triaud A. H. M. J., Turner O. D., Udry S., Vanhuysse M., West R. G., Wilson P. A., 2016, MNRAS, 463, 3276

Haywood R. D., Collier Cameron A., Queloz D., Barros S. C. C., Deleuil M., Fares R., Gillon M., Lanza A. F., Lovis C., Moutou C., Pepe F., Pollacco D., Santerne A., Ségransan D., Unruh Y. C., 2014, MNRAS, 443, 2517

Hecquet J., Coupinot G., 1985, Journal of Optics, 16, 21

Helled R., Bodenheimer P., Podolak M., Boley A., Meru F., Nayakshin S., Fortney J. J., Mayer L., Alibert Y., Boss A. P., 2014, Protostars and Planets VI, , 643

Hellier C., Anderson D. R., Cameron A. C., Delrez L., Gillon M., Jehin E., Lendl M., Maxted P. F. L., Pepe F., Pollacco D., Queloz D., Ségransan D., Smalley B., Smith A. M. S., Southworth J., Triaud A. H. M. J., Udry S., West R. G., 2014, MNRAS, 440, 1982

Hellier C., Anderson D. R., Cameron A. C., Delrez L., Gillon M., Jehin E., Lendl M., Maxted P. F. L., Neveu-VanMalle M., Pepe F., Pollacco D., Queloz D., Ségransan D., Smalley B., Southworth J., Triaud A. H. M. J., Udry S., Wagg T., West R. G., 2017, MNRAS, 465, 3693

Henden A. A., Templeton M., Terrell D., Smith T. C., Levine S., Welch D., 2016, VizieR Online Data Catalog, 2336

Henderson C. B., Poleski R., Penny M., Street R. A., Bennett D. P., Hogg D. W., Gaudi B. S., K2 Campaign 9 Microlensing Science Team, Zhu W., Barclay T., Barentsen G., Howell S. B., Mullally F., Udalski A., Szymański M. K., Skowron J., Mróz P., Kozłowski S., Wyrzykowski Ł., Pietrukowicz P., Soszyński I., Ulaczyk K., Pawlak M., OGLE Project T., Sumi T., Abe F., Asakura Y., Barry R. K., Bhattacharya A., Bond I. A., Donachie M., Freeman M., Fukui A., Hirao Y., Itow Y., Koshimoto N., Li M. C. A., Ling C. H., Masuda K., Matsubara Y., Muraki Y., Nagakane M., Ohnishi K., Oyokawa H., Rattenbury N., Saito T., Sharan A., Sullivan D. J., Tristram P. J., Yonehara A., MOA Collaboration, Bachelet E., Bramich D. M., Cassan A., Dominik M., Figuera Jaimes R., Horne K., Hundertmark M., Mao S., Ranc C., Schmidt R., Snodgrass C., Steele I. A., Tsapras Y., Wambsganss J., RoboNet Project T., Bozza V., Burgdorf M. J., Jørgensen U. G., Calchi Novati S., Ciceri S., D'Ago G., Evans D. F., Hessman F. V., Hinse T. C., Husser T.-O., Mancini L., Popovas A., Rabus M., Rahvar S., Scarpetta G., Skottfelt J., Southworth J., Unda-Sanzana E., The MiNDSTEp Team, Bryson S. T., Caldwell D. A.,

Haas M. R., Larson K., McCalmont K., Packard M., Peterson C., Putnam D., Reedy L., Ross S., Van Cleve J. E., K2C9 Engineering Team, Akeson R., Batista V., Beaulieu J.-P., Beichman C. A., Bryden G., Ciardi D., Cole A., Coutures C., Foreman-Mackey D., Fouqué P., Friedmann M., Gelino C., Kaspi S., Kerins E., Korhonen H., Lang D., Lee C.-H., Lineweaver C. H., Maoz D., Marquette J.-B., Mogavero F., Morales J. C., Nataf D., Pogge R. W., Santerne A., Shvartzvald Y., Suzuki D., Tamura M., Tisserand P., Wang D., 2016, PASP, 128(12), 124401

Henning T., Mancini L., Sarkis P., Bakos G. Á., Hartman J. D., Bayliss D., Bento J., Bhatti W., Brahm R., Ciceri S., Csubry Z., de Val-Borro M., Espinoza N., Fulton B. J., Howard A. W., Isaacson H. T., Jordán A., Marcy G. W., Penev K., Rabus M., Suc V., Tan T. G., Tinney C. G., Wright D. J., Zhou G., Durkan S., Lazar J., Papp I., Sari P., 2018, AJ, 155, 79

Henry G. W., Marcy G. W., Butler R. P., Vogt S. S., 2000, ApJL, 529, L41

Hippler S., Bergfors C., Brandner Wolfgang, Daemgen S., Henning T., Hormuth F., Huber A., Janson M., Rochau B., Rohloff R.-R., Wagner K., 2009, The Messenger, 137, 14

Hohenkerk C. Y., Sinclair A. T., 1985, HMNAO Technical Notes, 63

Holman M., Touma J., Tremaine S., 1997, Nature, 386, 254

Hormuth F., Hippler S., Brandner W., Wagner K., Henning T., 2008, Ground-based and Airborne Instrumentation for Astronomy II, Proc. SPIE, Vol. 7014, p. 701448

Howard A. W., Marcy G. W., Johnson J. A., Fischer D. A., Wright J. T., Isaacson H., Valenti J. A., Anderson J., Lin D. N. C., Ida S., 2010, Science, 330, 653

Howard A. W., Marcy G. W., Bryson S. T., Jenkins J. M., Rowe J. F., Batalha N. M., Borucki W. J., Koch D. G., Dunham E. W., Gautier, III T. N., Van Cleve J., Cochran W. D., Latham D. W., Lissauer J. J., Torres G., Brown T. M., Gilliland R. L., Buchhave L. A., Caldwell D. A., Christensen-Dalsgaard J., Ciardi

D., Fressin F., Haas M. R., Howell S. B., Kjeldsen H., Seager S., Rogers L., Sasselov D. D., Steffen J. H., Basri G. S., Charbonneau D., Christiansen J., Clarke B., Dupree A., Fabrycky D. C., Fischer D. A., Ford E. B., Fortney J. J., Tarter J., Girouard F. R., Holman M. J., Johnson J. A., Klaus T. C., Machalek P., Moorhead A. V., Morehead R. C., Ragozzine D., Tenenbaum P., Twicken J. D., Quinn S. N., Isaacson H., Shporer A., Lucas P. W., Walkowicz L. M., Welsh W. F., Boss A., Devore E., Gould A., Smith J. C., Morris R. L., Prsa A., Morton T. D., Still M., Thompson S. E., Mullally F., Endl M., MacQueen P. J., 2012, ApJS, 201, 15

Howell S. B., Sobeck C., Haas M., Still M., Barclay T., Mullally F., Troeltzsch J., Aigrain S., Bryson S. T., Caldwell D., Chaplin W. J., Cochran W. D., Huber D., Marcy G. W., Miglio A., Najita J. R., Smith M., Twicken J. D., Fortney J. J., 2014, PASP, 126, 398

Huang C., Wu Y., Triaud A. H. M. J., 2016, ApJ, 825, 98

Huber D., Carter J. A., Barbieri M., Miglio A., Deck K. M., Fabrycky D. C., Montet B. T., Buchhave L. A., Chaplin W. J., Hekker S., Montalbán J., Sanchis-Ojeda R., Basu S., Bedding T. R., Campante T. L., Christensen-Dalsgaard J., Elsworth Y. P., Stello D., Arentoft T., Ford E. B., Gilliland R. L., Handberg R., Howard A. W., Isaacson H., Johnson J. A., Karoff C., Kawaler S. D., Kjeldsen H., Latham D. W., Lund M. N., Lundkvist M., Marcy G. W., Metcalfe T. S., Silva Aguirre V., Winn J. N., 2013, Science, 342, 331

Husser T.-O., Wende-von Berg S., Dreizler S., Homeier D., Reiners A., Barman T., Hauschildt P. H., 2013, A&A, 553, A6

Janson M., Hormuth F., Bergfors C., Brandner W., Hippler S., Daemgen S., Kudryavtseva N., Schmalzl E., Schnupp C., Henning T., 2012, ApJ, 754, 44

Johnson J. A., Aller K. M., Howard A. W., Crepp J. R., 2010, PASP, 122, 905

Jovanovic N., Martinache F., Guyon O., Clergeon C., Singh G., Kudo T., Garrel V., Newman K., Doughty D., Lozi J., Males J., Minowa Y., Hayano Y., Takato N.,

Morino J., Kuhn J., Serabyn E., Norris B., Tuthill P., Schworer G., Stewart P., Close L., Huby E., Perrin G., Lacour S., Gauchet L., Vievard S., Murakami N., Oshiyama F., Baba N., Matsuo T., Nishikawa J., Tamura M., Lai O., Marchis F., Duchene G., Kotani T., Woillez J., 2015, PASP, 127, 890

Kains N., Bramich D. M., Arellano Ferro A., Figuera Jaimes R., Jørgensen U. G., Giridhar S., Penny M. T., Alsubai K. A., Andersen J. M., Bozza V., Browne P., Burgdorf M., Calchi Novati S., Damerdji Y., Diehl C., Dodds P., Dominik M., Elyiv A., Fang X.-S., Giannini E., Gu S.-H., Hardis S., Harpsøe K., Hinse T. C., Hornstrup A., Hundertmark M., Jessen-Hansen J., Juncher D., Kerins E., Kjeldsen H., Korhonen H., Liebig C., Lund M. N., Lundkvist M., Mancini L., Martin R., Mathiasen M., Rabus M., Rahvar S., Ricci D., Sahu K., Scarpetta G., Skottfelt J., Snodgrass C., Southworth J., Surdej J., Tregloan-Reed J., Vilela C., Wertz O., Williams A., 2013, A&A, 555, A36

Kallivayalil N., van der Marel R. P., Alcock C., Axelrod T., Cook K. H., Drake A. J., Geha M., 2006, ApJ, 638, 772

Kasdin N. J., Vanderbei R. J., Spergel D. N., Littman M. G., 2003, ApJ, 582, 1147

Kervella P., Thévenin F., Di Folco E., Ségransan D., 2004, A&A, 426, 297

Kervella P., Thévenin F., Lovis C., 2017, A&A, 598, L7

Knutson H. A., Fulton B. J., Montet B. T., Kao M., Ngo H., Howard A. W., Crepp J. R., Hinkley S., Bakos G. Á., Batygin K., Johnson J. A., Morton T. D., Muirhead P. S., 2014, ApJ, 785, 126

Koekemoer A. M., McLean B., McMaster M., Jenkner H., 2006, in Koekemoer A. M., Goudfrooij P., Dressel L. L., eds, The 2005 HST Calibration Workshop: Hubble After the Transition to Two-Gyro Mode, p. 417

Koekemoer A. M., Faber S. M., Ferguson H. C., Grogin N. A., Kocevski D. D., Koo D. C., Lai K., Lotz J. M., Lucas R. A., McGrath E. J., Ogaz S., Rajan A.,

Riess A. G., Rodney S. A., Strolger L., Casertano S., Castellano M., Dahlen T., Dickinson M., Dolch T., Fontana A., Giavalisco M., Grazian A., Guo Y., Hathi N. P., Huang K.-H., van der Wel A., Yan H.-J., Acquaviva V., Alexander D. M., Almaini O., Ashby M. L. N., Barden M., Bell E. F., Bournaud F., Brown T. M., Caputi K. I., Cassata P., Challis P. J., Chary R.-R., Cheung E., Cirasuolo M., Conselice C. J., Roshan Cooray A., Croton D. J., Daddi E., Davé R., de Mello D. F., de Ravel L., Dekel A., Donley J. L., Dunlop J. S., Dutton A. A., Elbaz D., Fazio G. G., Filippenko A. V., Finkelstein S. L., Frazer C., Gardner J. P., Garnavich P. M., Gawiser E., Gruetzbauch R., Hartley W. G., Häussler B., Herrington J., Hopkins P. F., Huang J.-S., Jha S. W., Johnson A., Kartaltepe J. S., Khostovan A. A., Kirshner R. P., Lani C., Lee K.-S., Li W., Madau P., McCarthy P. J., McIntosh D. H., McLure R. J., McPartland C., Mobasher B., Moreira H., Mortlock A., Moustakas L. A., Mozena M., Nandra K., Newman J. A., Nielsen J. L., Niemi S., Noeske K. G., Papovich C. J., Pentericci L., Pope A., Primack J. R., Ravindranath S., Reddy N. A., Renzini A., Rix H.-W., Robaina A. R., Rosario D. J., Rosati P., Salimbeni S., Scarlata C., Siana B., Simard L., Smidt J., Snyder D., Somerville R. S., Spinrad H., Straughn A. N., Telford O., Teplitz H. I., Trump J. R., Vargas C., Villforth C., Wagner C. R., Wandro P., Wechsler R. H., Weiner B. J., Wiklind T., Wild V., Wilson G., Wuyts S., Yun M. S., 2011, ApJS, 197, 36

Konacki M., Torres G., Jha S., Sasselov D. D., 2003, Nature, 421, 507

Koppenhoefer J., Saglia R. P., Fossati L., Lyubchik Y., Mugrauer M., Bender R., Lee C.-H., Riffeser A., Afonso P., Greiner J., Henning T., Neuhäuser R., Snellen I. A. G., Pavlenko Y., Verdugo M., Vogt N., 2013, MNRAS, 435, 3133

Kozai Y., 1962, AJ, 67, 591

Kraus A. L., Ireland M. J., 2012, ApJ, 745, 5

Kraus A. L., Ireland M. J., Huber D., Mann A. W., Dupuy T. J., 2016, AJ, 152, 8

Kuchner M. J., Lecar M., 2002, ApJL, 574, L87

Labeyrie A., 1970, A&A, 6, 85

Lafrenière D., Marois C., Doyon R., Nadeau D., Artigau É., 2007, ApJ, 660, 770

Langlois M., Dohlen K., Vigan A., Zurlo A., Moutou C., Schmid H. M., Mili J., Beuzit J.-L., Boccaletti A., Carle M., Costille A., Dorn R., Gluck L., Hubin N., Feldt M., Kasper M., Lizon L., Madec F., Le Mignant D., Mouillet D., Puget J.-P., Sauvage J.-F., Wildi F., 2014, Ground-based and Airborne Instrumentation for Astronomy V, Proc. SPIE, Vol. 9147, p. 91471R

Laplace P. S., 1796, The System of the World, Impremiere Cercle-Social, Paris, using the English translation of J. Pond, F.R.S., 1809

Lasker B. M., Sturch C. R., McLean B. J., Russell J. L., Jenkner H., Shara M. M., 1990, AJ, 99, 2019

Lasker B. M., Lattanzi M. G., McLean B. J., Bucciarelli B., Drimmel R., Garcia J., Greene G., Guglielmetti F., Hanley C., Hawkins G., Laidler V. G., Loomis C., Meakes M., Mignani R., Morbidelli R., Morrison J., Pannunzio R., Rosenberg A., Sarasso M., Smart R. L., Spagna A., Sturch C. R., Volpicelli A., White R. L., Wolfe D., Zacchei A., 2008, AJ, 136, 735

Law N. M., 2006, PhD thesis, Cambridge University

Law N. M., Mackay C. D., Dekany R. G., Ireland M., Lloyd J. P., Moore A. M., Robertson J. G., Tuthill P., Woodruff H. C., 2009, ApJ, 692, 924

Law N. M., Morton T., Baranec C., Riddle R., Ravichandran G., Ziegler C., Johnson J. A., Tendulkar S. P., Bui K., Burse M. P., Das H. K., Dekany R. G., Kulkarni S., Punnadi S., Ramaprakash A. N., 2014, ApJ, 791, 35

Law N. M., Mackay C. D., Baldwin J. E., 2006, A&A, 446, 739

Lee E. J., Chiang E., 2016, ApJ, 817, 90

Lee E. J., Chiang E., 2017, ApJ, 842, 40

Lee E. J., Chiang E., Ormel C. W., 2014, ApJ, 797, 95

Léger A., Rouan D., Schneider J., Barge P., Fridlund M., Samuel B., Ollivier M., Guenther E., Deleuil M., Deeg H. J., Auvergne M., Alonso R., Aigrain S., Alapini A., Almenara J. M., Baglin A., Barbieri M., Bruntt H., Bordé P., Bouchy F., Cabrera J., Catala C., Carone L., Carpano S., Csizmadia S., Dvorak R., Erikson A., Ferraz-Mello S., Foing B., Fressin F., Gandolfi D., Gillon M., Gondoin P., Grasset O., Guillot T., Hatzes A., Hébrard G., Jorda L., Lammer H., Llebaria A., Loeillet B., Mayor M., Mazeh T., Moutou C., Pätzold M., Pont F., Queloz D., Rauer H., Renner S., Samadi R., Shporer A., Sotin C., Tingley B., Wuchterl G., Adda M., Agogu P., Appourchaux T., Ballans H., Baron P., Beaufort T., Bellenger R., Berlin R., Bernardi P., Blouin D., Baudin F., Bodin P., Boisnard L., Boit L., Bonneau F., Borzeix S., Briet R., Buey J.-T., Butler B., Cailleau D., Cautain R., Chabaud P.-Y., Chaintreuil S., Chiavassa F., Costes V., Cuna Parrho V., de Oliveira Fialho F., Decaudin M., Defise J.-M., Djalal S., Epstein G., Exil G.-E., Fauré C., Fenouillet T., Gaboriaud A., Gallic A., Gamet P., Gavalda P., Grolleau E., Gruneisen R., Gueguen L., Guis V., Guivarc'h V., Guterman P., Hallouard D., Hasiba J., Heuripeau F., Huntzinger G., Hustaix H., Imad C., Imbert C., Johlander B., Jouret M., Journoud P., Karioty F., Kerjean L., Lafaille V., Lafond L., Lam-Trong T., Landiech P., Lapeyrere V., Larqué T., Laudet P., Lautier N., Lecann H., Lefevre L., Leruyet B., Levacher P., Magnan A., Mazy E., Mertens F., Mesnager J.-M., Meunier J.-C., Michel J.-P., Monjoin W., Naudet D., Nguyen-Kim K., Orcesi J.-L., Ottacher H., Perez R., Peter G., Plasson P., Plesseria J.-Y., Pontet B., Pradines A., Quentin C., Reynaud J.-L., Rolland G., Rollenhagen F., Romagnan R., Russ N., Schmidt R., Schwartz N., Sebbag I., Sedes G., Smit H., Steller M. B., Sunter W., Surace C., Tello M., Tiphène D., Toulouse P., Ulmer B., Vandermarcq O., Vergnault E., Vuillemin A., Zanatta P., 2009, A&A, 506, 287

Lelievre G., Nieto J.-L., Thouvenot E., Salmon D., Llebaria A., 1988, A&A, 200, 301

Lendl M., Delrez L., Gillon M., Madhusudhan N., Jehin E., Queloz D., Anderson D. R., Demory B.-O., Hellier C., 2016, A&A, 587, A67

Libralato M., Bellini A., Bedin L. R., Piotto G., Platais I., Kissler-Patig M., Milone A. P., 2014, A&A, 563, A80

Lidov M. L., 1962, Planet. Space Sci., 9, 719

Lin D. N. C., Bodenheimer P., Richardson D. C., 1996, Nature, 380, 606

Lissauer J. J., Hubickyj O., D'Angelo G., Bodenheimer P., 2009, Icarus, 199, 338

Lissauer J. J., Ragozzine D., Fabrycky D. C., Steffen J. H., Ford E. B., Jenkins J. M., Shporer A., Holman M. J., Rowe J. F., Quintana E. V., Batalha N. M., Borucki W. J., Bryson S. T., Caldwell D. A., Carter J. A., Ciardi D., Dunham E. W., Fortney J. J., Gautier, III T. N., Howell S. B., Koch D. G., Latham D. W., Marcy G. W., Morehead R. C., Sasselov D., 2011, ApJS, 197, 8

Lissauer J. J., Marcy G. W., Rowe J. F., Bryson S. T., Adams E., Buchhave L. A., Ciardi D. R., Cochran W. D., Fabrycky D. C., Ford E. B., Fressin F., Geary J., Gilliland R. L., Holman M. J., Howell S. B., Jenkins J. M., Kinemuchi K., Koch D. G., Morehead R. C., Ragozzine D., Seader S. E., Tanenbaum P. G., Torres G., Twicken J. D., 2012, ApJ, 750, 112

Lissauer J. J., Marcy G. W., Bryson S. T., Rowe J. F., Jontof-Hutter D., Agol E., Borucki W. J., Carter J. A., Ford E. B., Gilliland R. L., Kolbl R., Star K. M., Steffen J. H., Torres G., 2014, ApJ, 784, 44

Lloyd-Hart M., Brusa G., Wildi F. P., Miller D. L., Fisher D. L., Riccardi A., 2003, in Tyson R. K., Lloyd-Hart M., eds, Astronomical Adaptive Optics Systems and Applications, Proc. SPIE, , Vol. 5169, p. 79

Luger R., Agol E., Kruse E., Barnes R., Becker A., Foreman-Mackey D., Deming D., 2016, AJ, 152, 100

Luri X., Brown A. G. A., Sarro L. M., Arenou F., Bailer-Jones C. A. L., Castro-Ginard A., de Bruijne J., Prusti T., Babusiaux C., Delgado H. E., 2018, ArXiv e-prints

Lutz T. E., Kelker D. H., 1973, PASP, 85, 573

Lyot B., 1939, MNRAS, 99, 580

Maaswinkel F., D'Odorico S., Huster G., Bortoletto F., 1987, The Messenger, 48, 51

Macintosh B. A., Graham J. R., Palmer D. W., Doyon R., Dunn J., Gavel D. T., Larkin J., Oppenheimer B., Saddlemyer L., Sivaramakrishnan A., Wallace J. K., Bauman B., Erickson D. A., Marois C., Poyneer L. A., Soummer R., 2008, Adaptive Optics Systems, Proc. SPIE, Vol. 7015, p. 701518

Macintosh B., Graham J. R., Ingraham P., Konopacky Q., Marois C., Perrin M., Poyneer L., Bauman B., Barman T., Burrows A. S., Cardwell A., Chilcote J., De Rosa R. J., Dillon D., Doyon R., Dunn J., Erikson D., Fitzgerald M. P., Gavel D., Goodsell S., Hartung M., Hibon P., Kalas P., Larkin J., Maire J., Marchis F., Marley M. S., McBride J., Millar-Blanchaer M., Morzinski K., Norton A., Oppenheimer B. R., Palmer D., Patience J., Pueyo L., Rantakyro F., Sadakuni N., Saddlemyer L., Savransky D., Serio A., Soummer R., Sivaramakrishnan A., Song I., Thomas S., Wallace J. K., Wiktorowicz S., Wolff S., 2014, Proceedings of the National Academy of Science, 111, 12661

Mackay C. D., Tubbs R. N., Bell R., Burt D. J., Jerram P., Moody I., 2001, in Blouke M. M., Canosa J., Sampat N., eds, Sensors and Camera Systems for Scientific, Industrial, and Digital Photography Applications II, Proc. SPIE, Vol. 4306, p. 289

Mackay C., Rebolo-López R., Femenia Castellá B., Crass J., King D. L., Labadie L., Aisher P., Pérez Garrido A., Balcells M., Díaz-Sánchez A., Jimenez Fuensalida J.,

Lopez R. L., Oscoz A., Pérez Prieto J. A., Rodríguez-Ramos L. F., Villó I., 2012, Ground-based and Airborne Instrumentation for Astronomy IV, Proc. SPIE, Vol. 8446, p. 844621

Madau P., Ferguson H. C., Dickinson M. E., Giavalisco M., Steidel C. C., Fruchter A., 1996, MNRAS, 283, 1388

Maire A.-L., Langlois M., Dohlen K., Lagrange A.-M., Gratton R., Chauvin G., Desidera S., Girard J. H., Milli J., Vigan A., Zins G., Delorme P., Beuzit J.-L., Claudi R. U., Feldt M., Mouillet D., Puget P., Turatto M., Wildi F., 2016, Ground-based and Airborne Instrumentation for Astronomy VI, Proc. SPIE, Vol. 9908, p. 990834

Maíz Apellániz J., 2010, A&A, 518, A1

Mancini L., Giordano M., Mollière P., Southworth J., Brahm R., Ciceri S., Henning T., 2016, MNRAS, 461, 1053

Mancini L., Southworth J., Raia G., Tregloan-Reed J., Mollière P., Bozza V., Bretton M., Bruni I., Ciceri S., D'Ago G., Dominik M., Hinse T. C., Hundertmark M., Jørgensen U. G., Korhonen H., Rabus M., Rahvar S., Starkey D., Calchi Novati S., Figuera Jaimes R., Henning T., Juncher D., Haugbølle T., Kains N., Popovas A., Schmidt R. W., Skottfelt J., Snodgrass C., Surdej J., Wertz O., 2017, MNRAS, 465, 843

Marchetti E., Brast R., Delabre B., Donaldson R., Fedrigo E., Frank C., Hubin N., Kolb J., Lizon J.-L., Marchesi M., Oberti S., Reiss R., Santos J., Soenke C., Tordo S., Baruffolo A., Bagnara P., CAMCAO Consortium, 2007, The Messenger, 129, 8

Marois C., Lafrenière D., Doyon R., Macintosh B., Nadeau D., 2006, ApJ, 641, 556

Marois C., Macintosh B., Barman T., Zuckerman B., Song I., Patience J., Lafrenière D., Doyon R., 2008, Science, 322, 1348

Martinache F., Guyon O., 2009, Techniques and Instrumentation for Detection of Exoplanets IV, Proc. SPIE, , Vol. 7440, p. 74400O

Mason B. D., Wycoff G. L., Hartkopf W. I., Douglass G. G., Worley C. E., 2001, AJ, 122, 3466

Mathis J. S., Cardelli J. A., 1992, ApJ, 398, 610

Maxted P. F. L., Anderson D. R., Collier Cameron A., Doyle A. P., Fumel A., Gillon M., Hellier C., Jehin E., Lendl M., Pepe F., Pollacco D. L., Queloz D., Ségransan D., Smalley B., Southworth K., Smith A. M. S., Triaud A. H. M. J., Udry S., West R. G., 2013, PASP, 125, 48

Mayo A. W., Vanderburg A., Latham D. W., Bieryla A., Morton T. D., Buchhave L. A., Dressing C. D., Beichman C., Berlind P., Calkins M. L., Ciardi D. R., Crossfield I. J. M., Esquerdo G. A., Everett M. E., Gonzales E. J., Hirsch L. A., Horch E. P., Howard A. W., Howell S. B., Livingston J., Patel R., Petigura E. A., Schlieder J. E., Scott N. J., Schumer C. F., Sinukoff E., Teske J., Winters J. G., 2018, AJ, 155, 136

Mayor M., Queloz D., 1995, Nature, 378, 355

McAlister H. A., 1977, ApJ, 215, 159

McClure R. D., Grundmann W. A., Rambold W. N., Fletcher J. M., Richardson E. H., Stillburn J. R., Racine R., Christian C. A., Waddell P., 1989, PASP, 101, 1156

McCormac J., Pollacco D., Skillen I., Faedi F., Todd I., Watson C. A., 2013, PASP, 125, 548

McLaughlin D. E., Anderson J., Meylan G., Gebhardt K., Pryor C., Minniti D., Phinney S., 2006, ApJS, 166, 249

McNamara B., Sekiguchi K., 1986, AJ, 91, 557

Meléndez J., Asplund M., Gustafsson B., Yong D., 2009, ApJL, 704, L66

Michelson A. A., Pease F. G., 1921, ApJ, 53, 249

Michelson A. A., 1890, The Philosophical Magazine and Journal of Science, 5th Series, 30, 1

Michelson A. A., 1891, Nature, 45, 160

Moehler S., Lundin L. K., 2017a, *SPHERE IRDIS Imaging Reflex Tutorial*

Moehler S., Lundin L. K., 2017b, *SPHERE IFS Imaging Reflex Tutorial*

Möller-Nilsson O., Pavlov A., Thalmann C., Carson J., Feldt M., 2016, *SPHERE Data Reduction Pipeline Manual*

Monnier J. D., Zhao M., Pedretti E., Thureau N., Ireland M., Muirhead P., Berger J.-P., Millan-Gabet R., Van Belle G., ten Brummelaar T., McAlister H., Ridgway S., Turner N., Sturmann L., Sturmann J., Berger D., 2007, Science, 317, 342

Montet B. T., Morton T. D., Foreman-Mackey D., Johnson J. A., Hogg D. W., Bowler B. P., Latham D. W., Bieryla A., Mann A. W., 2015, ApJ, 809, 25

Montmerle T., Augereau J.-C., Chaussidon M., Gounelle M., Marty B., Morbidelli A., 2006, Earth Moon and Planets, 98, 39

Mortier A., Santos N. C., Sousa S. G., Fernandes J. M., Adibekyan V. Z., Delgado Mena E., Montalto M., Israelian G., 2013, A&A, 558, A106

Moutou C., Almenara J. M., Díaz R. F., Alonso R., Deleuil M., Guenther E., Pasternacki T., Aigrain S., Baglin A., Barge P., Bonomo A. S., Bordé P., Bouchy F., Cabrera J., Carpano S., Cochran W. D., Csizmadia S., Deeg H. J., Dvorak R., Endl M., Erikson A., Ferraz-Mello S., Fridlund M., Gandolfi D., Guillot T., Hatzes A., Hébrard G., Lovis C., Lammer H., MacQueen P. J., Mazeh T., Ofir A., Ollivier M., Pätzold M., Rauer H., Rouan D., Santerne A., Schneider J., Tingley B., Wuchterl G., 2014, MNRAS, 444, 2783

Močnik T., Clark B. J. M., Anderson D. R., Hellier C., Brown D. J. A., 2016, AJ, 151, 150

Moya A., Bouy H., Marchis F., Vicente B., Barrado D., 2011, A&A, 535, A110

Muñoz D. J., Lai D., Liu B., 2016, MNRAS, 460, 1086

Mugrauer M., Ginski C., 2015, MNRAS, 450, 3127

Mugrauer M., Neuhäuser R., 2005, MNRAS, 361, L15

Mugrauer M., Ginski C., Seeliger M., 2014, MNRAS, 439, 1063

Mulders G. D., Pascucci I., Apai D., 2015, ApJ, 798, 112

Munari U., Zwitter T., 1997, A&A, 318, 269

Naef D., Latham D. W., Mayor M., Mazeh T., Beuzit J. L., Drukier G. A., Perrier-Bellet C., Queloz D., Sivan J. P., Torres G., Udry S., Zucker S., 2001, A&A, 375, L27

Naoz S., 2016, ARA&A, 54, 441

Naoz S., Farr W. M., Lithwick Y., Rasio F. A., Teyssandier J., 2011, Nature, 473, 187

Naoz S., Farr W. M., Rasio F. A., 2012, ApJL, 754, L36

Narita N., Kudo T., Bergfors C., Nagasawa M., Thalmann C., Sato B., Suzuki R., Kandori R., Janson M., Goto M., Brandner W., Ida S., Abe L., Carson J., Egner S. E., Feldt M., Golota T., Guyon O., Hashimoto J., Hayano Y., Hayashi M., Hayashi S. S., Henning T., Hodapp K. W., Ishii M., Knapp G. R., Kusakabe N., Kuzuhara M., Matsuo T., McElwain M. W., Miyama S. M., Morino J.-I., Moro-Martin A., Nishimura T., Pyo T.-S., Serabyn E., Suenaga T., Suto H., Takahashi Y. H., Takami M., Takato N., Terada H., Tomono D., Turner E. L., Watanabe M., Yamada T., Takami H., Usuda T., Tamura M., 2010, PASJ, 62, 779

Nayakshin S., 2010, MNRAS, 408, L36

Neichel B., Rigaut F., Vidal F., van Dam M. A., Garrel V., Carrasco E. R., Pessev P., Winge C., Boccas M., d'Orgeville C., Arriagada G., Serio A., Fesquet V., Rambold W. N., Lührs J., Moreno C., Gausachs G., Galvez R. L., Montes V., Vucina T. B., Marin E., Urrutia C., Lopez A., Diggs S. J., Marchant C., Ebbers A. W., Trujillo C., Bec M., Trancho G., McGregor P., Young P. J., Colazo F., Edwards M. L., 2014, MNRAS, 440, 1002

Nelan E. P., Younger J., Makidon R. B., Lupie O. L., Holfeltz S. T., Taff L. G., Lattanzi M. G., Fresnau A., 2016, Fine Guidance Sensor Instrument Handbook Version 23.0

Nelson B. E., Ford E. B., Rasio F. A., 2017, AJ, 154, 106

Neveu-VanMalle M., Queloz D., Anderson D. R., Charbonnel C., Collier Cameron A., Delrez L., Gillon M., Hellier C., Jehin E., Lendl M., Maxted P. F. L., Pepe F., Pollacco D., Ségransan D., Smalley B., Smith A. M. S., Southworth J., Triaud A. H. M. J., Udry S., West R. G., 2014, A&A, 572, A49

Ngo H., Knutson H. A., Hinkley S., Crepp J. R., Bechter E. B., Batygin K., Howard A. W., Johnson J. A., Morton T. D., Muirhead P. S., 2015, ApJ, 800, 138

Ngo H., Knutson H. A., Hinkley S., Bryan M., Crepp J. R., Batygin K., Crossfield I., Hansen B., Howard A. W., Johnson J. A., Mawet D., Morton T. D., Muirhead P. S., Wang J., 2016, ApJ, 827, 8

Nieto J.-L., Thouvenot E., 1991, A&A, 241, 663

Nieto J.-L., Llebaria A., di Serego Alighieri S., 1987, A&A, 178, 301

Noethe L., 2002, in Wolf E., ed., Progress in Optics, Elsevier, Vol. 43, p. 1

Oke J. B., 1990, AJ, 99, 1621

Osborn J., Föhring D., Dhillon V. S., Wilson R. W., 2015, MNRAS, 452, 1707

Oscoz A., Rebolo R., López R., Pérez-Garrido A., Pérez J. A., Hildebrandt S., Rodríguez L. F., Piqueras J. J., Villó I., González J. M., Barrena R., Gómez G., García-Hernández D. A., Montañés P., Rosenberg A., Cadavid E., Calcines A., Díaz-Sánchez A., Kohley R., Martín Y., Peñate J., Sánchez V., 2008, Ground-based and Airborne Instrumentation for Astronomy II, Proc. SPIE, Vol. 7014, p. 701447

Pepper J., Pogge R. W., DePoy D. L., Marshall J. L., Stanek K. Z., Stutz A. M., Poindexter S., Siverd R., O'Brien T. P., Trueblood M., Trueblood P., 2007, PASP, 119, 923

Perlmutter S., Aldering G., Goldhaber G., Knop R. A., Nugent P., Castro P. G., Deustua S., Fabbro S., Goobar A., Groom D. E., Hook I. M., Kim A. G., Kim M. Y., Lee J. C., Nunes N. J., Pain R., Pennypacker C. R., Quimby R., Lidman C., Ellis R. S., Irwin M., McMahon R. G., Ruiz-Lapuente P., Walton N., Schaefer B., Boyle B. J., Filippenko A. V., Matheson T., Fruchter A. S., Panagia N., Newberg H. J. M., Couch W. J., Project T. S. C., 1999, ApJ, 517, 565

Petigura E. A., Schlieder J. E., Crossfield I. J. M., Howard A. W., Deck K. M., Ciardi D. R., Sinukoff E., Allers K. N., Best W. M. J., Liu M. C., Beichman C. A., Isaacson H., Hansen B. M. S., Lépine S., 2015, ApJ, 811, 102

Petigura E. A., Howard A. W., Lopez E. D., Deck K. M., Fulton B. J., Crossfield I. J. M., Ciardi D. R., Chiang E., Lee E. J., Isaacson H., Beichman C. A., Hansen B. M. S., Schlieder J. E., Sinukoff E., 2016, ApJ, 818, 36

Petigura E. A., Marcy G. W., Winn J. N., Weiss L. M., Fulton B. J., Howard A. W., Sinukoff E., Isaacson H., Morton T. D., Johnson J. A., 2017, ArXiv e-prints

Petrovich C., Tremaine S., 2016, ApJ, 829, 132

Petrovich C., 2015a, ApJ, 799, 27

Petrovich C., 2015b, ApJ, 805, 75

Piskorz D., Knutson H. A., Ngo H., Muirhead P. S., Batygin K., Crepp J. R., Hinkley S., Morton T. D., 2015, ApJ, 814, 148

Pollacco D. L., Skillen I., Collier Cameron A., Christian D. J., Hellier C., Irwin J., Lister T. A., Street R. A., West R. G., Anderson D. R., Clarkson W. I., Deeg H., Enoch B., Evans A., Fitzsimmons A., Haswell C. A., Hodgkin S., Horne K., Kane S. R., Keenan F. P., Maxted P. F. L., Norton A. J., Osborne J., Parley N. R., Ryans R. S. I., Smalley B., Wheatley P. J., Wilson D. M., 2006, PASP, 118, 1407

Pollacco D., Skillen I., Collier Cameron A., Loeillet B., Stempels H. C., Bouchy F., Gibson N. P., Hebb L., Hébrard G., Joshi Y. C., McDonald I., Smalley B., Smith A. M. S., Street R. A., Udry S., West R. G., Wilson D. M., Wheatley P. J., Aigrain S., Alsubai K., Benn C. R., Bruce V. A., Christian D. J., Clarkson W. I., Enoch B., Evans A., Fitzsimmons A., Haswell C. A., Hellier C., Hickey S., Hodgkin S. T., Horne K., Hrudková M., Irwin J., Kane S. R., Keenan F. P., Lister T. A., Maxted P., Mayor M., Moutou C., Norton A. J., Osborne J. P., Parley N., Pont F., Queloz D., Ryans R., Simpson E., 2008, MNRAS, 385, 1576

Pollack J. B., Hubickyj O., Bodenheimer P., Lissauer J. J., Podolak M., Greenzweig Y., 1996, Icarus, 124, 62

Pont F., Aigrain S., Zucker S., 2011, MNRAS, 411, 1953

Pont F., Husnoo N., Mazeh T., Fabrycky D., 2011, MNRAS, 414, 1278

Postman M., Coe D., Benítez N., Bradley L., Broadhurst T., Donahue M., Ford H., Graur O., Graves G., Jouvel S., Koekemoer A., Lemze D., Medezinski E., Molino A., Moustakas L., Ogaz S., Riess A., Rodney S., Rosati P., Umetsu K., Zheng W., Zitrin A., Bartelmann M., Bouwens R., Czakon N., Golwala S., Host O., Infante L., Jha S., Jimenez-Teja Y., Kelson D., Lahav O., Lazkoz R., Maoz D., McCully C., Melchior P., Meneghetti M., Merten J., Moustakas J., Nonino M., Patel B., Regös E., Sayers J., Seitz S., Van der Wel A., 2012, ApJS, 199, 25

Pourbaix D., Boffin H. M. J., 2016, A&A, 586, A90

Queloz D., Eggenberger A., Mayor M., Perrier C., Beuzit J. L., Naef D., Sivan J. P., Udry S., 2000, A&A, 359, L13

Queloz D., Mayor M., Udry S., Burnet M., Carrier F., Eggenberger A., Naef D., Santos N., Pepe F., Rupprecht G., Avila G., Baeza F., Benz W., Bertaux J.-L., Bouchy F., Cavadore C., Delabre B., Eckert W., Fischer J., Fleury M., Gilliotte A., Goyak D., Guzman J. C., Kohler D., Lacroix D., Lizon J.-L., Megevand D., Sivan J.-P., Sosnowska D., Weilenmann U., 2001, The Messenger, 105, 1

Queloz D., Bouchy F., Moutou C., Hatzes A., Hébrard G., Alonso R., Auvergne M., Baglin A., Barbieri M., Barge P., Benz W., Bordé P., Deeg H. J., Deleuil M., Dvorak R., Erikson A., Ferraz Mello S., Fridlund M., Gandolfi D., Gillon M., Guenther E., Guillot T., Jorda L., Hartmann M., Lammer H., Léger A., Llebaria A., Lovis C., Magain P., Mayor M., Mazeh T., Ollivier M., Pätzold M., Pepe F., Rauer H., Rouan D., Schneider J., Segransan D., Udry S., Wuchterl G., 2009, A&A, 506, 303

Queloz D., Anderson D. R., Collier Cameron A., Gillon M., Hebb L., Hellier C., Maxted P., Pepe F., Pollacco D., Ségransan D., Smalley B., Triaud A. H. M. J., Udry S., West R., 2010, A&A, 517, L1

Quinn S. N., White R. J., Latham D. W., Buchhave L. A., Cantrell J. R., Dahm S. E., Fűrész G., Szentgyorgyi A. H., Geary J. C., Torres G., Bieryla A., Berlind P., Calkins M. C., Esquerdo G. A., Stefanik R. P., 2012, ApJL, 756, L33

Quinn S. N., White R. J., Latham D. W., Buchhave L. A., Torres G., Stefanik R. P., Berlind P., Bieryla A., Calkins M. C., Esquerdo G. A., Fűrész G., Geary J. C., Szentgyorgyi A. H., 2014, ApJ, 787, 27

Quirrenbach A., 2009, Experimental Astronomy, 26, 49

Racine R., McClure R. D., 1989, PASP, 101, 731

Rafikov R. R., 2005, ApJL, 621, L69

Rafikov R. R., 2006, ApJ, 648, 666

Raghavan D., McAlister H. A., Henry T. J., Latham D. W., Marcy G. W., Mason B. D., Gies D. R., White R. J., ten Brummelaar T. A., 2010, ApJS, 190, 1

Ramírez I., Khanal S., Aleo P., Sobotka A., Liu F., Casagrande L., Meléndez J., Yong D., Lambert D. L., Asplund M., 2015, ApJ, 808, 13

Rasio F. A., Ford E. B., 1996, Science, 274, 954

Rauer H., Catala C., Aerts C., Appourchaux T., Benz W., Brandeker A., Christensen-Dalsgaard J., Deleuil M., Gizon L., Goupil M.-J., Güdel M., Janot-Pacheco E., Mas-Hesse M., Pagano I., Piotto G., Pollacco D., Santos Ċ., Smith A., Suárez J.-C., Szabó R., Udry S., Adibekyan V., Alibert Y., Almenara J.-M., Amaro-Seoane P., Eiff M. A.-v., Asplund M., Antonello E., Barnes S., Baudin F., Belkacem K., Bergemann M., Bihain G., Birch A. C., Bonfils X., Boisse I., Bonomo A. S., Borsa F., Brandão I. M., Brocato E., Brun S., Burleigh M., Burston R., Cabrera J., Cassisi S., Chaplin W., Charpinet S., Chiappini C., Church R. P., Csizmadia S., Cunha M., Damasso M., Davies M. B., Deeg H. J., Díaz R. F., Dreizler S., Dreyer C., Eggenberger P., Ehrenreich D., Eigmüller P., Erikson A., Farmer R., Feltzing S., de Oliveira Fialho F., Figueira P., Forveille T., Fridlund M., García R. A., Giommi P., Giuffrida G., Godolt M., Gomes da Silva J., Granzer T., Grenfell J. L., Grotsch-Noels A., Günther E., Haswell C. A., Hatzes A. P., Hébrard G., Hekker S., Helled R., Heng K., Jenkins J. M., Johansen A., Khodachenko M. L., Kislyakova K. G., Kley W., Kolb U., Krivova N., Kupka F., Lammer H., Lanza A. F., Lebreton Y., Magrin D., Marcos-Arenal P., Marrese P. M., Marques J. P., Martins J., Mathis S., Mathur S., Messina S., Miglio A., Montalban J., Montalto M., Monteiro M. J. P. F. G., Moradi H., Moravveji E., Mordasini C., Morel T., Mortier A., Nascimbeni V., Nelson R. P., Nielsen M. B., Noack L., Norton A. J., Ofir A., Oshagh M., Ouazzani R.-M., Pápics P., Parro V. C., Petit P., Plez B.,

Poretti E., Quirrenbach A., Ragazzoni R., Raimondo G., Rainer M., Reese D. R., Redmer R., Reffert S., Rojas-Ayala B., Roxburgh I. W., Salmon S., Santerne A., Schneider J., Schou J., Schuh S., Schunker H., Silva-Valio A., Silvotti R., Skillen I., Snellen I., Sohl F., Sousa S. G., Sozzetti A., Stello D., Strassmeier K. G., Švanda M., Szabó G. M., Tkachenko A., Valencia D., Van Grootel V., Vauclair S. D., Ventura P., Wagner F. W., Walton N. A., Weingrill J., Werner S. C., Wheatley P. J., Zwintz K., 2014, Experimental Astronomy, 38, 249

Rayleigh, 1879, The Philosophical Magazine and Journal of Science, 5th Series, 8, 49

Rice W. K. M., Armitage P. J., Hogg D. F., 2008, MNRAS, 384, 1242

Ricker G. R., Winn J. N., Vanderspek R., Latham D. W., Bakos G. Á., Bean J. L., Berta-Thompson Z. K., Brown T. M., Buchhave L., Butler N. R., Butler R. P., Chaplin W. J., Charbonneau D., Christensen-Dalsgaard J., Clampin M., Deming D., Doty J., De Lee N., Dressing C., Dunham E. W., Endl M., Fressin F., Ge J., Henning T., Holman M. J., Howard A. W., Ida S., Jenkins J., Jernigan G., Johnson J. A., Kaltenegger L., Kawai N., Kjeldsen H., Laughlin G., Levine A. M., Lin D., Lissauer J. J., MacQueen P., Marcy G., McCullough P. R., Morton T. D., Narita N., Paegert M., Palle E., Pepe F., Pepper J., Quirrenbach A., Rinehart S. A., Sasselov D., Sato B., Seager S., Sozzetti A., Stassun K. G., Sullivan P., Szentgyorgyi A., Torres G., Udry S., Villasenor J., 2014, Space Telescopes and Instrumentation 2014: Optical, Infrared, and Millimeter Wave, Proc. SPIE, Vol. 9143, p. 914320

Riess A. G., Filippenko A. V., Challis P., Clocchiatti A., Diercks A., Garnavich P. M., Gilliland R. L., Hogan C. J., Jha S., Kirshner R. P., Leibundgut B., Phillips M. M., Reiss D., Schmidt B. P., Schommer R. A., Smith R. C., Spyromilio J., Stubbs C., Suntzeff N. B., Tonry J., 1998, AJ, 116, 1009

Rigaut F., Gendron E., 1992, A&A, 261, 677

Rigaut F., 2015, PASP, 127, 1197

Robin A. C., Reylé C., Derrière S., Picaud S., 2003, A&A, 409, 523

Roell T., Neuhäuser R., Seifahrt A., Mugrauer M., 2012, A&A, 542, A92

Roettenbacher R. M., Monnier J. D., Korhonen H., Aarnio A. N., Baron F., Che X., Harmon R. O., Kővári Z., Kraus S., Schaefer G. H., Torres G., Zhao M., Ten Brummelaar T. A., Sturmann J., Sturmann L., 2016, Nature, 533, 217

Rouan D., Riaud P., Boccaletti A., Clénet Y., Labeyrie A., 2000, PASP, 112, 1479

Rowe J. F., Bryson S. T., Marcy G. W., Lissauer J. J., Jontof-Hutter D., Mullally F., Gilliland R. L., Issacson H., Ford E., Howell S. B., Borucki W. J., Haas M., Huber D., Steffen J. H., Thompson S. E., Quintana E., Barclay T., Still M., Fortney J., Gautier, III T. N., Hunter R., Caldwell D. A., Ciardi D. R., Devore E., Cochran W., Jenkins J., Agol E., Carter J. A., Geary J., 2014, ApJ, 784, 45

Sackett P. D., Gillon M., Bayliss D. D. R., Weldrake D. T. F., Tingley B., 2009, in Pont F., Sasselov D., Holman M. J., eds, Transiting Planets, IAU Symposium Vol. 253, p. 55

Safronov V. S., 1966, Soviet Ast., 9, 987

Safronov V. S., 1972, Evolution of the protoplanetary cloud and formation of the earth and planets.

Sahu K. C., Anderson J., Casertano S., Bond H. E., Bergeron P., Nelan E. P., Pueyo L., Brown T. M., Bellini A., Levay Z. G., Sokol J., aff1, Dominik M., Calamida A., Kains N., Livio M., 2017, Science, 356, 1046

Sajadian S., Rahvar S., Dominik M., Hundertmark M., 2016, MNRAS, 458, 3248

Sanchis-Ojeda R., Winn J. N., 2011, ApJ, 743, 61

Santerne A., Díaz R. F., Almenara J.-M., Bouchy F., Deleuil M., Figueira P., Hébrard G., Moutou C., Rodionov S., Santos N. C., 2015, MNRAS, 451, 2337

Santerne A., Moutou C., Tsantaki M., Bouchy F., Hébrard G., Adibekyan V., Almenara J.-M., Amard L., Barros S. C. C., Boisse I., Bonomo A. S., Bruno G., Courcol B., Deleuil M., Demangeon O., Díaz R. F., Guillot T., Havel M., Montagnier G., Rajpurohit A. S., Rey J., Santos N. C., 2016, A&A, 587, A64

Santos N. C., Israelian G., Mayor M., 2004, A&A, 415, 1153

Sarajedini A., Bedin L. R., Chaboyer B., Dotter A., Siegel M., Anderson J., Aparicio A., King I., Majewski S., Marín-Franch A., Piotto G., Reid I. N., Rosenberg A., 2007, AJ, 133, 1658

Scharmer G. B., Dettori P. M., Lofdahl M. G., Shand M., 2003, in Keil S. L., Avakyan S. V., eds, Innovative Telescopes and Instrumentation for Solar Astrophysics, Proc. SPIE, , Vol. 4853, p. 370

Schlafly E. F., Finkbeiner D. P., 2011, ApJ, 737, 103

Schmitt J. R., Tokovinin A., Wang J., Fischer D. A., Kristiansen M. H., LaCourse D. M., Gagliano R., Tan A. J. V., Schwengeler H. M., Omohundro M. R., Venner A., Terentev I., Schmitt A. R., Jacobs T. L., Winarski T., Sejpka J., Jek K. J., Boyajian T. S., Brewer J. M., Ishikawa S. T., Lintott C., Lynn S., Schawinski K., Schwamb M. E., Weiksnar A., 2016, AJ, 151, 159

Schröter S., Czesla S., Wolter U., Müller H. M., Huber K. F., Schmitt J. H. M. M., 2011, A&A, 532, A3

Service M., Lu J. R., Campbell R., Sitarski B. N., Ghez A. M., Anderson J., 2016, PASP, 128(9), 095004

Shabram M., Demory B.-O., Cisewski J., Ford E. B., Rogers L., 2016, ApJ, 820, 93

Shao M., Colavita M. M., 1992, ARA&A, 30, 457

Shporer A., Zhou G., Vanderburg A., Fulton B. J., Isaacson H., Bieryla A., Torres G., Morton T. D., Bento J., Berlind P., Calkins M. L., Esquerdo G. A., Howard A. W., Latham D. W., 2017, ApJL, 847, L18

Sinclair A. T., 1982, HMNAO Technical Notes, 59

Sinukoff E., Howard A. W., Petigura E. A., Schlieder J. E., Crossfield I. J. M., Ciardi D. R., Fulton B. J., Isaacson H., Aller K. M., Baranec C., Beichman C. A., Hansen B. M. S., Knutson H. A., Law N. M., Liu M. C., Riddle R., Dressing C. D., 2016, ApJ, 827, 78

Skottfelt J., Bramich D. M., Figuera Jaimes R., Jørgensen U. G., Kains N., Harpsøe K. B. W., Liebig C., Penny M. T., Alsubai K. A., Andersen J. M., Bozza V., Browne P., Calchi Novati S., Damerdji Y., Diehl C., Dominik M., Elyiv A., Giannini E., Hessman F., Hinse T. C., Hundertmark M., Juncher D., Kerins E., Korhonen H., Mancini L., Martin R., Rabus M., Rahvar S., Scarpetta G., Southworth J., Snodgrass C., Street R. A., Surdej J., Tregloan-Reed J., Vilela C., Williams A., 2013, A&A, 553, A111

Skottfelt J., Bramich D. M., Figuera Jaimes R., Jørgensen U. G., Kains N., Arellano Ferro A., Alsubai K. A., Bozza V., Calchi Novati S., Ciceri S., D'Ago G., Dominik M., Galianni P., Gu S.-H., Harpsøe K. B. W., Haugbølle T., Hinse T. C., Hundertmark M., Juncher D., Korhonen H., Liebig C., Mancini L., Popovas A., Rabus M., Rahvar S., Scarpetta G., Schmidt R. W., Snodgrass C., Southworth J., Starkey D., Street R. A., Surdej J., Wang X.-B., Wertz O., 2015a, A&A, 573, A103

Skottfelt J., Bramich D. M., Hundertmark M., Jørgensen U. G., Michaelsen N., Kjærgaard P., Southworth J., Sørensen A. N., Andersen M. F., Andersen M. I., Christensen-Dalsgaard J., Frandsen S., Grundahl F., Harpsøe K. B. W., Kjeldsen H., Pallé P. L., 2015b, A&A, 574, A54

Skrutskie M. F., Cutri R. M., Stiening R., Weinberg M. D., Schneider S., Carpenter J. M., Beichman C., Capps R., Chester T., Elias J., Huchra J., Liebert J., Lonsdale C., Monet D. G., Price S., Seitzer P., Jarrett T., Kirkpatrick J. D., Gizis J. E., Howard E., Evans T., Fowler J., Fullmer L., Hurt R., Light R., Kopan E. L., Marsh K. A., McCallon H. L., Tam R., Van Dyk S., Wheelock S., 2006, AJ, 131, 1163

Smalley B., Anderson D. R., Collier Cameron A., Gillon M., Hellier C., Lister T. A., Maxted P. F. L., Queloz D., Triaud A. H. M. J., West R. G., Bentley S. J., Enoch B., Pepe F., Pollacco D. L., Segransan D., Smith A. M. S., Southworth J., Udry S., Wheatley P. J., Wood P. L., Bento J., 2010, A&A, 520, A56

Smith R. M., Zavodny M., Rahmer G., Bonati M., 2008, High Energy, Optical, and Infrared Detectors for Astronomy III, Proc. SPIE, Vol. 7021, p. 70210J

Smith A. M. S., Anderson D. R., Collier Cameron A., Gillon M., Hellier C., Lendl M., Maxted P. F. L., Queloz D., Smalley B., Triaud A. H. M. J., West R. G., Barros S. C. C., Jehin E., Pepe F., Pollacco D., Segransan D., Southworth J., Street R. A., Udry S., 2012, AJ, 143, 81

Soummer R., Pueyo L., Larkin J., 2012, ApJL, 755, L28

Southworth J., 2009, MNRAS, 394, 272

Southworth J., 2010, MNRAS, 408, 1689

Southworth J., 2011, MNRAS, 417, 2166

Southworth J., 2012, MNRAS, 426, 1291

Southworth J., 2013, A&A, 557, A119

Southworth J., 2015, in Rucinski S. M., Torres G., Zejda M., eds, Living Together: Planets, Host Stars and Binaries, Astronomical Society of the Pacific Conference Series Vol. 496, p. 164

Southworth J., Hinse T. C., Jørgensen U. G., Dominik M., Ricci D., Burgdorf M. J., Hornstrup A., Wheatley P. J., Anguita T., Bozza V., Novati S. C., Harpsøe K., Kjærgaard P., Liebig C., Mancini L., Masi G., Mathiasen M., Rahvar S., Scarpetta G., Snodgrass C., Surdej J., Thöne C. C., Zub M., 2009, MNRAS, 396, 1023

Southworth J., Hinse T. C., Burgdorf M., Calchi Novati S., Dominik M., Galianni P., Gerner T., Giannini E., Gu S.-H., Hundertmark M., Jørgensen U. G., Juncher D., Kerins E., Mancini L., Rabus M., Ricci D., Schäfer S., Skottfelt J., Tregloan-Reed J., Wang X.-B., Wertz O., Alsubai K. A., Andersen J. M., Bozza V., Bramich D. M., Browne P., Ciceri S., D'Ago G., Damerdji Y., Diehl C., Dodds P., Elyiv A., Fang X.-S., Finet F., Figuera Jaimes R., Hardis S., Harpsøe K., Jessen-Hansen J., Kains N., Kjeldsen H., Korhonen H., Liebig C., Lund M. N., Lundkvist M., Mathiasen M., Penny M. T., Popovas A., Prof. S., Rahvar S., Sahu K., Scarpetta G., Schmidt R. W., Schönebeck F., Snodgrass C., Street R. A., Surdej J., Tsapras Y., Vilela C., 2014, MNRAS, 444, 776

Stark D. P., Swinbank A. M., Ellis R. S., Dye S., Smail I. R., Richard J., 2008, Nature, 455, 775

Stassun K. G., Mathieu R. D., Vaz L. P. R., Stroud N., Vrba F. J., 2004, ApJS, 151, 357

Steffen J. H., Ragozzine D., Fabrycky D. C., Carter J. A., Ford E. B., Holman M. J., Rowe J. F., Welsh W. F., Borucki W. J., Boss A. P., Ciardi D. R., Quinn S. N., 2012, Proceedings of the National Academy of Science, 109, 7982

Stetson P. B., 1987, PASP, 99, 191

Storch N. I., Lai D., 2015, MNRAS, 448, 1821

Storch N. I., Anderson K. R., Lai D., 2014, Science, 345, 1317

Straižys V., Lazauskaitė R., 2009, Baltic Astronomy, 18, 19

Street R. A., Simpson E., Barros S. C. C., Pollacco D., Joshi Y., Todd I., Collier Cameron A., Enoch B., Parley N., Stempels E., Hebb L., Triaud A. H. M. J., Queloz D., Segransan D., Pepe F., Udry S., Lister T. A., Depagne É., West R. G.,

Norton A. J., Smalley B., Hellier C., Anderson D. R., Maxted P. F. L., Bentley S. J., Skillen I., Gillon M., Wheatley P., Bento J., Cathaway-Kjontvedt P., Christian D. J., 2010, ApJ, 720, 337

Street R. A., Udalski A., Calchi Novati S., Hundertmark M. P. G., Zhu W., Gould A., Yee J., Tsapras Y., Bennett D. P., RoboNet Project, MiNDSTEp Consortium, Jørgensen U. G., Dominik M., Andersen M. I., Bachelet E., Bozza V., Bramich D. M., Burgdorf M. J., Cassan A., Ciceri S., D'Ago G., Dong S., Evans D. F., Gu S.-h., Harkonnen H., Hinse T. C., Horne K., Figuera Jaimes R., Kains N., Kerins E., Korhonen H., Kuffmeier M., Mancini L., Menzies J., Mao S., Peixinho N., Popovas A., Rabus M., Rahvar S., Ranc C., Tronsgaard Rasmussen R., Scarpetta G., Schmidt R., Skottfelt J., Snodgrass C., Southworth J., Steele I. A., Surdej J., Unda-Sanzana E., Verma P., von Essen C., Wambsganss J., Wang Y.-B., Wertz O., OGLE Project, Poleski R., Pawlak M., Szymański M. K., Skowron J., Mróz P., Kozłowski S., Wyrzykowski Ł., Pietrukowicz P., Pietrzyński G., Soszyński I., Ulaczyk K., Spitzer Team, Beichman C., Bryden G., Carey S., Gaudi B. S., Henderson C. B., Pogge R. W., Shvartzvald Y., MOA Collaboration, Abe F., Asakura Y., Bhattacharya A., Bond I. A., Donachie M., Freeman M., Fukui A., Hirao Y., Inayama K., Itow Y., Koshimoto N., Li M. C. A., Ling C. H., Masuda K., Matsubara Y., Muraki Y., Nagakane M., Nishioka T., Ohnishi K., Oyokawa H., Rattenbury N., Saito T., Sharan A., Sullivan D. J., Sumi T., Suzuki D., Tristram J., Wakiyama Y., Yonehara A., KMTNet Modeling Team, Han C., Choi J.-Y., Park H., Jung Y. K., Shin I.-G., 2016, ApJ, 819, 93

Temple L. Y., Hellier C., Albrow M. D., Anderson D. R., Bayliss D., Beatty T. G., Bieryla A., Brown D. J. A., Cargile P. A., Collier Cameron A., Collins K. A., Colón K. D., Curtis I. A., D'Ago G., Delrez L., Eastman J., Gaudi B. S., Gillon M., Gregorio J., James D., Jehin E., Joner M. D., Kielkopf J. F., Kuhn R. B., Labadie-Bartz J., Latham D. W., Lendl M., Lund M. B., Malpas A. L., Maxted P. F. L., Myers G., Oberst T. E., Pepe F., Pepper J., Pollacco D., Queloz D., Rodriguez J. E., Ségransan D., Siverd R. J., Smalley B., Stassun K. G., Stevens

D. J., Stockdale C., Tan T. G., Triaud A. H. M. J., Udry S., Villanueva S., West R. G., Zhou G., 2017, MNRAS, 471, 2743

ten Brummelaar T. A., McAlister H. A., Ridgway S. T., Bagnuolo, Jr. W. G., Turner N. H., Sturmann L., Sturmann J., Berger D. H., Ogden C. E., Cadman R., Hartkopf W. I., Hopper C. H., Shure M. A., 2005, ApJ, 628, 453

Teske J. K., Khanal S., Ramírez I., 2016, ApJ, 819, 19

Thalmann C., Schmid H. M., Boccaletti A., Mouillet D., Dohlen K., Roelfsema R., Carbillet M., Gisler D., Beuzit J.-L., Feldt M., Gratton R., Joos F., Keller C. U., Kragt, II J., Pragt J. H., Puget P., Rigal F., Snik F., Waters R., Wildi F., 2008, Ground-based and Airborne Instrumentation for Astronomy II, Proc. SPIE, Vol. 7014, p. 70143F

Thompson L. A., Ryerson H. R., 1984, in Boksenberg A., Crawford D. L., eds, Instrumentation in astronomy V, Proc. SPIE, Vol. 445, p. 560

Tody D., 1986, in Crawford D. L., ed., Instrumentation in astronomy VI, Proc. SPIE, Vol. 627, p. 733

Tody D., 1993, in Hanisch R. J., Brissenden R. J. V., Barnes J., eds, Astronomical Data Analysis Software and Systems II, Astronomical Society of the Pacific Conference Series Vol. 52, p. 173

Tokovinin A. A., 1982, Soviet Astronomy Letters, 8, 43

Tokovinin A., 2004, PASP, 116, 941

Tokovinin A., Thomas S., Sterzik M., Udry S., 2006, A&A, 450, 681

Tokovinin A., Mason B. D., Hartkopf W. I., Mendez R. A., Horch E. P., 2015, AJ, 150, 50

Tokovinin A., Mason B. D., Hartkopf W. I., Mendez R. A., Horch E. P., 2016, AJ, 151, 153

Tokovinin A., Mason B. D., Hartkopf W. I., 2010, AJ, 139, 743

Toomre A., 1964, ApJ, 139, 1217

Torres G., Fressin F., Batalha N. M., Borucki W. J., Brown T. M., Bryson S. T., Buchhave L. A., Charbonneau D., Ciardi D. R., Dunham E. W., Fabrycky D. C., Ford E. B., Gautier, III T. N., Gilliland R. L., Holman M. J., Howell S. B., Isaacson H., Jenkins J. M., Koch D. G., Latham D. W., Lissauer J. J., Marcy G. W., Monet D. G., Prsa A., Quinn S. N., Ragozzine D., Rowe J. F., Sasselov D. D., Steffen J. H., Welsh W. F., 2011, ApJ, 727, 24

Triaud A. H. M. J., 2017, ArXiv e-prints

Triaud A. H. M. J., Anderson D. R., Collier Cameron A., Doyle A. P., Fumel A., Gillon M., Hellier C., Jehin E., Lendl M., Lovis C., Maxted P. F. L., Pepe F., Pollacco D., Queloz D., Ségransan D., Smalley B., Smith A. M. S., Udry S., West R. G., Wheatley P. J., 2013a, A&A, 551, A80

Triaud A. H. M. J., Hebb L., Anderson D. R., Cargile P., Collier Cameron A., Doyle A. P., Faedi F., Gillon M., Gomez Maqueo Chew Y., Hellier C., Jehin E., Maxted P., Naef D., Pepe F., Pollacco D., Queloz D., Ségransan D., Smalley B., Stassun K., Udry S., West R. G., 2013b, A&A, 549, A18

Triaud A. H. M. J., Martin D. V., Ségransan D., Smalley B., Maxted P. F. L., Anderson D. R., Bouchy F., Collier Cameron A., Faedi F., Gómez Maqueo Chew Y., Hebb L., Hellier C., Marmier M., Pepe F., Pollacco D., Queloz D., Udry S., West R., 2017, A&A, 608, A129

Trilling D. E., Benz W., Guillot T., Lunine J. I., Hubbard W. B., Burrows A., 1998, ApJ, 500, 428

Tsiganis K., Gomes R., Morbidelli A., Levison H. F., 2005, Nature, 435, 459

Tubbs R. N., Baldwin J. E., Mackay C. D., Cox G. C., 2002, A&A, 387, L21

Turner O. D., Anderson D. R., Collier Cameron A., Delrez L., Evans D. F., Gillon M., Hellier C., Jehin E., Lendl M., Maxted P. F. L., Pepe F., Pollacco D., Queloz D., Ségransan D., Smalley B., Smith A. M. S., Triaud A. H. M. J., Udry S., West R. G., 2016, PASP, 128(6), 064401

Valencic L. A., Clayton G. C., Gordon K. D., 2004, ApJ, 616, 912

van Cittert P. H., 1934, Physica, 1, 201

van der Marel R. P., Anderson J., Cox C., Kozhurina-Platais V., Lallo M., Nelan E., 2007, Technical Report

Van Eylen V., Nowak G., Albrecht S., Palle E., Ribas I., Bruntt H., Perger M., Gandolfi D., Hirano T., Sanchis-Ojeda R., Kiilerich A., Prieto-Arranz J., Badenas M., Dai F., Deeg H. J., Guenther E. W., Montañés-Rodríguez P., Narita N., Rogers L. A., Béjar V. J. S., Shrotriya T. S., Winn J. N., Sebastian D., 2016, ApJ, 820, 56

Vanderburg A., Montet B. T., Johnson J. A., Buchhave L. A., Zeng L., Pepe F., Collier Cameron A., Latham D. W., Molinari E., Udry S., Lovis C., Matthews J. M., Cameron C., Law N., Bowler B. P., Angus R., Baranec C., Bieryla A., Boschin W., Charbonneau D., Cosentino R., Dumusque X., Figueira P., Guenther D. B., Harutyunyan A., Hellier C., Kuschnig R., Lopez-Morales M., Mayor M., Micela G., Moffat A. F. J., Pedani M., Phillips D. F., Piotto G., Pollacco D., Queloz D., Rice K., Riddle R., Rowe J. F., Rucinski S. M., Sasselov D., Ségransan D., Sozzetti A., Szentgyorgyi A., Watson C., Weiss W. W., 2015, ApJ, 800, 59

Vanhollebeke E., Groenewegen M. A. T., Girardi L., 2009, A&A, 498, 95

Vazan A., Helled R., 2012, ApJ, 756, 90

Vigan A., Moutou C., Langlois M., Allard F., Boccaletti A., Carbillet M., Mouillet D., Smith I., 2010, MNRAS, 407, 71

Vigan A., Gry C., Salter G., Mesa D., Homeier D., Moutou C., Allard F., 2015, MNRAS, 454, 129

Wallace P. T., 1994, in Crabtree D. R., Hanisch R. J., Barnes J., eds, Astronomical Data Analysis Software and Systems III, Astronomical Society of the Pacific Conference Series Vol. 61, p. 481

Weidenschilling S. J., Marzari F., 1996, Nature, 384, 619

Weiss L. M., Marcy G. W., 2014, ApJL, 783, L6

Weldrake D. T. F., Bayliss D. D. R., Sackett P. D., Tingley B. W., Gillon M., Setiawan J., 2008, ApJL, 675, L37

Wheatley P. J., West R. G., Goad M. R., Jenkins J. S., Pollacco D. L., Queloz D., Rauer H., Udry S., Watson C. A., Chazelas B., Eigmüller P., Lambert G., Genolet L., McCormac J., Walker S., Armstrong D. J., Bayliss D., Bento J., Bouchy F., Burleigh M. R., Cabrera J., Casewell S. L., Chaushev A., Chote P., Csizmadia S., Erikson A., Faedi F., Foxell E., Gänsicke B. T., Gillen E., Grange A., Günther M. N., Hodgkin S. T., Jackman J., Jordán A., Louden T., Metrailler L., Moyano M., Nielsen L. D., Osborn H. P., Poppenhaeger K., Raddi R., Raynard L., Smith A. M. S., Soto M., Titz-Weider R., 2018, MNRAS, 475, 4476

Winn J. N., Fabrycky D., Albrecht S., Johnson J. A., 2010, ApJL, 718, L145

Winn J. N., Petigura E. A., Morton T. D., Weiss L. M., Dai F., Schlaufman K. C., Howard A. W., Isaacson H., Marcy G. W., Justesen A. B., Albrecht S., 2017, AJ, 154, 270

Wöllert M., Brandner W., 2015, A&A, 579, A129

Wöllert M., Brandner W., Bergfors C., Henning T., 2015, A&A, 575, A23

Wolszczan A., Frail D. A., 1992, Nature, 355, 145

Woolfson M. M., 1993, QJRAS, 34

Wright J. T., Marcy G. W., Howard A. W., Johnson J. A., Morton T. D., Fischer D. A., 2012, ApJ, 753, 160

Wu Y., Lithwick Y., 2011, ApJ, 735, 109

Wu Y., Murray N., 2003, ApJ, 589, 605

Wu Y., Murray N. W., Ramsahai J. M., 2007, ApJ, 670, 820

Xiang-Gruess M., 2016, MNRAS, 455, 3086

Youdin A. N., 2011, ApJ, 742, 38

Young A. T., 1967, AJ, 72, 747

Yu L., Donati J.-F., Hébrard E. M., Moutou C., Malo L., Grankin K., Hussain G., Collier Cameron A., Vidotto A. A., Baruteau C., Alencar S. H. P., Bouvier J., Petit P., Takami M., Herczeg G., Gregory S. G., Jardine M., Morin J., Ménard F., Matysse Collaboration, 2017, MNRAS, 467, 1342

Yuan H. B., Liu X. W., Xiang M. S., 2013, MNRAS, 430, 2188

Zacharias N., Monet D. G., Levine S. E., Urban S. E., Gaume R., Wycoff G. L., 2004, American Astronomical Society Meeting Abstracts, Bulletin of the American Astronomical Society Vol. 36, p. 1418

Zernike F., 1934, MNRAS, 94, 377

Zernike F., 1938, Physica, 5, 785

Zhou G., Bakos G. Á., Hartman J. D., Latham D. W., Torres G., Bhatti W., Penev K., Buchhave L., Kovács G., Bieryla A., Quinn S., Isaacson H., Fulton B. J., Falco E., Csubry Z., Everett M., Szklenar T., Esquerdo G., Berlind P., Calkins M. L., Béky B., Knox R. P., Hinz P., Horch E. P., Hirsch L., Howell S. B., Noyes R. W., Marcy G., de Val-Borro M., Lázár J., Papp I., Sári P., 2017, AJ, 153, 211

Ziegler C., Law N. M., Morton T., Baranec C., Riddle R., Atkinson D., Baker A., Roberts S., Ciardi D. R., 2017, AJ, 153, 66

Ziegler C., Law N. M., Baranec C., Howard W., Morton T., Riddle R., Duev D. A., Salama M., Jensen-Clem R., Kulkarni S. R., 2018, AJ, 156, 83